KARAGANDA BUKETOV UNIVERSITY

ISSN 2518-7198 (Print)
ISSN 2663-5089 (Online)

BULLETIN
OF THE KARAGANDA UNIVERSITY

PHYSICS Series

Special Issue
Radiation processes in condensed matter

***Guest Editors*:**
Doctor of phys.-math. sciences, Professor,
Honored Scientist of the Russian Federation V.M. Lisitsyn

EFRE

9th International Congress on Energy Fluxes
and Radiation Effects (EFRE-2024)

16.09.2024-21.09.2024Tomsk, Russia

22nd SHCE
International Symposium on
High Current Electronics

16th CMM
International Conference on Modification of Materials
with Particle Beams and Plasma Flows

20th RPC
International Conference on Radiation Physics
and Chemistry of Condensed Matter

5th NMHT
International Conference on New Materials
and High Technologies

2024 • Volume 29 • Issue 4(116)

ISSN 2663-5089 (Online)
ISSN-L 2518-7198 (Print)
Индексі 74616
Индекс 74616

ҚАРАҒАНДЫ УНИВЕРСИТЕТІНІҢ ХАБАРШЫСЫ

ВЕСТНИК КАРАГАНДИНСКОГО УНИВЕРСИТЕТА

BULLETIN OF THE KARAGANDA UNIVERSITY

ФИЗИКА сериясы
Серия ФИЗИКА
PHYSICS Series

2024

Арнайы шығарылым / Специальный выпуск / Special issue

Конденсацияланған орталардағы радиациялық процестер
Радиационные процессы в конденсированных средах
Radiation processes in condensed matter

29-том • 4(116)-шығарылым
Том 29 • Выпуск 4(116)
Volume 29 • Issue 4(116)

1996 жылдан бастап шығады
Издается с 1996 года
Founded in 1996

Жылына 4 рет шығады
Выходит 4 раза в год
Published 4 times a year

Қарағанды / Караганда / Karaganda
2024

Бас редакторы

физ.-мат. ғыл. канд., проф. **А.К. Аймуханов**

Жауапты хатшы

PhD д-ры, қауымд. проф. **Д.Ж. Қарабекова**

Шақырылған редактор

физ.-мат. ғыл. д-ры, проф., Ресей Федерациясының ғылымына еңбек сіңірген қайраткер **В.М. Лисицын**

Редакция алқасы

Н.Х. Ибраев,	физ.-мат. ғыл. д-ры, проф., акад. Е.А. Бөкетов атындағы Қарағанды университеті (Қазақстан);
Б.Р. Нүсіпбеков,	техн. ғыл. канд., проф., акад. Е.А. Бөкетов атындағы Қарағанды университеті (Қазақстан);
А.О. Сәулебеков,	физ.-мат. ғыл. д-ры, проф., М.В. Ломоносов атындағы Мәскеу мемлекеттік университетінің Қазақстан филиалы, Астана (Қазақстан);
Б.Р. Ильясов,	PhD д-ры, қауымд. проф., Astana IT University, Астана (Қазақстан);
А.Д. Погребняк,	физ.-мат. ғыл. д-ры, проф., Сумы мемлекеттік университеті (Украина);
А.П. Суржиков,	физ.-мат. ғыл. д-ры, проф., Томск политехникалық университеті (Ресей);
И.П. Курытник,	техн. ғыл. д-ры, проф., Освенцимдегі В. Пилецкий атындағы Мемлекеттік жоғары кәсіптік мектебі (Польша);
М. Стоев,	PhD д-ры, инженерия д-ры, «Неофит Рильский» Оңтүстік-Батыс университеті, Благоевград (Болгария);
В.Ю. Кучерук,	техн. ғыл. д-ры, проф., Винница ұлттық техникалық университеті (Украина);
В.А. Кульбачинский,	физ.-мат. ғыл. д-ры, проф., М.В. Ломоносов атындағы Мәскеу мемлекеттік университеті (Ресей);
Bisquert Juan,	проф., физика проф., Хайме I университеті, Кастельо-де-ла-Плана (Испания);
Chun Li,	PhD д-ры, Чанчунь ғылым және технология университеті (Қытай);
Д.Т. Валиев,	физ.-мат. ғыл. канд., доц., Томск ұлттық политехникалық зерттеу университеті (Ресей);
Н.Қ. Танашева,	PhD д-ры, қауымд. проф., акад. Е.А. Бөкетов атындағы Қарағанды университеті (Қазақстан)

Редакцияның мекенжайы: 100024, Қазақстан, Қарағанды қ., Университет к-сі, 28
E-mail: vestnikku@gmail.com; karabekova71@mail.ru
Сайты: physics-vestnik.ksu.kz

Атқарушы редактор

PhD д-ры **Г.Б. Саржанова**

Корректорлары

Ж.Т. Нурмуханова, С.С. Балкеева, И.Н. Муртазина

Компьютерде беттеген

К.А. Форостьянова

Қарағанды университетінің хабаршысы. «Физика» сериясы. Арнайы шығарылым: Конденсацияланған орталардағы радиациялық процестер. — 2024. — 29-т., 4(116)-шығ. — 185 б. — ISSN-L 2518-7198 (Print). ISSN 2663-5089 (Online).

Меншік иесі: «Академик Е.А. Бөкетов атындағы Қарағанды университеті» КЕАҚ.

Қазақстан Республикасы Ақпарат және қоғамдық даму министрлігімен тіркелген. 30.09.2020 ж. № KZ38VPY00027378 қайта есепке қою туралы куәлігі.

Басуға 30.12.2024 ж. қол қойылды. Пішімі 60×84 1/8. Қағазы офсеттік. Көлемі 23,12 б.т. Таралымы 200 дана. Бағасы келісім бойынша. Тапсырыс № 127.

«Акад. Е.А. Бөкетов ат. Қарағанды ун-ті» КЕАҚ баспасының баспаханасында басылып шықты.
100024, Қазақстан, Қарағанды қ., Университет к-сі, 28. Тел. (7212) 35-63-16. E-mail: izd_karu@buketov.edu.kz

© Академик Е.А. Бөкетов атындағы Қарағанды университеті, 2024

Главный редактор

канд. физ.-мат. наук, проф. **А.К. Аймуханов**

Ответственный секретарь

д-р PhD, ассоц. проф. **Д.Ж. Карабекова**

Гостевой редактор

д-р физ.-мат. наук, проф., Заслуженный деятель науки Российской Федерации **В.М. Лисицын**

Редакционная коллегия

Н.Х. Ибраев,	д-р физ.-мат. наук, проф., Карагандинский университет им. акад. Е.А. Букетова (Казахстан);
Б.Р. Нусупбеков,	канд. техн. наук, проф., Карагандинский университет им. акад. Е.А. Букетова (Казахстан);
А.О. Саулебеков,	д-р физ.-мат. наук, проф., Казахстанский филиал Московского государственного университета им. М.В. Ломоносова, Астана (Казахстан);
Б.Р. Ильясов,	д-р PhD, ассоц. проф., Astana IT University, Астана (Казахстан);
А.Д. Погребняк,	д-р физ.-мат. наук, проф., Сумской государственный университет (Украина);
А.П. Суржиков,	д-р физ.-мат. наук, проф., Томский политехнический университет (Россия);
И.П. Курытник,	д-р техн. наук, проф., Государственная высшая профессиональная школа им. В. Пилецкого в Освенциме (Польша);
М. Стоев,	д-р PhD, д-р инженерии, Юго-Западный университет «Неофит Рильский», Благоевград (Болгария);
В.Ю. Кучерук,	д-р техн. наук, проф., Винницкий национальный технический университет (Украина);
В.А. Кульбачинский,	д-р физ.-мат. наук, проф., Московский государственный университет им. М.В. Ломоносова (Россия);
Bisquert Juan,	проф., проф. физики, Университет Хайме I, Кастельо-де-ла-Плана (Испания);
Chun Li,	д-р PhD, Чанчуньский университет науки и технологии (Китай);
Д.Т. Валиев,	канд. физ.-мат. наук, доц., Национальный исследовательский Томский политехнический университет (Россия);
Н.К. Танашева,	д-р PhD, ассоц. проф., Карагандинский университет им. акад. Е.А. Букетова (Казахстан)

Адрес редакции: 100024, Казахстан, г. Караганда, ул. Университетская, 28
E-mail: vestnikku@gmail.com; karabekova71@mail.ru
Сайт: physics-vestnik.ksu.kz

Исполнительный редактор

д-р PhD **Г.Б. Саржанова**

Корректоры

Ж.Т. Нурмуханова, С.С. Балкеева, И.Н. Муртазина

Компьютерная верстка

К.А. Форостьянова

Вестник Карагандинского университета. Серия «Физика». Спец. вып.: Радиационные процессы в конденсированных средах. — 2024. — Т. 29, вып. 4(116). — 185 с. — ISSN-L 2518-7198 (Print). ISSN 2663-5089 (Online).

Собственник: НАО «Карагандинский университет имени академика Е.А. Букетова».

Зарегистрирован Министерством информации и общественного развития Республики Казахстан. Свидетельство о постановке на переучет № KZ38VPY00027378 от 30.09.2020 г.

Подписано в печать 30.12.2024 г. Формат 60×84 1/8. Бумага офсетная. Объем 23,12 п.л. Тираж 200 экз. Цена договорная. Заказ № 127.

Отпечатано в типографии издательства НАО «Карагандинский университет им. акад. Е.А. Букетова».
100024, Казахстан, г. Караганда, ул. Университетская, 28. Тел.(7212) 35-63-16. E-mail: izd_karu@buketov.edu.kz

© Карагандинский университет им. акад. Е.А. Букетова, 2024

Chief Editor
Professor, Cand. of Phys. and Math. Sci. **A.K. Aimukhanova**

Responsible secretary
Associate Professor, PhD **D.Zh. Karabekova**

Guest Editor
Doctor of phys.-math. sciences, Professor, Honored Scientist of the Russian Federation **V.M. Lisitsyn**

Editorial board

N.Kh. Ibrayev,	Prof., Doctor of phys.-math. sciences, Karagandy University of the name of acad. E.A. Buketov (Kazakhstan);
B.R. Nussupbekov,	Prof., Cand. of techn. sciences, Karagandy University of the name of acad. E.A. Buketov (Kazakhstan);
A.O. Saulebekov,	Prof., Doctor of phys.-math. sciences, Kazakhstan branch of Lomonosov Moscow State University, Astana (Kazakhstan);
B.R. Ilyassov,	PhD, Assoc. Prof., Astana IT University (Kazakhstan);
A.D. Pogrebnjak,	Prof., Doctor of phys.-math. sciences, Sumy State University (Ukraine);
A.P. Surzhikov,	Prof., Doctor of phys.-math. sciences, Tomsk Polytechnic University (Russia);
I.P. Kurytnik,	Prof., Doctor of techn. sciences, The State School of Higher Education in Oświęcim (Auschwitz) (Poland);
M. Stoev,	PhD, Doctor of engineering, South-West University “Neofit Rilski”, Blagoevgrad (Bulgaria);
V.Yu. Kucheruk,	Prof., Doctor of techn. sciences, Vinnytsia National Technical University, Vinnitsia (Ukraine);
V.A. Kulbachinskii,	Prof., Doctor of phys.-math. sciences, Lomonosov Moscow State University (Russia);
Bisquert Juan,	Prof. of phys., Prof. (Full), Universitat Jaume I, Castellon de la Plana (Spain);
Chun Li,	PhD, Changchun University of Science and Technology (China);
D.T. Valiev,	Assoc. Prof., Cand. of phys.-math. sciences, National Research Tomsk Polytechnic University (Russia);
N.K. Tanasheva,	PhD, Assoc. Prof., Karagandy University of the name of acad. E.A. Buketov (Kazakhstan)

Postal address: 28, University Str., 100024, Karaganda, Kazakhstan
E-mail: vestnikku@gmail.com; karabekova71@mail.ru
Web-site: physics-vestnik.ksu.kz

Executive Editor
PhD **G.B. Sarzhanova**

Proofreaders
Zh.T. Nurmukhanova, S.S. Balkeyeva, I.N. Murtazina

Computer layout
K.A. Forostyanova

Bulletin of the Karaganda University. “Physics” Series. Special issue: Radiation processes in condensed matter. — 2024. — Vol. 29, Iss. 4(116). — 185 p. — ISSN-L 2518-7198 (Print). ISSN 2663-5089 (Online).

Proprietary: NLC “Karagandy University of the name of academician E.A. Buketov”.

Registered by the Ministry of Information and Social Development of the Republic of Kazakhstan. Rediscount certificate No. KZ38VPY00027378 dated 30.09.2020.

Signed in print 30.12.2024. Format 60×84 1/8. Offset paper. Volume 23,12 p.sh. Circulation 200 copies. Price upon request. Order № 127.

Printed in the Publishing house of NLC “Karagandy University of the name of acad. E.A. Buketov”.
28, University Str., Karaganda, 100024, Kazakhstan. Tel. (7212) 35-63-16. E-mail: izd_karu@buketov.edu.kz

© Karagandy University of the name of academician E.A. Buketov, 2024

МАЗМҰНЫ – СОДЕРЖАНИЕ – CONTENTS

КОНДЕНСАЦИЯЛАНҒАН ОРТАЛАРДАҒЫ РАДИАЦИЯЛЫҚ ПРОЦЕСТЕР
РАДИАЦИОННЫЕ ПРОЦЕССЫ В КОНДЕНСИРОВАННЫХ СРЕДАХ
RADIATION PROCESSES IN CONDENSED MATTER

PREFACE
ПРЕДИСЛОВИЕ
АЛҒЫСӨЗ

Dear colleagues!

Our special issue is devoted to the latest research and achievements in the field of radiation physics of condensed matter, reported by the authors at the 9th International Congress on Energy Fluxes and Radiation Effects (EFRE-2024), which was held from September 16 to 21, 2024. The International Congress EFRE-2024 is a traditional scientific event, which is held every two years and consists of 4 major conferences with a half-century history. More than 600 scientists from all over the world took part in the Congress, including scientists from Kazakhstan who were very active.

The field of science radiation physics of condensed matter is a rapidly developing area of research with significant potential for practical application: in medicine — tomography, treatment, sterilization of medical products, in engineering — introscopy, flaw detection, in technology — coating application, surface treatment, cutting, welding, spraying, synthesis, in science — information about space, structural and elemental analysis. Each specific application of specific materials requires in-depth studies of the nature of processes in materials to achieve optimal solutions. To generate radiation flows for such different applications, many different electrophysical installations and control devices have been and are being developed, ensuring the required quality of radiation exposure. For the purposes of radiation protection prevention, means and materials are needed to monitor the radiation situation, study radiation fields of different types and energies in the range from ultraviolet to infinity. The range of materials exposed to radiation has no boundaries. There are no and cannot be identical recommendations for each specific situation. Nevertheless, there are and are developing general ideas about radiation-initiated processes in condensed matter. The articles presented in this issue of the journal demonstrate the breadth of problems facing radiation physics of condensed matter.

All submitted articles have undergone a rigorous peer review process. We hope that the submitted articles will make a significant contribution to the overall development of science at the global level.

With respect,
Doctor of Physical and Mathematical Sciences, Professor of Tomsk Polytechnic University,
Honored Scientist of the Russian Federation
Viktor Lisitsyn

Уважаемые коллеги!

Наш Специальный выпуск журнала посвящен последним исследованиям и достижениям в области, связанной с проблемами радиационной физики конденсированного состояния, озвученным авторами на очередном IX Международном конгрессе по потокам энергии и радиационным эффектам (EFRE–2024), проходившем в г. Томске с 16 по 21 сентября 2024 года.

Международный конгресс EFRE–2024 представляет собой традиционное научное мероприятие, которое проводится с периодичностью в два года и состоит из 4-х крупных конференций, имеющих полувековую историю. В работе Конгресса приняли участие более 600 ученых со всего мира, в том числе большую активность проявили ученые из Казахстана.

Радиационная физика конденсированного состояния является быстро развивающейся областью исследований со значительным потенциалом для практического применения: в медицине — томография, лечение, стерилизация медицинских препаратов; в технике — интроскопия, дефектоскопия; в технологиях — нанесение покрытий, обработка поверхностей, резка, сварка, распыление, синтез; в науке — информация о космосе, структурный и элементный анализ.

Каждое конкретное использование конкретных материалов требует глубоких исследований природы процессов в материалах для достижения оптимальных решений. Для генерации потоков радиации столь разных применений разработано и изобретаются разнообразные электрофизические установки, приборы контроля, обеспечивающие нужное качество радиационного воздействия. В целях профилактики защиты от радиации необходимы средства и материалы осуществления контроля радиационной обстановки, изучения полей радиации разных видов и энергий в диапазоне от ультрафиолета до бесконечности. Круг материалов, подвергаемых радиационному воздействию, не имеет границ. Недопустимы одинаковые рекомендации для каждой конкретной ситуации. Тем не менее есть и развиваются общие представления об инициируемых радиацией процессах в конденсированных средах.

Представленные в настоящем выпуске журнала статьи демонстрируют широту проблем, которые стоят сегодня перед радиационной физикой конденсированного состояния. Все научные работы прошли строгий процесс рецензирования. Надеемся, что данные исследования внесут значительный вклад в общее развитие науки на мировом уровне.

С уважением,
доктор физико-математических наук, профессор Томского политехнического университета,
Заслуженный деятель науки Российской Федерации
Виктор Михайлович Лисицын

Құрметті әріптестер!

Біздің журналдың Арнайы шығарылымы 2024 жылдың 16-21 қыркүйегі аралығында Томск қаласында өткен кезекті IX Халықаралық энергия ағындары және радиациялық әсерлер конгресінде (EFRE–2024) көтерілген конденсацияланған күйдің радиациялық физика мәселелеріне қатысты соңғы зерттеулер мен жетістіктерге арналған.

EFRE–2024 Халықаралық конгресі екі жылда бір рет өткізілетін және жарты ғасырлық тарихы бар 4 ірі конференциядан тұратын дәстүрлі ғылыми іс-шара. Конгресс жұмысына әлемнің түкпір-түкпірінен 600-ден астам ғалым қатысты, оның ішінде Қазақстан ғалымдарының белсенділігі айрықша болды. Конденсацияланған күйдің радиациялық физикасы практикалық қолдану үшін айтарлықтай әлеуеті бар жылдам дамып келе жатқан зерттеу саласы. Атап айтсақ: медицинада — томография, емдеу, медициналық препараттарды зарарсыздандыру; техникада — интроскопия, дефектоскопия; технологияда — жабындар, беттерді өңдеу, кесу, дәнекерлеу, шашырату, синтез; ғылымда — ғарыш туралы ақпарат, құрылымдық және элементтік талдауда пайдаланылады.

Әр нақты материалды нақты пайдалануда оңтайлы шешімдерге қол жеткізу үшін материалдардағы процестердің табиғатын терең зерттеуді қажет етеді. Осындай әртүрлі қолданбалардың радиациялық ағындарын генерациялау үшін әртүрлі электрфизикалық қондырғылар, радиациялық әсердің қажетті сапасын қамтамасыз ететін приборлар әзірленді және жасалды. Радиациядан қорғаудың алдын алу үшін радиациялық жағдайды бақылауды жүзеге асырудың құралдары мен материалдары, ультракүлгін сәулелерден шексіздікке дейінгі диапазондағы әртүрлі түрлер мен энергиялардың радиациялық өрістерін зерттеу қажет. Радиациялық әсерге ұшыраған материалдар шеңберінің шегі жоқ. Әр нақты жағдай үшін бірдей ұсыныстар болмайды. Дегенмен, конденсацияланған орталарда радиация тудыратын процестер туралы жалпы түсініктер бар және дамып келеді. Журналдың осы санында ұсынылған мақалалар конденсацияланған күйдегі радиациялық физиканың алдында тұрған мәселелердің кең ауқымын және өзектілігін көрсетеді.

Жарияланған барлық мақалалар қатаң рецензиядан өтті. Бұл зерттеулер әлемдік деңгейдегі ғылымның жалпы дамуына елеулі үлес қосады деп үміттенеміз.

Құрметпен,
физика-математика ғылымдарының докторы, Томск политехникалық университетінің профессоры,
Ресей Федерациясының ғылымға еңбек сіңірген қайраткері
Виктор Михайлович Лисицын

Article
https://doi.org/10.31489/2024PH4/9-19
UDC: 535.37

Received: 10.06.2024
Accepted: 19.08.2024

G.K. Alpyssova[1], Zh.K. Bakiyeva[1*], I.P. Denisov[2], E.V. Kaneva[3],
E.V. Domarov[4], A.K. Tussupbekova[1]

[1] *Karaganda Buketov University, Karaganda, Kazakhstan;*
[2] *National Research Tomsk Polytechnic University, Tomsk, Russian Federation;*
[3] *X-ray Analysis Laboratory, Vinogradov Institute of Geochemistry SB RAS, Irkutsk, Russian Federation;*
[4] *Budker Institute of Nuclear Physics of the Siberian Branch of the Russian Academy of Sciences Novosibirsk, Russian Federation*
*(*Corresponding author's e-mail: shanar83@mail.ru)*

Dependence of the Radiation Synthesis Efficiency of Ceramics Based on Tungstates on the Flow Power

Ceramic samples of monocomponent (CaO, MgO, ZnO and WO_3) and two-component ($ZnWO_4$, $MgWO_4$, $CaWO_4$) compositions were synthesized by direct impact of high-energy electron flow on the charge of stoichiometric composition. Radiation synthesis of samples weighing about 50 g is realized in time of 10s without the use of any additional substances to stimulate the process. Systematic studies of the dependence of radiation synthesis of tungstate ceramics on the flux power density have been performed for the first time. It was found that the dependences of synthesis efficiency on the flux power density of monocomponent (CaO, MgO, ZnO and WO_3) and two-component ($ZnWO_4$, $MgWO_4$, $CaWO_4$) ceramic samples have the form of constantly increasing curves. There is a threshold above which the synthesis is realized for all synthesized samples. The effect of mutual influence of charge components on the efficiency of synthesis of two-component systems was found. Synthesis of $ZnWO_4$, $MgWO_4$, $CaWO_4$ ceramics is realized under the same conditions of radiation treatment, while the thresholds of synthesis realization of one-component samples of CaO, MgO and ZnO and WO_3 ceramics differ significantly. It is shown that at all used modes of radiation treatment the formation of ceramics with the same properties are realized. This effect is due to the inhomogeneous distribution of electron flux energy losses in the substance. Synthesis of two-component ($ZnWO_4$, $MgWO_4$, $CaWO_4$) ceramic samples is realized at the same power density above 1,0 kW/cm^2. The radiation synthesis of the $ZnWO_4$, $MgWO_4$, $CaWO_4$ ceramics is mainly determined by tungsten oxide.

Keywords: ceramics; metal tungstate, luminescence; radiation synthesis, X-ray diffraction spectra, EDX analysis, power density, optical properties of ceramics.

Introduction

Crystals and ceramics based on tungstate of alkaline-earth and rare-earth metals have found wide application as scintillation materials [1–3]. These materials have high absorption capacity of radiation, are resistant to external factors: temperature, aggressive media. They can be used both for registration of heavy particles, electrons and X-ray radiation [4–7].

Synthesis of these materials from metal oxides with high melting point is difficult. Moreover, the melting point of the main initial component, WO_3 (1473 °C), differs significantly from the melting points of other components, such as MgO (2825 °C), ZnO (1975 °C), CaO (2572 °C). Therefore, the synthesis methods used, most often Czochralski and Bridgman [8–11], are labor-intensive, time-consuming, and require the use of other substances to stimulate synthesis.

Radiation method is promising for the synthesis of ceramics based on metal oxides, fluorides. It realized and described first time in [12–14]. The radiation method showed that the impact of a powerful flow of electrons with an energy of 1.4, 2.5 MeV t power density up to 30 kW/cm^2 on the charge stoichiometric composition is possible to form ceramics based on metal oxides, including tungstate. It is established that the synthesis is realized by direct impact of the electron flux on the charge in the crucible for a time less than 1 s, with high efficiency, without the use of any additional substances that contribute to the process.

The present work is aimed at studying the dependence of the synthesis efficiency on the radiation ion treatment modes, in particular, on the power density of the electron flux falling on the charge.

Experimental

Radiation synthesis of ceramics was realized by direct impact of a powerful flow of high-energy electrons on the charge. The synthesis of materials was carried out by direct electron beam irradiation using the ELV6 electron accelerator at the facility UNU Stand ELV-6 of Budker Institute of Nuclear Physics, of the Siberian Branch of the Russian Academy of Sciences Novosibirsk, Russian Federation. The ELV-6 electron accelerator provides generation of electron flux with energies in the range from 1.4 to 2.5 MeV and power up to 100 kW. The electron beam output through the differential pumping system has a Gaussian distribution in cross-section. In our experiments, the beam area on the charge surface in the crucible was 1 cm^2. A scanning system was used for obtaining large area samples. The beam was scanned at a frequency of 50 Hz across the mixture surface in the transverse direction of a crucible with a width of 5 cm and a length of 10 cm. The crucible was displaced relative to the scanning beam at a speed of 1 cm/s for the entire length of the crucible. Each elementary section of the charge in the crucible was exposed to the radiation flux for 1 s. The total time of exposure of the electron flux to the treated surface of the charge in the crucible was always 10 s. The synthesis of ceramics was realized only due to the energy of the radiation flux, only from the charge materials, without additives of other materials facilitating the process.

Measurements of dispersity of initial powders used for synthesis of initial powders for obtaining ceramic samples were carried out by laser diffraction method using a laser particle size analyzer Shimadzu SALD-7101.

The X-ray diffraction patterns were obtained using a Bruker D8 ADVANCE (AXS, Berlin, Germany) diffractometer equipped with a scintillation detector.

The luminescence of the synthesized samples (luminescence excitation spectra and luminescence spectra) were measured using a Cary 5000 UV-Vis-NIR spectrophotometer.

Results and Discussion

Mixtures of WO_3, MgO, ZnO, CaO starting powders in stoichiometric ratio were prepared for synthesis. All the starting powders were obtained from Hebei Suoyi New Material Technology Co., Ltd, had a purity degree of at least 99,95 %.

It was shown in [15] that the results of radiation synthesis are largely determined by the prehistory of the starting materials, not only their purity but also their particle size distribution. All starting materials have significantly different melting temperatures [16]. In this connection, we investigated the particle size distribution and performed radiation synthesis of each of the starting materials prior to the synthesis of multicomponent ceramics.

The results of the particle size distribution study are shown in Figure 1. The figures show the distribution of particles in the used powders in the form of dependence of the number of particles on their size and dependence of the volume of the particles.

There are two groups of particles with sizes from 0,01 to 1 μm and from 1 μm to 50 μm for all powders. The number of small particles is dominant, but in the total volume of powders their volume is much smaller. Therefore, the synthesis result should be determined mainly by the number of the large particles. The ratio between the number of small and large particles in powders of different composition differs. As follows from the presented results, the distributions of large particles of ZnO and MgO overlap with the distribution of WO_3 particles. The size distribution range of large CaO particles is much wider than that of WO_3. We can expect a difference in the efficiency of synthesis of ceramics of tungstates of these two groups: a large difference in the size of the initial particles may appear in the express synthesis due to the existence of local non-stoichiometry [14].

The starting materials for the synthesis of two-component metal tungstate ceramics have significantly different melting points: WO_3 (1473 °C), MgO (2825 °C), ZnO (1975 °C), CaO (2572 °C), which can affect the efficiency of their synthesis [17]. However, for radiation synthesis, ionization processes play a dominant role in the formation of a new structure from the initial ones, while thermal processes contribute to their efficiency. It seems necessary to study the efficiency of radiation synthesis of ceramics of starting materials. We have carried out a series of studies of the dependence of the synthesis of ceramics from starting materials on the power density of the radiation flux. The charge for synthesis was simply initial powders of WO_3, ZnO, MgO, CaO. Radiation treatment of the charge was carried out under the conditions mentioned above in the “without scanning” mode. The dependence of the morphology of synthesized samples on the modes of radiation exposure and electron flux power density is shown in Figure 2.

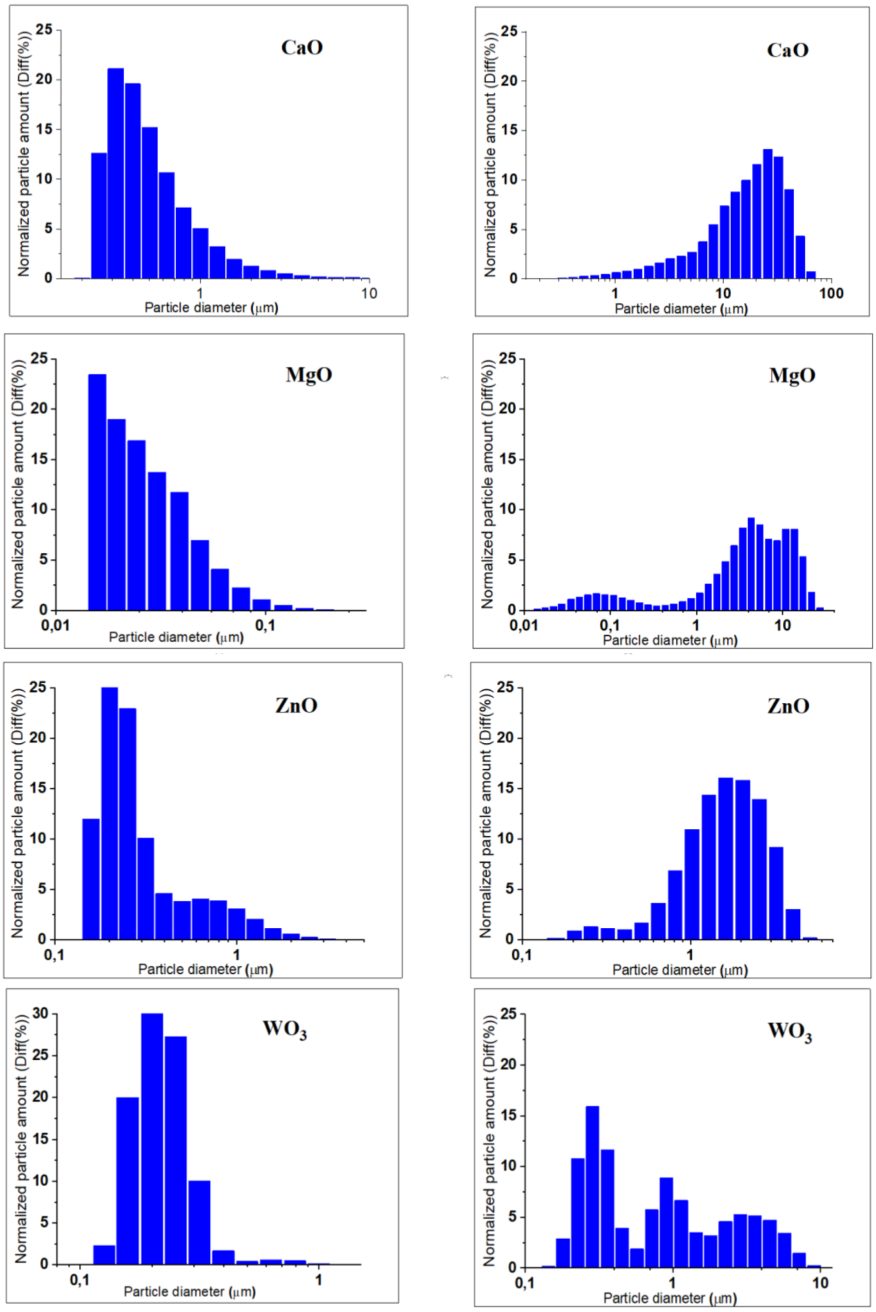

Figure 1. Particle number and volume distribution of the used powders

Figure 2 shows photos of ceramic samples from the initial materials. The value of power density is indicated in the figures. As follows from the presented photos for monocomponent ceramic samples, the dependence of the synthesis result on the electron flux power density is clearly visible. Especially clearly this dependence is seen on the example of WO_3 and ZnO. This dependence is less pronounced in the synthesis of

CaO ceramics. Synthesized MgO ceramics has high power densities, but the ceramic samples are formed under the surface of the charge, because the bulk density of the MgO charge (ρ=0.5 g/cm^3) is much less than WO_3 (ρ=2.6 g/cm^3) and ZnO (ρ=1.1 g/cm^3). WO_3 and ZnO differ significantly from MgO and CaO in melting temperatures. For CaO, a picture of a sample obtained using the "with scanning" mode is given as an example. The synthesis of ceramics from the whole charge in the crucible is realized in this mode. Accordingly, in order to fulfill the equality of absorbed energy in both modes, the power density in the "with scanning" mode is increased by a factor of 5.

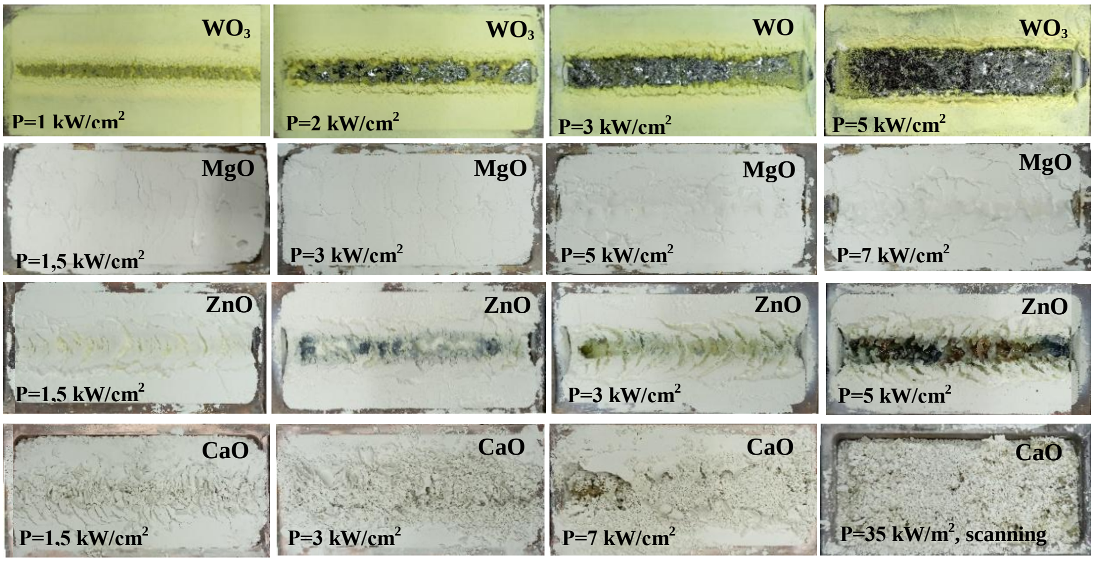

Figure 2. Dependence of morphology of synthesized samples on radiation exposure modes-electron flux power density

Quantitative dependences of synthesis efficiency on power density in the studied monocomponent compositions are shown in Figure 3. Synthesis efficiency in this work is understood as the weight of the synthesized sample. Such characterization of the process seems to be quite justified: the charge volume in our work is always the same using the same crucibles.

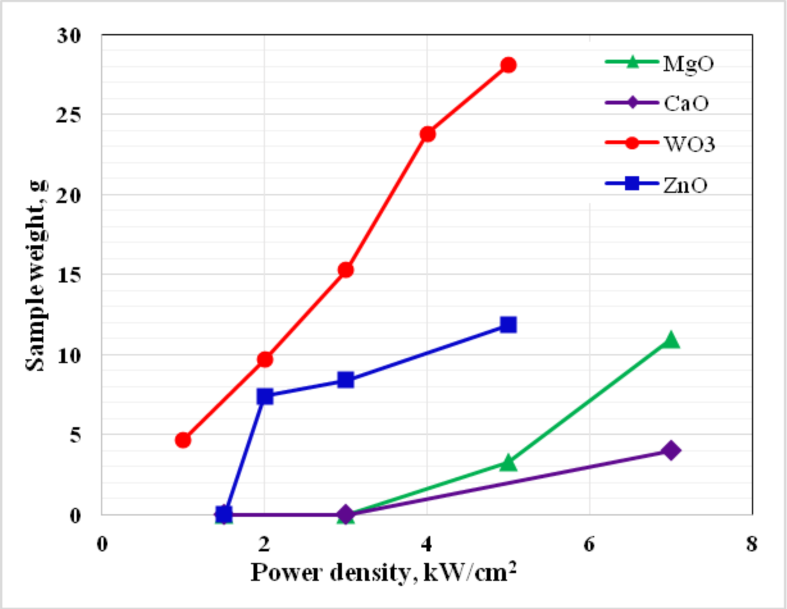

Figure 3.Dependence of ceramic synthesis efficiency from used initial monocomponent compositions on power density

The synthesis of WO_3 and ZnO ceramics is realized when the power density exceeds 1–1.5 kW/cm^2, whereas for the synthesis of MgO and CaO ceramics, power densities above 2.5 kW/cm^2 are required.

We consider that it is necessary to emphasize the following. To determine the weight of the synthesized sample using the "without scanning" mode, the sample is removed from the crucible and cleaned from the charge adhering to it. This procedure is easily realized when the charge is treated with high power radiation fluxes. It is impossible to clean the completely porous sample from the charge at low power densities. Therefore, the initial points on the dependences are determined with some error. Nevertheless, the full dependence quite unambiguously indicates that the threshold for the realization of the synthesis of WO_3 and ZnO ceramics is lower than that of MgO and CaO. It is necessary to pay attention to the existence of a constant growth of the sample weight at high power density. The growth of the sample weight is due to the increase of the sample area, as it is clearly seen for WO_3 and ZnO. The growth of the bandwidth of the formed ceramics is due to the fact that the electron beam has a Gaussian distribution. As the integral power of the beam increases, the width of its impact region increases with exceeding the threshold for synthesis, as can be seen from Figure 2

A charge was prepared from the above described monocomponent metal oxides and radiation synthesis was performed. The charge was prepared from oxide powders in stoichiometric ratio. Table 1 describes the compositions prepared for synthesis, radiation treatment modes used for synthesis, electron flux power density. The sample number means the serial number of the experiment according to the accounting system adopted by the authors. The masses of the charge in the crucible and the yield of the synthesis reaction are also given. Here, the yield of the synthesis reaction is understood as the ratio of the mass of the sample to the mass of the charge used. The synthesis was carried out in the "scanning" mode.

Table 1

Composition of synthesized ceramics when treated with 1.4 MeV electron flow

Sample, №	Sample description	P, kW/cm^2	M_s, g	Output, %
623	$ZnWO_4$ (ZnO 26 %), (WO_3 74 %)	15	64,63	91,29
624	$MgWO_4$ (MgO 14,8 %), (WO_3 85,2 %)	15	47,31	97,17
625	$CaWO_4$ (CaO 19,5 %), (WO_3 (80,5 %)	15	39,46	73,28
627	$ZnWO_4$ (ZnO 26 %), (WO_3 74 %)	15	62,56	93,36
738	$MgWO_4$ (MgO 14,8 %), (WO_3 85,2 %)	18	36,99	98,8
718*	$ZnWO_4$ (ZnO 26 %),(WO_3 74 %)	22	86,62	90,0

**Note* – 718 was obtained at an electron beam energy of 2.5 MeV.

Figure 4 shows photos of samples of synthesized ceramics in standard crucibles with internal dimensions of 100x50 mm.

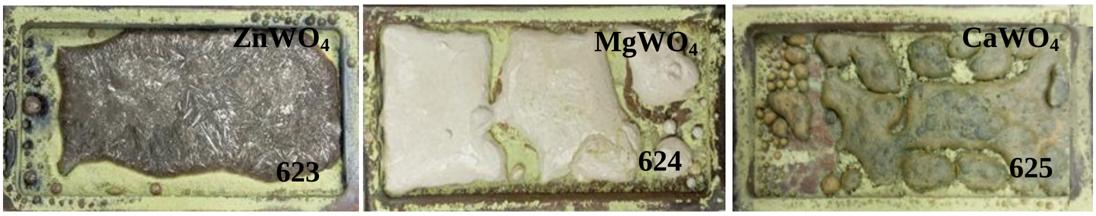

Figure 4. Photos of samples of synthesized ceramics $ZnWO_4$, $MgWO_4$, $CaWO_4$

The samples have the form of plates similar to solidified molten mass, about 5 mm thick, with a porous structure inside. Not the entire volume of the charge is involved in the synthesis of ceramics. They use three types of crucibles differing in depth: 7, 10 and 14 mm. For each experiment, differing in the composition of the synthesized ceramics, its bulk density, and electron energy, the one is chosen at which the electrons of the beam will be completely absorbed by the charge. Otherwise, atoms (ions) from the crucible will be introduced into the formed ceramics. Therefore, there always remains a layer of unused charge under the formed ceramics. Part of the charge may disappear during radiation treatment, atomized due to charging of particles by the electron beam. This process can be significant at low mass of dielectric particles of initial substances. We take into account in determining the yield of the synthesis reaction the existence of residues of the charge in the crucible and atomization during radiation treatment.

As can be seen in Table 1, the yield of the synthesis reaction in all samples synthesized in the “with scanning” mode has a value ranging from 73 % to 98 %. Two reasons for this difference are possible. CaO (2572 °C) has a melting point higher than ZnO (1975 °C) and WO_3 (1473 °C). But MgO (2825 °C) also has a melting point higher than ZnO and WO_3. Another factor that differentiates the starting materials is the difference in particle size distribution. In the dispersion spectra (Fig. 1), the number and volume of particles with sizes above 10 μmare are much larger in CaO than in WO_3, MgO and ZnO. It seems to us that this characteristic can determines the difference in the yields of the material synthesis reaction. Nevertheless, we do not deny the influence of the difference in melting temperatures on the synthesis process.

Studies of the dependence of the synthesis efficiency of $ZnWO_4$, $MgWO_4$, $CaWO_4$ ceramics in the “without scanning” mode were performed, as well as for monocomponent compositions shown in Figure 3. The results of the studies are presented in Table 2 and Figure 5. The weight of $CaWO_4$, $MgWO_4$, $ZnWO_4$ tungstate ceramics samples was measured during synthesis without scanning at different electron beam power densities with E=1.4 MeV.

Table 2

Efficiency of synthesis of tungstate ceramics

Power P, kW	Weight of $CaWO_4$, g	Weight of $MgWO_4$, g	Weight of $ZnWO_4$, g
1,5	8,74	11,07	9,57
2	12,97	14,55	13,47
3	16,88	18,26	20,14

Weight dependence of $CaWO_4$, $MgWO_4$ and $ZnWO_4$ tungstate ceramics during synthesis without scanning at different electron beam power densities with E=1.4 MeV.

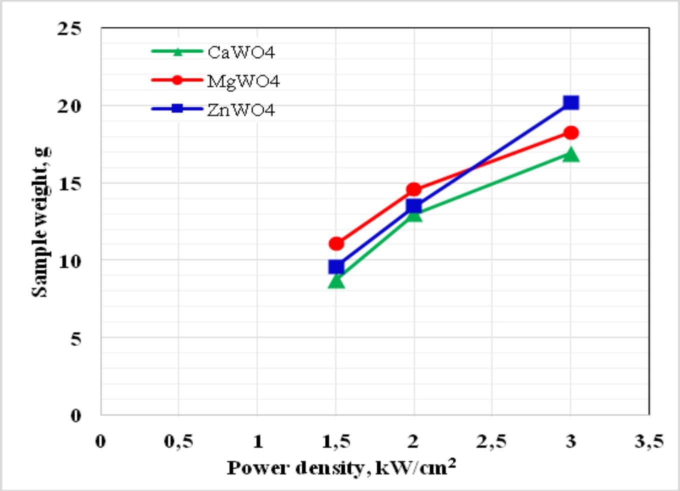

Figure 5. Weight dependence of $CaWO_4$, $MgWO_4$, $ZnWO_4$ tungsten ceramics on electron flux power density

As follows from the presented results, synthesis in all investigated samples of multicomponent ceramics is realized at the same regimes of radiation treatment. We emphasize that ceramics of monocomponent samples is realized at different regimes for CaO, MgO, WO_3 and ZnO. Note that equal conditions of electron beam energy losses during radiation treatment in the “without scanning” mode, for example 1.5 kW/cm^2, corresponds to 7–85 kW/cm^2 in the “with scanning” mode.

The structure of synthesized samples of $ZnWO_4$, $CaWO_4$ ceramics was studied by X-ray diffraction using a Bruker D8 ADVANCE diffractometer (AXS, Berlin, Germany) equipped with a scintillation detector in step-scan mode over a diffraction angle range of 10 to 90° 2θ and CuKα radiation as the source. Details of the research methodology and analysis are described in [15].

The results of the X-ray powder diffraction investigation are presented in Table 3. The qualitative phase analysis and indexing of the diffraction patterns utilized the data from the PDF-2 database (ICDD, 2007) as follows:

- PDF 01-088-0251 “Zinc tungsten oxide ($ZnWO_4$)”, symmetry — monoclinic lattice, space group — *P*2/*c* (#13), a = 4.6926 Å, b = 5.7213 Å, c = 4.9281 Å, β = 90.632 °.

- PDF 01-072-0257 “Calcium tungsten oxide ($CaWO_4$)”, symmetry — body-centered tetragonal lattice, space group — *I*41/*a* (#88), $a = 5.243$ Å, $c = 11.376$ Å.

- PDF 01-072-0677 “Tungsten oxide (WO_3)”, symmetry — monoclinic lattice, space group — *P*21/*n* (#14), $a = 7.306$ Å, $b = 7.54$ Å, $c = 7.692$ Å, $\beta = 90.881$ °.

Table 3

The results of the phase composition investigation

Sample	Phase	Degree of crystallinity	Crystallite size	Refined unit cell parameters
$ZnWO_4$	$ZnWO_4$	99.9 (±5) %	131 (±15) nm	*P*2/*c*, $a = 4.689(4)$ Å, $b = 5.716(7)$ Å, $c = 4.925(3)$ Å, $\beta = 90.6(1)$ °, $V = 132.0(1)$ Å^3
$CaWO_4$	$CaWO_4$ (~86 %)	99.9 (±5) %	167 (±35) nm	*I*41/*a*, $a = 5.243(2)$ Å, $c = 11.371(4)$ Å, $V = 312.5(2)$ Å^3
	WO_3 (~14 %)		114 (±28) nm	*P*21/*n*, $a = 7.311(2)$ Å, $b = 7.532(2)$ Å, $c = 7.694(2)$ Å, $\beta = 90.8(1)$ °, $V = 423.6(1)$ Å^3

The results of the study of $MgWO_4$ ceramics are not presented due to the absence of complete data on this material in our database [18]. As can be seen from the results presented in the table, during radiation synthesis in the samples ceramics formed crystalline phase in the form of crystallites with sizes of 100–170 nm. The dominant phase is $ZnWO_4$, $CaWO_4$ ceramics, with WO_3 as the accompanying phase [19].

The main functional characteristic of metal tungstates is luminescence and its properties [20]. Excitation and luminescence spectra were measured for $ZnWO_4$, $MgWO_4$, $CaWO_4$ ceramics samples [21]. The excitation and photoluminescence spectra were measured on a SM-2203 Solar spectrofluorimeter. Figure 6 shows the excitation and luminescence spectra of $ZnWO_4$, $MgWO_4$, $CaWO_4$.

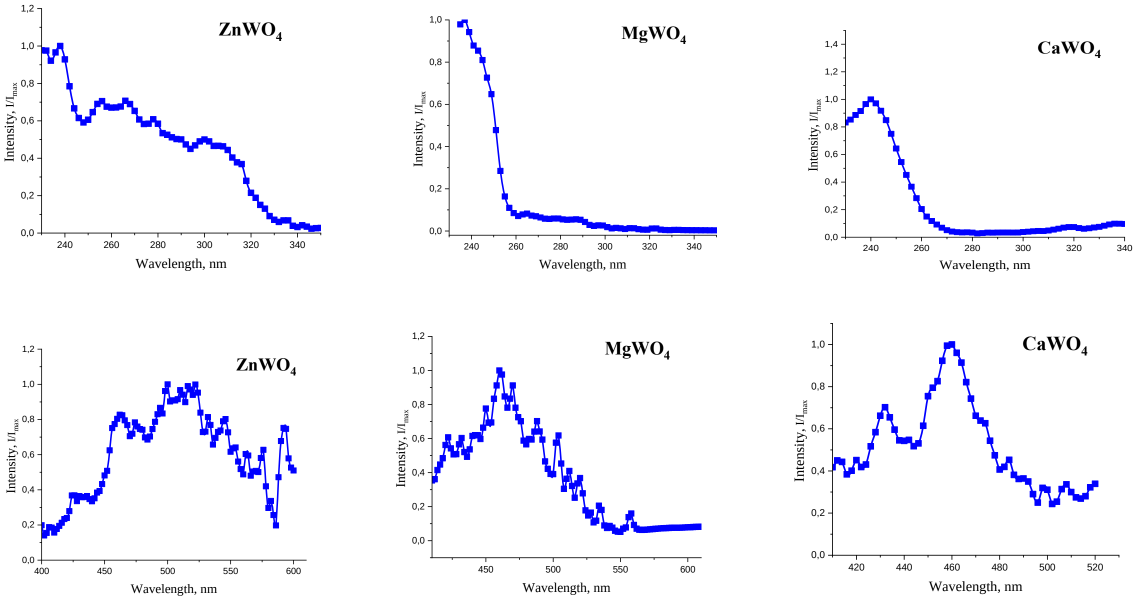

Figure 5. Excitation (top) and luminescence (bottom) spectra of $ZnWO_4$, $MgWO_4$, $CaWO_4$, respectively

In $ZnWO_4$ ceramics luminescence is excited by UV radiation from 230 to 320 nm, in $MgWO_4$230–250 nm, in $CaWO_4$ 230–260 nm [22]. The luminescence maxima occur in $ZnWO_4$ at 500 nm, in $MgWO_4$, at 460 nm, in $CaWO_4$ at 460 nm. In general, the spectral characteristics of photoluminescence correspond to those known for crystalline materials [23].

Conclusion

For the first time, systematic studies of the dependence of radiation synthesis of tungstate ceramics on the conditions of radiation treatment have been performed. The dependence of synthesis efficiency on the power density of high-energy electron flux of monocomponent (CaO, MgO, ZnO and WO_3) and two-component ($ZnWO_4$, $MgWO_4$, $CaWO_4$) ceramic samples has been established. It is shown that these dependences have the form of continuously increasing curves. Nevertheless, for all synthesized samples there is a threshold above which the synthesis is realized. The knowledge of thresholds and dependence on the electron flux power density allows us to choose the optimal conditions for the synthesis realization and contributes to the development of ideas about the processes in the charge in the radiation field that ensure the formation of ceramics.

The effect of the mutual influence of charge components on the synthesis efficiency of two-component systems is of interest. Synthesis of $ZnWO_4$, $MgWO_4$, $CaWO_4$ ceramics is realized under the same conditions of radiation treatment, while the thresholds for the synthesis of single-component CaO, MgO, ZnO and WO_3 ceramics samples differ significantly.

It is shown that at all used modes of radiation treatment the formation of ceramics with the same properties are realized. This effect is due to the inhomogeneous distribution of electron flux energy losses in the substance.

Acknowledgements

This research was funded by the Science Committee of the Ministry of Science and Higher Education of the Republic of Kazakhstan (Grant No. AP 19579177). And this research has been funded by TPU and INP SB RAS under the project of the Russian Science Foundation of the Russian Federation (GrantNo. 23-73-00108).

Funding

This research has been funded by the Science Committee of the Ministry of Science and Higher Education of the Republic of Kazakhstan (Grant No. AP19579177)

References

1 Гринев Б.В. Сцинтилляционные детекторы и системы контроля радиации на их основе / Б.В. Гринев, В.Д. Рыжиков, В.П. Семиноженко. — Киев: Наук. думка, 2007. — 447 с.

2 Grassmann H. Scintillation properties of ZnWO4 / H. Grassmann, H. -G. Moser // Journal of Luminescence. — 1985. — Vol. 33. — Issue 1. — P. 109–113. https://doi.org/10.1016/0022-2313(85)90034-1

3 Глобус М. Пути повышения радиационной стойкости неорганических сцинтилляционных кристаллов для физики высокий энергий / М. Глобус, Б. Гринев, В. Люблянский, Т. Хрупова // Вопросы атомной науки и техники. Сер. Физика радиационных повреждений и радиационное материаловедение. — 2003. — Т. 89. — № 6. — С. 89–97.

4 Nagirnyi, V. Energy transfer in ZnWO4 and CdWO4 scintillators / V. Nagirnyi, E. Feldbach, L. Jönsson, M. Kirm, A. Kotlov, A. Lushchik, V.A. Nefedov, B.I. Zadneprovski // Nuclear Instruments and Methods in Physics Research. — 2002. — Vol. 486. — P. 395–398. https://doi.org/10.1016/S0168-9002(02)00740-4

5 Kolobanov, V.N. Optical and luminescent properties of anisotropic tungstate crystals / V.N. Kolobanov, I.A. Kamenskikh, V.V. Mikhailin, I.N. Shpinkov, D.A. Spassky, B.I. Zadneprovsky, L.I. Potkin, G. Zimmerer // Nuclear Instruments and Methods in Physics Research. — 2002. — Vol. 486. — P. 496–503. https://doi.org/10.1016/S0168-9002(02)00760-X

6 Mikhailik, V.B. Cryogenic scintillators in searches for extremely rare events / V.B. Mikhailik, H. Kraus // Journal of Physics D. — 2006. — Vol. 39. — No. 6. — P. 1181–1191. DOI 10.1088/0022-3727/39/6/026

7 Minoru Itoha. Photo-stimulated luminescence and photo-induced infrared absorption in ZnWO4 / Itoha Minoru, Katagiria Tsuyoshi, Aokia Tomonori, Fujita Masami // Radiation Measurements. — 2007. — Vol. 42. — P. 545–548. https://doi.org/10.1016/j.radmeas.2007.01.049

8 Sarukura N. 4 — Czochralski Growth of Oxides and Fluorides. Handbook of Crystal Growth (2nd ed) / N. Sarukura, T. Nawata, H. Ishibashi, M. Ishii, T. Fukuda. — 2015. — P. 131–168. https://doi.org/10.1016/B978-0-444-63303-3.00004-3

9 Dabkowska H.A. Floating Zone Growth of Oxides and Metallic Alloys / In P. Rudolph (Ed.) / H.A. Dabkowska, A.B. Dabkowski, R. Hermann, J. Priede, G. Gerbeth // Handbook of Crystal Growth: Bulk Crystal Growth: Part A. — 2015. — Vol. 2. — P. 281–329. https://doi.org/10.1016/B978-0-444-63303-3.00008-0

10 Brandle, C.D. Czochralski growth of oxides / C.D. Brandle // Journal of Crystal Growth. — 2004. — Vol. 264. — No. 4. — P. 593–604. https://doi.org/10.1016/j.jcrysgro.2003.12.044

11 Колосов В.Н. Электронно-опосредованные реакции при металлотермическом восстановлении оксидных соединений молибдена и вольфрама / В.Н. Колосов, В.М. Орлов // Докл. РАН. — 2019. — Т. 484. — № 4. — С. 447–450. https://doi.org/10.31857/S0869-56524844447-450

12 Lisitsyn V.M. YAG based phosphors, synthesized in a field of radiation / 6th International Congress “Energy Fluxes and Radiation Effects” IOP Publishing / V.M. Lisitsyn, M.G. Golkovsky, D.A. Musakhanov, A.T. Tulegenova, Kh.A. Abdullin, M.B. Aitzhanov // Journal of Physics Conference Series. — 2018. — Vol. 1115. — No. 5. — P. 5. DOI:10.1088/1742-6596/1115/5/052007

13 Lisitsyn V.M. Formation of Luminescing High-Temperature Ceramics upon Exposure to Powerful High-Energy Electron Flux / V.M. Lisitsyn, L.A. Lisitsyna, M.G. Golkovskii, D.A. Musakhanov, A.V. Ermolaev // Russian Physics Journal. Optics and spectroscopy. — 2021. — Vol. 63. — No. 9. — P. 1615–1621. DOI: 10.1007/s11182-021-02213-9

14 Lisitsyn V. / Radiation Synthesis of High-Temperature Wide-Bandgap Ceramics / V. Lisitsyn, A. Tulegenova, M. Golkovski, E. Polisadova, L. Lisitsyna, D. Mussakhanov, G. Alpyssova // MDPI Journal. Micromachines. — 2023. — Vol. 14. — 2193 p. https://doi.org/10.3390/mi14122193

15 Lisitsyn V. The Optimization of Radiation Synthesis Modes for YAG: Ce Ceramics / V. Lisitsyn, D. Mussakhanov, A. Tulegenova, E. Kaneva, L. Lisitsyna, M. Golkovski, A.M. Zhunusbekov // MDPI Journal.Materials. — 2023. — Vol. 16. — 3158 p. https://doi.org/10.3390/ma16083158

16 Mikhailik V.B. Performance of scintillation materials at cryogenic temperatures / V.B. Mikhailik, H. Kraus // Wiley Online Library. Physica status solidi (b). Review Article. — 2010. — Vol. 247. — P. 1583–1599. https://doi.org/10.1002/pssb.200945500

17 Nikl M. Complex oxide scintillators: Material defects and scintillation performance / . Nikl, V.V. Laguta, A. Vedda // Physica status solidi (b). Feature Article. — 2008. — Vol. 245. — P. 1701–1722. https://doi.org/10.1002/pssb.200844039

18 Mikhailik V.B. Studies of electronic excitons in MgMoO4, CaMoO4 and CdMoO4 crystals using VUV synchrotron radiation / V.B. Mikhailik, H. Kraus, D. Wahl, M.S. Mykhaylyk // Wiley Online Library. Physica status solidi (b). — 2005. — Vol. 242. — Issue 2. — P. R17–R19. https://doi.org/10.1002/pssb.200409087

19 Itoh M. X-Ray Photoelectron Spectroscopy and Electronic Structures of Scheelite- and Wolframite-Type Tungstate Crystals / M. Itoh, N. Fujita, Y. Inabe // Journal of the Physical Society of Japan. — 2006. — Vol. 75. — No. 8. — P. 8. https://doi.org/10.1143/JPSJ.75.084705

20 Ржевская О.В. Оптические и люминесцентные свойства монокристаллов $CdWO_4$ и $CdWO_4$: Mo / О.В. Ржевская, Д.А. Спасский, В.Н. Колобанов, В.В. Михайлин, Л.Л. Нагорная, И.А. Тупицина, Б.И. Заднепровский // Оптика и спектроскопия. — 2008. — Т. 104. — № 3. — С. 407–414.

21 Pankratov V. Luminescence center excited state absorption in tungstates / V. Pankratov, L. Grigorieva, D. Millers, S. Chernov, A.S. Voloshinovskii // Journal of Luminescence. — 2001. — Vol. 94-95. — P. 427–432. https://doi.org/10.1016/S0022-2313(01)00326-X

22 Ovechkin A.E., Luminescence of ZnWO4 и CdWO4 crystals / A.E. Ovechkin, V.D. Ryzhikov, G. Tamulaitis, A. Zukauskas // Physica status solidi (a). — 1987. — Vol. 103. — P. 285–289.

23 Nagirnyi V. Luminescence study of pure and Fe- or Mo-dopped ZnWO4 crystals / V. Nagirnyi, L. Jonsson, M. Kirm, A. Kotlov, A. Lushchik, I. Martinson, A. Watterich, B.I. Zadneprovski // Radiation Measurements. — 2004. — Vol. 38. — P. 519–522. http://dx.doi.org/10.1016/j.radmeas.2004.01.024

Г.К. Алпысова, И.П. Денисов, Ж.К. Бакиева, Е.В. Канева, Е.В. Доморов, А.К. Тусупбекова

Вольфрамат негізіндегі керамиканың радиациялық синтезінің тиімділігінің ағын қуатына тәуелділігі

Монокомпонентті (CaO, MgO, ZnOжәнеWO_3) және екікомпонентті ($ZnWO_4$, $MgWO_4$, $CaWO_4$) композициялардың керамикалық үлгілері стехиометриялық құрамның шихтасына жоғары энергиялы электрон дарағының тікелей әсері арқылы синтезделді. Салмағы шамамен 50 г болатын үлгілердің радиациялық синтезі процесті ынталандыру үшін кез келген қосымша заттарды қолданбай 10 с уақыт ішінде жүзеге асырылады. Алғаш рет вольфрамат керамикасының радиациялық синтезінің ағын қуатының тығыздығына тәуелділігі туралы жүйелі зерттеулер жүргізілді. Синтез тиімділігінің біркомпонентті (CaO, MgO, ZnO және WO_3) және екікомпонентті ($ZnWO_4$, $MgWO_4$, $CaWO_4$) керамика үлгілерінің ағынының тығыздығына тәуелділігі үнемі өсіп келе жатқан қисықтар түрінде болатындығы анықталды. Барлық синтезделген үлгілер үшін шекті мән бар, оның үстінде синтез жүзеге асырылады. Екікомпонентті жүйелердің синтезінің тиімділігіне шихта компоненттерінің өзара әсерінің әсері анықталды. $ZnWO_4$, $MgWO_4$, $CaWO_4$ керамикасының синтезі бірдей жағдайларда, радиациялық өңдеуде жүзеге асырылады, ал CaO, MgO және ZnO және WO_3 керамикасының біркомпонентті үлгілерін синтездеу шектері айтарлықтай ерекшеленеді. Радиациялық өңдеудің барлық қолданылған режимдерінде бірдей қасиеттері бар керамиканың қалыптасуы жүзеге асырылатындығы көрсетілген. Бұл әсер заттағы электрондар ағынының энергия шығынының гетерогенді таралуына байланысты.

Кілт сөздер: керамика, металлвольфраматы, люминесценция, радиациялық синтез, рентген дифракциясының спектрлері, EDX-талдау, қуат тығыздығы, керамиканың оптикалық қасиеттері.

Г.К. Алпысова, Ж.К. Бакиева, И.П. Денисов, Е.В. Канева, Е.В. Домаров, А.К. Тусупбекова

Зависимость эффективности радиационного синтеза керамики на основе вольфраматов от мощности потока

Синтезированы образцы керамики монокомпонентных (CaO, MgO, ZnO и WO_3) и двухкомпонентных ($ZnWO_4$, $MgWO_4$, $CaWO_4$) составов посредством прямого воздействия потока высокоэнергетических электронов на шихту стехиометрического состава. Радиационный синтез образцов весом около 50 г реализуется за время 10 с без использования любых дополнительных веществ для стимуляции процесса. Впервые выполнены систематические исследования зависимости радиационного синтеза керамики вольфраматов от плотности мощности потока. Установлено, что зависимости эффективности синтеза от плотности мощности потока монокомпонентных (CaO, MgO, ZnO и WO_3) и двухкомпонентных ($ZnWO_4$, $MgWO_4$, $CaWO_4$) образцов керамики имеют вид постоянно нарастающих кривых. Для всех синтезированных образцов имеет место наличие порога, выше которого синтез реализуется. Обнаружен эффект взаимного влияния компонентов шихты на эффективность синтеза двухкомпонентных систем. Синтез $ZnWO_4$, $MgWO_4$, $CaWO_4$ керамики реализуется при одинаковых условиях, радиационной обработке, тогда как пороги реализации синтеза однокомпонентных образцов керамики CaO, MgO и ZnO и WO_3, существенно различаются. Показано, что при всех использованных режимах радиационной обработки реализуется формирование керамики с одинаковыми свойствами. Обусловлен этот эффект неоднородным распределением потерь энергии потока электронов в веществе.

Ключевые слова: керамика, вольфрамат металла, люминесценция, радиационный синтез, спектры рентгеновской дифракции, EDX-анализ, плотность мощности, оптические свойства керамики.

References

1 Grinev, B.V., Ryzhikov, V.D., & Seminozhenko, V.P. (2007). *Stsintilliatsionnye detektory i sistemy kontrolia radiatsii na ikh osnove [Scintillation detectors and radiation monitoring systems based on them].* Kyiv: Naukova dumka [in Russian].

2 Grassmann, H. & Moser, H.-G. (1985). Scintillation properties of ZnWO4. *Journal of Luminescence, 33*(1), 109–113. https://doi.org/10.1016/0022-2313(85)90034-1

3 Globus, M.E., Grinev, B.V., Liubinskii, V.R., Ratner, M.A., & Grineva, T.B. (2003). Puti povysheniia radiatsionnoi stoikosti neorganicheskikh stsintilliatsionnykh kristallov dlia fiziki vysokikh energii [Enhancement of radiation hardness of inorganic scintillation crystals for high-energy physics]. *Voprosy atomnoi nauki i tekhniki. Seriia Fizika radiatsionnykh povrezhdenii i radiatsionnoe materialovedenie — Issues of atomic science and technology. Series: Radiation Damage Physics and Radiation Materials Science, 6*(89), 89–97 [in Russian].

4 Nagirnyi, V., Feldbach, E., Jönsson, L., Kirm, M., Kotlov, A., Lushchik, A., Nefedov, V.A, & Zadneprovski, B.I. (2002). Energy transfer in ZnWO4 and CdWO4 scintillators. *Nuclear Instruments and Methods in Physics Research, 486,* 395–398. https://doi.org/10.1016/S0168-9002(02)00740-4

5 Kolobanov, V.N., Kamenskikh, I.A., Mikhailin, V.V., Shpinkov, I.N., Spassky, D.A., Zadneprovsky, B.I., Potkin, L.I., & Zimmerer, G. (2002). *Optical and luminescent properties of anisotropic tungstate crystals. Nuclear Instruments and Methods in Physics Research, 486,* 496–503. https://doi.org/10.1016/S0168-9002(02)00760-X

6 Mikhailik, V.B. & Kraus, H. (2006). Cryogenic scintillators in searches for extremely rare events. *Journal of Physics D, 39*(6), 1181–1191. DOI 10.1088/0022-3727/39/6/026

7 Minoru, Itoha, Tsuyoshi, Katagiria, Tomonori, Aokia, & Masami, Fujita (2007). Photo-stimulated luminescence and photo-induced infrared absorption in ZnWO4. *Radiation Measurements, 42,* 545–548. https://doi.org/10.1016/j.radmeas.2007.01.049

8 Sarukura, N., Nawata, T., Ishibashi, H., Ishii, M., & Fukuda, T. (2015). *4 — Czochralski Growth of Oxides and Fluorides. Handbook of Crystal Growth* (2nd ed), 131–168. https://doi.org/10.1016/B978-0-444-63303-3.00004-3

9 Dabkowska, H.A., Dabkowski, A.B., Hermann, R., Priede, J., & Gerbeth, G. (2015). Floating Zone Growth of Oxides and Metallic Alloys / In P. Rudolph (Ed.). *Handbook of Crystal Growth: Bulk Crystal Growth: Part A, 2,* 281–329. https://doi.org/10.1016/B978-0-444-63303-3.00008-0

10 Brandle, C.D. (2004). Czochralski growth of oxides. *Journal of Crystal Growth, 264*(4), 593–604. https://doi.org/10.1016/j.jcrysgro.2003.12.044

11 Kolosov, V.N. & Orlov, V.M. (2019). Elektronno-oposredovannye reaktsii pri metallotermicheskom vosstanovlenii oksidnykh soedineii molibdena i volframa [Electron-mediated reactions during metallothermic reduction of molybdenum and tungsten oxide compounds]. *Doklady Rossiiskoi akademii nauk — Report of the Russian Academy of Sciences, 4*(484), 447–450 [in Russian]. https://doi.org/10.31857/S0869-56524844447-450

12 Lisitsyn, V.M, Golkovsky, M.G., Musakhanov, D.A., Tulegenova, A.T., Abdullin, Kh.A., & Aitzhanov, M.B. (2018). YAG based phosphors, synthesized in a field of radiation / 6th International Congress “Energy Fluxes and Radiation Effects” IOP Publishing. *Journal of Physics Conference Series, 1115*(5), 5. DOI:10.1088/1742-6596/1115/5/052007

13 Lisitsyn, V.M., Lisitsyna, L.A., Golkovskii, M.G., Musakhanov, D.A., & Ermolaev, A.V. (2021). Formation of Luminescing High-Temperature Ceramics upon Exposure to Powerful High-Energy Electron Flux. *Russian Physics Journal. Optics and spectroscopy, 63*(9), 1615–1621. DOI: 10.1007/s11182-021-02213-9

14 Lisitsyn, V., Tulegenova, A., Golkovski, M., Polisadova, E., Lisitsyna, L., Mussakhanov, D., & Alpyssova, G. (2023). Radiation Synthesis of High-Temperature Wide-Bandgap Ceramics. *MDPI Journal. Micromachines, 14,* 2193 p. https://doi.org/10.3390/mi14122193

15 Lisitsyn, V., Mussakhanov, D., Tulegenova, A., Kaneva, E., Lisitsyna, L., Golkovski, M., & Zhunusbekov, A.M. (2023). The Optimization of Radiation Synthesis Modes for YAG: Ce Ceramics. *MDPI Journal Materials, 16,* 3158 p. https://doi.org/10.3390/ma16083158

16 Mikhailik, V.B. & Kraus, H. (2010). Performance of scintillation materials at cryogenic temperatures. *Wiley Online Library. Physica status solidi (b). Review Article, 247*, 1583–1599. https://doi.org/10.1002/pssb.200945500

17 Nikl, M., Laguta, V.V., & Vedda, A. (2008). Complex oxide scintillators: Material defects and scintillation performance. *Physica status solidi (b). Feature Article, 245,* 1701–1722. https://doi.org/10.1002/pssb.200844039

18 Mikhailik, V.B., Kraus, H., Wahl, D., & Mykhaylyk, M.S. (2005). Studies of electronic excitons in MgMoO4, CaMoO4 and CdMoO4 crystals using VUV synchrotron radiation. *Wiley Online Library. Physica status solidi (b), 242*(2), R17–R19. https://doi.org/10.1002/pssb.200409087

19 Itoh, M., Fujita, N., & Inabe, Y. (2006). X-Ray Photoelectron Spectroscopy and Electronic Structures of Scheelite- and Wolframite-Type Tungstate Crystals. *Journal of the Physical Society of Japan*, *75*(8), 8 p. https://doi.org/10.1143/JPSJ.75.084705

20 Rzhevskaia, O.V., Spasskii, D.A., Kolobanov, V.N., Mikhailin, V.V., Nagornaia, L.L., Tupitsina, I.A., & Zadneprovskii, B.I. (2008). Opticheskie i liuminestsentnye svoistva monokristallov CdWO4 i CdWO4: Mo [Optical and luminescent properties of CdWO4 and CdWO4 single crystals: Mo]. *Zhurnal Optika i spektroskopiia — Optics and Spectroscopy Journal, 104*(3), 407–414 [in Russian].

21 Pankratov, V., Grigorieva, L., Millers, D., Chernov, S., & Voloshinovskii, A.S. (2001). Luminescence center excited state absorption in tungstates. *Journal of Luminescence, 94-95*, 427–432. https://doi.org/10.1016/S0022-2313(01)00326-X

22 Ovechkin, A.E., Ryzhikov, V.D., Tamulaitis, G., & Zukauskas, A. (1987). Luminescence of ZnWO4 и CdWO4 crystals. *Physica status solidi (a), 103,* P. 285–289.

23 Nagirnyi, V., Jonsson, L., Kirm, M., Kotlov, A., Lushchik, A., Martinson, I., Watterich, A., & Zadneprovski, B.I. (2004). Luminescence study of pure and Fe- or Mo-dopped ZnWO4 crystals. *Radiation Measurements, 38,* 519–522. http://dx.doi.org/10.1016/j.radmeas.2004.01.024

Information about the authors

Gulnur Alpyssova — PhD, Department of Radiophysics and Electronics, Karaganda Buketov University, University str., 28, Karaganda, Kazakhstan; 100028; e-mail: *gulnur-0909@mail.ru*; ORCID ID: 0000-0002-7164-2188

Zhanara Bakiyeva (corresponding author) — 1st year PhD student, Karaganda Buketov University, University str., 28, Karaganda, Kazakhstan; 100028; e-mail: *shanar83@mail.ru* ORCID ID: 0009-0005-1949-4535

Igor Denisov — Researcher, Department of Materials Science, National Research Tomsk Polytechnic University, Tomsk, Russian Federation

Ekaterina Kaneva — PhD, X-ray Analysis Laboratory, Vinogradov Institute of Geochemistry SB RAS, 1A, Favorsky Str., Irkutsk 664033, Russian Federation; e-mail: kev604@mail.ru ORCID ID: 0000-0001-7155-6784

Evgeny Domarov — Researcher, Budker Institute of Nuclear Physics of the Siberian Branch of the Russian Academy of Sciences Novosibirsk, Russian Federation; e-mail: *domarov88@mail.ru*; ORCID ID: 0000-0003-2422-1513.

Ainur Tussupbekova — PhD, Department of Radiophysics and Electronics, Karaganda Buketov University, University str., 28, Karaganda, Kazakhstan; 100028; e-mail: *aintus_070482@mail.ru*; ORCID ID: 0000-0001-5299-9977.

Article
https://doi.org/10.31489/2024PH4/20-26
UDC 621.3.038.624

Received: 28.06.2024
Accepted: 15.08.2024

E.V. Domarov*, D.S. Vorobev, Y.I. Golubenko, A.I. Korchagin, N.K. Kuksanov,
R.A. Salimov, S.N. Fadeev, V.G. Cherepkov, I.K. Chakin

Budker Institute of Nuclear Physics SB RAS, Novosibirsk, Russia
*(*Corresponding author's e -mail: domarov88@mail.ru)*

Electron beam oscillations in ELV-type accelerators, their diagnostics and suppression method

In the article a method for diagnosing electron beam oscillations in ELV-type accelerators associated with the penetration of a transverse magnetic field from the primary and secondary windings into the accelerating tube was described. A method for suppressing these oscillations was developed and tested using the ELV-8 accelerator with an extraction device capable of extract a focused electron beam into the atmosphere. After suppressing the oscillations, it was possible to extract a focused electron beam with a power of 100 kW into the atmosphere and increase the service life of the diaphragms.

Keywords: electron accelerator, ELV, focused electron beam, electron beam oscillations, electron beam oscillation suppression method, electron beam oscillation diagnostics.

Introduction

In ELV-type accelerators, there are electron beam oscillations associated with the penetration of the transverse magnetic field into the accelerating tube from the primary and secondary windings of the accelerator, since the accelerating tube is located inside these windings and may be non-coaxial or tilted due to the accelerator design. For accelerators with an extraction device with a foil, these oscillations are not critical. Since in this case the electron beam passes through a diaphragm with an opening diameter of 50 mm, and then is extraction into the atmosphere through a titanium foil and unfolds in the length of the foil by 1500 mm and in the width by 70 mm [1]. However, for ELV accelerators that are capable of extracting a focused electron beam into the atmosphere, beam oscillations lead to the destruction of the diaphragms in the differential vacuum pumping system. Their destruction leads to a deterioration in the vacuum in the accelerating tube, which is unacceptable [2, 3].

Therefore, we needed to diagnose these oscillations and propose a solution to suppress them in order to increase the service life of the diaphragms.

Shot description construction of the accelerator capable of extraction a focused electron beam into the atmosphere

The general appearance of the ELV accelerator capable of extraction a focused electron beam into the atmosphere (Fig. 1). The primary winding and rectifier sections, which contain the secondary winding of the accelerator, are located inside the high-pressure vessel filled with SF_6 gas. The number of sections ranges from 20 to 68 pieces, depending on the required energy of the accelerator. The operating frequency of the accelerator can be from 400 Hz to 800 Hz. An alternating voltage with the operating frequency is induced in the windings of the sections, which is subsequently rectified using a voltage doubling circuit. The total voltage of the column of rectifier sections is applied to the accelerating tube.

In this particular case, the ELV-8 accelerator with 68 sections and an operating frequency of 438 Hz was used, the operating energy range of this accelerator is from 1.4-2.5 MeV, the maximum beam current is 50 mA and the maximum beam power is 100 kW.

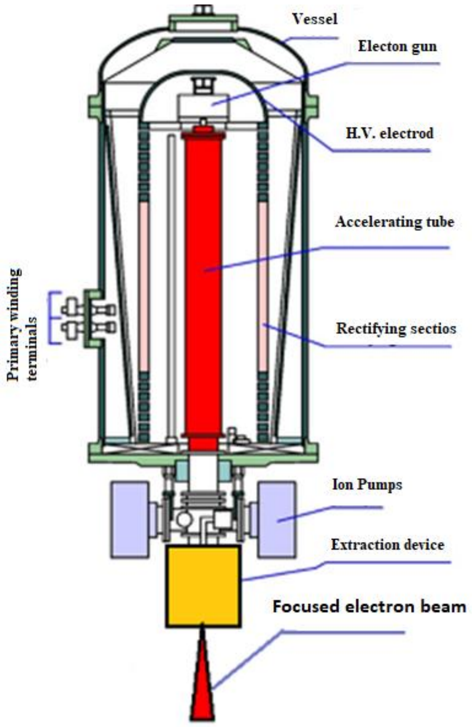

Figure 1. General view of the ELV accelerator capable of extraction a focused electron beam into the atmosphere

The optical diagram of the extraction device (Fig. 2) [2].

The lens L1 is located directly at the lower end of the accelerating tube. After passing the lens L1, the beam is focused to pass the diaphragm D6 with a diameter of 12 mm, a length of 100 mm, and the diaphragm D5, which is a tube with a diameter of 10 mm and a length of 200 mm. The diaphragms separate the stages of the differential pumping system. To guide the beam along the axis of the diaphragms, there are correction coils C1, C2, C3.

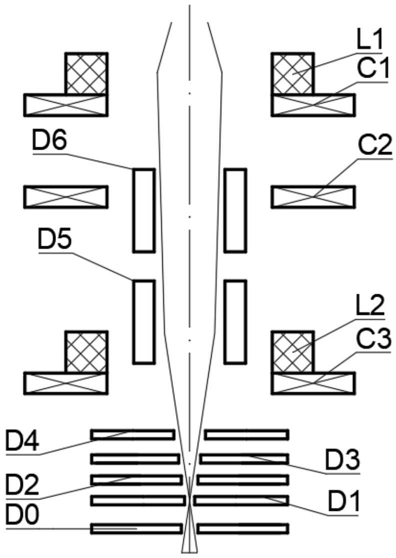

Figure 2. Optical diagram of the output device: D0 — Additional stage with a hole diameters of 5 mm;
D1, D2, D3, D4 — diaphragms with holes diameters of 2.5; 3; 4 and 4.5 mm respectively;
D5 — water-cooled diaphragm with hole diameter of 10 mm and a length of 200 mm;
D6 — water-cooled diaphragm with hole diameter of 12 mm and a length of 100 mm;
C1, C2, C3 — correction coils; L1, L2 — focusing electromagnetic lenses

The size of the holes in the diaphragms is set in accordance with the calculated value of the beam envelope. For these hole diameters, air leakages were calculated and pumps for the differential pumping system were selected, which provide the ability to obtain a pressure difference from atmospheric outside the extraction device to 10^{-6} Torr in the accelerating tube. The lens and correction coils are located outside the vacuum chamber. Diaphragm D5 is cooled with water through a tube sealed into the diaphragm housing and is designed to remove a power of about 1-1.5 kW. Diaphragms D1, D2, D3, D4 are cooled due to direct contact with the copper water-cooled extraction device. Cooling of the housing allows removing a power of up to 1-2 kW, provided that each of the four diaphragms accepts a power of up to 0.5 kW. The detailed design of the exhaust device is described in other papers [2–4].

Electron beam oscillation diagnostic method

To analyze the oscillations of the electron beam and suppress these oscillations, as well as the correct passage of the electron beam along the axis of the output device, the circuit shown in Figure 3 was used.

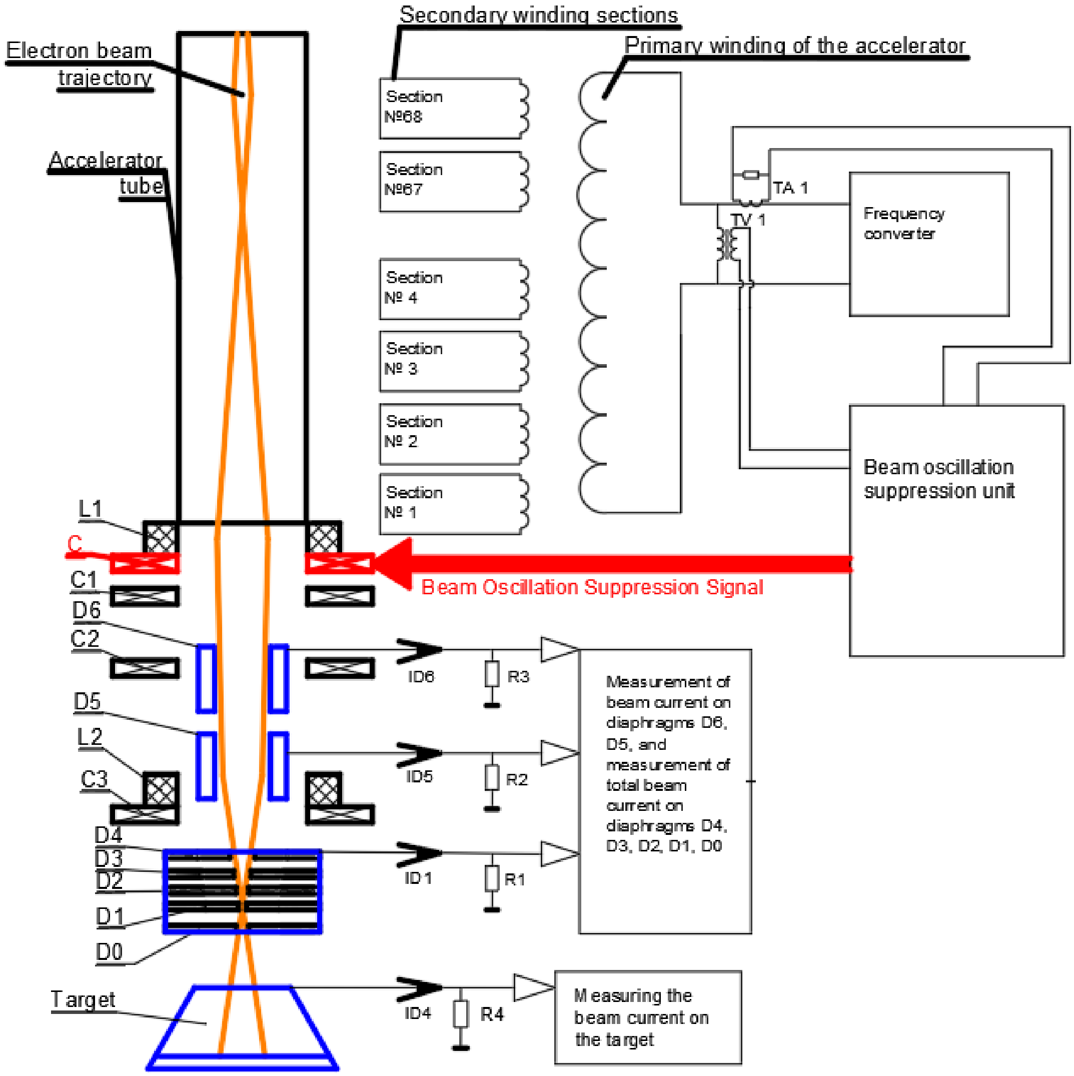

Figure 3. Oscillation suppression circuit: TA1 — current transformer; TV1 — voltage transformer;
C — anti-oscillation coils; R1, R2, R3, R4 — measuring resistances;
ID1 — total signal of current of diaphragms D0, D1, D2, D3, D4, caused by electrons deflecting from the axis;
ID5 — signal of current of diaphragm D5, caused by electrons deflecting from the axis;
ID6 — signal of current of diaphragm D6, caused by electrons deflecting from the axis; ID4 — target current.

Diaphragms D6, D5 and the box body are isolated from the ground by means of caprolon flanges. The signals of the electron beam current deposition on the diaphragms and the box are measured from resistors R3, R2 and R1 (Fig. 3) (ID6 — electron beam current deposition on diaphragm D6, ID5 — electron beam current deposition on diaphragm D5, ID1 — total electron beam current deposition on diaphragms D0, D1, D2, D3, D4). It is not possible to separately monitor the current of each of the diaphragms D0, D1, D2, D3 and D4, since they have electrical contact with the body of the extraction device.

Before starting the work on the accelerator to develop the technologies using the beam, it was necessary to receive the beam extract into the atmosphere onto the target. This target is a four-angel pyramid. The bottom of the pyramid is cooled with water, and the sidewalls protect the surrounding objects from scattered electrons and ozone. Ozone is evacuating through an opening in the pyramid into the ventilation. The entire pyramid and water-cooled targets are isolated from the ground via a resistor R4 = 86 Ohm (Fig. 3). Thus, using an oscilloscope in real time, we can diagnose the electron beam received by the target.

During the accelerator operation, electron beam oscillations were detected due to the penetration of the transverse magnetic field from the primary and secondary windings of the accelerator, since the accelerator tube is located inside these windings and may be misaligned or tilted due to the accelerator design. The beam current signal from the target is shown in Figure 4

Figure. 4. Oscillogram of the target current signal, with a beam current of I_0 = 15 mA and a beam energy of E = 2.5 MeV. The green beam is the total target current. The zero for the green signal on the oscillogram is located at the top; ΔI = 2.3 mA is the value of the target current decrease. Peak 1 and 2 are the decrease in the total target current associated with the electron beam touching the opposite sides of the diaphragm holes.

From the oscillogram (Fig. 4) it is evident that the maximum ratio $\Delta I/I_0$ = 2.3 mA/15 mA = 0.15, and the period between peaks 1 and 2 is 1.14 ms or 876 Hz — this corresponds to the double frequency of the supply voltage to the primary winding. With this frequency, the electron beam touches the diaphragms and the target current decreases by the value of the diaphragm touch current. The double frequency is obtained due to the electron beam touching two sides of the diaphragms. In this case, the integral beam current touch the diaphragms are ID6 = 0 µA, ID5 = 20 µA, ID1 = 600 µA. The total power of the beam deposited on the diaphragms D0, D1, D2, D3, D4 is 1.5 kW, further increase in the beam current will lead to the destruction of these diaphragms, it is necessary to release an electron beam into the atmosphere with a value of 40 mA. Therefore, it is necessary to reduce beam oscillations.

Method of suppressing electron beam oscillations

To suppress electron beam oscillations, standard correction coils used in serial ELV accelerators were used. These coils “C” (Fig. 3) will be referred to as anti-oscillation coils in the future. They are located below the focusing lens L1. Anti-oscillation coils are capable of moving the electron beam in two coordinates “X” and “Y”, which are located at 90^0 relatives to each other. Voltage signals supplied to the coils “Ux” and “Uy” were measured using an oscilloscope directly on the coils themselves. The total resistance of the coils at a frequency of 438 Hz was 73 Ohm along the coordinates “X” and “Y”.

The coils were pre-calibrated using the D6 diaphragm by touching the electron beam at a level of 100 μA [2]. The calibration of this coil was 123 mA/mm, for beam energy of 2.5 MeV.

For complete compensation of electron beam oscillations, it is necessary to suppress the resulting component of the transverse magnetic field. The phase of this transverse magnetic field is determined by the phases of the primary and secondary windings, and the phases of these windings are shifted between each other. As a feedback, a total correcting signal is fed to the anti-oscillation coils: the current of the primary winding from the current transformer TA1 and the voltage of the primary winding from the step-down voltage transformer TV1. Summation and adjustment of these signals is carried out using laboratory autotransformers. This made it possible not only to change the amplitude of the current of the anti-oscillation coils, but also to change their phase along the coordinates “X” and “Y”.

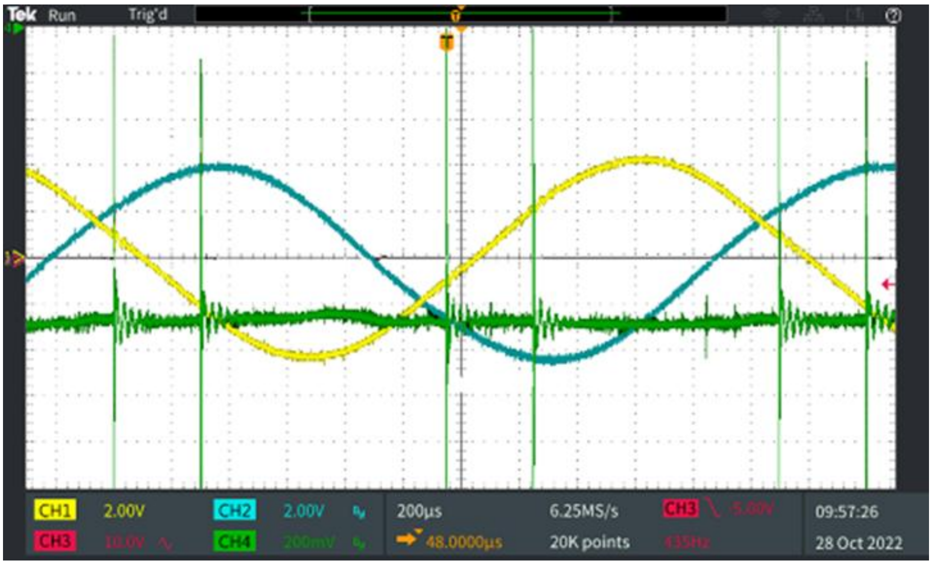

Figure 5. Oscillogram of beam oscillation suppression using current and voltage signals of the primary winding of the accelerator at beam energy of 2.5 MeV and beam current of 15 mA. The green beam is the total targetcurrent, which corresponds to 15 mA. The yellow beam is the current in the anti-oscillation coil along the “X” coordinate, the amplitude is 60 mA. The blue beam is the current in the anti-oscillation coil along the “Y”coordinate, the amplitude is 55 mA.

The oscillogram of electron beam oscillation suppression using primary winding current and primary winding voltage signals is shown in Figure 5. It is evident from the oscillogram that we managed to suppress oscillations to the noise level. In this case, the amplitudes of the currents in the anti-oscillation coils along the “X” and “Y” coordinates are approximately the same and are 60 mA and 55 mA, respectively, and the phases are shifted between themselves by 120^0. Taking into account the calibration of the anti-oscillation coils, the electron beam has oscillations in the D6 diaphragm along the “X” coordinate of $\Delta x = \pm 0.48$ mm, and along the “Y” coordinate of $\Delta y = \pm 0.44$ mm. The beam current deposition on the diaphragms has decreased dramatically and is ID6 = 0 μA, ID5 = 0 μA, ID1 = 20 μA

Conclusions

By means of beam oscillation suppression, it was possible to extract an electron beam with a power of 100 kW with minimal touch of beam current the diaphragms. At an energy of 2.5 MeV and a beam current of

40 mA, the current touch the diaphragms was ID6 = 0 μA, ID5 = 30 μA, ID1 = 50 μA. Due to this, the service life of the diaphragms increased.

References

1 Салимов Р.А. Мощные ускорители электронов для промышленного применения / Р.А. Салимов // УФН 170. — 2000. — Т. 170(2). — С. 197–201. doi: 10.3367/UFNr.0170.200002h.0197.

2 Domarov E.V. Research of Parameters of the Powerful Electron Beam of Industrial Accelerator ELV / E.V. Domarov, D.S. Vorobyov, M.G. Golkovsky, Yu. I. Golubenko, A.I. Korchagin, N.K. Kuksanov, A.V. Lavrukhin, P.I. Nemytov, R.A. Salimov, A.V. Semenov, A.V. Sorokin, S.N. Fadeev, I.K. Chakin, V.G. Cherepkov // Sib. Fiz. Zh. — 2019. — Vol. 14(2). — P. 5–20. doi: 10.25205/2541-9447-2019-14-2-5-20.

3 Domarov E.V. Upgrated the extraction device of focused electron beam into the atmosphere / E.V. Domarov, I. Chakin, V.G. Cherepkov, S. Fadeev, M. Golkovsky, Yu.I. Golubenko, A.I. Korchagin, N.K. Kuksanov, A. Lavrukhin, P.I. Nemytov, R.A. Salimov, A.V. Semenov // 27th Russian Particle Acc. Conf. RuPAC2021. — 2021. — P. 114–116. — JACoW Publishing. doi:10.18429/JACoW-RuPAC2021-FRB03.

4 Domarov E.V. Device for creating a pressure differential using differential pumping / E.V. Domarov, Yu.I. Golubenko, N.K. Kuksanov, R.A. Salimov, S.N. Fadeev, I.K. Chakin // Journal of Applied Mechanics and Technical Physics. — 2022. — Vol. 63(1). — P. 41–46. doi: 10.1134/S0021894422010072

Е.В. Домаров, Д.С. Воробьев, Ю.И. Голубенко, А.И. Корчагин, Н.К. Куксанов,
Р.А. Салимов, С.Н. Фадеев, В.Г. Черепков, И.К. Чакин

ЭЛВ типті үдеткіштердегі электронды сәуленің тербелісі, олардың диагностикасы және басу әдісі

Мақалада көлденең магнит өрісінің бастапқы және қайталама орамалардан үдеткіш түтікке енуіне байланысты ЭЛВ типті үдеткіштердегі электронды сәуленің тербелістерін диагностикалау әдісі сипатталған. Бұл тербелістерді басу әдісі атмосфераға фокусталған электронды сәулені жеткізуге қабілетті сору құрылғысы бар ЭЛВ-8 үдеткішінің мысалында әзірленді және сыналды. Тербелістерді басқаннан кейін атмосфераға қуаты 100 квт фокусталған электронды сәулені шығаруға және диафрагмалардың қызмет ету мерзімін ұзартуға мүмкіндік туды.

Кілт сөздер: электронды үдеткіш, ЭЛВ, фокусталған электронды сәуле, электронды сәуленің тербелісі, электронды сәуленің тербелісін басу әдісі, электронды сәуленің тербелісін диагностикалау.

Е.В. Домаров, Д.С. Воробьев, Ю.И. Голубенко, А.И. Корчагин, Н.К. Куксанов,
Р.А. Салимов, С.Н. Фадеев, В.Г. Черепков, И.К. Чакин

Колебания электронного пучка в ускорителях типа ЭЛВ, их диагностика и метод подавления

В статье описан метод диагностики колебаний электронного пучка в ускорителях типа ЭЛВ, связанный с проникновением в ускорительную трубку поперечного магнитного поля от первичной и вторичной обмоток. Был разработан и испытан метод подавления этих колебаний на примере ускорителя ЭЛВ–8 с выпускным устройством, способным выводить сфокусированный электронный пучок в атмосферу. После подавления колебаний удалось выпустить сфокусированный электронный пучок мощностью 100 кВт в атмосферу и увеличить ресурс диафрагм.

Ключевые слова: ускоритель электронов, ЭЛВ, сфокусированный электронный пучок, колебания электронного пучка, метод подавления колебаний электронного пучка, диагностика колебаний электронного пучка.

References

1 Salimov, R.A. (2000). *Moshchnye uskoriteli elektronov dlia promyshlennogo primeneniia. UFN.170 [Powerful electron accelerators for industrial applications. UFN.170]*. doi: 10.3367/UFNr.0170.200002h.0197 [in Russian].

2 Domarov, E.V., Vorobyov, D.S., Golkovsky, M.G., Golubenko, Yu. I., Korchagin, A.I., Kuksanov, N.K., Lavrukhin, A.V., Nemytov, P.I., Salimov, R.A., Semenov, A.V., Sorokin, A.V., Fadeev, S.N., Chakin, I.K., & Cherepkov, V.G. (2019). Research of Parameters of the Powerful Electron Beam of Industrial Accelerator ELV. *Sib. Fiz. Zh., 14*(2), 5–20. doi: 10.25205/2541-9447-2019-14-2-5-20.

3 Domarov, E.V., Chakin, I., Cherepkov, V.G., Fadeev, S., Golkovsky, M., Golubenko, Yu.I., Korchagin, A.I., Kuksanov, N.K., Lavrukhin, A., Nemytov, P.I., Salimov, R.A., & Semenov, A.V. (2021). Upgrated the extraction device of focused electron beam into the atmosphere. *27th Russian Particle Acc. Conf. RuPAC2021*, 114–116. JACoW Publishing. doi:10.18429/JACoW-RuPAC2021-FRB03.

4 Domarov, E.V., Golubenko, Yu.I., Kuksanov N.K., Salimov R.A., Fadeev S.N., & Chakin I.K. (2022). Device for creating a pressure differential using differential pumping. *Journal of Applied Mechanics and Technical Physics, 63*(1), 41–46, doi: 10.1134/S0021894422010072

Information about the authors

Domarov Evgeny Vadimovich (corresponding author) — Researcher, Budker Institute of Nuclear Physics, Novosibirsk, Academician Lavrentiev Avenue, 11, 630090, Novosibirsk, Russian; *e-mail*: *domarov88@mail.ru*; https://orcid.org/0000-0003-2422-1513;

Vorobev Denis Sergeevich — Engineer, Budker Institute of Nuclear Physics, Novosibirsk, Academician Lavrentiev Avenue, 11, 630090, Novosibirsk, Russian; *e-mail*: *D.S. Vorobev@inp.nsk.su*;

Golubenko Yurii Ivanovich — Senior researcher, Budker Institute of Nuclear Physics, Novosibirsk, Academician Lavrentiev Avenue, 11, 630090, Novosibirsk, Russian; *e-mail*: *Yu.I.Golubenko@inp.nsk.su,*

Korchagin Alexey Ivanovich — Candidate of technical sciences, Senior researcher, Budker Institute of Nuclear Physics, Novosibirsk, Academician Lavrentiev Avenue, 11, 630090, Novosibirsk, Russian; *e-mail: A.I. Korchagin@inp.nsk.su*;

Kuksanov Nikolai Konstantinovich — Doctor of technical sciences, Chief researcher, Budker Institute of Nuclear Physics, Novosibirsk, Academician Lavrentiev Avenue, 11, 630090, Novosibirsk, Russian; *e-mail*: *kuksanov47@mail.ru*;

Salimov Rustam Abelevich — Doctor of technical sciences, Chief researcher, Budker Institute of Nuclear Physics, Novosibirsk, Academician Lavrentiev Avenue, 11, 630090, Novosibirsk, Russian; *e-mail*: *salimov41@mail.ru*;

Fadeev Sergey Nikolaevich — Candidate of technical sciences, Head of Research Laboratory No. 12, Budker Institute of Nuclear Physics, Novosibirsk, Academician Lavrentiev Avenue, 11, 630090, Novosibirsk, Russian; *e-mail*: *faddeev1960@mail.ru*;

Cherepkov Viktor Grigorievich — Candidate of technical sciences, Senior researcher, Budker Institute of Nuclear Physics, Novosibirsk, Academician Lavrentiev Avenue, 11, 630090, Novosibirsk, Russian; *e-mail*: *V.G. Cherepkov@inp.nsk.su*;

Chakin Ivan Konstantinovich — Research engineer, Budker Institute of Nuclear Physics, Novosibirsk, Academician Lavrentiev Avenue, 11, 630090, Novosibirsk, Russian; *e-mail*: *chak_in2003@bk.ru*; https://orcid.org/0000-0003-0529-2017

.

Article
https://doi.org/10.31489/2024/PH4/27-34
UDC 666.762:537.63

Received: 01.07.2024
Accepted: 20.08.2024

S.A. Ghyngazov*, V.A. Boltueva, I.P. Vasil'ev

National Research Tomsk Polytechnic University, Tomsk, Russian Federation
*(*Corresponding author's e -mail: ghyngazov@tpu.ru)*

Synthesis of oxide ceramics in a beam of fast electrons

The development of technology for obtaining high-entropy ceramic materials opens up new possibilities for obtaining new heat-shielding materials. In this work, such a material is synthesized using aluminum-yttrium garnet. The effect of rapid synthesis of high-entropy ceramics within a few seconds was achieved by using an unconventional method of heating the initial mixture of powder reagents with a powerful beam of high-energy electrons. The initial mixture of Y_2O_3, Yb_2O_3, Lu_2O_3, Eu_2O_3, Er_2O_3, Al_2O_3 oxides in a stoichiometric ratio was subjected to a short-term action of a powerful beam of fast electrons under atmospheric conditions. During the radiation exposure, the powder mixture underwent melting, which led to the synthesis of high-entropy ceramics $(Y_{0.2}Yb_{0.2}Lu_{0.2}Eu_{0.2}Er_{0.2})_3Al_5O_{12}$. It was found that the melt has the form of drops with a large number of pores. The efficiency of mixture melting depends mainly on the irradiation modes and to a lesser extent on the modes of preliminary mechanical treatment of the mixture. A necessary condition for synthesis is melting of the powder mixture.

Keywords: high-entropy ceramics, thermal barrier coatings, synthesis, electron beams.

Introduction

Ceramics are the most promising material for creating thermal barrier coatings (TBC). Such outstanding parameters as high melting point, high mechanical strength, resistance to aggressive environments, the ability to vary the coefficient of linear expansion depending on the composition most fully meet the requirements for TBC. The use of simple oxides as TBC is limited due to their high thermal conductivity, the presence of phase transformations and a tendency to destruction at high temperatures. Aluminum-ytterbium garnet ($Yb_3Al_5O_{12}$) is free from the listed disadvantages inherent in simple oxides. This material is a promising candidate for their replacement. However, it is not without disadvantages such as a relatively low coefficient of thermal expansion and high thermal conductivity. One of the ways to improve these characteristics is to create a high-entropy ceramic (HEC) material based on aluminum-ytterbium garnet. At present, the HEC of the composition $(Y_{0.2}Yb_{0.2}Lu_{0.2}Eu_{0.2}Er_{0.2})_3Al_5O_{12}$ is considered as a material capable of improving the properties of $Yb_3Al_5O_{12}$. In [1, 2], it is shown that this HEC is promising for obtaining TBC. The characteristics of HECs can be varied over a wide range by selecting their composition. The emergence of HECs is largely due to the successful development of the technology for obtaining high-entropy alloys [3, 4]. Recently, a large number of types of HECs for various purposes have been created. For example, in [5], the production of $(Ti_{0.2}V_{0.2}Nb_{0.2}Mo_{0.2}W_{0.2})Si$ with high hardness (11.8 ± 0.4 GPa) and elastic modulus (387.2 ± 46.8 GPa) is reported. This material demonstrated excellent wear resistance compared to traditional single-phase ceramics. In [6], it is reported about the creation of a high-temperature ceramic of the composition $(Yb_{0.2}Tm_{0.2}Lu_{0.2}Sc_{0.2}Gd_{0.2})_2Si_2O_7$ for TBC. This material exhibits a surprisingly low thermal conductivity (1.146 $W\ m^{-1}\ K^{-1}$ at 1100 °C), which is even about 45.85 % lower than that of the most widely used YSZ TBC material at 1000 °C. Seven types of thermal barrier coating materials (high-entropy rare earth tantalates $5RETaO_4$, RE= Nd, Sm, Eu, Gd, Dy, Ho, Y, Eu, Tm, Y) were synthesized in [7]. It was also shown there that $(Nd_{0.2}Dy_{0.2}Ho_{0.2}Y_{0.2}Eu_{0.2})TaO_4$ ceramics have low thermal conductivity and a suitable coefficient of thermal expansion. The methods for synthesizing HECs are diverse. In [5], HEC was obtained by spark plasma sintering, and in [6, 7], by solid-phase synthesis. In [8], HEC $(La_{0.2}Nd_{0.2}Sm_{0.2}Eu_{0.2}Gd_{0.2})_2Zr_2O_7$ was obtained by combining combustion synthesis and sintering at ultra-high pressure. In [9], zirconate rare earth ceramic powders with high entropy and low thermal conductivity were obtained by a one-pot synthesis method. In [10], HEC $(La_{1/7}Nd_{1/7}Sm_{1/7}Eu_{1/7}Gd_{1/7}Dy_{1/7}Ho_{1/7})_2Zr_2O_7$ was obtained by reactive spark plasma sintering. In [11], a dense oxide HEC $(La_{0.2}Y_{0.2}Sm_{0.2}Eu_{0.2}Gd_{0.2})_2Zr_2O_7$ with a relative density of 93.7 % was synthesized using the cold isostatic pressing method in combination with the pressureless sintering method. This ceramic is intended for the creation of TBC.

All known methods of HECs synthesis are characterized by high temperatures, durations and their implementation requires special efforts to obtain a given phase composition of the resulting material. In this regard, a new method based on the treatment of a powder mixture of the initial components with a powerful beam of fast electrons (PBFE) is of great interest for the synthesis of HEC. The high efficiency of this method is confirmed by data on the synthesis of phosphors [12–14], zirconium corundum [15]. A feature of this method is the radiation heating of the powder mixture of the initial oxides to the melting temperature with simultaneous ionization of the mixture components by high-energy (more than 1 MeV) electrons. In this case, the synthesis of ceramics in the liquid phase occurs at an enormous speed. Ionization contributes to the acceleration of synthesis. Its stimulating effect on the synthesis of a number of ceramic materials has been convincingly proven in [11, 16–20]. To date, it has been established that synthesis under the influence of PBFE occurs in a short time with high efficiency, provided that the melting temperature of at least one of the components of the initial powder mixture is reached [15]. At the same time, the influence of sample preparation, in particular the modes of preliminary mechanical treatment, the parameters of the electron beam, especially its energy, is practically not presented in the literature.

In this work, the synthesis of HEC $(Y_{0.2}Yb_{0.2}Lu_{0.2}Eu_{0.2}Er_{0.2})_3Al_5O_{12}$ was carried out by heating the initial powder mixture with a PBFE. The regularities of melt formation depending on the conditions of mechanical treatment of the initial powder mixture of oxides and the parameters of the electron beam during irradiation and the influence of all the listed factors on the efficiency of melt formation were established.

Materials and experimental methods

Commercial powders of Y_2O_3, Yb_2O_3, Lu_2O_3, Eu_2O_3, Er_2O_3, Al_2O_3 (HK MOS-INTERNATIONAL COMPANY LIMITED, China), the purity of which was 99.9 %, were taken in accordance with the stoichiometric ratio: $3Y_2O_3 + 3Yb_2O_3 + 3Lu_2O_3 + 3Eu_2O_3 + 3\ Er_2O_3 + 25Al_2O_3 = 10(Y_{0.2}Yb_{0.2}Lu_{0.2}Eu_{0.2}Er_{0.2})_3Al_5O_{12}$. The powders were thoroughly mixed by the wet method in a planetary mill. Two processing modes were used — 500 rpm, mixing time 30 minutes (mixture 1) and 300 rpm, mixing time 90 minutes (mixture 2). The dried powder mixture was poured into the volume of a massive copper cuvette and exposed to PBFE. The value of the mass thickness was selected depending on the magnitude of the accelerating voltage, based on the condition of complete absorption of electrons in the volume of the powder mixture. Electron processing was carried out on an electron accelerator (Unique scientific installation “ELV-6 Stand”, INP SB RAS, Novosibirsk) at an accelerating voltage of 1.4 MeV, 2 MeV and 2.5 MeV. The efficiency of synthesis was determined by the ratio of the mass of the synthesized ceramic product to the mass of the powder poured into the cuvette for subsequent electron processing. During irradiation, the cuvette was moved in the plane of incidence of the electron beam with the help of a movable table at speeds of 1 cm/s and 0.5 cm/s. In all cases, the beam was scanned at a frequency of 50 Hz across the width of the recess in the cuvette. Scanning electron microscopy (SEM) was carried out on a TESCAN VEGA 3 SBU electron microscope (TESCAN, Czech Republic) equipped with an OXFORD X-Max 50 attachment for X-ray fluorescence energy dispersive analysis (EDS) with a Si/Li crystal detector. X-ray phase analysis (XRD) of the initial powder mixture and the synthesized ceramic product was carried out on an X’TRA X-ray diffractometer (ARL, Switzerland).

Results and Discussion

Figure 1 shows photographs of the powder mixture of the initial oxides before processing (Fig. 1 a) and after processing with PBFE with an energy of U=1.4 MeV (Fig. 1 b), 2 MeV (Fig. 1 c) and 2.5 MeV (Fig. 1 d).

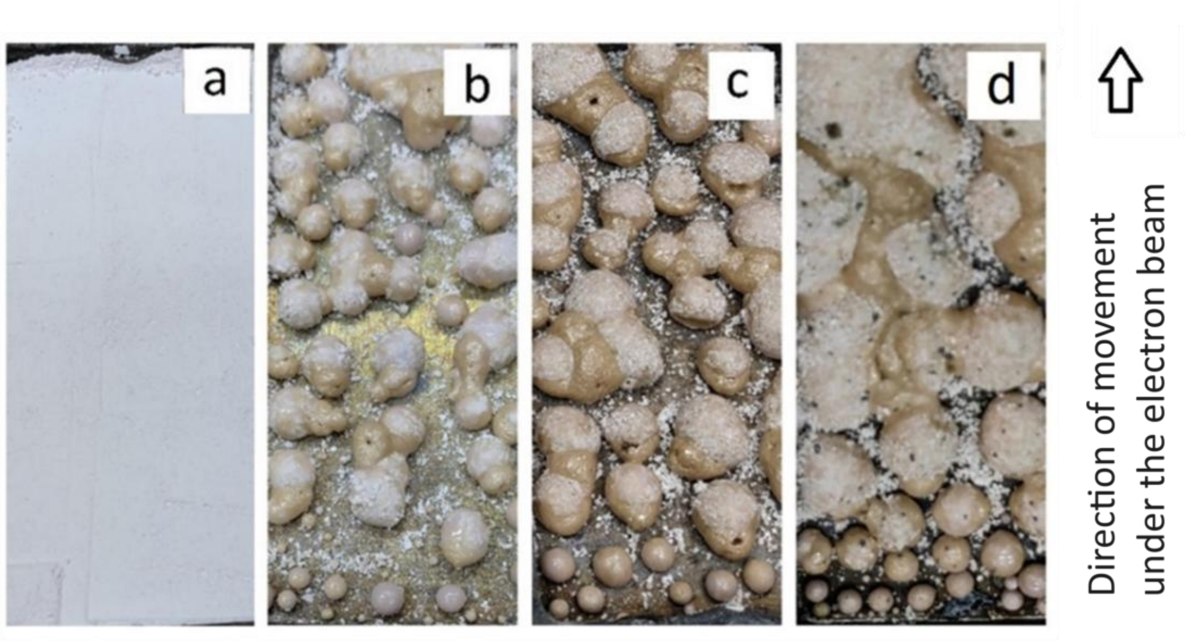

Figure 1. Effect of beam energy on melting results:
a — initial powder mixture: b — U=1.4 MeV; c — U=2.0 MeV; d — U=2.5 MeV. Beam current I=12 mA

It is evident from Figure 1 that as the accelerating voltage increases, the size of the droplets of the synthesized HEC $(Y_{0.2}Yb_{0.2}Lu_{0.2}Eu_{0.2}Er_{0.2})_3Al_5O_{12}$ increases. The characteristic decrease in the droplet size in each case as they move under the beam is explained by the end effect of energy accumulation. Regardless of the value of U, the droplets are a highly porous product (Fig. 2). The pore size increases as U increases.

Figure 2. Optical images of transverse cleavages of droplets of synthesized HEC $(Y_{0.2}Yb_{0.2}Lu_{0.2}Eu_{0.2}Er_{0.2})_3Al_5O_{12}$ at different values of accelerating voltage

The influence of mechanical treatment of the powder mixture of the initial oxides and the PBFE parameters, as well as the speed of movement of the cuvette with the powder mixture under the beam, are illustrated by the optical images of the synthesized HEC, presented in Figure 3. The PBFE parameters provided the same amount of input power. From the examination of Figure 3 it is evident that mechanical treatment affects the average size of the HEC droplet product. In this case, droplet formation strongly depends on the speed of movement of the cuvette with the powder mixture under the beam. The amount of powder product that did not participate in the formation of ceramic droplets, i.e. the efficiency of synthesis, depends on these same parameters.

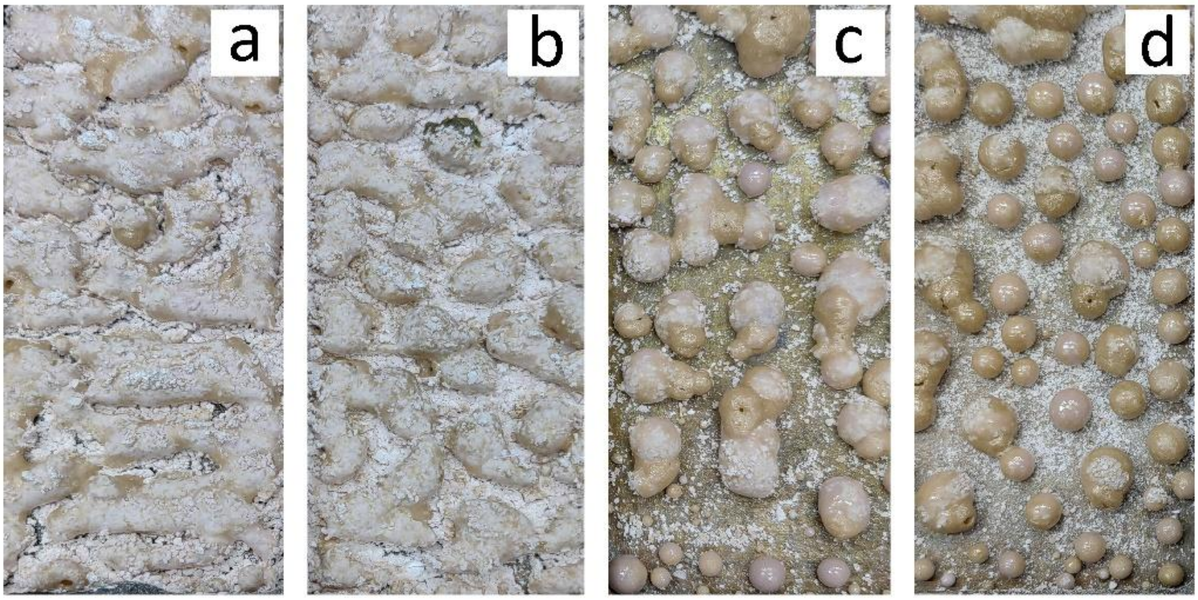

Figure 3. The influence of electron beam parameters (a, b — U=2 MeV, I=4 mA, V=0.5 cm/s, c, d — U=1.4 MeV, I=12 mA, V=1.0 cm/s) and mechanical treatment (a, c — mixture 1; b, d — mixture 2) on the formation of melt droplets

According to SEM data (Fig. 4), the outer surface of the ceramic droplets has a structured appearance with a small number of through pores (Fig. 4 a). The surface of the internal large pores in the volume of the droplet has a layered appearance with clearly defined boundaries (Fig. 4 b). On the transverse cleavage of the droplet, the crystalline structure is not traced in the interpore space, but the structure itself has a characteristic block appearance (Fig. 4 c).

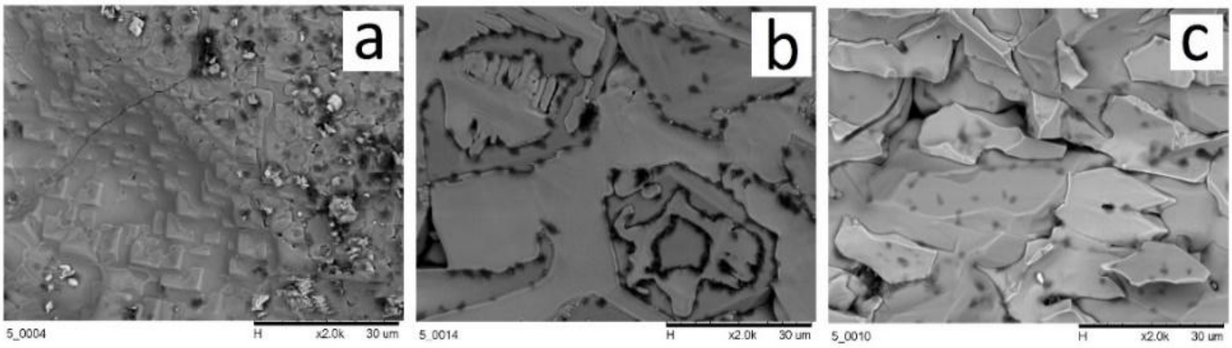

Figure 4. SEM image of a drop of synthesized HEC (U=2 MeV, I=12 mA):
a — outer surface; b — inner pore surface; c — transverse cleavage surface

Weight measurements showed that the melt formation efficiency weakly depends on the conditions of mechanical processing of the initial powder mixture of oxides. At the same time, the efficiency significantly depends on the value of U and the electron beam current (Fig. 5). According to the data in Figure 6, the highest melting efficiency is achieved at U = 2 MeV.

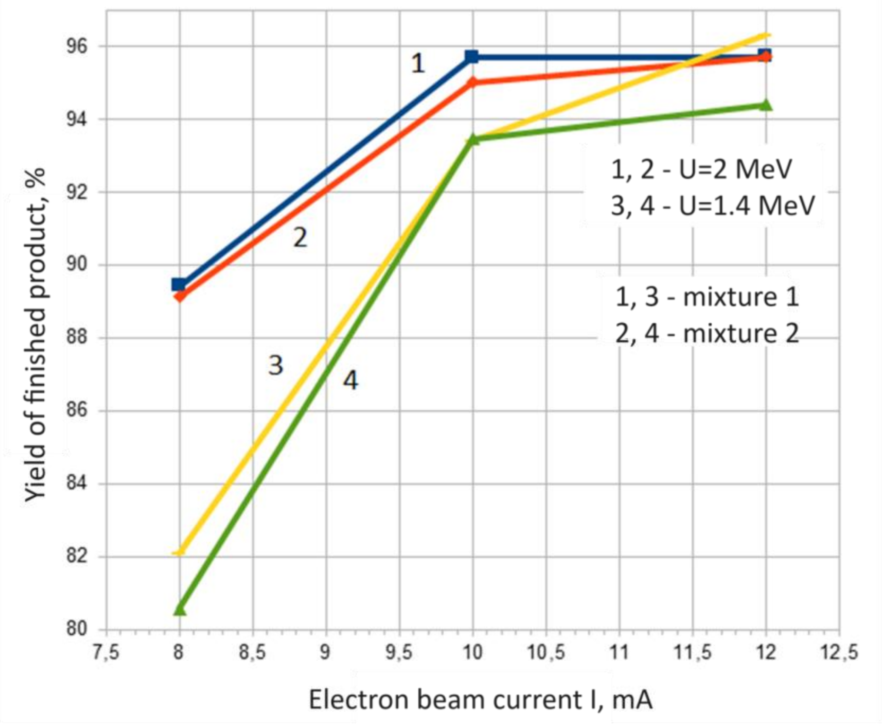

Figure 5. Dependences of the melting efficiency of mixture 1 and mixture 2 at an accelerating beam voltage of 1.4 MeV and 2 MeV on the beam current

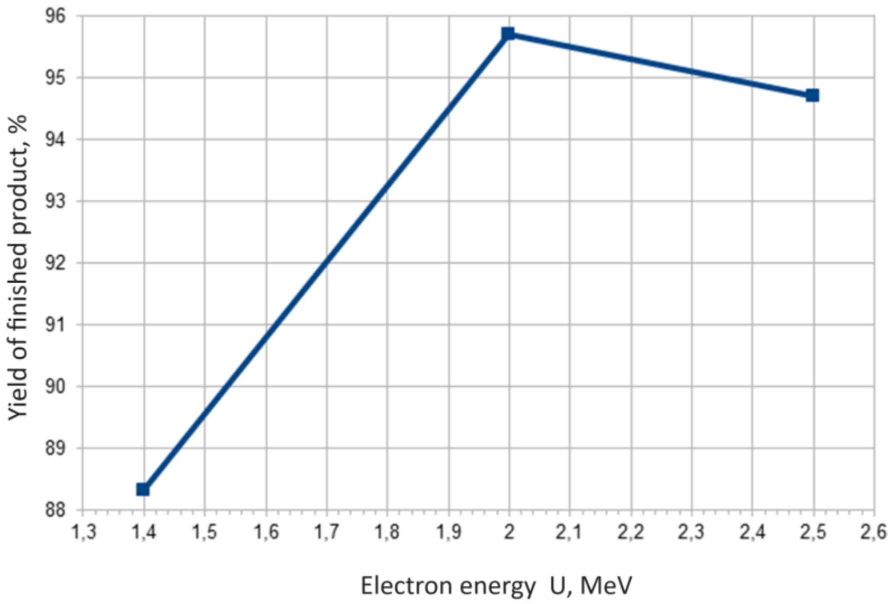

Figure 6. Effect of electron energy on the melting efficiency of powder mixture 2 at a beam current of 12 mA and a feed speed of 1 cm/s

Regardless of the mechanical processing conditions of the initial powder mixture and the PBFE processing modes, the melt droplets are HEC $(Y_{0.2}Yb_{0.2}Lu_{0.2}Eu_{0.2}Er_{0.2})_3Al_5O_{12}$. This is evidenced by the XRD data presented in Figure 7.

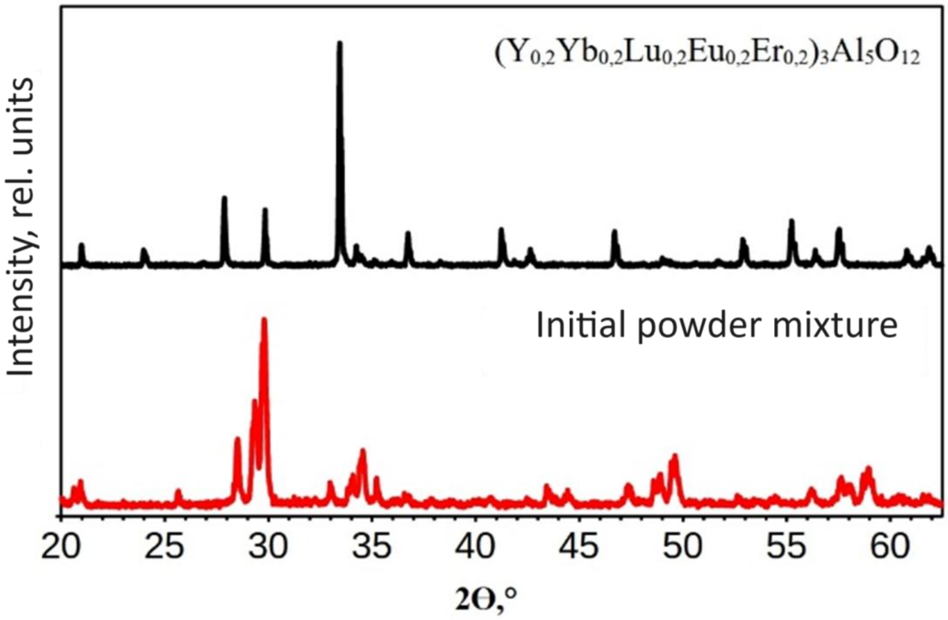

Figure 7. Diffraction patterns of the initial powder mixture of oxides and the high-entropy ceramic product $(Y_{0.2}Yb_{0.2}Lu_{0.2}Eu_{0.2}Er_{0.2})_3Al_5O_{12}$ synthesized in a powerful beam of fast electrons

Conclusions

It is shown that short-term treatment of the powder mixture of Y_2O_3, Yb_2O_3, Lu_2O_3, Eu_2O_3, Er_2O_3, Al_2O_3 oxides with a powerful beam of fast electrons leads to the synthesis of HEC $(Y_{0.2}Yb_{0.2}Lu_{0.2}Eu_{0.2}Er_{0.2})_3Al_5O_{12}$. A necessary condition for the synthesis is melting of the powder mixture. Melting leads to the formation of a highly porous ceramic product mainly in the form of drops. Preliminary mechanical treatment of the powder mixture has little effect on the melting process. The melting efficiency mainly depends on the electron energy, beam current and the speed of movement of the cuvette with the powder mixture under the beam. Regardless of the modes, the droplet ceramic product formed is high-entropy ceramics. Thus, treatment in a powerful beam of fast electrons is a new promising method for the synthesis of high-entropy ceramic materials.

Acknowledgments

This work was supported by the Russian Science Foundation [grant No. 23-79-00014].

References

1 Chen H., Zhao Z., Xiang H., Liu J., & Zhou Y. (2020). High entropy (Y0.2Yb0.2Lu0.2Eu0.2Er0.2)3Al5O12: A novel high temperature stable thermal barrier material. *Journal of Materials Science and Technology,* 48, 57–62, https://doi.org/10.1016/j.jmst.2020.01.056.

2 Wang K., Zhu J., Wang H., Zhou Y., & He J. (2022). Air plasma-sprayed high-entropy (Y0.2Yb0.2Lu0.2Eu0.2Er0.2)3Al5O12 coating with high thermal protection performance. *Journal of Advanced Ceramics, 11*(10), 1571–1582, https://doi.org/10.1007/s40145-022-0630-2.

3 Tsuru T., Han S., Matsuura S., George E.P., & Inui H. (2024). Intrinsic factors responsible for brittle versus ductile nature of refractory high-entropy alloys. *Nature Communications*, *15*(1), 1706, https://doi.org/10.1038/s41467-024-45639-8.

4 Chen Z.W., Li J., Ou P., Singh C.V., & Jiang Q. (2024). Unusual Sabatier principle on high entropy alloy catalysts for hydrogen evolution reactions. *Nature Communications*, *15*(1), 359, https://doi.org/10.1038/s41467-023-44261-4.

5 Li J., Chen S., Fan H., Zhou Y., & Zhang Y. (2024). High-entropy $(Ti_{0.2}V_{0.2}Nb_{0.2}Mo_{0.2}W_{0.2})Si_2$ with excellent high-temperature wear resistance. *Journal of the American Ceramic Society*, *107*(4), 2750–2764, https://doi.org/10.1111/jace.19592.

6 Wei F., Zhang D., Liu Y., Zhang X., & Wang Y. (2024). Novel $(Yb_{0.2}Tm_{0.2}Lu_{0.2}Sc_{0.2}Gd_{0.2})_2Si_2O_7$: exploring its potential for comprehensive performance in environmental barrier coatings. *Journal of the European Ceramic Society*, *44*(4), 2512–2521, https://doi.org/10.1016/j.jeurceramsoc.2023.11.025.

7 Zhang Y., Zhu J., Zou H., Wang H., & He J. (2024). Effect of lattice distortion on thermal conduction behavior in a novel high-entropy rare-earth tantalates. *Journal of Alloys and Compounds*, 976, 172942, https://doi.org/10.1016/j.jallcom.2023.172942.

8 Lin M., Wu Z., Zou J., Ji W., & Fu Z. (2024). Fully dense nanocrystalline $(La_{0.2}Nd_{0.2}Sm_{0.2}Eu_{0.2}Gd_{0.2})_2Zr_2O_7$ high-entropy ceramics fabricated under ultra-high pressure. *Open Ceramics*, 17, 100552, https://doi.org/10.1016/j.oceram.2024.100552.

9 Lan Y., Cui J., Dai B., Yu L., & Xu Y. (2024). One pot synthesis of high entropy rare earth zirconate ceramics with low thermal conductivity for high performance thermal-barrier coatings, *Materials Science and Engineering: B*, 301, 117186, https://doi.org/10.1016/j.mseb.2024.117186.

10 Teng Z., Wang P., Zeng, S., Tan. Y., & Peng S. (2024). Reactive spark plasma sintering of high-entropy $(La_{1/7}Nd_{1/7}Sm_{1/7}Eu_{1/7}Gd_{1/7}Dy_{1/7}Ho_{1/7})_2Zr_2O_7$ pyrochlore ceramic. *Ceramics International*, *50*(4), 6892–6897, https://doi.org/10.1016/j.ceramint.2023.12.035.

11 Fu S., Jia Z., Wan D., & Bao Y. (2024). Synthesis, microstructure and thermophysical properties of $(La_{0.2}Y_{0.2}Sm_{0.2}Eu_{0.2}Gd_{0.2})_2Zr_2O_7$ high-entropy oxide ceramic. *Ceramics International*, *50*(3), 5510–5515, https://doi.org/10.1016/j.ceramint.2023.11.306.

12 Karipbayev Zh.T., Lisitsyn V.M., Mussakhanov D.A., Alpyssova G.K., Popov A.I., Polisadova, E.F., Elsts E., Akilbekov A.T., Kukenova A.B., Kemere M., Sarakovskis A., & Lushchik A. (2020). Time-resolved luminescence of YAG: Ce and YAGG: Ce ceramics prepared by electron beam assisted synthesis. *Nuclear Instruments and Methods in Physics Research, Section B: Beam Interactions with Materials and Atoms*, 479, 222–228, https://doi.org/10.1016/j.nimb.2020.06.046.

13 Lisitsyn V.M., Lisitsyna L.A., Golkovskii M.G., Musakhanov D.A., & Ermolaev A.V. (2021). Formation of luminescing high-temperature ceramics upon exposure to powerful high-energy electron flux. *Russian Physics Journal*, *63*(7), 1615–1621, https://doi.org/10.1007/s11182-021-02213-9.

14 Karipbaeyev Z., Polisadova E., Ermolaev A., Lisitsyn V., Alpyssova G., Mussakhanov D., Kukenova A., & Abil Z. (2020). Dependence of the efficiency electron beam assisted synthesis of YAG: Ce ceramics on the power density of the electron flow. *Proceedings — 2020 7th International Congress on Energy Fluxes and Radiation Effects, EFRE*, 892, https://doi.org/10.1109/EFRE47760.2020.9242038.

15 Ghyngazov S.A., Vasil'ev I.P., Boltueva V.A., & Vlasov V.A. (2023). Synthesis of technical ceramics in a beam of fast electrons. *Russian Physics Journal*, *66*(4), 391–397, https://doi.org/10.1007/s11182-023-02952-x.

16 Surzhikov A.P., Nikolaev E.V., Lysenko E.N., Nikolaeva S.A., Karabekova D.Z., & Ghyngazov A.S. (2020). Formation of Microstructure of Lithium-Titanium Ferrite during its Synthesis in a 2.4 MeV Electron Beam. *Russian Physics Journal*, *63*(5), 894-897, https://doi.org/10.1007/s11182-020-02114-3.

17 Kostishin V.G., Shakirzyanov R.I., Nalogin A.G., Shcherbakov S.V., Isaev I.M., Nemirovich M.A., Mikhailenko M.A., Korobeinikov M.V., Mezentseva M.P., & Salogub D.V. (2021). Electrical and Dielectric Properties of Yttrium–Iron Ferrite Garnet Polycrystals Grown by the Radiation–Thermal Sintering Technology. *Physics of the Solid State*, *63*(3), 435, https://doi.org/10.1134/S1063783421030094.

18 Isaev I.M., Shcherbakov S.V., Kostishin V.G., Nalogin A.G., Mokljak V.V., Ostafijchuk B.K., Alekseev A.A., Korovushkin V.V., Belokon' E.A., Kalinyuk M.V., Mihaylenko M.A., Korobeynikov M.V., Bryazgin A.A., & Salogub D.V. (2019). Peculiarities of the crystal structure and texture of isotropic and anisotropic polycrystalline hexagonal ferrites $BaFe_{12}O_{19}$ synthesized by radiation-thermal sintering. *Russian Microelectronics*, *48*(8), 531–544, https://doi.org/10.1134/S1063739719080079.

19 Lysenko E.N., Vlasov V.A., Surzhikov A.P., & Ghyngazov S.A. (2023). Magnetization and curie point of LiZn ferrite synthesized by electron beam heating of mechanically activated reagents, *Russian Physics Journal*, *65*(11), 1886–1892, https://doi.org/10.1007/s11182-023-02847-x.

20 Lysenko E.N., Vlasov V.A., Nikolaev E.V., Surzhikov A.P., & Korobeynikov M.V. (2023). Microstructure and magnetization study of Li and Li–Zn ferrites synthesized by an electron beam. *Materials Chemistry and Physics*, 302, 127722, https://doi.org/10.1016/j.matchemphys.2023.127722.

С.А. Гынгазов, В.А. Болтуева, И.П. Васильев

Жылдам электрондар шоғырындағы оксидті керамиканың синтезі

Жоғары энтропиялы керамикалық материалдарды алу технологиясының дамуы жаңа жылудан қорғайтын материалдарды алудың жаңа мүмкіндіктерін ашады. Мақалада мұндай материал алюминий-иттрий гар-торының көмегімен синтезделеді. Бірнеше секунд ішінде жоғары энтропиялы керамиканың жылдам синтезінің әсері ұнтақ реагенттерінің бастапқы қоспасын жоғары энергиялы электрондардың қуатты шоғымен қыздырудың дәстүрлі емес әдісін қолдану арқылы қол жеткізілді. Y2O3, Yb2O3, Lu2O3, Eu2O3, Er2O3, Al2O3 оксидтерінің бастапқы қоспасы стехиометриялық қатынаста атмосфералық жағдайларда жылдам электрондардың қуатты шоғының қысқа мерзімді әсеріне ұшырады. Радиациялық әсер ету кезінде ұнтақ қоспасы балқудан өтті, бұл жоғары энтропиялық керамиканың (Y0.2Yb0.2Lu0.2Eu0.2Er0.2)3Al5O12 синтезіне әкелді. Балқыманың кеуектері көп тамшылар түрінде болатыны анықталды. Қоспаны балқытудың тиімділігі негізінен сәулелену режимдеріне және аз дәрежеде қоспаны алдын ала механикалық өңдеу режимдеріне байланысты. Синтездің қажетті шарты ұнтақ қоспасын балқыту болып табылады.

Кілт сөздер: жоғары энтропиялы керамика, термиялық тосқауыл жабындары, синтез, электронды сәулелер.

С.А. Гынгазов, В.А. Болтуева, И.П. Васильев

Синтез оксидной керамики в пучке быстрых электронов

Разработка технологии получения высокоэнтропийных керамических материалов открывает новые возможности для получения новых теплозащитных материалов. В статье такой материал синтезирован с использованием алюмоиттриевого граната. Эффект быстрого синтеза высокоэнтропийной керамики в течение нескольких секунд был достигнут за счет использования нетрадиционного метода нагрева исходной смеси порошковых реагентов мощным пучком высокоэнергетических электронов. Исходная смесь оксидов Y2O3, Yb2O3, Lu2O3, Eu2O3, Er2O3, Al2O3 в стехиометрическом соотношении подвергалась кратковременному воздействию мощного пучка быстрых электронов в атмосферных условиях. В процессе радиационного воздействия порошковая смесь претерпевала плавление, что приводило к синтезу высокоэнтропийной керамики (Y0.2Yb0.2Lu0.2Eu0.2Er0.2)3Al5O12. Установлено, что расплав имеет вид капель с большим количеством пор. Эффективность плавления смеси зависит в основном от режимов облучения и в меньшей степени от режимов предварительной механической обработки смеси. Необходимым условием синтеза является плавление порошковой смеси.

Ключевые слова: высокоэнтропийная керамика, теплозащитные покрытия, синтез, электронные пучки.

Information about the authors

Ghyngazov Sergei Anatolyevich (*corresponding author*) — Doctor of technical sciences, Professor, Leading Researcher, National Research Tomsk Polytechnic University, Lenin street, 30, 634950, Tomsk, Russia; *e-mail: ghyngazov@tpu.ru*; https://orcid.org/0000-0002-2524-9238

Vasil'ev Ivan Petrovich — Candidate of technical sciences, Researcher, National Research Tomsk Polytechnic University, Lenin street, 30, 634950, Tomsk, Russia; *e-mail: zarkvon@tpu.ru*; https://orcid.org/0000-0002-4077-7012

Boltueva Valeria Aleksandrovna — Candidate of technical sciences, Junior Researcher, National Research Tomsk Polytechnic University, Lenin street, 30, 634950, Tomsk, Russia; *e-mail: kostenkova@tpu.ru*; https://orcid.org/0000-0001-8128-9042

Article
https://doi.org/10.31489/2024PH4/35-45
UDC 544.42+519.242.7

Received: 06.06.2024
Accepted: 05.08.2024

M.G. Golkovski[1*], I.P. Denisov[2], S.A. Ghyngazov[2], I.P. Vasil'ev[2], I.K. Chakin[1]

[1]*Budker Institute of Nuclear Physics, Siberian Branch, Russian Academy of Sciences, Novosibirsk, Russia;*
[2]*National Research Tomsk Polytechnic University, Tomsk, Russia*
*(*Corresponding author's e-mail: golkovski@mail.ru)*

Efficiency of liquid-phase synthesis of ceramic materials under the influence of an electron beam with high penetrating power

The research conducted during of last few years showed the advantages of the method of producing of the luminescence ceramic materials as well as the other purposes ceramics with using of electron beam with high penetrating power. In this technology, an industrial accelerator generates the beam and then it enters the atmosphere throw the hole of small diameter. The accelerating voltage of the electrons is regulated in the range of 1.4 — 2.5 MV, which, in combination with the high beam power, allows for a volumetric effect on the powder material, producing its melting in about 1 s, with virtually no contact between the melt and the walls of the crucible in which the initial batch is placed. The paper proposes a method for calculating the energy efficiency of a beam during the synthesis of two-component oxide ceramics. The measurements show that the beam efficiency is on average about 50 %, and in many cases exceeds 80 %, regardless of the melting temperature of the synthesized ceramics and the heat required to heat and melt it.

Keywords: high voltage electron beam, electron beam output into the atmosphere, electron beam melting, release of beam energy in substances, oxide ceramics synthesis, efficiency of the ceramics synthesis.

1. Introduction

The development of ceramic materials for a specific industry primarily involves synthesis from powder raw materials. The currently used synthesis methods have disadvantages such as long process duration, changes in the stoichiometric composition of the starting components during the synthesis process (ceramic synthesis method), low purity of the synthesized product (co-precipitation method, SHS method), etc. A new method for synthesizing ceramic materials makes it possible to eliminate these shortcomings by activating heating of the initial powder reaction mixtures with a powerful beam of fast electrons. In this method, electrons with energy of more than 1 MeV carry out volumetric heating of the reaction mixture in a short time, ensuring, in addition to a high synthesis rate, high chemical purity, and preservation of the stoichiometric composition and phase homogeneity of the synthesized ceramic materials. These characteristics are especially important in obtaining phosphors [1, 2] and high entropy ceramics, in particular heat-protective ones for creating thermal barrier coating [3] and perovskite structure [4, 5] for solar energetics.

The parameters of electron beams achieved by modern accelerators are sufficient to heat practically any substance in air to the melting point in a time not exceeding a second. This makes possible to carry out the synthesis of ceramic materials in a fast electrons beam under conditions of achieving a liquid-phase state in the reaction mixture. In this case, the efficiency of the synthesis of ceramic materials is the highest, because in the liquid phase the mass transfer in the mixture of reagents is most intense. The combination of high penetrating ability and high beam power allows for the production of ceramic materials with a productivity of 20 kg/h and higher. In a number of works carried out in recent years, V.M. Lisitsyn and co-authors showed that the express synthesis of luminescent ceramics is successfully implemented under conditions of heating the reaction mixture with a powerful beam of fast electrons [6–9]. V.M. Lisitsyn and co-authors beside luminescent ceramics obtained other purpose ceramic materials. Using this method, S.A. Ghyngazov and co-authors synthesized high-entropy ceramic alloys. The last mentioned works conclude that issues of optimizing the conditions of radiation heating should be the subject of special studies.

The aim of this work is to relate the physical characteristics of ceramic powders with the required parameters of their electron beam irradiation modes to achieve the liquid phase of the original powders. The numerical estimates were based on the fact that ceramic powder is a weakly heat-conducting medium, therefore the volumetric heat supply to the material, realized during electron beam processing, will be close to adiabatic. The authors compared two experimental values: the heat required to heat and melt the material according to thermodynamic data and the heat calculated using the irradiation parameters based on the known distribution of the energy release of the electron beam in the material depending on the depth of its penetration. Since this study represents an initial step in obtaining numerical characteristics of the process, it presents the results only for two-component systems. Another reason for choosing only two-component systems is the availability of data on the temperature dependences of enthalpies.

We characterize the energy efficiency of synthesis by a value called beam efficiency, which is understood as the ratio of the energies mentioned above: the energy required to heat and melt the volume of the initial powder material that has passed into a liquid state, and the energy actually introduced into this volume. This coefficient is denoted below by the letter η. When calculating the beam efficiency η, the authors assumed that when an electron beam impacts the powder, the role of radiation effects is negligible, and that the synthesis of ceramics occurs in the liquid phase. If it turns out that radiation plays a significant role in the synthesis, the no-radiation-effect approach is still useful for identifying its contribution.

2. Equipment and experimental procedure

The work was carried out at the Budker Institute of Nuclear Physics of the Siberian Branch of the Russian Academy of Sciences on the “UNU Stand ELV-6” facility. An Industrial accelerator generated a dc current electron beam with an accelerating voltage set in the range of 1.4 — 2.5 MeV. The beam is released into the atmosphere through a 2 mm diameter hole. The distance from the beam release hole to the surface of the material being processed was 9 cm. During the experiments, the values of the electron energy (accelerating voltage) E and the beam current I were established, and the beam power was determined by their product. The beam has a Gaussian distribution of the power flux density in its cross-section. Its Gaussian diameter at a distance of 9 cm from the outlet is approximately 12 mm for electron energy of 1.4 MeV, 10 mm for energy of 2 MeV and 9 mm for energy of 2.5 MeV. Electron beam processing was performed with or without beam scanning. The scanning frequency was 50 Hz. The initial powder was placed in a rectangular massive copper crucible. The internal space of the crucible, where the powder was placed, had dimensions of 50x100xH mm, where the depth H was selected based on the penetrating ability of the beam and the bulk density of the material placed in the crucible and took values of 7, 10 or 14 mm. Initially, the beam was directed to the target to set the required parameters. Then the crucible began to move under the beam, moving along its length perpendicular to the beam scanning direction at a speed of 1 cm/s. In the beam scanning mode, the entire surface of the powder placed in the crucible was processed, for which the scanning span was set equal to the crucible width l=5 cm. In the non-scanning mode, a processed track with a width comparable to the beam diameter was formed in the material layer.

During the experiments, a parameter called the mass thickness of the processed material σ was monitored. It was determined by the formula:

$$\sigma = \frac{m}{S}, \tag{1}$$

where m is the mass of the material in the crucible, S is the area of its bottom. Three types of mass m were recorded: the mass of the material before irradiation, the mass of the contents of the crucible after irradiation, and the mass of the ceramics synthesized because of irradiation. Accordingly, three mass thicknesses were recorded: σ_1, σ_2 and σ_{melt}. Obviously, the mass thickness of ceramics makes sense and was determined only in scanning modes.

3. Calculation formulas

3.1. Definition of the term beam efficiency in this paper

As stated in the Introduction, by beam efficiency η we mean the ratio of the heat required to melt the synthesized volume of ceramics to the heat introduced by the beam into this volume. The value of η can be determined by the formula:

$$\eta = \frac{h_{melt}}{w_{melt}}, \tag{2}$$

where h_{melt} is the energy required to heat 1 g of material from room temperature to the melting point and then melt it at this temperature, w_{melt} is the value of energy actually introduced in 1 g of molten material.

The heat required to melt ceramic powders was determined based on thermodynamic databases [10, 11, 12] as the difference between the enthalpies of the molten material at the melting temperature and the material in the initial state at room temperature according to the formula:

$$h_{melt} = \frac{H_{liq}\ \ T_{пл}\ \ - H_{sol}\ \ 300K}{M}, \tag{3}$$

where $H_{liq}(T_{пл})$ and $H_{sol}(300K)$ are molar enthalpies of material at liquid state at melting temperature and solid state at room temperature, M is molar mass in g. The amount of energy expended per 1 g of ceramics w_{melt} is determined based on the parameters of the irradiation mode and the known distributions of energy release by electrons according to the depth of their penetration into the material.

3.2. Calculation of expended beam energy w_{melt}.

As was indicated in Section 2, the beam has a non-uniform Gaussian distribution of the power flux density in its cross-section. Its Gaussian diameter is comparable to the depth of beam penetration into the powder material. However, when scanning the beam with simultaneous movement of the crucible in the direction perpendicular to the scanning, we obtain a large surface area, almost simultaneously processed by the beam. The distribution of energy released inside the material will be close to that which would be observed from a wide beam with a uniform distribution of the power flux density over the area of its cross-section. The size of this cross-section in the scanning direction coincides with the scanning span, i.e. is equal to approximately 5 beam diameters. In the direction perpendicular to scanning, it is equal to at least 2...3 beam diameters, since due to the poor thermal conductivity of the ceramic powder, the heat is retained in the volume where it was introduced for a noticeable time. During this time, the crucible has time to move several beam diameters. Based on the above, the beam can be considered wide, with a uniform distribution of the power flow over its cross-section and dimensions that are many times greater than the depth of its penetration. The problem of energy loss distribution in the material for such beams can be considered one-dimensional.

For wide beams, the distribution of energy release by accelerated electrons by the depth of their penetration into the material depending on the initial electron energy E and the composition of the material has been studied many times. T. Tabata et al. presented these results in analytical form in a number of works, in particular [13, 14]. Figure 1 presents the distributions constructed on the basis on the indicated works for some characteristic modes for which measurements were performed in this work. The ordinate axis of the distributions shows the mass thickness of the material z in g/cm^2, measured from the powder surface. The abscissa axis shows the derivative of the electron energy E (in MeV) with respect to z. The $\frac{}{\mathrm{dz}}\frac{dE}{dz}$ value characterizes the intensity of energy losses by electrons in the material and is measured accordingly in —————— ——————. In the graphs in Figure 1, to the left of the vertical axis, after the chemical formulas of the processed substances, the initial energies of electrons in MeV are given in brackets in the second position. The presented distributions can only be used to calculate the energy release inside materials during beam scanning processing. They are not applicable to narrow beam processing without scanning.

If the ceramic synthesis occurs in a certain layer of powder from depth z_1 to z_2, the mass thickness of the melt is equal to $\sigma_{melt} = z_2 - z_1$. The energy loss per electron in MeV when passing from layer z_1 to layer z_2 will be $-\quad\int_{z_1}^{z_2}\frac{dE}{dz}dz$. The beam power released between layers with coordinates z_1 and z_2 is equal to $P = \int_{z_1}^{z_2}\frac{dE}{dz}dz \cdot I$, where I is the beam current. The mass of ceramics melted in 1 s is equal to $\sigma_{melt} \cdot l \cdot v$, where σ_{melt} is the mass thickness of the melted ceramics, l is the width of the scanning, v is the speed of movement of the crucible under the beam. Dividing the power spent on melting the ceramics by the mass of the ceramics obtained in 1 s gives the beam energy consumption per unit mass of the ceramics:

$$w_{melt} = \frac{\int_{z_1}^{z_2}\frac{dE}{dz}dz \cdot I}{\sigma_{melt} \cdot l \cdot v} = \frac{\left(\frac{dE}{dz}\right)_{mid} \cdot I}{l \cdot v}, \tag{4}$$

where $\left(\frac{dE}{dz}\right)_{mid}$ is the average value of the intensity of energy loss by each electron in the region between z_1 and z_2.

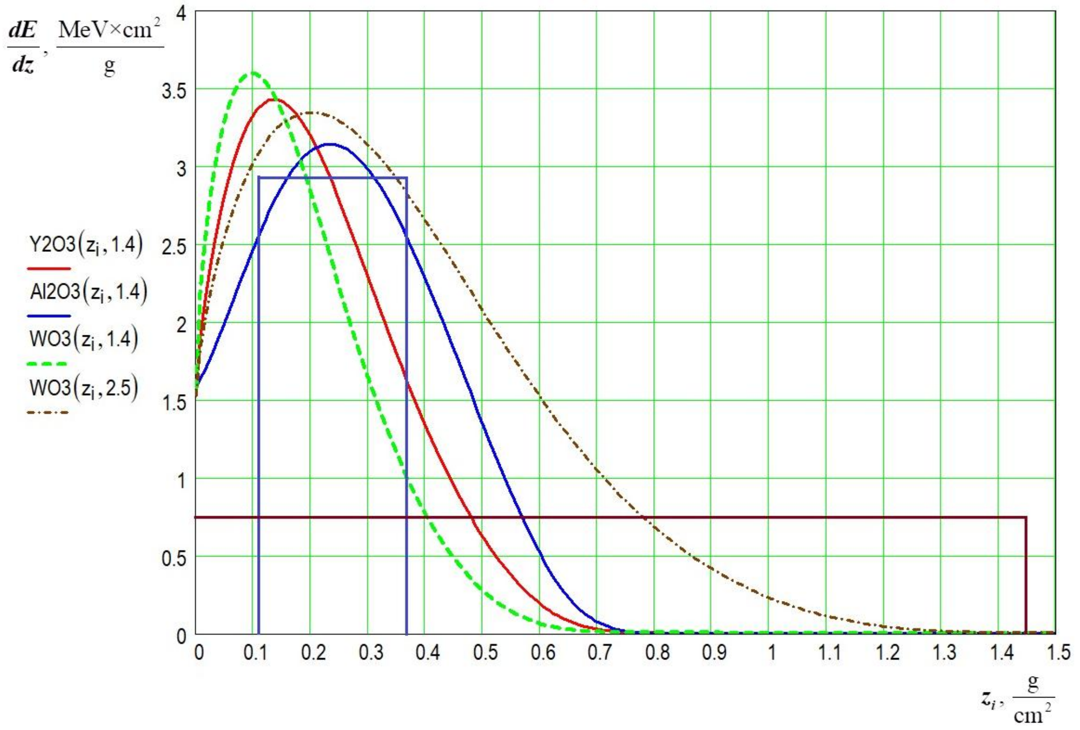

Figure 1. Distributions of electron energy losses as a function of mass thickness, normalized to one electron. The distributions represent the characteristic modes given in Table 1

In Figure 1, as an example, the vertical lines indicate the values of z_1 and z_2 for samples synthesized from Al_2O_3 and WO_3 powders. For a sample of WO_3, z_1=0. The horizontal lines for these samples indicate the average values of the intensity of energy losses. In the case where the mass thickness of the melt layer σ_{melt} approaches or exceeds the mass thickness of beam penetration, the energy expended on melting will be equal to the entire energy introduced by the beam, since the absorption of the beam energy will occur entirely in the melt. Then the entire beam power P, with the exception of the power carried away by reflected electrons and bremsstrahlung, will be introduced into the melt and the efficiency can be written using a simpler formula, representing w_{melt} as

$$w_{1melt} = \frac{1-\gamma \ Pt}{m_{melt}}, \tag{5}$$

and beam efficiency in this case will be equal:

$$\eta_1 = \frac{h_{melt} m_{melt}}{1-\gamma \ Pt}, \tag{6}$$

where P is the beam power; γ is the beam reflection coefficient by power, the reflection coefficient γ depends on the composition of the substance and is close to 0.1; t is the time it takes for the crucible to pass under the beam, in the experiments it is equal to 10 s; h_{melt} is the energy required to heat and melt 1 g of material; m_{melt} is the mass of the melt.

If the mass thickness of the melt is noticeably less than the beam penetration depth, formula (4) must be used, since (6) will give underestimated beam efficiency values.

When conducting experiments without scanning, the beam cannot be considered wide. The calculation of the expended energy according to (4), using the distribution for wide beams, is incorrect. However, formula (6) remains valid, since it does not use the distribution of energy losses by depth. It is only necessary that the condition of exceeding the mass thickness of the powder fill compared to the beam penetration depth be met. In addition, it should be borne in mind that in threshold modes without scanning, at low powers corresponding to the beginning of the melt appearance, formula (6) will give underestimated values of the beam efficiency.

4. Results and Discussion

During the work, a synthesis was carried out and the beam efficiency was calculated for several dozen samples from different materials with and without beam scanning under different irradiation parameters. In order to reduce the volume of the article, the authors selected 11 characteristic modes with scanning (Table 1) and 7 modes without scanning (Table 2) for analysis. The samples in the tables are arranged in order of increasing energy h_{melt} required for their heating and melting. Figure 2 shows the appearance of some samples from Table 1, Figure 3 — from Table 2.

4.1. Modes with scanning of the beam.

It should be noted that the data on the modes for Y_2O_3, Al_2O_3 (405), MgF_2, BaF_2 presented in Table 1 are quite reliable, since they have been confirmed by 4–8 experiments under similar conditions for each of the substances. The first column of Table 1 indicates the powder material and (in brackets) their marking according to the laboratory classification. Remaining columns use the following designations:

$T_{пл}$ — melting point of the material;
h_{melt} — the energy required to heat and melt 1 g of material (see (3));
E — energy (accelerating voltage) of beam electrons;
P — beam power;
Powder scattering — loss of mass of crucible contents during irradiation in %;
σ_2 — mass thickness of the crucible contents after irradiation (melt + remaining powder);
σ_{melt} — mass thickness of the melt;
η — beam efficiency coefficient calculated according to (2).

Table 1

Processing modes with scanning of the beam

Composition and marking of powder	$T_{пл}$, °C	h_{melt}, kJ/g	E, MeV	P, kW	Powder scatter, %	σ_2, g/cm^2	σ_{melt}, g/cm^2	Beam efficiency, η
BaF_2 (520)	1368	0.905	1.4	16	0.5 %	1.55	1.52	0.53
WO_3 (438)	1472	0.935	1.4	16	3.4 %	1.74	1.45	0.56
WO_3 (439	1472	0.935	2.5	24	35 %	1.31	0.93	0.24
MgF_2 (516)	1263	0.942	1.4	15	0.4 %	0.85	0.84	0.27
Ga_2O_3 (474)	1807	1.75	1.4	17	0.8 %	1.06	1.06	0.61
SiO_2 (sand)	1600	1.87	2	17	1.4 %	1.01	0.59	0.42
Y_2O_3 (490)	2439	2.05	1.4	25	1.3 %	1.11	1.03	0.47
Al_2O_3 (816)	2054	3.5	1.4	10	0.1 %	0.94	0.26	0.84
Al_2O_3 (413)	2054	3.5	1.4	26	0.8 %	0.98	0.88	0.61
Al_2O_3 (sand)	2054	3.5	2	24	0.1 %	1.02	0.78	0.63
MgO (485)	2832	5.66	1.4	25	5.7 %	0.51	0.49	0.63

Appearance of synthesized ceramics in the modes with beam scanning. Figure 2 a and b show the “borderline” mode, in which the synthesis of ceramics in the thickness of the material under the surface of the powder is just beginning. As a result, in the Al2O3 (816) mode, a thin plate was formed lying under a layer of powder. During the cleaning process, it broke into separate fragments. Figure 2b shows them joined in their original form. The remaining photos show samples with the melt reaching the surface of the powder. After solidification, the melt is either flat drops that can merge to form plates (Fig. 2 c), or merged rollers oriented along the beam scanning direction (Fig. 2 d), or thickened plates with smooth surfaces (Fig. 2 e, f, h). Fig. 2 g, h shows a sample obtained from coarse-dispersed material in the form of quartz sand of technical purity with a particle size of up to 500 µm. As can be seen from Table 1, the large particle size is not a factor that significantly reduces the beam efficiency.

Beam efficiency in the modes with scanning of electron beam. In their calculations, the authors assumed that the synthesis of ceramics occurs in a layer of a certain thickness. In most cases, the melt is formed from the surface of the powder bed $z_1=0$ to a certain depth, $z=\sigma_{melt}$. This situation is observed for all samples presented in Table 1, with the exception of the Al_2O_3 (816) sample (Fig. 2 a, b). As indicated in section 3.2, in the graphs of Figure 1, as an example, for samples of Al_2O_3 (816) and WO_3 (438) the melt boundaries and average values of electron energy losses in the melt thickness — — — are indicated. The melt thickness of the WO_3 (438) sample significantly exceeds the beam penetration depth. This means that heat transfer from the beam-heating zone to the underlying melt layers occurred due to convection in the melt.

a) Al2O3 (816), appearance after irradiation, σ2=0.94 g/cm2

b) Al2O3 (816), σmelt=0.26 g/cm2

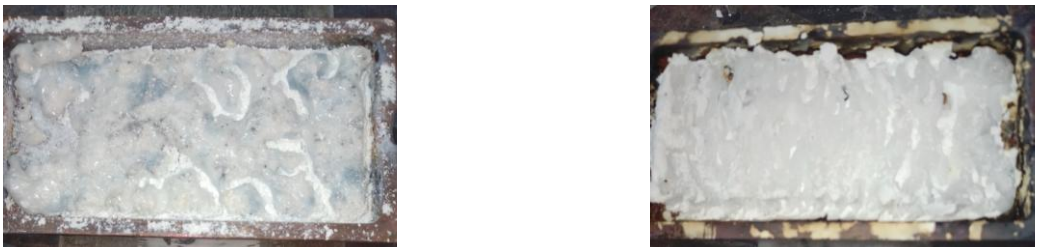

c) Ga2O3 (474), σ2=1.06 g/cm2

d) MgO (485), σ2=0.51 g/cm2

e) MgF2 (516), σ2=0.85 g/cm2

f) Y2O3 (490), σ2=1.03 g/cm2

g) SiO2 before treatment sand, σ2=1.01 g/cm2

h) SiO2 after treatment sand, σmelt=0.59 g/cm2

Figure 2. Appearance of samples after scanning beam treatment:
a, c, d, e, f — appearance of samples after irradiation, b — fragments of synthesized plate of Al_2O_3 (816),
g — SiO2 sand before treatment and h — ceramic plate synthesized from it, raised above the crucible

In a number of modes, low electron beam efficiency is observed, down to 0.2. Such modes usually occur under the following circumstances:

— The mass thickness of the initial powder is noticeably less than the beam penetration depth, due to which the melt reach the bottom of the crucible, and a noticeable part of the heat leaks into the thick-walled copper bottom of the crucible.

— The beam power exceeds that required to melt the powder placed in the crucible. For example, in the MgF_2 (516) mode, the surface density of the introduced energy required to melt the powder should be $0.84 g/cm^2 \cdot 0.942 kJ/g = 0.79 kJ/cm^2$. Taking into account the beam efficiency, for example, 0.5, this value can increase to 1.6 kJ/cm^2. In reality, the specific energy introduced was $15 kW/5 cm^2/s = 3 kJ/cm^2$, which resulted in the melt touching the bottom of the crucible (Fig. 2e).

— There is observed a noticeable scattering of the original powder during the irradiation process, for example, in the WO_3 mode (439). The reasons for the scattering have not been precisely determined. These may include: the presence of volatile impurities in the powder, which can cause both the powder to fly apart and small droplets of melt to splash; the nano-sized range of powder particles; electrification of powder particles when irradiated with electrons. Due to their low bulk density, nano-sized powders cannot be placed in a crucible with sufficient mass thickness. In addition, the thickness of the nanopowder contains a large volume of air, which, when heated, expands and can cause the powder to scatter. The acceptable powder particle size is 5–500 μm. The influence of electrification has not been confirmed, since high efficiency modes are observed on some high-purity dielectric powders (see modes with Al_2O_3 and MgO in Table 1). In the case of the WO_3 (439) sample, the reason for the large spread and low efficiency could have been the combination of an excess (at least 2 times greater than necessary) beam power with an increased penetration depth. In the photo of this sample after irradiation (not included in the article), one can see the scattering of powder and small drops of melt beyond the crucible.

4.2. Processing modes without beam scanning.

In Table 2 which presents the characteristic modes without beam scanning (track modes), the following designations are used:

h_{melt} — the energy required to heat and melt 1 g of material (see (3));

P — beam power;

E — energy (accelerating voltage) of beam electrons;

m_{melt} — mass of sintered (molten) material in a crucible;

Powder scattering — the loss of powder mass during irradiation in g;

σ_2 — mass thickness of the crucible contents after beam processing;

η_1 — efficiency coefficient (6), in the calculation of which the expended energy (5) is defined as the total energy introduced by the beam minus the energy reflected from the surface of the material.

Table 2

Processing modes without scanning of the beam

Composition and marking of powder	$T_{пл}$, °C	h_{melt}, kJ/g	P, kW	E, MeV	m_{melt}, g	Powder scatter, g	σ_2, g/cm^2	Beam efficiency η_1
BaF_2 (518)	1368	0.905	4	1.4	22.29	1.24	1.69	0.64
WO_3 (437)	1472	0.935	4	1.4	25.63	0.49	1.6	0.82
MgF_2 (515)	1263	0.942	4	1.4	19.09	0.13	0.92	0.46
Ga_2O_3 (473)	1807	1.75	4	1.4	15.25	0.21	1.1	0.75
Y_2O_3 (489)	2439	2.05	4	1.4	10.24	0.42	1.18	0.61
ZnO (468)	1977	2.15	4	1.4	12.39	0.62	0.50	0.75
Al_2O_3 (405)	2054	3.5	4	1.4	9.43	0.24	0.82	0.85
MgO (484)	2832	5.66	7	1.4	9.79	0.2	0.58	0.82

a) Ga2O3 (473), σ2=1.1 g/cm2, η=0.75

b) Y2O3 (489), σ2=1.18 g/cm2, η=0.61

c) ZnO (468), σ2=0.50 g/cm2, η=0.75

d) MgO (484), σ2=0.58 g/cm2, η=0.82

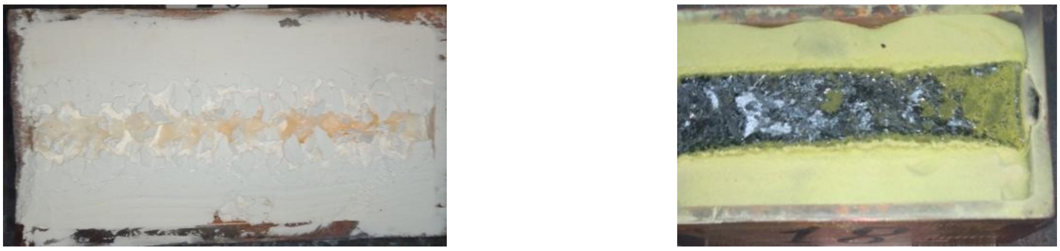

e) Al2O3 (405), σ2=0.82 g/cm2, η=0.85

f) WO3 (437), σ2=1.6 g/cm2, η=0.82

Figure 3. Appearance of samples after processing without beam scanning (in track mode)

All modes in Table 2, with the exception of ZnO (468), Al_2O_3 (405) and MgO (484), are performed on the same materials as the modes in Table 1, so that when comparing modes with and without scanning, the material influence factor is excluded. Comparison of the efficiency of η and η_1 in Table 1 and Table 2 shows that the energy input efficiency in modes without scanning is higher. This seems strange and requires a separate discussion.

The beam is non-uniform in cross section. The maximum power flux density is realized near the beam axis. As you move away from the axis, it decreases approximately according to Gauss's law. The movement of the material under a stationary beam leads to the formation of a melting track in it. The power flux density at some distance from the beam axis is already insufficient to melt the material. That is, part of the beam power is spent on heating the edges of the track without melting them. When scanning the beam, the power flux density is averaged across the scanning area and the edge zones of the beam contribute to the averaged power flux density, as a result of which the entire beam power is utilized and, it would seem, the efficiency during scanning should be higher.

In practice, we observe the opposite picture. The explanation seems to be as follows: In the non-scanning mode, the maximum beam energy is released on the axis of the melting track on some depth under the surface of treated material. In the region of maximum energy release, the beam overheats the melt above the melting temperature. Due to convection and thermal conductivity inside the melt, the temperature spreads from the central region of the melt to the periphery, heats it, and powder particles are drawn into the zone of overheated melt and in turn melt. Thus, the size of the melt zone becomes larger than the zone heated by the beam to the melting temperature. In modes with scanning, the situation is different. Thermal insulation is worse. Either plates or large drops are formed. They come into contact with the powder mainly only from below. The relative amount of peripheral powder entering the overheated zone of the melt is less.

Conclusions

1. Accelerated synthesis of ceramics under the influence of an electron beam for two-component oxides can be explained by the formation of a liquid phase according to an equilibrium thermodynamic mechanism without taking into account radiation effects. The energy introduced by the electron beam is more than enough to melt the powder material.
2. The method for producing ceramics using an electron beam with MeV-range electron energy is characterized by high beam energy efficiency, which is expressed through the beam efficiency coefficient η proposed in this work. Its average value, regardless of the energy required to melt the material and the melting temperature, exceeds 50 %, and in some cases, the beam efficiency exceeds 80 %.
3. For most of the studied substances, the loss of powder mass during the synthesis process does not exceed several percent.
4. Efficiency values less than one third are observed in the following cases:

- during processing, significant powder dispersion occurs;
- the selected beam power significantly exceeds that required to melt the material placed in the crucible;
- the mass thickness of the initial powder layer is less than the mass thickness of the beam penetration.

Acknowledgments

The work was supported by the Russian Science Foundation, grant No. 23-79-00014.

References

1 Lv, Xiang et al. Recent progress on modulating luminescence thermal quenching properties of bi3+-activated phosphors / Xiang, Lv et al. // Inorganic Chemistry Frontiers. — 2024. — Vol. 11. — No. 6. — P. 1668–1682. https://doi.org/10.1039/d3qi02588h.

2 Haider, Asif Ali, et al. Advances in reversible luminescence modification and applications of inorganic phosphors based on Chromism reaction / Asif Ali, Haider // Advanced Optical Materials. — 2023. — Vol. 12. — No. 5. https://doi.org/10.1002/adom.202302265.

3 Zhou, Ming et al. Reaction mechanisms of (re0.2nd0.2sm0.2eu0.2gd0.2)2zr2o7 (re = la or YB) under Cao-MgO-Al2O3-SiO2 (cmas) attack / Ming, Zhou et al. // Journal of the European Ceramic Society. — 2024. — Vol. 44. — No. 6. — P. 4055–4063. https://doi.org/10.1016/j.jeurceramsoc.2024.01.014.

4 Li, Xudong et al. Enhanced redox electrocatalysis in high-entropy perovskite fluorides by tailoring D–P hybridization / Xudong, Li et al. // Nano-Micro Letters. — 2023. — Vol. 16. — No. 1. https://doi.org/10.1007/s40820-023-01275-3.

5 Wang, Yuhao et al. High-entropy perovskites for Energy Conversion and storage: Design, synthesis, and potential applications / Yuhao, Wang et al. // Small Methods. — 2023. — Vol. 7. — No. 4. https://doi.org/10.1002/smtd.202201138.

6 Lisitsyn, Victor, et al. Radiation synthesis of high-temperature wide-bandgap ceramics / Victor, Lisitsyn et al. // Micromachines. — 2023. — Vol. 14. — No. 12. — P. 2193. https://doi.org/10.3390/mi14122193.

7 Lisitsyn, Victor et al. The optimization of Radiation Synthesis Modes for YAG: CE Ceramics / Victor, Lisitsyn et al. // Materials. — 2023. — Vol. 16. — No. 8. — P. 3158. https://doi.org/10.3390/ma16083158.

8 Lisitsyn, Victor et al. Express synthesis of YAG: CE ceramics in the high-energy electrons flow field / Victor, Lisitsyn et al. // Materials. — 2023. — Vol. 16. — No. 3. — P. 1057. https://doi.org/10.3390/ma16031057.

9 Ghyngazov, S.A. et al. Synthesis of technical ceramics in a beam of fast electrons / S.A. Ghyngazov // Russian Physics Journal. — 2023. — Vol. 66. — No. 4. — P. 391–397. https://doi.org/10.1007/s11182-023-02952-x.

10 NIST Chemistry Webbook, SRD 69. Chemical Formula Search. — [Electronic resource]. — Access mode: webbook.nist.gov/chemistry/form-ser/. Accessed 16 Oct. 2024.

11 Глушко В.П. (ред.). Термодинамические свойства индивидуальных веществ: Справоч. изд.: [В 4-х т.]. — 3-е изд. / В.П. Глушко (ред.), Л.В. Гурвич и др. — М.: Т. 1 — 1978; Т. 2 — 1979; Т. 3 — 1981; Т. 4 — 1982.

12 Термодинамические свойства индивидуальных веществ: Справоч. изд. — Т. 5 (онлайн версия). — [Электронный ресурс]. — Режим доступа: https://www.chem.msu.su/rus/tsiv/

13 Tabata, Tatsuo et al. An algorithm for depth–dose curves of electrons fitted to Monte Carlo data / Tatsuo, Tabata // Radiation Physics and Chemistry. — 1998. — Vol. 53. — No. 3. — P. 205–215. https://doi.org/10.1016/s0969-806x(98)00102-9.

14 Tabata, Tatsuo et al. (1994). Energy deposition through radiative processes in absorbers irradiated by electron beams / Tatsuo, Tabata // Nuclear Instruments and Methods in Physics Research Section B: Beam Interactions with Materials and Atoms. — Vol. 93. — No. 4. — P. 447–456, https://doi.org/10.1016/0168-583x(94)95633-2.

М.Г. Голковский, И.П. Денисов, С.А. Гынгазов, И.П. Васильев, И.К. Чакин

Жоғары ену қабілеті бар электронды сәуленің әсерінен керамикалық материалдардың сұйық фазалық синтезінің тиімділігі

Соңғы бірнеше жылда жүргізілген зерттеулер люминесцентті керамикалық материалдарды, сондай-ақ жоғары ену қабілеті бар электронды сәулені қолданатын басқа мақсаттағы керамиканы алу әдісінің артықшылықтарын көрсетті. Сәулені өнеркәсіптік электронды үдеткіш жасайды және атмосфераға шағын диаметрлі тесік арқылы шығарылады. Электрондардың үдеткіш кернеуі 1,4 – 2,5 МВ диапазонында реттеледі, бұл сәуленің жоғары қуатымен бірге ұнтақ материалға көлемдік әсер етуге мүмкіндік береді, оны шамамен 1 с уақыт ішінде балқытады, яғни балқыманың бастапқы шихта орналасқан тигель қабырғаларымен жанасуынсыз. Жұмыста екі компонентті оксидті керамиканы синтездеу кезінде сәуленің энергетикалық тиімділігін есептеу әдісі ұсынылған. Сәуленің тиімділігі синтезделген керамиканың балқу температурасына және оны қыздыру мен балқыту үшін қажет жылуға қарамастан, орташа есеппен 50% құрайды және көптеген жағдайларда 80%-дан асады.

Кілт сөздер: жоғары вольтты электронды сәуле, электронды сәулені атмосфераға шығару, электронды сәулені балқыту, заттардағы сәулелік энергияны бөлу, оксидті керамика синтезі, керамика синтезінің тиімділігі.

М.Г. Голковский, И.П. Денисов, С.А. Гынгазов, И.П. Васильев, И.К. Чакин

КПД жидкофазного синтеза керамических материалов под воздействием электронного пучка с высокой проникающей способностью

Проведённые в последние несколько лет исследования показали преимущества метода получения люминесцентных керамических материалов, а также керамик другого назначения с применением электронного пучка с высокой проникающей способностью. Пучок генерируется промышленным ускорителем электронов и выпускается в атмосферу через отверстие малого диаметра. Ускоряющее напряжение электронов регулируется в диапазоне 1,4–2,5 МВ, что в сочетании с высокой мощностью пучка позволяет оказывать объёмное воздействие на порошковый материал, производя его расплавление за время около 1 с, практически без соприкосновения расплава со стенками тигля, в который помещается исходная шихта. В статье предложен способ расчёта энергетического КПД воздействия пучка при синтезе двухкомпонентных оксидных керамик. Показано, что КПД пучка в среднем составляет около 50 %, а во многих случаях превышает 80 %, вне зависимости от температуры плавления синтезируемой керамики и тепла, необходимого для её нагрева и расплавления.

Ключевые слова: высоковольтный электронный пучок, вывод электронного пучка в атмосферу, электронно-лучевая плавка, выделение энергии пучка в веществах, синтез оксидной керамики, КПД синтеза керамики.

References

1 Lv, Xiang et al. (2024). Recent progress on modulating luminescence thermal quenching properties of bi3+-activated phosphors. *Inorganic Chemistry Frontiers, 11*(6), 1668–1682. https://doi.org/10.1039/d3qi02588h.

2 Haider, Asif Ali, et al. (2023). Advances in reversible luminescence modification and applications of inorganic phosphors based on Chromism reaction. *Advanced Optical Materials, 12*(5). https://doi.org/10.1002/adom.202302265.

3 Zhou, Ming et al. (2024). Reaction mechanisms of (re0.2nd0.2sm0.2eu0.2gd0.2)2zr2o7 (re = la or YB) under Cao-MgO-Al2O3-SiO2 (cmas) attack. *Journal of the European Ceramic Society, 44*(6), 4055–4063. https://doi.org/10.1016/j.jeurceramsoc.2024.01.014.

4 Li, Xudong et al. (2023). Enhanced redox electrocatalysis in high-entropy perovskite fluorides by tailoring D–P hybridization. *Nano-Micro Letters, 16*(1). https://doi.org/10.1007/s40820-023-01275-3.

5 Wang, Yuhao et al. (2023). High-entropy perovskites for Energy Conversion and storage: Design, synthesis, and potential applications. *Small Methods, 7*(4). https://doi.org/10.1002/smtd.202201138.

6 Lisitsyn, Victor, et al. (2023). Radiation synthesis of high-temperature wide-bandgap ceramics. *Micromachines, 14*(12), 2193. https://doi.org/10.3390/mi14122193.

7 Lisitsyn, Victor et al. (2023). The optimization of Radiation Synthesis Modes for YAG: CE Ceramics. *Materials, 16*(8), 3158. https://doi.org/10.3390/ma16083158.

8 Lisitsyn, Victor et al. (2023). Express synthesis of YAG: CE ceramics in the high-energy electrons flow field. *Materials, 16*(3), 1057, https://doi.org/10.3390/ma16031057.

9 Ghyngazov, S.A. et al. (2023). Synthesis of technical ceramics in a beam of fast electrons. *Russian Physics Journal, 66*(4), 391–397, https://doi.org/10.1007/s11182-023-02952-x.

10 NIST Chemistry Webbook, SRD 69. Chemical Formula Search. Retrieved from webbook.nist.gov/chemistry/form-ser/. Accessed 16 Oct. 2024.

11 Glushko, V. (Ed.), Gurvich, L. & et al. (1978, 1979, 1981, 1982). *Termodinamicheskie svoistva individualnykh veshchestv: Spravochnoe izdanie: [V 4-kh tomakh], 3-e izdanie [Thermodynamic Properties of Individual Substances. Reference Edition in 4 Volumes, 3rd Edition]*. Moscow [in Russian].

12 Termodinamicheskie svoistva individualnykh veshchestv: Spravochnoe izdanie. Tom 5 (online versiia) [Thermodynamic Properties of Individual Substances. Reference Edition Volume 5, online version]. Retrieved from https://www.chem.msu.su/rus/tsiv/ [in Russian].

13 Tabata, Tatsuo et al. (1998). An algorithm for depth–dose curves of electrons fitted to Monte Carlo data. *Radiation Physics and Chemistry, 53*(3), 205–215. https://doi.org/10.1016/s0969-806x(98)00102-9.

14 Tabata, Tatsuo et al. (1994). Energy deposition through radiative processes in absorbers irradiated by electron beams. *Nuclear Instruments and Methods in Physics Research Section B: Beam Interactions with Materials and Atoms, 93*(4), 447–456. https://doi.org/10.1016/0168-583x(94)95633-2.

Information about the authors

Golkovski M.G. (corresponding author) — Candidate of physical and mathematical sciences, Senior researcher, Budker Institute of Nuclear Physics, Academician Lavrentiev avenue, 11, Novosibirsk, Russia, e-mail: *golkovski@mail.ru*. ORCID ID: https://orcid.org/0000-0003-4399-444X

Denisov I.P. — Candidate of physical and mathematical sciences, Senior researcher, National Research Tomsk Polytechnic University, Lenin avenue 30, Tomsk, Russia; e-mail: *dip@tpu.ru*

Ghyngazov S.A. — Doctor of technical sciences, Professor, Leading Researcher, National Research Tomsk Polytechnic University, Lenin avenue 30, Tomsk, Russia, e-mail: *ghyngazov@tpu.ru*. https://orcid.org/0000-0002-2524-9238

Vasil'ev I.P. — Candidate of technical science, Senior researcher, National Research Tomsk Polytechnic University, Lenin avenue 30, Tomsk, Russia, e-mail*: zarkvon@tpu.ru*. https://orcid.org/0000-0002-4077-7012

Chakin I.K. — Research Engineer, Budker Institute of Nuclear Physics, Academician Lavrentiev avenue, 11, Novosibirsk, Russia, e-mail: *chak_in2003@bk.ru* ORCID ID: https://orcid.org/0000-0003-0529-2017

Article
https://doi.org/10.31489/2024PH4/46-53
UDC 536-12; 544.454.2

Received: 21.06.2024
Accepted: 19.08.2024

A.V. Kalenskii[*], A.A. Zvekov, A.P. Borovikova, E.V. Galkina, P.O. Vinodiktov

Kemerovo State University, Kemerovo, Russia
([*]Corresponding author's e-mail: kalenskyav@gmail.com)

The laser initiation of energetic materials doped with metal nanoparticles having oxide shell explosive decomposition

The work is devoted to the development of the model describing laser initiation composite materials being an explosive matrix with metal nanoparticles covered with oxide shell. The model considers the oxide shell as a dielectric that does not absorb light. The example of aluminum nanoparticles covered with alumina is the main one in the paper. The model describes the thermal transfer in the system metal core-oxide shell-explosive material, exothermic decomposition of the explosive considered as a one-step reaction with Arrhenius dependence on the rate on temperature, and light absorption of the core-shell interface. The model is written as a system of the equations and respective computer program is developed. The semi-quantitative analysis of the model using the typical thickness of the heated layer of the matrix is performed. It is shown that the radius of the nanoparticle heated most is proportional to the thickness of the heated layer of the explosive matrix as in the previous versions of the model though the coefficient depends on the oxide shell thickness. The numerical analysis is done. The dependencies of critical energy density on the oxide shell thickness at constant nanoparticle's radius and on the radius at constant shell thickness are calculated. The dependence on radius shows the existence of the optimal particle minimizing the critical energy density whose radius depends on the shell thickness.

Keywords: laser initiation, thermal explosion, hot-spot model, core-shell nanoparticles, energetic materials.

Introduction

The development of laser initiation approaches of explosive decomposition is essential for safety increasing in the explosives' utilization as well as for ecology risks and technological catastrophes minimization. One of the solution steps of this relevant task is the development of explosive blends selectively sensible to laser impact. The decreasing of neodymium laser pulse critical energy density of pentaerythritol tetranitrate (PETN) explosion in one hundred times was achieved earlier by mixing the explosive with aluminum nanoparticles [1]. The significant influence (13 times) of the oxide shell of the nanoparticles on the critical energy density of the PETN initiation was discovered in [2]. The respective model was suggested in [3].

The optic detonators based on primary explosives such as silver azide have not been applied extensively as they show low thresholds not only to laser impact but also to heat and electric stimulus. Another ways of the problem solution are development of optic detonators based on the high-energy metal complexes with nitrogen-rich ligands [4, 5] or application of secondary explosives which critical energy density of the laser impact was diminished with some additives. The sensibilization of the transparent secondary explosives was done with metal nanoparticles introduced in small quantities (about 1 %) in the works [1, 6, 7]. Significant decreasing in the critical energy density of the laser pulse appears due to both effective linear absorption coefficient increasing [8] and heating of just nanoparticles and thin layer of the explosive around it that is a negligible part of the sample. For that reason, the minimal energy density of secondary explosive PETN laser initiation with aluminum [6, 7], nickel and cobalt [9, 10] is about 1 J/cm^2 at the main wavelength of the neodymium laser. The perspectives of gold nanoparticles with diameter 60 nm showing maximum of the plasmon resonance band at 532 nm as a sensibilizing additive to hexogen comparing to carbon particles of soot and nanotubes was pointed out in [11]. Several papers were devoted to changing of the nanoparticles' shape aiming at fitting the plasmon absorption band to the wavelength of the commercially available continuous-wave lasers [12–15]. The sensibilization of 1,1-diamino-2,2-dinitroethene with gold nanorods was performed in [12] that made it possible to initiate them with continuous-wave laser at 808 nm and power 8 W with reaching the pressure of 1.5 GPa at the rear side of the charge which is enough for the typically secondary explosives' detonation initiation. The additive of black carbon leads to initiation threshold of 17 W in similar conditions [13]. The application of gold-copper alloy additives in the nano-stars shape allows one to initiate hexogen with continuous-wave laser irradiation at power 41 W which is 6 times lower than for pure hexogen [14]. Silver nano-plates of various shapes (round, triangle, and cracked triangles) utilization showed that the cracked triangles are the most efficient as hexogen sensibilizing additives though the absorption spectra of the samples are close [15].

The micro hot-spot conception of the thermal explosion based on the light absorption by metal nanoparticles in the explosive's volume was suggested in [16] for silver and lead azides. The relevance of the optic detonators using secondary explosives linked with safety issues attracted researchers to this model. The hot-spot model applied to secondary explosives initiation was formulated in [1, 8, 10, 17] with phase transitions and optical properties of the composites taking into account. As a result, the most of experimental data on the laser pulse initiation of explosives found qualitative and partly quantitative explanation, including the dependence of the critical energy density on the pulse duration. A few new effects were predicted and discovered afterwards such as dependence of the initiation threshold on the laser wavelength, radius and mass fraction of the sensibilizing nanoparticles. The dielectric shell of the nanoparticles was included in the hot-spot model in [3] where its influence on the optic and thermal properties was discussed. The calculation of absorption and scattering efficiency factors of the nanoparticles with metal core-dielectric shell structure was performed. The maximum temperatures of the core-shell particles heated in the inert medium were calculated varying the nanoparticle's radius. It was shown that oxide shell changes drastically the optic properties of the nanoparticle. The further research into hot-spot model is relevant due to their fundamental significance in the point of mechanisms of laser initiation understanding and practice linked with optic detonators' composition optimization.

The aim of the present work is research into laser initiation regularities of PETN taking into account oxide shell of the aluminum sensibilizing nanoparticle. The main task is to perform the kinetic analysis of the composites PETN/Al/Al_2O_3 laser initiation model at variation of the both nanoparticle's radius and shell thickness in the wide range. The model is analyzed for the practically important case of composite PETN-aluminum nanoparticles. The dependence of the critical energy density on this composite on the oxide content in the nanoparticle was studied experimentally earlier [2].

The hot-spot model of laser initiation in the case of core-shell nanoparticles

The differential equations of the hot-spot model in the core-shell particle case are as follows [3]:

$$\begin{aligned}
&\frac{\partial T}{\partial t}=\alpha\cdot\left(\frac{\partial^2 T}{\partial x^2}+\frac{2}{x}\cdot\frac{\partial T}{\partial x}\right)+k_0\frac{nQ}{c}\cdot\exp\left(-\frac{E}{k_B T}\right) && x>R\\
&\frac{\partial n}{\partial t}=-k_0 n\cdot\exp\left(-\frac{E}{k_B T}\right) && x>R\\
&\frac{\partial T}{\partial t}=\alpha_0\left(\frac{\partial^2 T}{\partial x^2}+\frac{2}{x}\cdot\frac{\partial T}{\partial x}\right) && r<x<R \qquad (1)\\
&\frac{\partial T}{\partial t}=\alpha_M\left(\frac{\partial^2 T}{\partial x^2}+\frac{2}{x}\cdot\frac{\partial T}{\partial x}\right) && x<r\\
&\frac{\partial n}{\partial t}=0\,,\ n=0, && x<R
\end{aligned}$$

where lower index 0 marks the shell, M marks the core, α is thermal diffusivity, c is volumic heat capacity, n is the content of the unreacted explosive substance, k_0 is preexponential factor, E is activation energy, Q is heat released at decomposition of 1 cm^3 of the explosive substance, R is nanopartciles radius, r is radius of the core. The metal core absorbs light in the core of core-shell particles case. The energy absorbed is consumed on heating the core then the shell is heated and only after it the heat is transferred to the surrounding explosive's layer initiating its decomposition.

Thus, on the boundaries shell-explosive and core-shell respective boundary conditions arise making contrast to initial micro hot-spot model:

$$-c_0\alpha_0 \cdot \frac{\partial T}{\partial x}\bigg|_{(x\to R-0)} + c\alpha \cdot \frac{\partial T}{\partial x}\bigg|_{(x\to R+0)} = 0 \qquad (2.a)$$

$$J - c_M\alpha_M \cdot \frac{\partial T}{\partial x}\bigg|_{x\to r-0} + c_0\alpha_0 \cdot \frac{\partial T}{\partial x}\bigg|_{x\to r+0}. \qquad (2.b)$$

The calculations were done using parameters from [1–3]. The temporal dependence of the function J was taken in the normal distribution shape according to the pulse shape of the experimentally used lasers [10]. It is reasonable to get rid of one of the parameters counting time from the pulse maximum and starting calculation earlier (3):

$$J(t) = \sqrt{\pi} \cdot Q_{abs} R^2 k_i H_0 \cdot \exp\left(-k_i^2 t^2\right), \qquad (3)$$

where k_i determines the pulse duration at the half width according to the expression $\tau = 2 \cdot k_i \big/ \sqrt{\ln 2}$. The value of absorption efficiency Q_{abs} determines the intensity of light interaction with nanoparticle and we discussed it thoroughly in [18, 19].

Results and discussion

An important task in the model analysis is determination of the nanoparticle's radius heated by the laser pulse to maximum temperature neglecting the explosive's decomposition. Denoting $\sqrt{\frac{3c}{c_1}}$ as K in the case of micro hot-spot model this radius is proportional to the matrix heated layer thickness $R_m=Kh$, where $h \approx \sqrt{2\alpha/k_i}$, while the maximum temperature augmentation takes form:

$$\delta T = \frac{\pi R H}{4\!/\!_3\, \pi c_1 R^2 + 4\pi c\left(Rh + h^2\right)} = = \frac{\pi K h H}{4\!/\!_3\, \pi \frac{3c}{K^2} h^2 K^2 + 4\pi c\left(hKh + h^2\right)} = \frac{KH}{4ch(K+2)}. \qquad (4)$$

A similar analysis was performed in the case of the core-shell particles. The estimation of the maximum heating temperature in the case of particle having oxide shell with thickness (R — r) we will use the ration of nanoparticles and core radii $Z=R/r$. The expression for temperature augmentation can be written as follows:

$$\Delta T = \frac{Q}{c} = \frac{H \cdot \pi r^2}{c_A \cdot \frac{4}{3}\pi r^3 + c_0 \cdot \frac{4}{3}\pi r^3\left(Z^3 - 1\right) + c_m 4\pi Z^2 r^2 h + 4\pi c_m h^2 Z r}.$$

The particles with the most pronounced temperature increasing are determined applying maximum conditions:

$$\Delta T' = 0$$

$$\left(\frac{H \cdot r^2}{r^3\left(\frac{4}{3}c_A + \frac{4}{3}c_0 \cdot \left(Z^3 - 1\right)\right) + 4c_m Z^2 r^2 h + 4c_m h^2 Z r}\right)' = 0 \qquad (5)$$

$$R_m = \sqrt{\frac{3c_m Z h^2}{c_A - c_0 \cdot \left(Z^3 - 1\right)}}.$$

It can be deduced from (5) that the radius of the most heated nanoparticle R_m does not depend on the pulse energy density but depends on pulse duration which presents through the thickness of the matrix heated layer h. For that reason, we calculated the dependence of the maximum temperature of the heated nanoparticle in the inert matrix with PETN parameters on the radius at different pulse durations. The results are shown in Figures 1 and 2 at the pulse duration 14 and 20 ns respectively. The energy density values were 25, 50, and 75 mJ/cm^2. The ration of core and nanoparticle radii was 0.75. The range of radii was taken rather wide, so the value of R_m fell in it. The self-accelerating mode of the reaction was excluded due to taking preexponential factor equal to 0.

At the energy density value 25 mJ/cm^2 the maximum temperature increases from 437 to 604 K when radius increases from 10 to 60 nm and is decreased to 565 K as the radius gets to 120 nm. When the energy density increases to 50 J/cm^2, the maximum temperature of the nanopartilces increases to 538 K for 10 nm and 909 K for 60 nm, while it becomes equal to 835, if the radius is 120 nm. If the energy density is 75 J/cm^2 the respective maximum temperatures for 10, 60 and 120 nm particle radii are 710, 1213 and 1102 K. The augmentation of temperature is proportional to the energy density of the pulse. The most heated particle has radius 60 nm in this case.

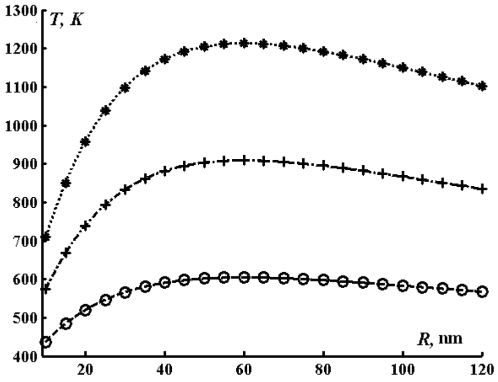

Figure 1. Calculated dependencies of the maximum temperature of the aluminum nanoparticles heated in PETN on its radius at *r/R*=0.75 and pulse duration 14 ns.

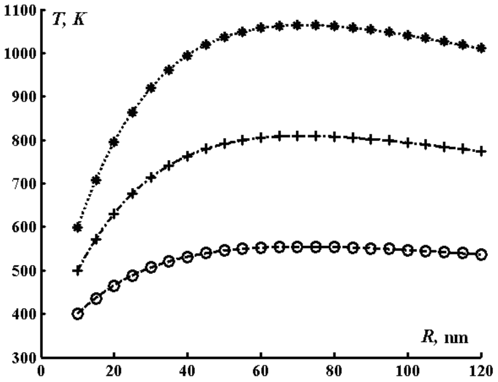

Figure 2. Calculated dependencies of the maximum temperature of the aluminum nanoparticles heated in PETN on its radius at *r/R*=0.75 and pulse duration 20 ns.

Figure 2 shows similar dependencies of maximum temperature of the aluminum nanoparticle at the pulse duration 20 ns. Other conditions are the same. The maximum temperature of the particle heated with 20 ns pulse and energy density 25 J/cm^2 is 555 K when radius is 71.8 nm. The temperature decreases for both smaller and bigger particles reaching 399 K at 10 nm and 536 at 120 nm. The maximum temperatures for energy density 75 J/cm^2 for 10, 71.8, and 120 nm are 600, 1064, and 1010 K. Thus the maximum heating temperature is achieved at the definite radius of the nanoparticle dependent on the pulse duration and independent on its energy or power density.

We analyzed thoroughly the temperature distributions in the heating of aluminum nanoparticles covered with alumina in the PETN matrix at the minimal pulse energy density provided explosive decomposition. The temperature distribution arising at the energy density 137 mJ/cm^2 in the case of nanoparticle's radius 50 nm with core radius 35 nm and shell thickness 15 nm are presented in Figure 3. The moments of time counted from the pulse maximum are shown on the legend; they correspond to the slow temperature evolution in the reaction hot-spot linked with reaction energy releasing and heat transfer competition [20].

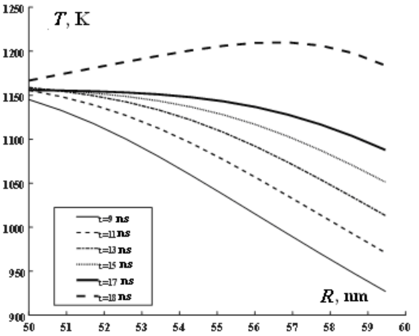

Figure 3. Temperature distributions in PETN at the time moments shown on the legend in the PETN layer surrounding the nanoparticle with radius 50 nm (35 nm core and 15 shell thickness)

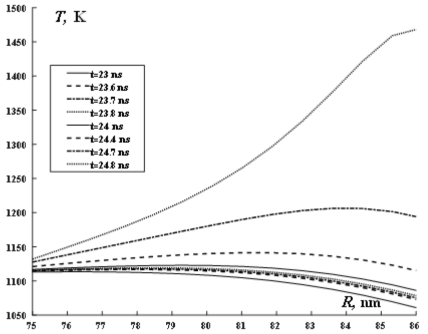

Figure 4. Temperature distributions in PETN surrounding nanoparticle with radius 75 nm (50 nm core and 25 nm shell) at the time momonts shown in the legend

The maximum temperature 1145.1 K is observed on the boundary oxide shell- PETN (50 nm) and the hot-spot thickness is estimated as 2.6 nm at the time 9 ns when the pulse intensity is only 0.318 % of the maximal one. We determined here the hot-area as the part of the PETN matrix where the second derivative is negative as it has to be positive inside the matrix in the case of exothermic reaction absence. Further at time 17 ns the temperature maximum increases to 1155.8 K while the hot layer is widened to 8.8 nm. The pulse intensity at 17 ns is 0.0168 % of the maximum one. Then at 18 ns the temperature on the alumina shell — PETN boundary increases to 1170 K; the hot layer thickness increases to 12.5 nm. It is essential that heat evolving in the exothermal reaction forms temperature maximum leading to explosive decomposition.

Figure 4 shows the temperature distributions in PETN matrix in the case of nanoparticle with radius 75 nm (50 nm core radius and 15 nm shell thickness) in the case of energy density 104.17 mJ/cm^2. The temperature on the boundary decreases slightly between 23 and 24 ns. At the same time the layer of the heated PETN widens, so the temperature gradient decreases. For that reason at time moment 24 ns the heating from the exothermal decomposition reaction overcomes the heat transferring from the hot layer and the temperature increasing begins. The temperature jumps rapidly at the time moment 24.8 ns counting from the pulse maximum evidencing the beginning of the explosive decomposition at the given energy density of the pulse.

Thus, the analysis of temperature field evolution in the system PETN — aluminum nanoparticle with alumina shell varying the energy density of the laser pulse gives one an opportunity to estimate the critical energy density.

The method of the explosive decomposition critical parameters calculation in the case of the composites PETN — aluminum nanoparticles covered with alumina is close to used earlier [20]. In the case of interest one needs to take into account the thermal transfer in the oxide shell. The developed computer program calculated critical energy density H_c at given nanoparticle's radius, radius of the core, shell thickness, and pulse duration. The results are presented in Figure 5 as dependencies of critical energy density of the PETN explosive decomposition on the nanoparticlers' shell thickness at the definite radii of the nanoparticles in the radius range from 15 to 70 nm and shell thickness range from 0 to 30 nm. The calculations were done in the assumption of the absorption cross section equality to the geometrical one.

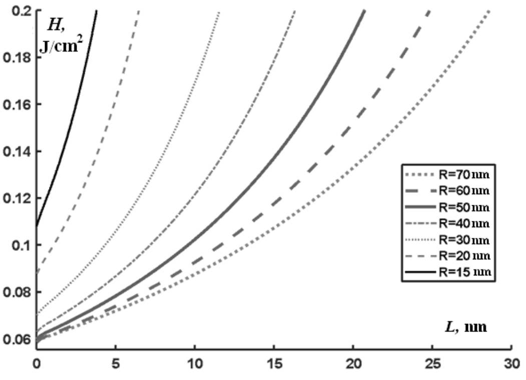

Figure 5. The calculated dependencies of laser pulse critical energy density of PETN- Al/Al_2O_3 explosive decomposition on the oxide shell thickness at definite nanoparticles' radii presented on the legend

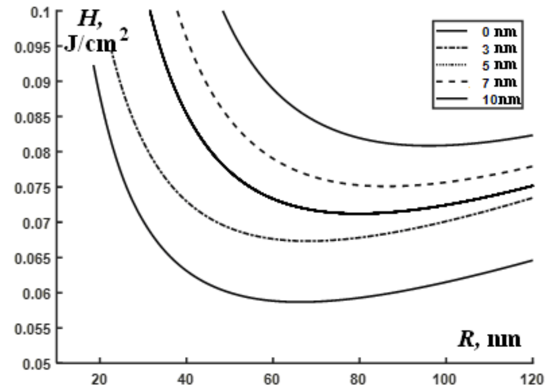

Figure 6. The calculated dependencies $H_c(R)$ for unoxidized aluminum nanoparticles and with oxide shell thickness shown on the legend

The dependencies (Fig. 5) show the increasing of critical energy density when the thickness of the oxide shell increases. It means that the function extremum lays at the zero thickness of the oxide shell minimizing the critical energy density. On the other hand, if one presents the calculation results as dependencies of critical energy density on the nanoparticles' radius at definite oxide shell thickness the minimum points appear (Fig. 6). Thus, as for original hot-spot model of laser initiation in the model taking into account the oxide shell discussed the radius of the most heated nanoparticle (or the optimal radius) appears, but it becomes a function of the thickness of the oxide shell. The dependencies in Figure 6 are of the same type showing the decreasing in the critical energy density from 15 nm to the minimal point and then increasing. The minimum position is a function of the oxide shell thickness; the thickness increasing leads to the optimal radius of the nanoparticle rising.

This trend could be also found from the equation (5). The minimum positions (minimal H_c and respective R values) at several shell thickness values are presented in Table. The optimal radius of the metal nanoparticle existing in terms of the model could be determined in two ways: (i) one is able to find the radius of the most heated nanoparticle in the under-threshold mode; (ii) one can calculate the dependence of critical energy density on the nanoparticle's radius and find its minimum. The existence of the optimal radius of the nanoparticle providing the minimal energy density other conditions are the same is inherited in the model taking into account the oxide shell from the initial model of the entirely metallic particles. As in the model a new parameter appears that is shell thickness, it is not surprising that optimal radius becomes its function. The optimal radius increases when the oxide shell becomes thicker, for instance, when the shell thickness increase from 0 to 10 nm the optimal radius increases in 1.5 times.

Table

Minimum coordinates on the critical energy dependence on the nanopartciles radius at fixed oxide shell thickness values

L, нм	0	3	5	7	10
H_c, mJ/cm^2	58,7	67,3	71,2	75,1	80,8
R_m, nm	66,18	68,08	79,71	86,27	96

Conclusion

The model describing the laser initiation of explosive linked with radiative heating of metal nanoparticle with oxide shell in the explosive matrix was developed and analyzed. We showed that the optimal radius of the nanoparticle providing the minimum threshold of the ignition depends on the oxide shell thickness. The model is a new step towards application of the hot-spot theory to real explosive-metal nanopartilces composites. The optical properties will be incorporated in the future which will make it possible to compare the calculation results with the experimental one.

This research was funded by the Ministry of Science, Higher Education and Youth Policy of Kuzbass (agreement No. 5 dated Nov.11, 2022).

References

1 Aduev, B.P., Nurmukhametov, D.R., Furega, R.I., Zvekov, A.A., & Kalenskii, A.V. (2013). Explosive Decomposition of PETN with Nanoaluminum Additives under the Influence of Pulsed Laser Radiation at Different Wavelengths. *Russian Journal of Physical Chemistry B, 7*(4), 453–456. https://doi.org/10.1134/S199079311304012X

2 Aduev, B.P., Nurmukhametov, D.R., Zvekov, A.A., & Nelyubina, N.V. (2014). Influence of the mass fraction of oxide in aluminum nanoparticles on the explosive decomposition threshold and light absorption efficiency in petn-based compounds. *Combustion, Explosion, and Shock Waves,* 50(5), 578–581. https://doi.org/10.1134/S001050821405013X

3 Kalenskii, A.V., Anan'eva, M.V., Galkina, E.V., Kriger, V.G., & Zvekov, A.A. (2018). Micro hot-spot model of thermal explosion taking into account dielectric shell of sensitizing nanoparticle. *Journal of Physics: Conference Series,* 1115, 052017. https://doi.org/10.1088/1742-6596/1115/5/052017

4 Yang, J., Zhang, Gu-D., Zhang, J.-G., Chen, D., & Zhang, Qi. (2022). New perspectives on the laser initiation for metal tetrazine complexes: a theoretical study. *Phys Chem Chem Phys*, 24, 305–312. https://doi.org/10.1039/D1CP02319E

5 Lang, Q., Li. X., Zhou, J., Xu, Y., Lin, Q., & Lu, M. (2023). Two silver energetic coordination polymers based on a new N-amino-contained ligand: Towards good detonation performance and excellent laser-initiating ability. *Chemical Engineering Journal*, 452, 139473. https://doi.org/10.1016/j.cej.2022.139473

6 Akhmetshin, R., Razin, A., Ovchinnikov, V., Skripin, A., Tsipilev, V., Oleshko, V., Zarko, V., & Yakovlev, A. (2014). Effect of laser radiation wavelength on explosives initiation thresholds. *Journal of Physics: Conference Series*, 552, 012015. https://doi.org/10.1088/1742-6596/552/1/012015

7 Aduev, B.P., Nurmukhametov, D.R., Belokurov, G.M., Nelyubina, N.V., Kalenskii, A.V., & Aluker, N.L. (2017). Spectrokinetic characteristics of light emission at the early stages of the laser-initiated explosive decomposition of petn-based composites containing metal nanoparticle inclusions. *Russian Journal of Physical Chemistry B, 11*(3), 460–465. https://doi.org/10.1134/S1990793117030137

8 Kalenskii, A.V., Zvekov, A.A., Anan'eva, M.V., Nikitin, A.P., & Aduev, B.P. (2017). Effect of multiple scattering on the critical density of the energy used to initiate a PETN–aluminum compound by a neodymium laser pulse. *Combustion, Explosion, and Shock Waves, 53*(1), 82–92. https://doi.org/10.1134/S0010508217010129

9 Aduev, B.P., Nurmukhametov, D.R., Kolmykov, R.P., Nikitin, A.P., Anan'eva, M.V., Zvekov, A.A., & Kalenskii, A.V. (2016). Explosive decomposition of pentaerythritol tetranitrate pellets containing nickel nanoparticles with various radii. *Russian Journal of Physical Chemistry B, 10*(4), 621–627. https://doi.org/10.1134/S1990793116040187

10 Kalenskii, A.V., Anan'eva, M.V., Zvekov, A.A., & Zykov, I.Yu. (2015). Explosive decomposition kinetics of tetranitropentaerythrite aluminum pellets. *Technical Physics, 60*(3), 437–441. https://doi.org/10.1134/S1063784215030081

11 Fang, X., Stone, M., & Stennett, Ch. (2020). Pulsed laser irradiation of a nanoparticles sensitised RDX crystal. *Combustion and Flame*, 214, 387–393. https://doi.org/10.1016/j.combustflame.2020.01.009

12 Fang, X., Stennett, Ch., & Gaulter, S. (2023). Enhancement of laser ignitibility of insensitive energetic materials (FOX-7). *Propellants, Explos., Pyrotech*., 48, e202300079. https://doi.org/10.1002/prep.202300079

13 Fang X., & Walton, A.J. (2023). Optical sensitising of insensitive energetic material for laser ignition. *Optics & Laser Technology*, 158, 108767. https://doi.org/10.1016/j.optlastec.2022.108767

14 Bai, W., Wang, L., Tang, D., Yang, F., Qiao, Z., Lin, D., He, R., Zhu, W., & Qin, W. (2022). Constructing hotspots through star-shaped gold-copper alloy nanocrystals for laser initiation of explosives. *Optics & Laser Technology*, 152, 108120. https://doi.org/10.1016/j.optlastec.2022.108120

15 Bai, W., Qin, W., Tang, D., Ji, F., Chen, H., Yang, F., Qiao, Zh., Duan, T., Lin, D., He, R., Zhu, W., & Wang, L. (2021). Constructing interparticle hotspots through cracking silver nanoplates for laser initiation of explosives. *Optics & Laser Technology*, 139, 106989. https://doi.org/10.1016/j.optlastec.2021.106989

16 Alexandrov, E.I., & Tsipilev, V.P. (1984). Effect of the pulse length on the sensitivity of lead azide to laser radiation. *Combustion, Explosion and Shock Waves, 20*(6), 690–694. https://doi.org/10.1007/BF00757322

17 Zvekov, A.A., Nikitin, A.P., Galkina, E.V., & Kalenskii, A.V. (2016). The dependence of the critical energy density and hot-spot temperature on the radius metal nanoparticles in PETN. *Nanosystems: physics, chemistry, mathematics, 7*(6), https://doi.org/1017–1023. 10.17586/2220-8054-2016-7-6-1017-1023

18 Kalenskii, A.V., Zvekov, A.A., Nikitin, A.P., Anan'eva, M.V., & Aduev, B.P. (2015). Specific Features of Plasmon Resonance in Nanoparticles of Different Metals. *Optics and Spectroscopy, 118*(6), 978–987. https://doi.org/10.1134/S0030400X15060119

19 Zvekov, A.A., Aduev, B.P., Anan'eva, M.V., Kalenskii, A.V., & Galkina, E.V. (2019). Method for calculating the optical properties of composites based on a transparent matrix with residual porosity and metal nanoparticles. *Journal of Applied Spectroscopy, 86*(3), 470–478. https://doi.org/10.1007/s10812-019-00843-z

20 Kalenskii, A.V., Gazenaur, N.V., Zvekov, A.A., & Nikitin, A.P. (2017). Critical conditions of reaction initiation in the petn during laser heating of light-absorbing nanoparticles. *Combustion, Explosion, and Shock Waves, 53*(2), 219–228. https://doi.org/10.1134/S0010508217020137

А.А. Звеков, А.В. Каленский, А.П. Боровикова, Е.В. Галкина, П.О. Винодиктов

Оксидті қабықшаның жарылғыш ыдырауы бар металл нанобөлшектерімен легирленген энергетикалық материалдардың лазерлік инициациясы

Мақала лазерлік инициациялық композициялық материалдардың оксидті қабықпен қапталған металл нанобөлшектері бар жарылғыш матрица болуын сипаттайтын модельді әзірлеуге арналған. Модельде оксид қабығын жарықты сіңірмейтін диэлектрик ретінде қарастырады. Негізгі нәтижелер алюминий оксидімен қапталған алюминий нанобөлшектеріне арналған. Модель шеңберінде «металл ядросы–оксидті қабық–жарылғыш зат» жүйесіндегі жылу беру процестері, Аррениус температурасына тәуелділікпен бірінші ретті реакция ретінде модельденген жарылғыш заттың экзотермиялық ыдырауы және «ядро–қабық» шекарасындағы сәулеленуді сіңіру зерттелген. Модель дифференциалдық теңдеулер жүйесі түрінде жазылып, сандық орындауға арналған компьютерлік бағдарлама жасалған. Модельдің жартылай сандық талдауы сәулелену импульсінің әрекеті кезінде қыздырылған матрицалық қабаттың сипаттамалық қалыңдығын пайдалана отырып жүргізілді. Ең жоғары температураға жеткен нанобөлшектің радиусы қыздырылған матрицалық қабаттың қалыңдығына пропорционал болатыны көрсетілген, бұл модельдің алдыңғы нұсқасына сәйкес келеді, бірақ пропорционалдық коэффициенті оксид қабықшасының қалыңдығына байланысты. Модельге сандық талдау жасалды. Инициация энергиясының критикалық тығыздығының нанобөлшектің тұрақты радиусындағы оксид қабығының қалыңдығына және қабықтың тұрақты қалыңдығындағы нанобөлшек радиусына тәуелділігі есептеледі. Радиусқа тәуелділік минималды инициация шегіне әкелетін оңтайлы нанобөлшектің болуын көрсетеді. Оңтайлы нанобөлшектің радиусы қабықтың қалыңдығына байланысты.

Кілт сөздер: лазерлік инициация, термиялық жарылыс, ыстық нүкте моделі, ядро қабықшасының нанобөлшектері, энергетикалық материалдар.

А.А. Звеков, А.В. Каленский, А.П. Боровикова, Е.В. Галкина, П.О. Винодиктов

Закономерности лазерного инициирования взрыва энергетических материалов, допированных наночастицами

Статья посвящена развитию модели лазерного инициирования взрыва композитных материалов, представляющих собой матрицу взрывчатого вещества, содержащую наночастицы металлов с оксидной оболочкой. В рамках модели оксидная оболочка рассмотрена как диэлектрик прозрачный для лазерного излучения. Основные результаты представлены для наночастиц алюминия, покрытых оксидом алюминия. В рамках модели изучены процессы теплопереноса в системе «металлическое ядро–оксидная оболочка–взрывчатое вещество», экзотермическое разложение взрывчатого вещества, моделируемое как реакция первого порядка с Аррениусовской температурной зависимостью, и поглощение излучения на границе «ядро–оболочка». Модель записана в виде системы дифференциальных уравнений, и разработана компьютерная программа для численной реализации. Выполнен полуколичественный анализ модели с использованием величины характерной толщины слоя прогретой матрицы за время действия импульса излучения. Показано, что радиус наночастицы, достигающей наибольшей температуры, пропорционален толщине прогретого слоя матрицы, что согласуется с предыдущим вариантом модели, однако коэффициент пропорциональности зависит от толщины оксидной оболочки. Проведен численный анализ модели. Рассчитаны зависимости критической плотности энергии инициирования от толщины оксидной оболочки при постоянном радиусе наночастицы и радиуса наночастицы при постоянной толщине оболочки. Зависимость от радиуса свидетельствует о существовании оптимальной наночастицы, приводящей к минимальному порогу инициирования. Радиус оптимальной наночастицы зависит от толщины оболочки.

Ключевые слова: лазерное инициирование, тепловой взрыв, микроочаговая модель, наночастицы, ядро–оболочка, энергетические материалы.

Information about the authors

Alexander Kalenskii (corresponding author) — Doctor of physical and math science, Head of the Department of Solid State Chemistry and Material Science, Kemerovo State University, Krasnaya st., 6, 650000, Kemerovo, Russia; *e-mail: kalenskyav@gmail.com*; https://orcid.org/0000-0002-6658-0787

Alexander Zvekov — Doctor of physical and math science, Professor, Department of Solid State Chemistry and Material Science, Kemerovo State University, Krasnaya st., 6, 650000, Kemerovo, Russia; *e-mail: zvekovaa@gmail.com*, https://orcid.org/0000-0002-2941-9783

Anastasia Borovikova — Candidate of physical and math science, Head of Scientific and Innovation Office, Kemerovo State University, Krasnaya st., 6, 650000, Kemerovo, Russia; *e-mail: science@kemsu.ru*, https://orcid.org/0000-0002-4987-3406

Elena Galkina — Candidate of physical and math science, Tutor, Department of Solid State Chemistry and Material Science, Kemerovo State University, Krasnaya st., 6, 650000, Kemerovo, Russia; *e-mail: keltrilla@gmail.com*

Pavel Vinodiktov — 2nd year PhD student, Kemerovo State University, Krasnaya st., 6, 650000, Kemerovo, Russia; *e-mail: vinodiktovpavel@yandex.ru*

Article
https://doi.org/10.31489/2024PH4/54-59
UDC 535.376

Received: 20.05.2024
Accepted: 27.07.2024

A.A. Karnaukhova[*], V.Y. Yakovlev

Tomsk Polytechnic University, Tomsk, Russia
([*]Corresponding author's e-mail: meleshko@tpu.ru)

Cathodoluminescence properties of oxide and fluoride ceramics synthesized in the field of high-energy electrons flux

Traditionally, the synthesis of refractory ceramics is a complex and time-consuming process. Some time ago, a new, much faster method was proposed — the method of synthesis of luminescent ceramics in the field of a powerful flux of high-energy electrons. In the synthesis of multicomponent oxide phosphors, it is not an easy task to determine the dependencies of the properties of the resulting material on the composition of the raw mixture and the modes of the synthesis process. In this regard, it seems logical to study the properties of ceramics made by radiation synthesis from simple oxides, which are components of more complex phosphors. An investigation of the spectral and kinetic patterns of cathodoluminescence of ceramic samples of metal oxides (Ga_2O_3, Al_2O_3, Y_2O_3) and fluorides (MgF_2, BaF_2) obtained by radiation synthesis method was carried out. The paper presents an analysis of the cathodoluminescence spectra of the studied samples with the allocation of elementary bands, conclusions about the dynamics of luminescence decay are made. The obtained results are compared with the known data on single crystal samples. It is shown that, unlike oxide ceramics, the spectral characteristics of MgF_2 and BaF_2 ceramic samples show good agreement with the data on single crystals of these compounds.

Keywords: oxide ceramics, fluoride ceramics, cathodoluminescence, radiation synthesis, spectra, time resolution, Ga_2O_3, Al_2O_3, Y_2O_3.

Introduction

YAG ceramics with activators is a promising material, including for use as phosphors for LEDs. The synthesis of refractory ceramics is a complex and time-consuming process. Some time ago, in the works of V.M. Lisitsyn [1, 2], another, much faster method was proposed — the method of synthesis of luminescent ceramics in the field of a powerful high-energy electron flux. The samples for this work were synthesized by direct exposure of the raw materials to an electron beam with an energy of 1.4 MeV and a power density of 20 kW/cm^2, in the mode of scanning electron beam. Each section of the surface of the synthesized substances was exposed to a radiation beam for about 1 s. The total exposure time of the supplied electron beam to the crucible was 10 s. The ELV-6 accelerator at the Institute of Nuclear Physics of the Siberian Branch of the Russian Academy of Sciences was used for synthesis [1].

The synthesis of oxide ceramics using a fundamentally new technology requires a comprehensive study of the properties of this ceramic. In the synthesis of multicomponent oxide phosphors, it is not an easy task to determine the dependencies of the properties of the resulting material on the composition of the raw mixture and the modes of the synthesis process. In this regard, it seems logical to study the properties of ceramics made by radiation synthesis from simple oxides, which are components of more complex phosphors. The purpose of this work is to study the spectral and kinetic patterns of cathodoluminescence (CL) of ceramic samples of metal oxides and fluorides obtained by radiation synthesis method and compare the results obtained with known data on single crystal samples.

Experimental

Ceramic samples of metal oxides (Ga_2O_3, Al_2O_3, Y_2O_3), including those with an admixture of 0.5 wt.% Ce_2O_3, and metal fluorides (MgF_2, BaF_2) synthesized by the radiation method were used for research [1]. It should be noted that the samples of oxide ceramics obtained by radiation synthesis, unlike monocrystalline samples, are mechanically fragile glassy formations. Whereas the strength of fluoride ceramic samples is significantly higher and comparable to monocrystalline samples.

CL of the samples was excited by an electron beam with a duration $t_{1/2}$ = 10 ns, an average electron energy in a pulse of 250 keV and an energy density of 0.05 J/cm^2. Measurements of the spectral and kinetic characteristics of CL were carried out using an MDR-3 monochromator, a FEU-106 photomultiplier and a LECROY WR6030A oscilloscope with a time resolution of 7 ns.

Results and Discussion

1. Spectra and kinetics of Ga_2O_3 CL

The spectrum of Ga_2O_3 CL, recorded at the time of the maximum of the luminescence flash, is represented by a wide band in the region of 2.5 — 4 eV with a maximum of about 3.4 eV. Figure 1 shows the spectrum taken at the moment of the maximum luminescence pulse and 200 ns after. The type of the CL decay curve at 3.44 eV is shown in Figure 2. It can be seen that the decay of Ga_2O_3 CL occurs according to a non-elementary law. The curve has a fast exponential component with a characteristic decay time of 40 ns, as well as a slow hyperbolic one:

$$\mathrm{I(t)} = \frac{0{,}83}{(1+2{,}8\mathrm{t})^2} + 1{,}35 \cdot \exp\left(-\frac{\mathrm{t}}{0{,}04}\right) I(t) = \frac{0{,}83}{(1+2{,}7t)^2} + 1{,}35 \cdot \exp\left(-\frac{t}{0{,}04}\right), \quad (1)$$

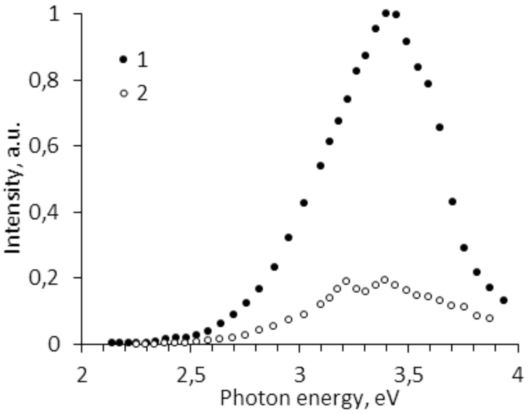

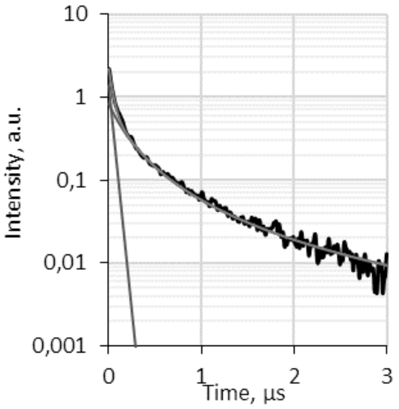

Figure 1. CL spectrum of Ga_2O_3 sample: 1 — taken at amplitude value of a pulse, 2 — in 200 ns.

Figure 2. Decay curve of Ga_2O_3 CL at 3.44 eV.

The spectrum of the fast component obtained from the total spectrum (Fig. 3) can be decomposed into two Gaussian bands peaking at 3.05 and 3.45 eV with a width of 0.47 eV. Bands similar in position were observed by the authors of [3] in single crystals of β-Ga_2O_3 under continuous electron irradiation and were associated with the luminescence of point defects.

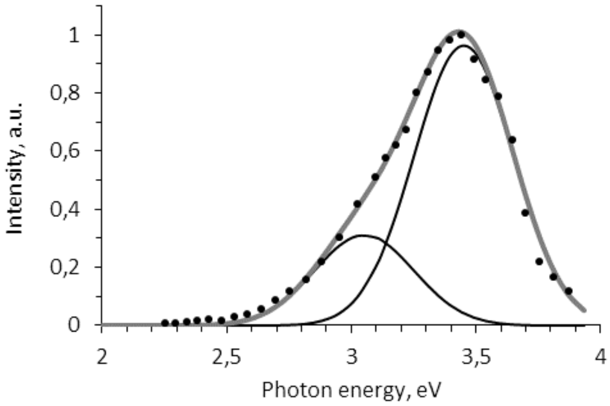

Figure 3. Spectrum of a fast component of Ga_2O_3 CL decay.
Dots — experimental data, solid lines — fitting by Gaussian curves.

2. Spectra and kinetics of Al_2O_3 CL

As for the Al_2O_3 ceramic samples, their spectral and kinetic parameters are difficult to reconcile with the data on single crystals. During the study, we measured the CL spectra of Al_2O_3 and Al_2O_3: Ce 0.5 % samples in the range of 1.3 — 5.3 eV. As can be seen from the data in Figure 4, the most intense glow is observed in the UV region and represents a wide band. Elementary bands with peaks at about 5 eV and 4.3 eV can be distinguished in it, and in samples with an admixture of Ce_2O_3, an additional band appears at 3.4 eV. The band at 4.3 eV was previously observed during irradiation of α-Al_2O_3 with heavy ions [4], but its nature has not been clearly determined. It has been suggested that diffusion-controlled tunnel recombination of self-trapped hole is possible.

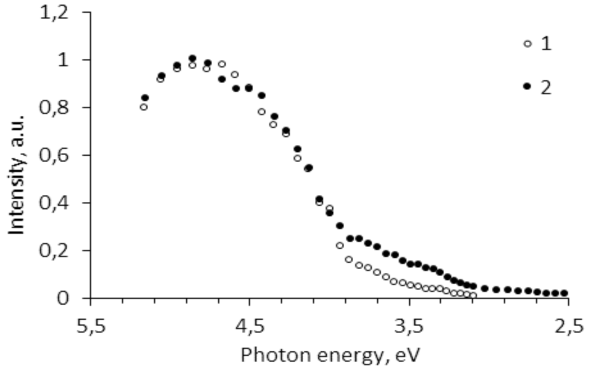

Figure 4. CL spectra of Al_2O_3 (1) and Al_2O_3: Ce 0,5 % (2) samples.

3. Spectra and kinetics of Y_2O_3 CL

The spectral and kinetic characteristics of Y_2O_3 and Y_2O_3 with the addition of 0.5 wt % Ce_2O_3 CL were measured. In general, their spectra, registered by the amplitude values of the flash, are similar (see Figures 5 and 6) and represent a wide band in the region of 2.5 — 4.5 eV, however, the glow of Y_2O_3 with cerium decays much faster. By the time 500 ns after the maximum of the CL pulse, the intensity values are so small that they could not be registered (Figю 6, curve 2). The spectra of the slow and fast decay components of the Y_2O_3 sample CL can be described well by bands with parameters E_{max} = 2.92 eV, FWHM = 0.86 eV and E_{max} = 3.5 eV, FWHM = 0.89 eV, respectively. In the CL spectrum of the Y_2O_3: Ce sample there is only a band at 3.5 eV with FWHM = 0.89 eV.

It should also be noted that the intensity of the emission of the sample containing cerium was more than 10 times lower than that of the sample without cerium. That is, the doping of Y_2O_3 with cerium led to a general decrease in the yield of CL and a decrease in the contribution of relatively long processes associated with the conversion of excitation energy.

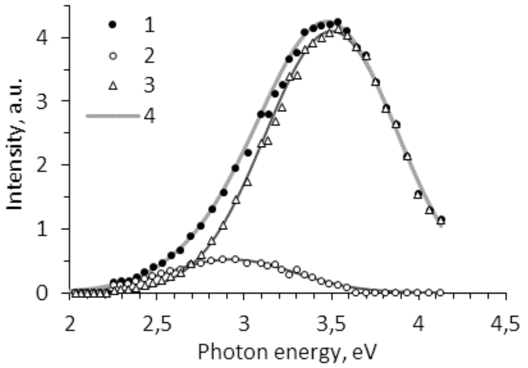

Figure 5. CL spectra of Y_2O_3. 1 — taken by amplitude values of a pulse, 2 — in 500 ns, 3 — spectrum of a fast component, 4 — fitting by a sum of Gaussian curves.

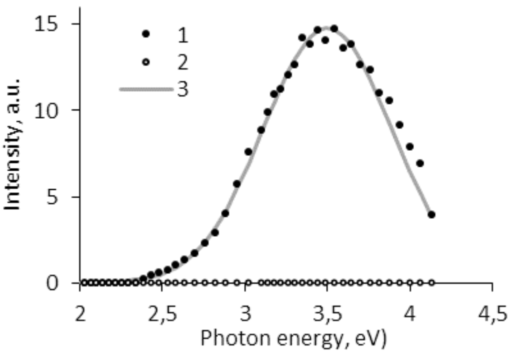

Figure 6. CL spectra of Y_2O_3: Ce 0,5 %. 1 — taken by amplitude values of a pulse, 2 — in 500 ns, 3 — fitting by a Gaussian curve.

4. Spectra and kinetics of MgF_2 и BaF_2 CL

Figure 7 shows the results of MgF_2 and BaF_2 ceramic samples CL spectra measurement. In the MgF_2 spectrum, registered in the 2–4 eV region by peak values of CL pulse, a band at 3 eV with a width of 0.33 eV prevails, in the BaF_2 spectrum in the 2–5 eV region, a band at 4.2 eV with a width of 0.86 eV stands out. The shape and position of the spectra are in good agreement with the data of [5], the authors of which associate these bands with the radiative recombination of self-trapped excitons.

Thus, unlike oxide ceramics, the spectral characteristics of MgF_2 and BaF_2 ceramic samples show good agreement with the data on single crystals of these compounds. This suggests that in compounds with an ionic bond, regardless of their structure (ceramics or single crystal), the short-range order is largely preserved and similar centers of luminescence are formed.

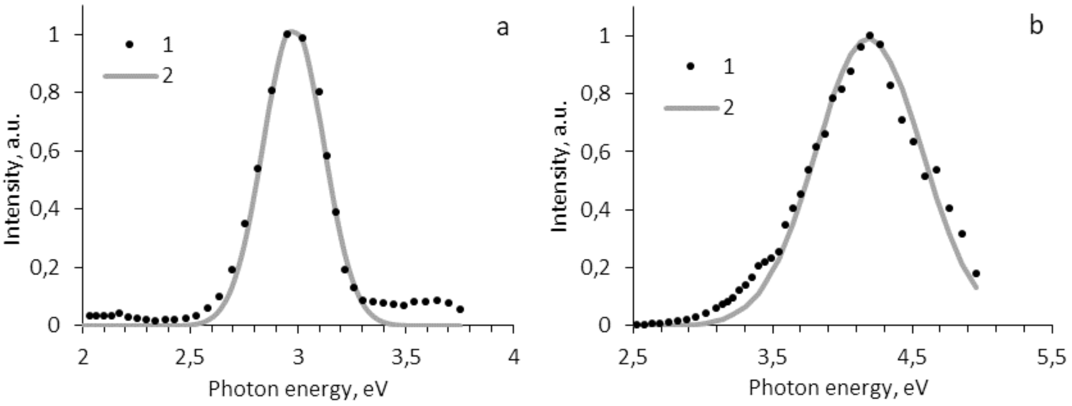

Figure 7. CL spectra of MgF_2 (a) and BaF_2 (б) samples. 1 — experimental data, 2 — fitting.

Conclusions

The study of the spectral and kinetic patterns of the CL of ceramic samples of metal oxides and fluorides obtained by radiation synthesis showed that all studied compounds have a maximum of the CL spectrum in the range of 3–5 eV. Decay of Ga_2O_3 CL occurs according to a non-elementary law. There is a fast exponential component and a slow hyperbolic one in the pulse. Moreover, the spectrum of the fast component can be decomposed into two bands (3.05 and 3.45 eV) close in position to those observed by the authors of [3] in single crystals of β-Ga_2O_3 under continuous electron irradiation and associated with the luminescence of point defects.

In the spectra of Al_2O_3 CL, elementary bands with maxima at 5 eV and 4.3 eV can be distinguished, and in samples doped with Ce_2O_3 an additional peak at 3.4 eV, which was observed earlier when irradiated with α- Al_2O_3 with heavy ions. Its origin has not been definitively determined.

The spectra of Y_2O_3 CL without and with a dopant of Ce_2O_3 are similar, but the luminescence of Y_2O_3: Ce decays much faster and the intensity of this emission is significantly reduced. That is, the introduction of cerium into Y_2O_3 leads to an overall decrease in the yield of CL and a decrease in the contribution of relatively long processes associated with the conversion of excitation energy.

The spectra of MgF_2 and BaF_2 ceramic samples show good agreement with the data on single crystals of these compounds, unlike oxide ceramics. This indicates that in compounds with an ionic bond, regardless of their structure (ceramics or single crystal), the short-range order is largely preserved and similar centers of luminescence are formed.

Acknowledgments

The work was supported by the Russian Science Foundation of the Russian Federation (Grant No. 23-73-00108).

References

1 Lisitsyn V. Radiation Synthesis of High-Temperature Wide-Bandgap Ceramics / V. Lisitsyn, A. Tulegenova, M. Golkovski, E. Polisadova, L. Lisitsyna, D. Mussakhanov, G. Alpyssova // Micromachines. — 2023. — 14. — P. 2193–2221. https://doi.org/10.3390/mi14122193.

2 Lisitsyn V. Express Synthesis of YAG: Ce Ceramics in the High-Energy Electrons Flow Field / V. Lisitsyn, A. Tulegenova, E. Kaneva, D. Mussakhanov, B. Gritsenko // Materials. — 2023. — 16(3). — P. 1057–1068. https://doi.org/10.3390/ma16031057

3 Иванова Е.В. Исследование ловушек носителем заряда в объемном оксиде галлия β-Ga_2O_3 / Е.В. Иванова, П.А. Дементьев, М.В. Заморянская, Д.А. Закгейм, Д.Ю. Панов, В.А. Спиридонов, А.В. Кремлева, М.А. Однолюбов, Д.А. Бауман, А.Е. Романов, В.Е. Бугров // Физика твердого тела. — 2021. — № 63(4). — С. 421–426.

4 Аль Саид Мохамед А.А. Люминесценция *alfa-Al_2O_3*, стимулированная тяжелыми ионами с энергией > *1 MeV/a.e.m.* / А.А. Аль Саид Мохамед. — Дубна, 1996.

5 Song K.S. *Self trapped excitons /* K.S. Song, R.T. Williams Springer. — 1993. https://doi.org/10.1007/978-3-642-97432-8.

А.А. Карнаухова, В.Ю. Яковлев

Жоғары энергиялы электрондар ағыны саласында синтезделген оксидті және фторлы керамиканың катодолюминесценция қасиеттері

Дәстүр бойынша отқа төзімді керамиканың синтезі күрделі және көп уақытты қажет ететін процесс. Біраз уақыт бұрын жаңа, әлдеқайда жылдам әдіс — жоғары энергиялы электрондардың қуатты ағыны саласындағы люминесцентті керамиканы синтездеу әдісі ұсынылды. Көп компонентті оксидті фосфорларды синтездеу кезінде алынған материалдың қасиеттерінің шикізат қоспасының құрамына және синтез процесінің режимдеріне тәуелділігін анықтау оңай шаруа емес. Осыған байланысты күрделі фосфорлардың құрамдас бөліктері болып табылатын қарапайым оксидтерден радиациялық синтез арқылы жасалған керамиканың қасиеттерін зерттеу қисынды болып көрінеді. Жұмыста радиациялық синтез әдісімен алынған металл оксидтерінің (Ga_2O_3, Al_2O_3, Y_2O_3) және фторидтердің (MgF_2, BaF_2) керамикалық үлгілерінің катодолюминесценциясының спектрлік және кинетикалық заңдылықтарына зерттеу жүргізілді. Люминесценция импульсі 250 кэВ болатын электрондардың орташа энергиясы бар электрондар шоғырымен қозғалды. Спектрлер мен люминесценция кинетикасын тіркеу үшін 7 нс уақыт ажыратымдылығы бар импульстік спектрометрия әдісі қолданылды. Авторлар зерттелген үлгілердің катодолюминесценция спектрлеріне қарапайым жолақтарды бөліп көрсете отырып, жеке жолақтардағы люминесценцияның әлсіреу динамикасы туралы қорытынды жасайды. Алынған нәтижелерді монокристалды үлгілер бойынша белгілі деректермен салыстыру жүргізілді. Оксидті керамикадан айырмашылығы, MgF_2 және BaF_2 керамикалық үлгілерінің спектрлік сипаттамалары осы қосылыстардың монокристалдары туралы мәліметтермен жақсы үйлесетіндігін көрсетеді.

Кілт сөздер: оксидті керамика, фторлы керамика, катодолюминесценция, радиациялы синтез, спектрлер, уақыт ажыратымдылығы, Ga_2O_3, Al_2O_3, Y_2O_3.

А.А. Карнаухова, В.Ю. Яковлев

Свойства катодолюминесценции оксидной и фторидной керамики, синтезированной в поле потока высокоэнергетических электронов

Традиционно синтез тугоплавкой керамики является сложным и долгим процессом. Некоторое время назад был предложен новый, намного более быстрый метод — метод синтеза люминесцентной керамики в поле мощного потока высокоэнергетических электронов. Синтез оксидной керамики по принципиально новой технологии требует всестороннего изучения свойств этой керамики. При синтезе многокомпонентных оксидных люминофоров непростой задачей является определение зависимостей свойств получаемого материала от состава исходного сырья, режимов процесса синтеза. Образцы для данной работы были синтезированы путем прямого воздействия на сырье электронного пучка. В работе исследовались закономерности катодолюминесценции образцов керамики оксидов металлов (Ga_2O_3, Al_2O_3, Y_2O_3) и фторидов металлов (MgF_2, BaF_2), синтезированной радиационным методом. Люминесценция возбуждалась пучком электронов со средней энергией электронов в импульсе 250 кэВ. Для регистрации спектров и кинетик люминесценции использовался метод импульсной спектрометрии с временным разрешением 7 нс. Авторами представлен анализ спектров катодолюминесценции изученных образцов с выделением элементарных полос, сделаны заключения о динамике затухания люминесценции в отдельных полосах. Проведено сравнение полученных результатов с известными данными по монокристаллическим образцам. Показано, что, в отличие от оксидной керамики, спектральные характеристики образцов керамик MgF_2, BaF_2 показывают хорошее соответствие с данными по монокристаллам этих соединений.

Ключевые слова: оксидная керамика, фторидная керамика, катодолюминесценция, радиационный синтез, спектры, временное разрешение, Ga_2O_3, Al_2O_3, Y_2O_3.

References

1 Lisitsyn, V., Tulegenova, A., Golkovski, M., Polisadova, E., Lisitsyna, L., Mussakhanov, D., & Alpyssova, G. (2023). Radiation Synthesis of High-Temperature Wide-Bandgap Ceramics. *Micromachines*, 14, 2193–2221. https://doi.org/10.3390/mi14122193.

2 Lisitsyn, V., Tulegenova, A., Kaneva, E., Mussakhanov, D., & Gritsenko, B. (2023). Express Synthesis of YAG: Ce Ceramics in the High-Energy Electrons Flow Field. *Materials, 16*(3), 1057–1068. https://doi.org/10.3390/ma16031057

3 Ivanova, E.V., Dement'ev, P.A., Zamoryanskaya, M.V., Zakgeim, D.A., Panov, D.Yu., Spiridonov, V.A., Kremleva, A.V., Odnobludov, M.A., Bauman, D.A., Romanov, A.E., & Bugrov, V.E. (2021). Issledovanie lovushek nositelem zariada v obemnom okside galliia β-Ga_2O_3 [Research of charge carriers traps in gallium oxide beta-Ga_2O_3]. *Fizika tverdogo tela — Solid state physics, 63*(4), 421–426. https://doi.org/10.21883/FTT.2021.04.50705.236 [in Russian].

4 Al Said Mohamed, A.A. (1996). *Luminestsentsiia alfa-Al_2O_3, stimulirovannaia tiazhelymi ionami s energiei > 1 MeV/a.e.m. (Luminescence of alfa-Al_2O_3, stimulated by heavy ions with energy > 1 MeV/a.m.u.)*. Dubna [in Russian].

Information about the authors

Anna Karnaukhova (corresponding author) — Candidate of physical and mathematical sciences, Associate professor, Tomsk Polytechnic University, Lenin av., 30, 634050, Tomsk, Russia; *e-mail: meleshko@tpu.ru*; https://orcid.org/0000-0002-3542-4300

Victor Yakovlev — Doctor of physical and mathematical sciences, Professor, Tomsk Polytechnic University, Lenin av., 30, 634050, Tomsk, Russia; *e-mail: yak999@rambler.ru*; https://orcid.org/0000-0003-3636-3623

Article
https://doi.org/10.31489/2024PH4/60-67
UDC 539.184.5

Received: 25.06.2024
Accepted: 19.08.2024

A.G. Kochur*, A.P. Chaynikov, A.I. Dudenko, V.P. Levitskaya

Rostov State Transport University, Rostov-on-Don, Russia
*(*Corresponding author's e-mail: agk@rgups.ru)*

Final ion formation and energy reemission upon a cascade decay of single vacancies in the *K* and *L* electron shells of atomic platinum

Cascade decay of single vacancies in 1s, 2s, $2p_{1/2}$, and $2p_{3/2}$ subshells of an isolated platinum atom are simulated by the method of construction and analysis of the cascade decay trees. The yields of final ions and the spectra of cascade electrons and photons are calculated. Mean charges of the final ions formed as a result of the cascade decays of 1s, 2s, $2p_{1/2}$, and $2p_{3/2}$ vacancies in the platinum atom are 7.75, 9.82, 7.80, and 7.95, respectively. The energies stored in final cascade ions, and the energies reemitted with cascade electrons and photons are calculated for the decays of each initial inner-shell vacancy. In the case of decay of vacancies in the 2s, $2p_{1/2}$, and $2p_{3/2}$ subshells, most of the energy initially acquired by the atom during the creation of an initial inner-shell vacancy is re-emitted by Auger and Coster–Kronig cascade electrons. In the case of 1s vacancy decay, most of the energy is carried away by cascade photons, predominantly *KL*. The prospects of using platinum-based agents as radiosensitizers in photon activation therapy of cancer are discussed.

Keywords: platinum, vacancy cascade, decay tree, ion yields, cascade energy reemission, radiosensitization, Auger therapy, photon activation therapy.

Introduction

Creation of an inner-shell vacancy in an atom produces a high-energy excited state which then decays through a sequence of radiative and non-radiative transitions into terminal (often highly charged) stable ionic states [1–4]. Cascade decay of vacancies, also called vacancy cascades, is a fundamental atomic process occurring whenever an inner-shell vacancy is created. The energy acquired by the atom upon ionization is reemitted into the environment with numerous cascade electrons and photons. This circumstance makes it possible to use heavy bio-neutral atoms as radiosensitizers in photon activation therapy (PAT) of malignant tumors [5, 6]. Radiosensitizers are the agents introduced into the tumor prior to irradiation in order to increase the damage to cancer cells.

Radiosensitization effect is two-fold. In the first place, due to large photoionization cross sections of the high-Z radiosensitizing atoms, the absorption of energy from an incident ionizing radiation beam is localized in the tumor, so less harm is made to healthy tissues. What is important, the energy absorbed by a radiosensitizing atom does not stay with it, a large portion of the absorbed energy is reemitted with cascade-produced electrons and photons into surrounding tissues causing direct and indirect damage to cancer cells' DNA. Energy reemission following inner-shell ionization has been studied in iron [7], gold [8], silver [9, 10] and iodine [11] atoms by theoretical cascade simulations.

Platinum is a popular radiosensitizer introduced into tumors within chemical compounds or in nanoparticles. It is often contained in chemotherapeutic drugs; a PAT using chemotherapeutic radiosensitizers is called chemoradiotherapy (CRT) [12, 13].

In this work we study the cascade decays of single 1s, 2s, $2p_{1/2}$, and $2p_{3/2}$ vacancies in an isolated platinum atom by straightforward construction of the cascade decay trees. The yields of final cascade ions, and energies *a*) stored in final ions, *b*) reemitted with cascade-produced electrons, and *c*) reemitted with cascade-produced photons are calculated. The prospects of using platinum atoms as radiosensitizers are discussed.

Theory

To simulate the cascade decay of vacancies, we use the method of construction and analysis of decay trees described in detail in [14, 15]. A brief review of the method is given in this Section.

A cascade decay tree consists of branching points and branches connecting them. The branching points are ionic configurations — an initial inner-shell-vacancy one, and those appearing during the cascade transitions. The branches of the decay tree are the cascade transitions — radiative with the emission of photons, and non-radiative (Auger, Coster–Kronig, super-Coster–Kronig) with the emission of electrons.

Cascade decay trees for specific initial inner-shell vacancy states were built as follows. Let $C^{(0)}$ be the starting branching point of the tree, i.e. the initial configuration with a single inner-shell vacancy. It decays into lower-in-energy ionic states which form a set of the first-decay-step configurations $\{C_i^{(1)}\}$. Some of the configurations $C_i^{(1)}$ can still have inner vacancies and can decay further. Their decays form a second-decay-step set of configurations $\{C_j^{(2)}\}$, etc. The tree is completely built when after the n^{th} decay step none of the configurations $\{C_k^{(n)}\}$ can decay further having vacancies only in the uppermost subshells. The decay trees for the cascades with deep vacancies in heavy atoms are very complex. This is illustrated in Table 1 which lists the number of different ionic configurations appearing after each decay step during the cascade decay of single vacancies in 1s, 2s, $2p_{1/2}$, and $2p_{3/2}$ subshells of the platinum atom. One can see that the number of decay steps reaches 23, and tens of thousands of different ionic configurations can appear after several consecutive decay steps. The bottom line of Table 1 shows the total numbers of branches in the decay trees; they amount to tens of millions.

Table 1

Numbers of different ionic configurations appearing after each decay step during the cascade relaxation of single vacancies in 1s, 2s, $2p_{1/2}$ and $2p_{3/2}$ subshells of an isolated platinum atom, and total numbers of branches (N_{br}) in respective decay trees

Decay step	1s	2s	$2p_{1/2}$	$2p_{3/2}$
1	177	166	153	144
2	1333	1051	950	873
3	5878	4582	3876	3528
4	15079	13374	9695	8477
5	23506	24503	14633	12152
6	27077	31099	16699	13260
7	26766	32711	16009	12554
8	23855	30353	13629	10554
9	19298	25360	10407	7819
10	14288	19345	7111	5198
11	9606	13319	4438	3166
12	6000	8515	2673	1923
13	3624	5164	1686	1289
14	2096	3220	1223	956
15	1418	2163	914	693
16	1006	1593	641	459
17	705	1184	393	281
18	447	791	222	138
19	242	469	97	61
20	110	248	32	18
21	39	109	5	
22		28		
23		2		
N_{br}	2.12E7	1.962E7	8.222E6	5.902E6

The cascade decay tree can be built if for each branching point $C_i^{(m)}$ relative probabilities of all allowed transitions into lower-in-energy ionic states $C_j^{(m+1)}$ are known. These relative probabilities, also known as branching ratios, are calculated with

$$\chi(C_i^{(m)} \to C_j^{(m+1)}) = \frac{\Gamma(C_i^{(m)} \to C_j^{(m+1)})}{\sum_k \Gamma(C_i^{(m)} \to C_k^{(m+1)})}, \tag{1}$$

where Γ are partial transition widths which in atomic units coincide with the probabilities of transitions per unit time. The summation is performed over all energy- and symmetry-allowed radiative and non-radiative transition from $C_i^{(m)}$. Partial transition widths were calculated using the radial parts of bound- and continuous-state atomic wave functions calculated in Pauli–Fock (PF) approximation [16]. They were calculated for single-vacancy ions, and then modified so as to take into account actual electron configurations of decaying ions as described in [14, 15].

Mean energies of cascade transitions $C_i \to C_f$ are calculated using mean total PF energies E_i and E_f of initial and final ionic configurations of the transitions. If the multiplets of C_i and C_f overlapped, only the transitions between the multiplet components allowed by the energy conservation law were considered when calculating mean transition energies and partial transition widths. The multiplets of ionic configurations were simulated with Gaussian probability density distributions using the methods of global characteristics of spectra [17, 18].

In a decay tree, all terminal configurations are those of final ion states with specific ion charges. Let $\{C_i(q)\}$ be the set of terminal ionic states in a $+q$ charge state found in the decay tree. The probability to discover an atom in a specific charge state $+q$ (ion yield) is the sum of probabilities to get from $C^{(0)}$ to each $C_i(q)$ through all possible decay pathways:

$$P_{C^{(0)}}(q)=\sum_i \sum_{\text{pathways}} P_{\text{pathway}}(C^{(0)} \to C_i(q)) \quad (2)$$

In its turn, the probability of getting from $C^{(0)}$ to $C_i(q)$ along a given pathway is a product of the branching ratios of all the transitions throughout the pathway:

$$P_{\text{pathway}}(C^{(0)} \to C_i(q))=\chi(C^{(0)} \to C_a^{(1)})\chi(C_a^{(1)} \to C_b^{(2)})...\chi(C_p^{(n-2)} \to C_r^{(n-1)})\chi(C_r^{(n-1)} \to C_i^{n}(q)) \quad (3)$$

Mean final ion charges upon decays of initial single-vacancy states $C^{(0)}$ are calculated with

$$\left\langle q_{C^{(0)}} \right\rangle = \sum_q q P_{C^{(0)}}(q) \quad (4)$$

The spectra of electrons and photons produced by the cascade relaxation of an inner-shell-vacancy configuration $C^{(0)}$ are the probabilities of emission of electrons $P^{\text{el}}_{C^{(0)}}(i)$ and photons $P^{\text{phot}}_{C^{(0)}}(k)$ against respective electron $E^{\text{el}}_{C^{(0)}}(i)$ and photon $E^{\text{phot}}_{C^{(0)}}(k)$ energies:

$$Sp^{\text{el}}_{C^{(0)}}=\{E^{\text{el}}_{C^{(0)}}(i),P^{\text{el}}_{C^{(0)}}(i)\},\ Sp^{\text{phot}}_{C^{(0)}}=\{E^{\text{phot}}_{C^{(0)}}(k),P^{\text{phot}}_{C^{(0)}}(k)\} \quad (5)$$

In the above notations, i and k number spectral components, i.e. cascade transitions during the cascade relaxation of $C^{(0)}$. Probability of any cascade transition $P(C_i \to C_f)$ is the product of the probability of the initial-state configuration C_i to appear, and the transition branching ratio:

$$P(C_i \to C_f)=P(C_i)\chi(C_i \to C_f) \quad (6)$$

The appearance probabilities $P(C_i)$ are calculated in the same way as the probabilities to discover the configurations of final ions, see (2), (3).

Upon nl_j ionization, the atom acquires the energy $E_{\text{in}}(nl_j)$ equal to the threshold ionization energy of the nl_j orbital. We split the acquired energy $E_{\text{in}}(nl_j)$ into the following redistribution channels: *a*) mean energy stored in final cascade ions $E^{\text{ion}}(nl_j)$, *b*) mean energy reemitted with cascade electrons $E^{\text{el}}_{\text{out}}(nl_j)$, and *c*) mean energy reemitted with cascade photons $E^{\text{phot}}_{\text{out}}(nl_j)$. $E^{\text{el}}_{\text{out}}(nl_j)$ and $E^{\text{phot}}_{\text{out}}(nl_j)$ are calculated using electron and photon spectra emitted upon the decay of respective single-vacancy states $C^{(0)}=nl_j^{-1}$:

$$E^{\text{el}}_{\text{out}}(nl_j)=\sum_i P^{\text{el}}_{nl_j^{-1}}(i)E^{\text{el}}_{nl_j^{-1}}(i),\quad E^{\text{phot}}_{\text{out}}(nl_j)=\sum_k P^{\text{phot}}_{nl_j^{-1}}(k)E^{\text{phot}}_{nl_j^{-1}}(k) \quad (7)$$

Evidently,

$$E^{\text{ion}}(nl_j)=E_{\text{in}}(nl_j)-E^{\text{el}}_{\text{out}}(nl_j)-E^{\text{phot}}_{\text{out}}(nl_j) \quad (8)$$

Note that when a cascade relaxation of an atom happens within an organism tissue as in the case of PAT, the energy of the cascade ions $E^{\text{ion}}(nl_j)$ will be also eventually deposited to the environment via ions neutralization.

Results and Discussion

Calculated final ion yields (ion charge spectra) upon the decay of 1s, 2s, $2p_{1/2}$ and $2p_{3/2}$ initial single vacancies in the platinum atom are shown in Figure 1. Mean final ion charges are given in respective panels. One can see that quite large degree of cascade ionization can be reached: the ions with charges up to +18 are produced. Mean final ion charges are also large, e.g. in the case of the 2s vacancy relaxation mean ion charge is 9.82.

Note that the charge spectra upon the decay of 1s, $2p_{1/2}$ and $2p_{3/2}$ vacancies are very much alike. This is because the main channels of the first-step decay of the 1s vacancy are the radiative transitions into $2p_{1/2}$ and $2p_{3/2}$ states with the emission of KL_{23} ($K\alpha_{12}$) photons. According to our calculations, a combined branching ratio of this transition is 0.78, and the decay trees for $2p_{1/2}$ and $2p_{3/2}$ initial vacancies do not differ much. In the case of the initial 2s vacancy, the cascade is more complex. Its decay tree contains additional $L_1L_{23}N$ and $L_1L_{23}O$ Coster–Kronig branches causing additional emission of electrons. The charge spectra of the cascades in platinum are very much the same as those of the cascades in gold. The latter are discussed in detail in ref. [19].

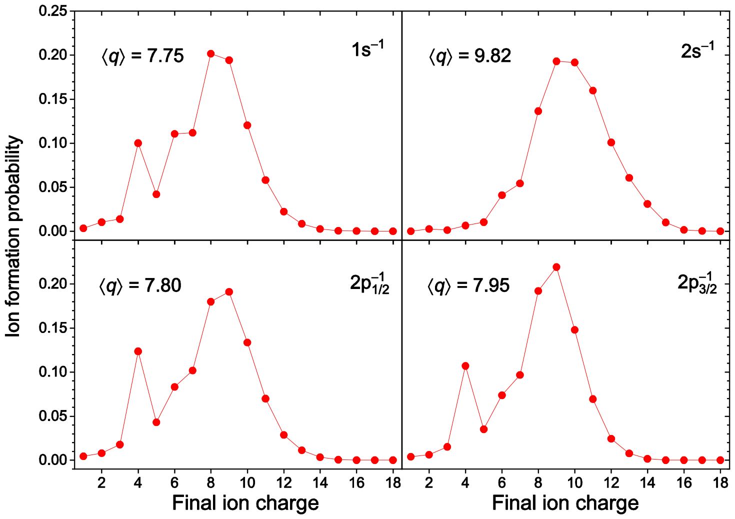

Figure 1. Final ion yields upon the cascade decay of single 1s, 2s, $2p_{1/2}$ and $2p_{3/2}$ vacancies in atomic Pt

As an example, Figure 2 shows the spectra of electrons and photons emitted during the cascade decay of the 1s vacancy in the platinum atom. A typical feature of all the deep-initial-vacancy cascade spectra is their complex multicomponent structure caused by the fact that the cascade transitions occur in a multitude of different multivacancy ionic configurations.

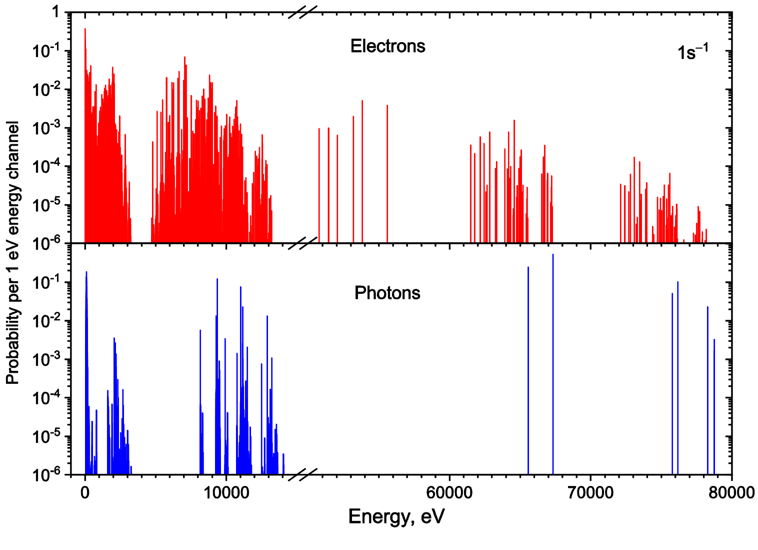

Figure 2. Spectra of electrons and photons emitted during the cascade decay of 1s vacancy in an isolated Pt atom. Energy bin is 1 eV

Table 2 shows calculated energies acquired by the platinum atom on ionization of its 1s, 2s, $2p_{1/2}$ and $2p_{3/2}$ subshells, and the energies stored in final cascade ions and reemitted with cascade electron and photons after cascade relaxation of vacancies. Also shown in the Table are relative weights of energy redistribution channels (in parentheses). It is seen from Table 2 that upon *K* and *L* ionization of Pt, only a small portion of the acquired energy rests with the platinum ions. Most of the energy is reemitted into the environment by cascade electrons and photons. Energy reemitted by electrons is the principal energy redistribution channel in the case of *L* ionizations making 59 to 66 % of the acquired energy. In the case of 1s ionization, most of the energy is carried away by cascade photons, predominantly KL_{23}.

To be able to draw conclusions about the role of cascade electrons and photons in PAT, it is necessary to analyze their mean free paths in organism tissues. Most effective in causing damage to tumor cells will be the particles with small inelastic free paths in the organism tissue medium. They will depose their energy to tumor cells in the nearest vicinity of the emitting atom, and with large doses. The particles with large free paths will spread their energy in larger volumes and with smaller doses.

Table 2

Energies acquired upon nl_j ionization of atomic platinum $E_{\text{in}}(nl_j)$, energies stored in final platinum ions $E^{\text{ion}}(nl_j)$, and energies reemitted with cascade electrons $E^{\text{el}}_{\text{out}}(nl_j)$ and cascade photons $E^{\text{phot}}_{\text{out}}(nl_j)$

nl_j	$E_{\text{in}}(nl_j)$, eV	$E^{\text{ion}}(nl_j)$, eV	$E^{\text{el}}_{\text{out}}(nl_j)$, eV	$E^{\text{phot}}_{\text{out}}(nl_j)$, eV
1s	78814	614 (0.8 %)*	7827 (10.0 %)	70373 (89.2 %)
2s	13917	939 (6.8 %)	9039 (65.0 %)	3939 (28.2 %)
$2p_{1/2}$	13236	534 (6.8 %)	7762 (58.7 %)	4939 (37.3 %)
$2p_{3/2}$	11492	525 (4.6 %)	7621 (66.3 %)	3346 (29.1 %)
*Note – Relative weights of energy redistribution channels				

Figure 3 shows mean inelastic free paths of electrons and photons in liquid water calculated in [8]. Water is a commonly accepted simulation of organism tissues. As seen from Figures 3 and 4, mean inelastic free paths of cascade electrons are rather small; they are three to four orders of magnitude less than typical cell size, it is shown in Figure 4 with horizontal lines. This means that all the cascade electrons will contribute to the PAT effect. As for photons, their free paths in most cases are by orders of magnitude greater than the cell size which makes them hardly effective in PAT. Only a small portion of emitted cascade photons have free paths smaller than the cell size. Proportions of the energy reemitted with such PAT-prospective photons are 0.2 %, 2.5 %, 1.4 % and 1.7 % in 1s- 2s- $2p_{1/2}$- and $2p_{3/2}$-cascades, respectively.

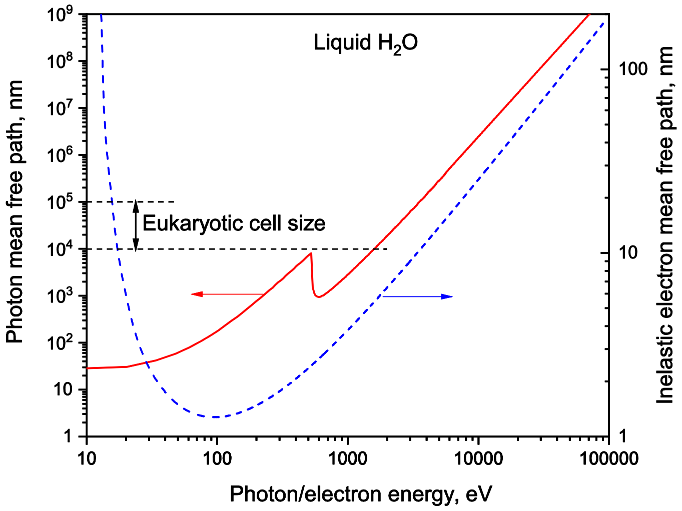

Figure 5. Electron and photon inelastic free paths in water calculated in [8].

The studies on cascade energy reemission in gold [8], silver [9, 10] and iodine [11] atoms have shown that photoelectrons can also contribute to the PAT effect giving contribution to the emitted energy comparable to that from cascade electrons. Although we did not address the role of photoelectrons in this study, we believe that in the case of platinum, they will give considerable contribution to the PAT effect, too.

Conclusions

The method of construction and analysis of the decay trees is applied to simulate cascade decay of single 1s, 2s, $2p_{1/2}$ and $2p_{3/2}$ vacancies in an isolated platinum atom. Final ion charge spectra and the spectra of cascade electrons and photons are calculated. It is shown that most of the energy acquired by the atom upon ionization is reemitted by cascade electrons and photons. All the cascade electrons having rather short inelastic mean free paths are effective in photon activation therapy of cancer when platinum is used as a radiosensitizing agent. Only a small portion of cascade photons is PAT effective.

Acknowledgments

This research was funded by the Russian Science Foundation (project no. 23–22–00222, https://rscf.ru/project/23-22-00222/).

References

1 Krause, M. O., Vestal, M. L., Johnston, W. H., & Carlson, T. A. (1964). Readjustment of the Neon Atom Ionized in the K Shell by X Rays. *Physical Review*, *133*(2A), A385–A390. https://doi.org/10.1103/PhysRev.133.A385

2 Carlson, T. A., & Krause, M. O. (1965). Atomic Readjustment to Vacancies in the K and L Shells of Argon. *Physical Review*, *137*(6A), A1655–A1662. https://doi.org/10.1103/PhysRev.137.A1655

3 Krause, M. O., & Carlson, T. A. (1966). Charge Distributions of Krypton Ions Following Photo-Ionization in the M Shell. *Physical Review*, *149*(1), 52–58. https://doi.org/10.1103/PhysRev.149.52

4 Krause, M. O., & Carlson, T. A. (1967). Vacancy Cascade in the Reorganization of Krypton Ionized in an Inner Shell. *Physical Review*, *158*(1), 18–24. https://doi.org/10.1103/PhysRev.158.18

5 Laster, B. H., Thomlinson, W. C., & Fairchild, R. G. (1993). Photon Activation of Iododeoxyuridine: Biological Efficacy of Auger Electrons. *Radiation Research*, *133*(2), 219. https://doi.org/10.2307/3578359

6 6 Ceresa, C., Nicolini, G., Semperboni, S., Requardt, H., Le Duc, G., Santini, C., Pellei, M., Bentivegna, A., Dalprà, L., Cavaletti, G., & Bravin, A. (2014). Synchrotron-based Photon Activation Therapy Effect on Cisplatin Pre-treated Human Glioma Stem Cells. *Anticancer Research*, *34*(10), 5351–5356.

7 Kochur, A. G., Chaynikov, A. P., Dudenko, A. I., & Yavna, V. A. (2022). Cascade reemission of energy by inner-shell-ionized iron atom. *Journal of Quantitative Spectroscopy and Radiative Transfer*, *286*, 108200. https://doi.org/10.1016/j.jqsrt.2022.108200

8 Chaynikov, A. P., Kochur, A. G., Dudenko, A. I., & Yavna, V. A. (2023). Cascade energy reemission after inner-shell ionization of atomic gold. Role of photo- and cascade-produced electrons in radiosensitization using gold-containing agents. *Journal of Quantitative Spectroscopy and Radiative Transfer*, *302*, 108561. https://doi.org/10.1016/j.jqsrt.2023.108561

9 Chaynikov, A. P., Kochur, A. G., Dudenko, A. I., & Yavna, V. A. (2023). Energy reemission and possible radiosensitizing effect caused by the cascade decay of single vacancies in the K, L, M, and N shells of atomic silver. *Journal of Quantitative Spectroscopy and Radiative Transfer*, *310*, 108714. https://doi.org/10.1016/j.jqsrt.2023.108714

10 Chaynikov, A. P., Kochur, A. G., & Dudenko, A. I. (2024). Cascade energy reemission by the silver atom ionized by 0.01–100 keV photons. Possible application of silver-based radiosensitizing agents in photon beam radiation therapy. *Journal of Electron Spectroscopy and Related Phenomena*, *275*, 147472. https://doi.org/10.1016/j.elspec.2024.147472

11 Chaynikov, A. P., Kochur, A. G., & Dudenko, A. I. (2024). Cascade energy reemission by the iodine atom irradiated by 0.01–100 keV photons. Role of photo- and cascade-produced electrons in radiosensitization using iodine-containing agents. *Journal of Quantitative Spectroscopy and Radiative Transfer*, *322*, 109024. https://doi.org/10.1016/j.jqsrt.2024.109024

12 Rousseau, J., Boudou, C., Barth, R. F., Balosso, J., Estève, F., & Elleaume, H. (2007). Enhanced Survival and Cure of F98 Glioma–Bearing Rats following Intracerebral Delivery of Carboplatin in Combination with Photon Irradiation. *Clinical Cancer Research*, *13*(17), 5195–5201. https://doi.org/10.1158/1078-0432.CCR-07-1002

13 Yaray, K., Norbakhsh, A., Rashidzadeh, H., Mohammadi, A., Mozafari, F., Ghaffarlou, M., Mousazadeh, N., Ghaderzadeh, R., Ghorbani, Y., Nasehi, L., Danafar, H., & Ertas, Y. N. (2023). Chemoradiation therapy of 4T1 cancer cells with methotrexate conjugated platinum nanoparticles under X-Ray irradiation. *Inorganic Chemistry Communications*, *150*, 110457. https://doi.org/10.1016/j.inoche.2023.110457

14 Kochur, A. G., Dudenko, A. I., Sukhorukov, V. L., & Petrov, I. D. (1994). Direct Hartree-Fock calculation of multiple Xe^{i+} ion production through inner shell vacancy de-excitations. *Journal of Physics B: Atomic, Molecular and Optical Physics*, *27*(9), 1709–1721. https://doi.org/10.1088/0953-4075/27/9/011

15 Kochur, A. G., Sukhorukov, V. L., Dudenko, A. J., & Demekhin, P. V. (1995). Direct Hartree-Fock calculation of the cascade decay production of multiply charged ions following inner-shell ionization of Ne, Ar, Kr and Xe. *Journal of Physics B: Atomic, Molecular and Optical Physics, 28*(3), 387–402. https://doi.org/10.1088/0953-4075/28/3/010

16 Kau, R., Petrov, I. D., Sukhorukov, V. L., & Hotop, H. (1997). Experimental and theoretical cross sections for photoionization of metastable Xe* (6s $^3P_2$, $^3P_0$) atoms near threshold. *Zeitschrift Für Physik D Atoms, Molecules and Clusters, 39*(4), 267–281. https://doi.org/10.1007/s004600050137

17 Bauche-Arnoult, C., Bauche, J., & Klapisch, M. (1979). Variance of the distributions of energy levels and of the transition arrays in atomic spectra. *Physical Review A, 20*(6), 2424–2439. https://doi.org/10.1103/PhysRevA.20.2424

18 Kučas, S., & Karazija, R. (1993). Global characteristics of atomic spectra and their use for the analysis of spectra. I. Energy level spectra. *Physica Scripta, 47*(6), 754–764. https://doi.org/10.1088/0031-8949/47/6/012

19 Chaynikov, A. P., Kochur, A. G., Dudenko, A. I., Petrov, I. D., & Yavna, V. A. (2023). Final ion charge spectra upon cascade decay of inner-shell vacancies in atomic Au. *Physica Scripta, 98*(2), 025406. https://doi.org/10.1088/1402-4896/acb407

А.Г. Кочур, А.П. Чайников, А.И. Дуденко, В.П. Левицкая

Ақырлы иондардың түзілуі және платина атомының K және L электронды қабықшаларындағы жалғыз бос орындардың каскадты ыдырауы кезінде энергияның қайта шығарылуы

Каскадты ыдырау ағаштарын құру және талдау әдісімен оқшауланған платина атомының 1s, 2s, $2p_{1/2}$ және $2p_{3/2}$ ішкі қабықшаларындағы бір жұмыс орындарының каскадты ыдырауын модельдеу жүргізілді. Соңғы иондардың шығуы және каскадты электрондар мен фотондардың спектрлері есептеледі. PT атомындағы 1s, 2s, $2p_{1/2}$ және $2p_{3/2}$ қуыстарының каскадты ыдырауынан пайда болған соңғы иондардың орташа зарядтары сәйкесінше 7,75, 9,82, 7,80 және 7,95 құрайды. Әрбір бастапқы ішкі қуыстың ыдырауы үшін соңғы каскадты иондарда жинақталған энергия және каскадты электрондар мен фотондар қайта шығаратын энергия есептеледі. 2s, $2p_{1/2}$ және $2p_{3/2}$ ішкі қабықшаларындағы бос орындар ыдыраған жағдайда, бастапқы ішкі қуысты жасау кезінде атом қабылдаған энергияның көп бөлігі каскадтың Оже және Костер–Крониговски электрондары арқылы қайта бөлінеді. *1s*-бос орны ыдыраған кезде энергияның көп бөлігі каскадты фотондармен, негізінен *K, L* арқылы тасымалданады. Қатерлі ісіктің фотонды активтендіру терапиясында радиосенсибилизатор ретінде платина негізіндегі препараттарды қолдану перспективалары талқыланды.

Кілт сөздер: платина, жұмыс каскады, ыдырау ағашы, ион өнімділігі, каскадтан энергияны қайта шығару, радиосенсибилизация, Оже терапиясы, фотонды белсендіру терапиясы.

А.Г. Кочур, А.П. Чайников, А.И. Дуденко, В.П. Левицкая

Образование конечных ионов и переизлучение энергии при каскадном распаде одиночных вакансий в *K* и *L* электронных оболочках атома платины

Методом построения и анализа деревьев каскадного распада проведено моделирование каскадных распадов одиночных вакансий в 1s, 2s, $2p_{1/2}$ и $2p_{3/2}$ подоболочках изолированного атома платины. Рассчитаны выходы конечных ионов и спектры каскадных электронов и фотонов. Средние заряды конечных ионов, образующихся в результате каскадных распадов 1s, 2s, $2p_{1/2}$ и $2p_{3/2}$ вакансий в атоме Pt, равны 7,75; 9,82; 7,80 и 7,95 соответственно. Для распадов каждой исходной внутренней вакансии рассчитаны энергии, запасенные в конечных каскадных ионах, и энергии, переизлученные с каскадными электронами и фотонами. В случае распада вакансий в подоболочках 2s, $2p_{1/2}$ и $2p_{3/2}$ большая часть энергии, первоначально полученной атомом при создании начальной внутренней вакансии, переизлучается каскадными Оже и Костер-Крониговскими электронами. При распаде *1s*-вакансии большая часть энергии уносится каскадными фотонами, преимущественно *K, L*. Обсуждены перспективы использования препаратов на основе платины в качестве радиосенсибилизаторов в фотонно-активационной терапии рака.

Ключевые слова: платина, каскад вакансий, дерево распада, выходы ионов, каскадное переизлучение энергии, радиосенсибилизация, Оже терапия, фотонно-активационная терапия.

Information about the authors

Andrei Kochur — Doctor of physical and mathematical sciences, Head of Department of Physics, Rostov State Transport University, Rostovskogo Strelkovogo Polka Narodnogo Opolcheniya Sq., 2, 344038, Rostov-on-Don, Russia; *e-mail: agk@rgups.ru*; https://orcid.org/0000-0002-2063-9691

Alexander Chaynikov (corresponding author) — Candidate of physical and mathematical sciences, Associate professor, Rostov State Transport University, Rostovskogo Strelkovogo Polka Narodnogo Opolcheniya Sq., 2, 344038, Rostov-on-Don, Russia; *e-mail: chaynikov.a.p@gmail.com*; https://orcid.org/0000-0002-4076-2347

Aleksey Dudenko — Candidate of physical and mathematical sciences, Associate professor, Rostov State Transport University, Rostovskogo Strelkovogo Polka Narodnogo Opolcheniya Sq., 2, 344038, Rostov-on-Don, Russia; *e-mail: lesha_11@mail.ru*; https://orcid.org/0000-0002-8297-8912

Victoria Levitskaya — Graduate student, Rostov State Transport University, Rostovskogo Strelkovogo Polka Narodnogo Opolcheniya Sq., 2, 344038, Rostov-on-Don, Russia; *e-mail: Lvenokvika@yandex.ru*

Article
https://doi.org/10.31489/2024PH4/68-73
UDC: 621.384.658

Received: 27.06.2024
Accepted: 22.08.2024

N.K. Kuksanov*, D.S. Vorobev, E.V. Domarov, Yu.I. Golubenko, A.I. Korchagin, R.A. Salimov, S.N. Fadeev, I.K. Chakin, A.V. Semenov, V.G. Cherepkov, M.G. Golkovsky, A.V. Lavrukhin

Budker Institute of Nuclear Physics, Siberian Branch of the Russian Academy of Sciences, Novosibirsk, Russia
(**E-mail: n.k.kuksanov@inp.nsk.su*)

50'th anniversary of Industrial ELV Accelerators

The article highlights the 50-year development of ELV electron beam accelerators at the Budker Institute of Nuclear Physics for industrial applications. ELV accelerators are used primarily for radiation modification of polymers, such as cable insulation, and are known for their high reliability, ease of use, and adaptability to various industrial needs. The evolution of these accelerators is traced from early models with 20 kW power to modern versions reaching up to 100 kW, and even a unique 400 kW machine. The article also discusses the integration of automated systems and specialized equipment that enhance the efficiency and quality of radiation-chemical processes. Applications include a wide range of industries, from telecommunications to nuclear power, where reliability under harsh conditions is essential. Despite past challenges, such as economic disruptions, the production of ELV accelerators continues to thrive, with over 220 units delivered worldwide. The institute is focused on advancing these technologies to meet future demands.

Keywords: ELV accelerators, electron accelerators, industrial accelerators, cross-linking.

Introduction

Since 1971, the Budker Institute of Nuclear Physics, Siberian Branch of the Russian Academy of Sciences (BINP SB RAS), has been developing and producing ELV-type electron beam accelerators for use in industrial and research radiation technology installations. ELV-type accelerators are built using standardized systems and components, allowing cost-effective customization to meet specific customer requirements, such as energy range, electron beam power, beam window length, and so on. The design and circuit solutions provide for long-term, continuous, round-the-clock operation under industrial conditions. The distinct qualities of ELV accelerators include simplicity of design, ease of operation, and high reliability.

Status

Recently, it marked 50 years since the final testing of the ELV-1 accelerator as part of the interdepartmental commission program at the Experimental Plant of the All-Union Research Institute of Cable Industry in Podolsk. The commission was formed by the Ministry of Electrical Industry and included nine representatives: accelerator specialists (BINP and the Efremov Institute), the cable industry (VNIICP), radiation technology experts (VNIIRT and NPO PLASTIK), and the Ministry of General Engineering.

As a result of these tests, the commission recommended the accelerator for industrial use and mass production. The BINP immediately began fulfilling an order for 15 accelerators for the Ministry of Electrical Industry's enterprises. Today, the institute offers a series of ELV electron accelerators, covering an energy range from 0.3 to 4 MeV, with beam currents of up to 100 mA and a maximum power of up to 100 kW. The ELV accelerator is the most mass-produced and popular domestic accelerator. Since 1974, over 220 machines have been manufactured and delivered, with 120 of them still in operation. The oldest one installed abroad has been in the Czech Republic since 1980. We also work with partners in South Korea and China. It's worth noting that the Moscow Electromechanical Plant named after Vladimir Ilyich also produced ELV accelerators, but production was halted due to economic collapse, although several units were still made.

The energy range of the ELV family now covers from 0.3 to 4 MeV. The electron beam power reaches 100 kW, and there is a unique machine with a beam output power of 400 kW. It should be noted that the power of the first accelerators was only 20 kW, while today's 100 kW meets consumer demands, and there is no sharp increase in power expected. Figure 1 shows a diagram of a typical ELV, and Figure 2 depicts the most popular ELV-8 accelerator in China [1–3].

Applications

ELV accelerators are used in almost all radiation-chemical technological processes, but mainly for the radiation modification of various polymer products: cable insulation, heat-shrinkable tapes and tubes, the production of foam polyethylene, and more. The quality of the radiation treatment depends on both the accelerator itself and the technological equipment: systems for transporting products under the electron beam in the irradiation zone, take-up and pay-off devices, synchronization between the accelerator and the transportation equipment.

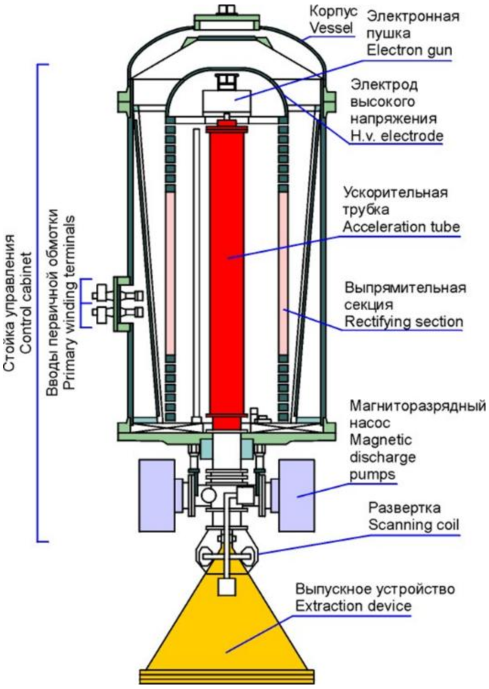

Figure 1. Common design of ELV accelrators

Figure 2. ELV-8 accelerator

The use of electron beam technology has enabled the production of a wide range of cables, wires, and heat-shrinkable products for various markets: power plants, telecommunications, electronics, the oil and gas, nuclear power plants, submarines, aviation, and railway transport. These industries require high reliability during installation and operation under harsh conditions and unusual situations. Therefore, great attention is given to improving productivity and the quality of electron beam processing.

Additionally, the accelerator and technological equipment are integrated into automated synchronized complexes. These complexes ensure impeccable quality of radiation modification across a wide range of energies and product types, as shown in Figures 3 and 4. Within the automated complex, it is possible to control both the accelerator via signals from the technological line and the technological line via signals from the accelerator. The interaction protocol between the accelerator and technological equipment is compatible with all technologies and equipment produced by various companies. Figure 5 shows the complex's control panel, and Figure 6 shows the produced products. In an automated complex, the operator does not need to be at the control panel. Process parameters are controlled automatically, and the operator can monitor them from various points in the technology hall without approaching the equipment. The time remaining before changing the processed reel is displayed on the control panel.

Key features of ELV accelerators:

- High beam power across a wide energy range, indicating high productivity of electron beam processing.
- High efficiency in converting electrical energy to accelerated electron beam energy. The efficiency ranges from 70 % to 90 %, depending on the power.
- ELV accelerators operate stably with energy and current fluctuations not exceeding +/-3 %.

- Simple control procedures due to an automated control system. This allows synchronization of accelerator operation with technological equipment, and the accelerator can be part of a fully automated technological line.
- The control system includes a comprehensive set of hardware and software covering all accelerator nodes requiring operational control, monitoring, and diagnostics.
- The accelerator itself has a simple design and high reliability.

Figure 3. Extraction device with four-side irradiation system equipped

Figure 4. Irradiation line in the South Korea company LG cable

In collaboration with EBTech (Electron Beam Technologies, South Korea), we developed a mobile ELV accelerator variant that can be moved along a track. This machine is housed in a trailer and equipped with local radiation protection. It can perform electron beam processing of liquids, gases, and bulk materials. It is shown in Figure 7. The energy of this accelerator is up to 650 keV, with a power of up to 30 kW. It has been transported within Korea and sent to Saudi Arabia, and returned after conducting experiments.

Together with the same company, a full-scale electron beam processing installation for dyeing wastewater was developed. It used an accelerator with a 400 kW beam power. The reaction chamber is shown in Figure 8. This accelerator uses 3 acceleration tubes and three output devices [3].

Ускоритель ЭЛВ-4
Комплекс П6
Энергия электронов, МэВ 1.15
Ток пучка, мА 30
Скорость, м/мин 225
Остаток з/г кабеля на П6, м(мин) -3423(-15)

Figure 5. External status screen in the Podolsk cable plant

Figure 6. Irradiated production (India)

Beam extraction to the atmosphere through an aperture

A.M. Budker was an advocate for using accelerators in various sectors. He correctly believed that accelerator applications extend beyond radiation-chemical processes for polymer material modification. The thermal impact of a powerful focused electron beam can be utilized in metallurgical processes, cutting, welding, and working with inorganic materials. To release the focused beam into the atmosphere, an output device with a multi-stage differential pumping system is used. The electron beam is focused by magnetic lenses, and apertures are installed in its crossover for beam passage [3].

Continuous vacuum pumps evacuate gas entering through the apertures. Using a series of such chambers, the pressure is gradually reduced from atmospheric to the working pressure of the accelerating device. At the output of the device, the beam size does not exceed 1-1.5 mm, allowing a beam power density of 106 W/cm^2 or higher with 100 kW beam power. Figure 9 shows the glow of the concentrated beam released into the atmosphere. The decrease in brightness with distance from the output aperture is due to beam scattering in the air. Three versions of atmospheric beam release have been developed and produced: one for a magnetic focusing tube, one for a large-aperture tube, and one for adiabatically compressed electron beam output with up to 1 A current and 500 kW power [3, 4].

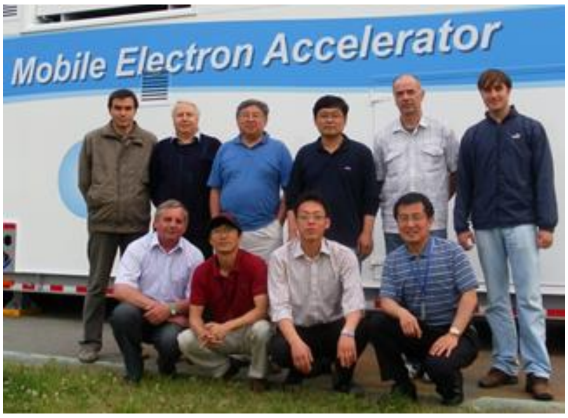

Figure 7. Russia-SouthKoreateam in front of trailer with accelerator inside

Figure 8. Waste water treatment room in the dying center. Daegu, South Korea

At the BINP, numerous successful experiments have been conducted on various materials (metals and alloys, rocks, ceramics, plastics, etc.) using the focused electron beam released into gas at atmospheric pressure. The beam has been released into both air and protective atmospheres (argon, helium). However, this beam release system has not found widespread application in industrial processes. Subsequently, this setup received the status of a unique scientific installation (USI). Currently, numerous experiments are being conducted with this accelerator, equipped with a focused beam atmospheric release system, in collaboration with various Soviet, Russian, and foreign organizations. These experiments include developing technological modes and obtaining valuable scientific results in steel hardening (including coating wear-resistant layers on copper plates for continuous steel casting), various radiation-thermal processes in solid-state chemistry (including technology for producing inexpensive high-activity ammonia synthesis catalysts from catalyst production waste), and developing high-performance methods for producing metal and oxide nanopowders by direct evaporation from melts, as well as other high-temperature technological processes [5].

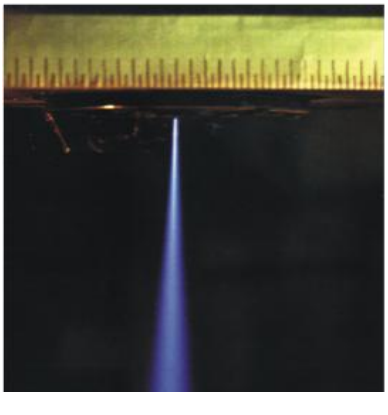

Figure 9. Electron beam extracted into the atmosphere

Conclusions

For more than 50 years, the Budker Institute of Nuclear Physics in Novosibirsk has been developing ELV industrial electron accelerators, which have found widespread use both in Russia and abroad. These accelerators have gained recognition for their high reliability, ease of maintenance, and adaptability to a wide range of technologies. Nevertheless, the institute continues to develop new types of ELV accelerators and modify existing models. The main goal of this activity is to be ready for future demands for accelerators with higher parameters, should new breakthrough technologies arise.

References

1 Vorobev D.S. ELV-15 – New Accelerator for Industrial Applications / D.S. Vorobev, E.V. Domarov, N.K. Kuksanov, et al. // Proceedings of the 8th International Congress on Energy Fluxes and Radiation Effects (EFRE-2022). — 2022. https://doi.org/10.56761/EFRE2022.C1-O-039701

2 Куксанов Н.К. Источник высоковольтного питания ускорителя ЭЛВ-15 / Н.К. Куксанов, Д.С. Воробьев, Р.А. Салимов, С.Н. Фадеев // Сиб. физ. журн. — 2022. — 17. — № 1. — С. 23–33.

3 Bryazgin A.A. Industrial Electron Accelerators Developed at the Budker Institute of Nuclear Physics, SB RAS / A.A. Bryazgin, N.K. Kuksanov, R.A. Salimov // Uspekhi Fizicheskikh Nauk, Russian Academy of Sciences. — 2018. — № 61. — C. 601–612. https://doi.org/10.3367/ufne.2018.03.038344

4 Домаров Е.В. Исследование параметров мощного электронного пучка промышленного ускорителя ЭЛВ / Е.В. Домаров, Д.С. Воробьев, М.Г. Голковский // Сиб. физ. журн. — 2019. — 14. — № 2. — С. 5–20. https://doi.org/10.25205/2541-9447-2019-14-2-5-20

5 Golkovsky M.G. Hardening and Cladding by Relativistic Electron Beam Outside of Vacuum / M.G. Golkovsky // LAP LAMBERT Academic Publishing, 2013.

Н.К. Куксанов, Д.С. Воробьев, Е.В. Домаров, Ю.И. Голубенко, А.И. Корчагин, Р.А. Салимов, С.Н. Фадеев, И.К. Чакин, А.В. Семенов, В.Г. Черепков, М.Г. Голковский, А.В. Лаврухин

ЭЛВ үдеткішіне 50 жыл

Мақалада Г.И. Будкер атындағы Ядролық физика институтының ЭЛВ өнеркәсіптік электронды үдеткіштерінің елу жылдық дамуы баяндалады. Негізінен ЭЛВ үдеткіштері полимерлерді радиациялық модификациялау үшін қолданылады (кабельді оқшаулау және т.б.) және жоғары сенімділігімен, пайдаланудың қарапайымдылығымен және әртүрлі өндірістік қажеттіліктерге бейімделуімен танымал. Бұл үдеткіштердің эволюциясы 20 кВт-тың алғашқы модельдерінен 100 кВт-қа дейін жететін заманауи нұсқаларға, тіпті 400 кВт-қа дейінгі бірегей машинаға дейін байқалады. Авторлар радиациялық-химиялық процестердің тиімділігі мен сапасын арттыратын автоматтандырылған жүйелер мен мамандандырылған жабдықтардың интеграциясын талқылайды. Қолдану салалары телекоммуникациядан бастап ядролық энергетикаға дейінгі салалардың кең ауқымын қамтиды, яғни мұнда қатал жағдайларда сенімділік өте маңызды. Экономикалық тоқырау сияқты бұрынғы мәселелерге қарамастан, ЭЛВ үдеткіш өндірісінің өркендеуі жалғасуда, бүкіл әлем бойынша 220-дан астам қондырғы қойылды. Институт болашақ қажеттіліктерді қанағаттандыру үшін осы технологияларды ілгерілетуге бағытталған.

Кілт сөздер: ЭЛВ үдеткіштері, электронды үдеткіштер, өнеркәсіптік үдеткіштер, біріктіру.

Н.К. Куксанов, Д.С. Воробьев, Е.В. Домаров, Ю.И. Голубенко, А.И. Корчагин, Р.А. Салимов, С.Н. Фадеев, И.К. Чакин, А.В. Семенов, В.Г. Черепков, М.Г. Голковский, А.В. Лаврухин

50 лет ускорителям ЭЛВ

В статье освещается пятьдесят лет разработки промышленных ускорителей электронов ЭЛВ в Институте ядерной физики имени Г.И. Будкера. В основном ускорители ЭЛВ используются для радиационной модификации полимеров (кабельная изоляция и пр.), и известны своей высокой надежностью, простотой использования и адаптивностью к различным промышленным потребностям. Эволюция этих ускорителей прослеживается от ранних моделей мощностью 20 кВт до современных версий, достигающих мощности до 100 кВт, и даже уникальной машины мощностью 400 кВт. Авторами обсуждается интеграция автоматизированных систем и специализированного оборудования, которые повышают эффективность и качество радиационно-химических процессов. Области применения включают широкий спектр отраслей промышленности, от телекоммуникаций до ядерной энергетики, где надежность в суровых условиях имеет решающее значение. Несмотря на прошлые проблемы, такие как экономические потрясения, производство ускорителей ELV продолжает процветать, по всему миру поставлено более 220 единиц. Институт сосредоточен на продвижении этих технологий для удовлетворения будущих потребностей.

Ключевые слова: ускорители ЭЛВ, ускорители электронов, промышленные ускорители, сшивка.

References

1 Vorobev, D.S., Domarov, E.V., Kuksanov, N.K., et al. (2022). ELV-15 — New Accelerator for Industrial Applications. *Proceedings of the 8th International Congress on Energy Fluxes and Radiation Effects (EFRE-2022).* https://doi.org/10.56761/EFRE2022.C1-O-039701

2 Kuksanov, N.K., Vorobev, D.S., Salimov, R.A., & Fadeev, S.N. (2022). Istochnik vysokovoltnogo pitaniia uskoritelia ELV-15 [High-Voltage Power Supply for the ELV-15 Accelerator]. *Sibirskii fizicheskii zhurnal — Siberian Journal of Physics, 17*(1), 23–33 [in Russian].

3 Bryazgin, A.A., Kuksanov, N.K., & Salimov, R.A. (2018). Industrial Electron Accelerators Developed at the Budker Institute of Nuclear Physics, SB RAS. *Uspekhi fizicheskikh nauk — Advances in Physical Sciences,* 61, 601–612. Russian Academy of Sciences. https://doi.org/10.3367/ufne.2018.03.038344

4 Domarov, E.V., Vorobev, D.S., & Golkovsky, M.G., et al. (2019). Issledovanie parametrov moshchnogo elektronnogo puchka promyshlennogo uskoritelia ELV [Research of Parameters of the Powerful Electron Beam of Industrial Accelerator ELV]. *Siberian Journal of Physics, 14*(2), 5–20. https://doi.org/10.25205/2541-9447-2019-14-2-5-20 [in Russian].

5 Golkovsky, M.G. (2013). *Hardening and Cladding by Relativistic Electron Beam Outside of Vacuum.* LAP LAMBERT Academic Publishing.

Information about the authors

Nikolay Kuksanov — Doctor of technical sciences, Chief researcher, Budker Institute of Nuclear Physics SB RAS, 11 Academician Lavrentiev Ave., Novosibirsk, 630090, Russian Federation, e-mail: *n.k.kuksanov@inp.nsk.su*

Denis Vorobev — Lead-engineer, Budker Institute of Nuclear Physics SB RAS, 11 Academician Lavrentiev Ave., Novosibirsk, 630090, Russian Federation, e-mail: *d.s.vorobev@inp.nsk.su*; https://orcid.org/0009-0003-8791-7419

Evgeny Domarov — Researcher, Budker Institute of Nuclear Physics SB RAS, 11 Academician Lavrentiev Ave., Novosibirsk, 630090, Russian Federation, e-mail: *domarov88@mail.ru*; https://orcid.org/0000-0003-2422-1513

Yuri Golubenko — Senior researcher, Budker Institute of Nuclear Physics SB RAS, 11 AcademicianLavrentiev Ave., Novosibirsk, 630090, Russian Federation, e-mail: *yu.i.golubenko@inp.nsk.su*

Alexey Korchagin — Candidate of technical sciences, Senior researcher, Budker Institute of Nuclear Physics SB RAS, 11 Academician Lavrentiev Ave., Novosibirsk, 630090, Russian Federation, e-mail: *aikochagin@mail.ru*

Rustam Salimov — Doctor of technical sciences, Chief researcher, Budker Institute of Nuclear Physics SB RAS, 11 Academician Lavrentiev Ave., Novosibirsk, 630090, Russian Federation, e-mail: *rsalimov41@mail.ru*

Sergei Fadeev — Candidate of technical sciences, Head of the Research Laboratory, Budker Institute of Nuclear Physics SB RAS, 11 Academician Lavrentiev Ave., Novosibirsk, 630090, Russian Federation, e-mail: *s.n.fadeev@inp.nsk.su*

Ivan Chakin — Engineer-researcher, Budker Institute of Nuclear Physics SB RAS, 11 AcademicianLavrentiev Ave., Novosibirsk, 630090, Russian Federation, e-mail: *chak_in2003@bk.ru*; https://orcid.org/0000-0003-0529-2017

Alexey Semenov — Research assistant, Budker Institute of Nuclear Physics SB RAS,11 AcademicianLavrentiev Ave., Novosibirsk, 630090, Russian Federation, e-mail: *a.v.semenov@inp.nsk.su*

Viktor Cherepkov — Candidate of technical sciences, Senior researcher, Budker Institute of Nuclear Physics SB RAS, 11 Academician Lavrentiev Ave., Novosibirsk, 630090, Russian Federation, e-mail*: v.g.cherepkov@inp.nsk.su*

Mikhail Golkovsky — Candidate of physical and mathematical sciences, Senior researcher, Budker Institute of Nuclear Physics SB RAS, 11 Academician Lavrentiev Ave., Novosibirsk, 630090, Russian Federation, e-mail: *golkovski@mail.ru*; https://orcid.org/0000-0003-4399-444X

Alexander Lavrukhin — Lead-engineer, Budker Institute of Nuclear Physics SB RAS, 11 AcademicianLavrentiev Ave., Novosibirsk, 630090, Russian Federation, e-mail: *a.v.lav@mail.ru*

Article
https://doi.org/10.31489/2024PH4/74-82
UDC 536.46
Received: 22.05.2024
Accepted: 19.08.2024

K.A. Moldosanov*, V.M. Lelevkin

Kyrgyz-Russian Slavic University, Bishkek, Kyrgyzstan
*(*Corresponding author's e-mail: altair1964@yandex.ru)*

Method for Effective Increasing the Decomposition Rate of Ammonium Perchlorate in Solid Rocket Fuel

Ammonium perchlorate (AP) is a common oxidizer in solid rocket propellants. For devices, the most important parameter of which is the speed of movement, the key correlation is between the jet thrust and the combustion rate of fuels and, consequently, the rate of thermal decomposition of the AP. To increase the decomposition rate of AP, fuel, aluminum powder, is used in the form of nanoparticles. The aim of this work is to identify the decomposition mechanism of AP molecules under conditions where aluminum nanoparticles, in addition to acting as a fuel, also act as catalysts for the decomposition of AP. The result of spraying aluminum nanoparticles into multiple nanoclusters in the fuel combustion zone due to the melting of nanoparticle cores and the destruction of aluminum oxide shells is considered. In this case, aluminum nanoclusters become sources of terahertz (THz) radiation. Since the frequencies of vibrational and rotational oscillations in AP molecules are in the THz range, irradiation of AP molecules with THz photons promotes their decomposition. It is proposed to use emission of THz photons by aluminum nanoclusters, increasing its intensity by introducing 3*d* impurities into aluminum, which increase the density of electron states near the Fermi level of aluminum.

Keywords: aluminum nanoparticle, ammonium perchlorate, catalysis, nanocluster, terahertz.

Introduction

Improving the performance of solid rocket fuel by reducing the particle size scale of the oxidizer, ammonium perchlorate (AP) NH_4ClO_4 [1], and the fuel, dispersed aluminum [2], from the micrometric to the nanometric level has been the subject of research over the last decade. One of the main goals of the research was to find a way to effectively increase the rate of thermal decomposition of AP in fuel in order to increase jet thrust.

Of particular value are studies on the dispersion of aluminum nanoparticles into nanoclusters in the fuel combustion zone [3–6] — as a result of melting of the nanoparticle core, rupture of the oxide shell on them, and splashing of molten aluminum due to high internal pressure in the molten core. Nanoclusters are fragments of molten aluminum nanoparticles several nanometers in size. These works [3–6] suggest that in the fuel combustion zone, in addition to accelerating the decomposition of AP due to the grinding of aluminum nanoparticles (increasing the area of interaction of aluminum with the oxidizer), aluminum nanoclusters become sources of spontaneous terahertz (THz) radiation, which can be used to accelerate the decomposition of AP molecules. Although there is insufficient data on the absorption spectra of AP in the THz range, and the available information is contradictory and fragmentary, it is still known that the frequencies of the lattice vibrations of the NH_4ClO_4 crystal and the rotation of the NH_4^+ ion in the crystal [7–10] lie in the THz range.

Spontaneous emission of THz photons by aluminum nanoclusters

The physical mechanism of THz photon emission by an aluminum nanocluster is illustrated in Figure 1, where a Fermi electron with momentum $\boldsymbol{p}_F$ absorbs a vibrational mode (longitudinal phonon) with momentum $\boldsymbol{q}^*_{vm}$ propagating along the nanocluster diameter D. An excited electron with momentum $\boldsymbol{s}$ moves along a chord H, Figure 1(*a*). In the energy–momentum space, this process is illustrated in Figure 1(*b*), where the paraboloid is the dispersion surface of electrons, and the cone-shaped bells are the dispersion surfaces of longitudinal phonons. Relevant formulas to Figure 1 and numerical values of the parameters: $s = [2m\cdot(E_F + E_{vm})]^{1/2}$; $\gamma = \arccos[(2m\cdot E_{vm} + q^{*2}_{vm})/(2s\cdot q^*_{vm})]$; Fermi energy in Al: $E_F = 11.7$ eV [11; 51]; energy of dominant longitudinal phonons in Al: $E_{vm} \approx 34.8$ meV; magnitude of the momentum of dominant longitudinal phonons in Al: $q^*_{vm} \approx 1.2\ 10^{-19}$ g cm s^{-1}; with these parameters, the angle $\gamma = 71°$.

The excited electron, due to the Coulomb interaction with the positive aluminum ions, could induce a secondary longitudinal phonon with a momentum collinear to the momentum $\boldsymbol{s}$; and this would be a way of relaxation of the excited electron. However, in nanoclusters smaller than the electron mean free path, this mechanism is impossible, and relaxation occurs through photon emission. Other reasons that take into account the confinement of electrons and longitudinal phonons in nanoclusters are the following.

The first reason conditioning the emission is the difference in the quantization steps of momenta of longitudinal phonons propagating along the nanocluster's diameter D and the chord H, equal to h/D and h/H, respectively (here h is Planck's constant). Consequently, the steps of energy quantization for these two directions of phonon propagation also do not coincide. Due to the mismatch of quantized energy levels, the energy transfer from the excited electron to the secondary phonon is impossible (indeed, the Fermi electron received energy from the primary phonon quantized with a certain step, and it cannot generate a secondary phonon, energy of which would be quantized with a different step).

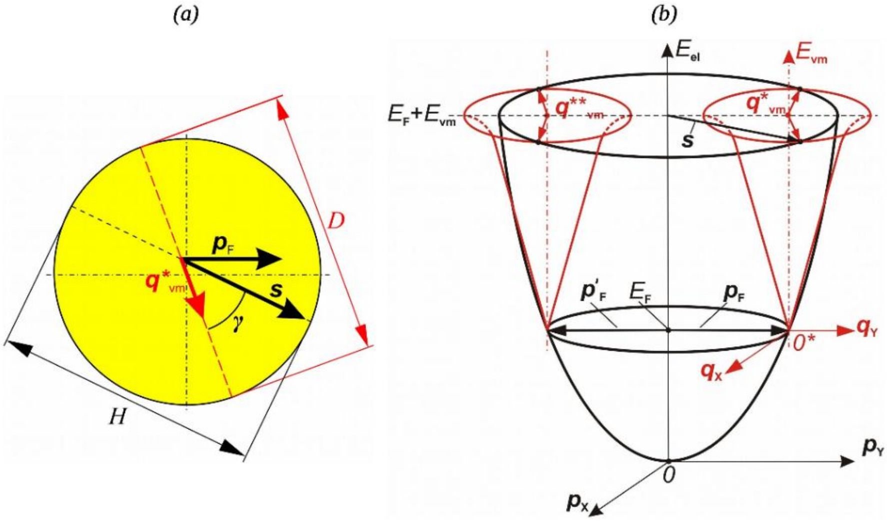

Figure 1. Absorption of a vibrational mode (longitudinal phonon) with momentum $\boldsymbol{q}^*_{\mathrm{vm}}$ by a Fermi electron with momentum $\boldsymbol{p}_{\mathrm{F}}$ in an aluminum nanocluster. The excited electron with momentum $\boldsymbol{s}$ moves along the chord H.

Another reason that excludes the excitation of a secondary phonon and, therefore, favors the emission of a photon is the following. As the nanoparticle diameter decreases, the gap between the energy levels of longitudinal phonons for the direction of propagation along the vector $\boldsymbol{s}$ increases, and eventually a situation may arise where the gap exceeds the full width at half maximum of the peak of the longitudinal phonon energy distribution $\mathrm{FWHM_L}$. Figure 2 shows the threshold state at which the energy step of vibration modes in a nanocluster $\Delta E_{\mathrm{vm}H}$, propagating along the chord H with momentum $\boldsymbol{s}$, exceeds the value of $\mathrm{FWHM_L}$. As a result, the energy level of the excited electron "hangs" between the levels of longitudinal phonons for the $\boldsymbol{s}$ direction: there are no levels to which the electron could transfer its energy. Consequently, the electron will relax, scattering at the boundary of the nanocluster, with the emission of a photon (the electron cannot leave the nanoparticle, since its energy is less than the work function of the electron in aluminum, ≈4.25 eV [11; 364]).

For the direction "along the chord H", the quantization steps of vibrational modes in momentum and energy are equal, respectively, to h/H and $\Delta E_{\mathrm{vm}H} \approx v^*_{\mathrm{L}} \cdot (h/H)$, where v^*_{L} is the propagation velocity of longitudinal phonons with energies within the FWHML region. The value of the velocity v^*_{L} is less than the nominal speed of sound in aluminum $v_{\mathrm{L}} = 6.5\ 10^5$ cm s^{-1} due to the curvature of the dispersion curve of longitudinal phonons near the boundary of the Brillouin zone, where the energies of longitudinal phonons corresponding to the $\mathrm{FWHM_L}$ are located.

Obviously, the gap between energy levels must take into account the consequence of Heisenberg's uncertainty principle. As a criterion for "complete divergence" of phonon levels, a situation was chosen in which two adjacent energy levels moved apart by an amount exceeding the $\mathrm{FWHM_L}$, taking into account the uncertainty in the energy of the levels. Such a threshold situation is shown in Figure 2, where the value of $\delta E_{\mathrm{vm}H}$ is calculated taking into account the Heisenberg uncertainty relation for the phonon momentum and coordinate, $\delta E_{\mathrm{vm}H} \geq v^*_{\mathrm{L}} \cdot h/(2\pi H)$. The inequality that determines the corresponding threshold chord length (such that at shorter chord lengths intense photon emission occurs) is as follows:

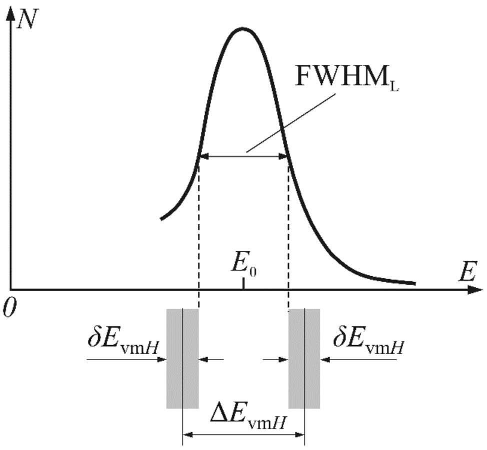

Figure 2. The threshold state at which the energy step of vibrational modes in a nanocluster ΔE_{vmH}, propagating along the chord H with momentum $\boldsymbol{s}$, exceeds the FWHM$_L$ value for the energy distribution of longitudinal phonons in an aluminum nanocluster.

$$\Delta E_{vmH} > \mathrm{FWHM_L} + (\delta E_{vmH}/2) + (\delta E_{vmH}/2) \geq \mathrm{FWHM_L} + v^*_L \cdot h/(2\pi H) \qquad (1)$$

Substituting the value $\Delta E_{vmH} \approx v^*_L \cdot (h/H)$ into the left-hand side of inequality (1), we obtain:

$$v^*_L \cdot (h/H) > \mathrm{FWHM_L} + v^*_L \cdot (h/2\pi H)$$

$$\text{or } H < [1 - \cdot (1/2\pi)] \cdot v^*_L \cdot (h/\mathrm{FWHM_L}). \qquad (2)$$

If this inequality is satisfied, excited electrons will not be able to relax with the excitation of secondary phonons — they will emit photons. In this case, the energies of the emitted photons will correspond to the THz range, since the energies of the dominant primary phonons belong to the THz energy region: in aluminum, the FWHM$_L$ region of the longitudinal phonon energy distribution lies in the band ≈31–38 meV [12], that is, in the frequency range ≈7.5–9 THz.

It should be noted that so-called two-phonon processes can take place: an excited electron, if it cannot excite a secondary phonon with an energy exactly equal to the energy acquired E_1 from the primary phonon, can excite a secondary phonon of lower energy E_2, and transfer the difference in the energies of the primary and secondary phonons $\Delta E = E_1 — E_2$ to the electron [13]. And the electron will not be able to relax with the excitation of the phonon and emits a photon. Then the region of frequencies generated by the nanocluster will expand and, possibly, cover a sufficient part of the phonon spectrum in the AP molecule.

Substituting the numerical values of the quantities ($v^*_L \approx 4{,}7 \cdot 10^5$ cm s^{-1}; FWHM$_L$ ≈7.9 meV) into inequality (2), we obtain an estimate of the chord lengths for which the vibration mode levels diverge by an energy gap $\Delta E_{vmH} > \mathrm{FWHM_L}$: $H < 2.1$ nm.

Let the "threshold" chord of length $H_0 = 2.1$ nm be the chord of minimum length of all chords that form an angle of $\gamma = 71°$ with the nanocluster diameter; it contacts the nanocluster diameter on its surface. Then the "threshold" diameter of the nanocluster $D_0 = H_0/\cos\gamma = 6.45$ nm. Aluminum nanoclusters are smaller than D_0 will be the most intense sources of THz photons.

Let $\Delta E_D \approx v^*_L \cdot (h/D)$ be the energy step for longitudinal phonons traveling along the diameter of the nanocluster. The greater the stacking multiplicity of the energy step ΔE_D within the FWHM$_L$ width (for example, with an increase in the nanocluster diameter D), that is, the greater the value of (FWHM$_L$/ΔE_D), the higher the probability of superposition of the energy level extended to δE_{vmH} on the energy level of the primary phonon, which will lead to relaxation of the excited electron with the generation of a secondary phonon (with the energy of the primary phonon). And the lower the intensity of spontaneous emission of photons, and the lower the catalytic activity of the nanocluster.

Method for increasing the intensity of THz photon emission by aluminum nanoclusters

Spontaneous emission of THz photons by aluminum nanoclusters can be used to accelerate the decomposition of AP molecules. To do this, it is necessary to use nanoparticles of aluminum containing impurity atoms of the so-called 3*d*-metals, elements of the 4th row of the Periodic Table: V, Cr, Mn. In such systems, the energies of the electron *d*-levels of impurity atoms are located near the Fermi level of aluminum, due to which the density of states of Fermi electrons increases significantly. The use of nanoparticles from the Al-

V, Al-Cr and Al-Mn systems would make it possible to obtain in the nanoclusters of these systems increased numbers of electrons participating in the processes of absorption of longitudinal phonons and emission of THz photons, due to which it would be possible to increase the intensity of irradiation of AP molecules with THz radiation and accelerate their decomposition.

Figure 3 shows a summary picture of the density of states of electrons in aluminum with impurities of 3*d* elements (based on the results of works [14–19]). The energy axis shows the position of the Fermi level E_F for the intermetallic compound FeAl.

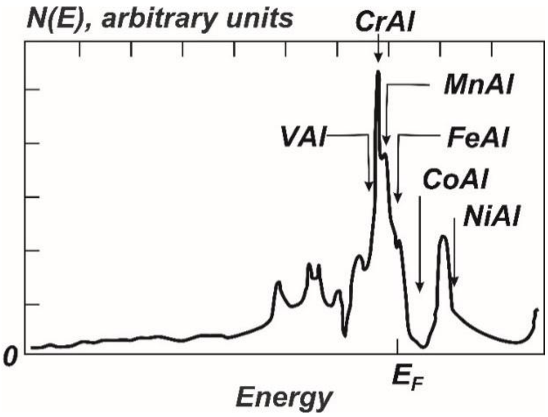

Figure 3. Summary picture of the locations of Fermi levels (indicated by arrows) in intermetallic compounds of Al and 3*d* metals on the distribution of the electron density of states by energy (based on the results of works [14–19]).

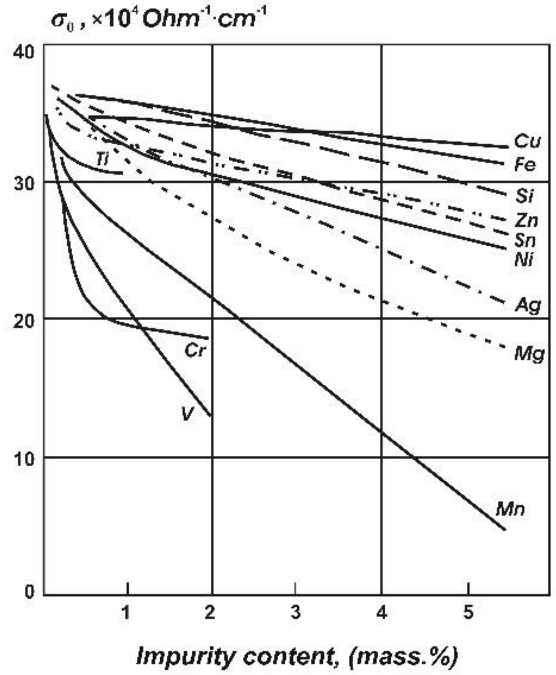

Figure 4. Change in the direct current specific electrical conductivity of Al when impurities are introduced into it [20].

The feasibility of the proposed approach is confirmed by data on the behavior of the specific electrical conductivity of aluminum when introducing even a small amount of impurities of V, Cr and Mn (~ 1–4 mass.%) [20] (Fig. 4).

From Figure 4 it is evident that with impurities of ~1 mass.% V or Cr the conductivity of Al decreases by approximately 2 times; this means that the mean free path of electrons l_{mfp} also decreases by 2 times. For bulk aluminum, $l_{mfp} \approx 18.9$ nm [21]. This means that for aluminum with 1 mass% V or Cr, the electron mean free path is $l_{mfp} \approx 9.45$ nm. Approximately the same length $l_{mfp} \approx 9$ nm will be for aluminum with

2 mass.% Mn. Therefore, if the size of aluminum nanoclusters-splashes containing such concentrations of impurity atoms of V, Cr or Mn is less than 9 nm, then they will emit THz photons and become catalysts for the decomposition of AP molecules. A rough estimate of the size of aluminum nanoclusters-splashes obtained as a result of dispersion of melts of 20–120 nm nanoparticles is known [3, 4]: 5–10 nm. Aluminum 5–10 nm nanoclusters with an unoxidized surface are already produced in the form of polymer nanocomposites (the binder is hydroxyl-terminated polybutadiene (HTPB) containing aluminum nanoclusters grown *in situ*) and demonstrate a high combustion rate, more than five times higher than that of conventional ALEX aluminum nanopowders [22].

The concept of *in situ* nanocluster formation in polymer nanocomposites [23], in principle, also includes the idea of obtaining nanoclusters-splashes of molten aluminum *in situ* — in the combustion zone, in already burning fuel, with fuel from a mixture of a polymer binder and aluminum nanoparticles, and an oxidizer, AP.

Unfortunately, we were unable to find data on the absorption of HTPB in the THz frequency range.

One of the possible ways to further increase the intensity of spontaneous emission of THz photons by nanoclusters is the use of *f*-element impurity atoms in aluminum instead of 3*d* impurities. So-called electron systems with “heavy fermions” are known [24, 25], characterized by a very high density of states of *f*-electrons near the Fermi level — more significant than in the case of using 3*d*-element impurities, for example, the compound $CeAl_3$. It seems appropriate to conduct studies of the decomposition rate of ammonium perchlorate using dispersed aluminum in the form of a mixture of nanoparticles of ordinary aluminum and $CeAl_3$ nanoparticles with a variation in the composition of the mixture.

Discussion

How to implement the approach using aluminum nanoparticles with 3*d* metal impurities? There are industrially produced aluminum alloys with an impurity element Mn (“alloying component”), of which the AMц1 alloy (Table), containing a sufficient amount of manganese, appears to be a promising alloy. This alloy could become a raw material for the production of nanoparticles.

Table 1

Composition of industrial aluminum alloys

lloy brand	Alloying components, mass%			
	Al	Cu	Mg	Mn
AMts [20]	Base of the alloy	–	–	1.0–1.6
AMts1 [26]	Same	?	?	2.0–4.5
MM [20]	Same	–	0.2–0.5	1.0–1.4
AMg6 [20]	Same	–	5.8–6.8	0.5–0.8
D16 [20]	Same	3.8–4.9	1.2–1.8	0.3–0.9

From Table 2 [26] it can be seen that, compared to other 3*d* metals, the solubility of Mn in Al is increased. Nanoparticles of aluminum intermetallic compounds could be produced from alloys obtained by the method of self-propagating high-temperature synthesis of aluminides [27–30] or by the method of exploding wires from the AMts1 alloy — this method of industrial production of metal nanopowders has been mastered [31].

Conclusions

Recently, the concept of forming nanoparticles *in situ* — directly in the matrix or binder — has been developed in the development of polymer composites. It has also found application in the production of polymer fuel in the form of 5–10 nm aluminum nanoclusters grown *in situ* in a polymer binder, hydroxyl-terminated polybutadiene (HTPB).

In this paper, it is proposed to develop this concept to obtain nanoclusters-splashes of molten aluminum containing impurity atoms of V, Cr or Mn, *in situ* — in **burning** fuel, with a fuel consisting of a polymer binder (hydroxyl-terminated polybutadiene) and 100–120 nm nanoparticles of Al-V, Al-Cr or Al-Mn intermetallic compounds, and an oxidizer (ammonium perchlorate).

Table 2

Maximum solubility of a number of 3*d* metals in aluminum [27]

System	Maximum solubility, mass.%	
	Equilibrium solubility	Nonequilibrium solubility
Al-Ti	0.24	0.35
Al-Cr	0.77	5.7
Al-Mn	1.82	10.2
Al-Fe	0.052	0.2

It has been shown that nanoclusters of aluminum containing impurity atoms of V, Cr or Mn, smaller than 9 nm in size, can become sources of terahertz radiation and contribute to the acceleration of the decomposition of ammonium perchlorate molecules in solid rocket fuel. This should result in increased jet thrust.

A promising development is the study of the decomposition rate of ammonium perchlorate using dispersed aluminum in the form of a mixture of nanoparticles of ordinary aluminum and nanoparticles of $CeAl_3$– with a variation in the composition of the mixture.

References

1 Abdelhafiz M. Self-catalyzed nanoscale ammonium perchlorate for advanced composite solid rocket propellant / M. Abdelhafiz, M. Yehia, H.E. Mostafa and T. Wafy // Nano Express. — 2021. — Vol. 2. — P. 030008. DOI: 10.1088/2632-959X/ac2568.

2 Zhu Y. -L. Effects of aluminum nanoparticles on thermal decomposition of ammonium perchlorate / Y. -L. Zhu, H. Huang, H. Ren, Q. -J. Jiao // Journal of the Korean Chemical Society. — 2013. — Vol. 57. — P. 109–114. DOI: 10.5012/jkcs.2013.57.1.109.

3 Levitas V.I. Mechanochemical mechanism for reaction of aluminium nano- and micrometre-scale particles / V.I. Levitas // Phil. Trans. R. Soc. A. — 2013. — Vol. 371. — P. 20120215. DOI:10.1098/rsta.2012.0215.

4 Levitas V.I. Burn time of aluminum nanoparticles: strong effect of the heating rate and melt-dispersion mechanism / V.I. Levitas // Combustion and Flame. — 2009. — Vol. 156, No. 2. — P. 543–546.DOI: 10.1016/j.combustflame.2008.11.006.

5 Watson K.W. Fast reactions with nano- and micrometer aluminum: A study on oxidation versus fluorination / K.W. Watson, M.L. Pantoya, V.I. Levitas // Combustion and Flame. — 2008. — Vol. 155, No. 4. — P. 619–634. DOI: 10.1016/j.combustflame.2008.06.003.

6 Levitas V.I. Mechanochemical mechanism for fast reaction of metastable intermolecular composites based on dispersion of liquid metal / V.I. Levitas, B.W. Asay, S.F. Son, M. Pantoya // Journal of Applied Physics. — 2007. — Vol. 101. — P. 083524. DOI: 10.1063/1.2720182.

7 Wu Q. Comparative DFT and DFT-D studies on structural, electronic, vibrational and absorption properties of crystalline ammonium perchlorate / Q. Wu, C. Li, L. Tan, Z. Hang, W. Zhu // RSC Advances. — 2016. — Vol. 6, No. 54. — P. 48489–48497. DOI: 10.1039/c6ra09743j.

8 Zhu W. Comparative DFT study of crystalline ammonium perchlorate and ammonium dinitramide / W. Zhu, T. Wei, W. Zhu, H. Xiao // The Journal of Physical Chemistry A. — 2008. — Vol. 112, No. 20. — P. 4688–4693. DOI: 10.1021/jp800693e.

9 Janik J.A. Quasi-free rotation of the ammonium ion in crystalline NH_4ClO_4 / J.A. Janik, J.M. Janik, J. Mayer // Physica Status Solidi B. — 1971. — Vol. 44, No. 1. — P. 437–441. DOI: 10.1002/pssb.2220440144.

10 Hennel J.W. Proton spin relaxation and phonons in ammonium salts / J.W. Hennel, Z.T. Lalowicz // J. Phys. C: Solid State Phys. — 1978. — Vol. 11. — P. L707–L711. DOI: 10.1088/0022-3719/11/16/006.

11 Ашкрофт Н. Физика твердого тела / Н. Ашкрофт, Н. Мермин. — Т. 1. — М.: Мир, 1979. — 400 с.

12 Kresch M. Phonons in aluminum at high temperatures studied by inelastic neutron scattering / M. Kresch, M. Lucas, O. Delaire, J.Y.Y. Lin, B. Fultz // Phys. Rev. B. — 2008. — Vol. 77. — P. 024301. DOI: 10.1103/PhysRevB.77.024301.

13 Postnikov A.V. Suggested design of gold-nanoobjects-based terahertz radiation source for biomedical research / A.V. Postnikov, K.A. Moldosanov // Nanotechnology. — 2018. — Vol. 29, No. 28. — P. 285704. DOI: 10.1088/1361-6528/aabf10.

14 Nieminen R.M. 3*d* impurities in Al: density functional results / R.M. Nieminen, M. Puska // Journal of Physics F: Metal Physics. — 1980. — Vol. 10, No. 5. — P. L123–L127. DOI: 10.1088/0305-4608/10/5/001.

15 Deutz J. Local density of states of impurities in Al / J. Deutz, P.H. Dederichs, R. Zeller // Journal of Physics F: Metal Physics. — 1981. — Vol.11, No. 9. — P. 1787–1800. DOI: 10.1088/0305-4608/11/9/008.

16 Müller C. Local partial DOS and experimental Al K spectra of transition metal aluminides. Charge transfer trend / C. Müller, W. Blau, P. Ziesche // Phys. Stat. Sol. (b). — 1983. — Vol. 116, No. 2. — P. 561–573. DOI: 10.1002/pssb.2221160218.

17 Morinaga M. Alloying effect on the electronic structure of aluminium / M. Morinaga, S. Nasu, H. Adachi, J. Saito, N. Yukawa // Journal of Physics: Condensed Matter. — 1991. — Vol. 3, No. 35. — P. 6817–6828. DOI: 10.1088/0953-8984/3/35/011.

18 Singh P.P. First-principles calculations of the electronic properties of 3*d* transition-metal impurities in Al / P.P. Singh // Journal of Physics: Condensed Matter. — 1991. — Vol. 3, No. 19. — P. 3285–3300. DOI: 10.1088/0953-8984/3/19/007.

19 Singh P.P. Self-consistent electronic structure of 3*d*-transition-metal impurities in aluminum using the recursion method / P.P. Singh // Phys. Rev. B. — 1991. — Vol. 43, No. 5. — P. 3975–3985. DOI: 10.1103/physrevb.43.3975.

20 Смирягин А.П. Промышленные цветные металлы и сплавы: справоч. / А.П. Смирягин, Н.А. Смирягина, А.В. Белова. — М.: Металлургия, 1974. — 488 с.

21 Gall D. Electron mean free path in elemental metals / D. Gall // Journal of Applied Physics. — 2016. — Vol. 119, No. 8. — P. 085101. DOI: 10.1063/1.4942216.

22 Fisher M. *In situ* manufacturing of polymer nanocomposites for energetic applications / M. Fisher // DSIAC Journal. — 2017. — Vol. 4, No. 1. — P. 4–10. https://dsiac.org/articles/in-situ-manufacturing-of-polymer-nanocomposites-for-energetic-applications/ (accessed 11 September 2024).

23 Kelarakis A. In situ generation of nanoparticles on and within polymeric materials / A. Kelarakis // Polymers. — 2024. — Vol. 16. — P. 1611. DOI: 10.3390/polym16111611.

24 Хомский Д.И. Редкоземельные соединения с промежуточной валентностью: спектроскопические исследования / Д.И. Хомский // Спектроскопия кристаллов: моногр. / отв. ред. А.А. Каплянский. — Л.: Наука, 1985. — С. 118–149.

25 Хомский Д.И. Необычные электроны в кристаллах (Промежуточная валентность и тяжелые фермионы) / Д.И. Хомский. — М.: Знание, 1987. — 64 с.

26 Авиационные материалы: справоч. в девяти томах. — Т.4. Алюминиевые и бериллиевые сплавы. Ч. I. Деформируемые алюминиевые сплавы и сплавы на основе бериллия. Кн. 1. ВИАМ; ОНТИ. — М., 1982. — С. 36.

27 Варич Н.И. Влияние третьего компонента на состояние твердого раствора в системе Al–Cr, полученного при больших скоростях охлаждения / Н.И. Варич, Л.М. Буров, К.Е. Колесниченко // Изв. вузов. Сер. Цветная металлургия. — 1967. — Вып. 3. — С. 111–114.

28 Итин В.И. Высокотемпературный синтез интерметаллических соединений / В.И. Итин, Ю.С. Найбороденко. — Томск: Изд-во Том. ун-та, 1989. — 214 с.

29 Подергин В.А. Синтез алюминидов некоторых переходных металлов / В.А. Подергин, В.А. Неронов, В.Д. Яровой, М.Д. Маланов // Процессы горения в химической технологии и металлургии: моногр. / под ред. А.Г. Мержанова. — Черноголовка, 1975. — С. 118–127.

30 Письменская Е.Б. Высокотемпературный синтез интерметаллических соединений в режиме динамического теплового взрыва: автореф. дис. ... канд. физ.-мат. наук. Спец. 01.04.17 — «Химическая физика, в том числе физика горения и взрыва» / Е.Б. Письменская. — Черноголовка, 2000. — 24 с.

31 Company ADVANCED POWDER TECHNOLOGIES LLC (APT). — [Electronic resource]. — Access mode: http://www.nanosized-powders.com/ (accessed 11 September 2024).

К.А. Молдосанов, В.М. Лелевкин

Қатты ракета отынында аммоний перхлоратының ыдырау жылдамдығын тиімді арттыру әдісі

Аммоний перхлораты (АП) қатты зымыран отындарында кең таралған тотықтырғыш. Ең маңызды параметрі қозғалыс жылдамдығы болып табылатын құрылғылар үшін негізгі корреляция ағынның күші мен жанармайдың жану жылдамдығы, демек, АП термиялық ыдырау жылдамдығы арасында болады. АП ыдырау жылдамдығын арттыру үшін отын, алюминий ұнтағы, нанобөлшек түрінде қолданылады. Жұмыстың мақсаты алюминий нанобөлшектері отын ретінде әрекет етумен қатар, АП ыдырауының катализаторы ретінде де әрекет ететін жағдайларда АП молекулаларының ыдырау механизмін анықтау. Алюминий нанобөлшектерін нанобөлшектердің өзектерінің балқуына және алюминий оксидінің қабықшаларының бұзылуына байланысты жанармай жану аймағындағы көптеген нанокластерлерге шашырату нәтижесі қарастырылады. Бұл жағдайда алюминий нанокластерлері терагерц (ТГц) сәулелену көздеріне айналады. АП молекулаларындағы тербеліс және айналу тербелістерінің жиіліктері ТГц диапазонында болғандықтан, ТГц фотондарымен АП молекулаларының сәулеленуі олардың ыдырауына ықпал етеді. Алюминийдің Ферми деңгейіне жақын электрон күйлерінің тығыздығын арттыратын алюминийге 3*d*-қоспаларды енгізу арқылы оның қарқындылығын арттыра отырып, алюминий нанокластерлерінің ТГц фотондарының эмиссиясын пайдалану ұсынылады.

Кілт сөздер: алюминий нанобөлшегі, аммоний перхлораты, катализ, нанокластер, терагерц.

К.А. Молдосанов, В.М. Лелевкин

Способ эффективного повышения скорости разложения перхлората аммония в твердом ракетном топливе

Перхлорат аммония (ПХА) — распространенный окислитель в твердых ракетных топливах. Для устройств, важнейшей характеристикой которых является скорость движения, ключевая корреляция — между реактивной тягой и скоростью горения топлив и, следовательно, скоростью термического разложения ПХА. Для повышения скорости разложения ПХА, горючее, порошок алюминия, применяют в виде наночастиц. Цель этой работы — выявление механизма разложения молекул ПХА в условиях, когда наночастицы алюминия, помимо выполнения роли горючего, являются и катализаторами разложения ПХА. Рассматривается результат распыления наночастиц алюминия на множество нанокластеров в зоне горения топлива из-за плавления ядер наночастиц и разрушения оболочек оксида алюминия. При этом нанокластеры алюминия становятся источниками спонтанного терагерцевого (ТГц) излучения. Поскольку частоты колебательных и вращательных осцилляций в молекулах ПХА находятся в ТГц диапазоне, облучение молекул ПХА ТГц фотонами способствует их разложению, так как вынужденные осцилляции молекул ослабляют внутримолекулярные связи. Авторами предложено использовать спонтанную эмиссию ТГц фотонов нанокластерами алюминия, повысив её интенсивность путём внедрения в алюминий 3*d*-примесей, повышающих плотность состояний электронов вблизи уровня Ферми алюминия.

Ключевые слова: катализ, нанокластер, наночастица алюминия, перхлорат аммония, терагерц.

References

1 Abdelhafiz, M., Yehia, M., Mostafa, H.E., & Wafy, T. (2021). Self-catalyzed nanoscale ammonium perchlorate for advanced composite solid rocket propellant. *Nano Express, 2,* 030008. DOI: 10.1088/2632-959X/ac2568.

2 Zhu, Y. -L., Huang, H., Ren, H., & Jiao, Q.-J. (2013). Effects of aluminum nanoparticles on thermal decomposition of ammonium perchlorate. *Journal of the Korean Chemical Society, 57,* 109–114. DOI: 10.5012/jkcs.2013.57.1.109.

3 Levitas, V.I. (2013). Mechanochemical mechanism for reaction of aluminium nano- and micrometre-scale particles. *Phil. Trans. R. Soc. A, 371,* 20120215. DOI:10.1098/rsta.2012.0215.

4 Levitas, V.I. (2009). Burn time of aluminum nanoparticles: strong effect of the heating rate and melt-dispersion mechanism. *Combustion and Flame, 156*(2), 543–546. DOI:10.1016/j.combustflame.2008.11.006.

5 Watson, K.W., Pantoya, M.L., & Levitas, V.I. (2008). Fast reactions with nano- and micrometer aluminum: A study on oxidation versus fluorination. *Combustion and Flame, 155*(4), 619–634. DOI:10.1016/j.combustflame.2008.06.003.

6 Levitas, V.I., Asay, B.W., Son, S.F., & Pantoya, M. (2007). Mechanochemical mechanism for fast reaction of metastable intermolecular composites based on dispersion of liquid metal. *Journal of Applied Physics, 101,* 083524.DOI: 10.1063/1.2720182.

7 Wu, Q., Li, C., Tan, L., Hang, Z., & Zhu, W. (2016). Comparative DFT and DFT-D studies on structural, electronic, vibrational and absorption properties of crystalline ammonium perchlorate. *RSC Advances, 6*(54), 48489–48497. DOI: 10.1039/c6ra09743j.

8 Zhu, W., Wie, T., Zhu, W., & Xiao, H. (2008). Comparative DFT study of crystalline ammonium perchlorate and ammonium dinitramide. *The Journal of Physical Chemistry A, 112*(20), 4688–4693. DOI: 10.1021/jp800693e.

9 Janik, J.A., Janik, J.M., & Mayer, J. (1971). Quasi-free rotation of the ammonium ion in crystalline NH_4ClO_4. *Physica Status Solidi B, 44*(1), 437–441. DOI: 10.1002/pssb.2220440144.

10 Hennel, J.W., & Lalowicz, Z.T. (1978). Proton spin relaxation and phonons in ammonium salts. *J. Phys. C: Solid State Phys., 11,* L707–L711.DOI: 10.1088/0022-3719/11/16/006.

11 Ashcroft, N., & Mermin, N. (1979). *Fizika tverdogo tela* [*Solid State Physics]*. Moscow: Mir [in Russian].

12 Kresch, M., Lucas, M., Delaire, O., Lin, J.Y.Y., & Fultz, B. (2008). Phonons in aluminum at high temperatures studied by inelastic neutron scattering. *Phys. Rev. B., 77,* 024301. DOI: 10.1103/PhysRevB.77.024301.

13 Postnikov, A.V., & Moldosanov, K.A. (2018). Suggested design of gold-nanoobjects-based terahertz radiation source for biomedical research. *Nanotechnology, 29*(28), 285704. DOI: 10.1088/1361-6528/aabf10.

14 Nieminen, R.M. & Puska, M. (1980). 3*d* impurities in Al: density functional results. *Journal of Physics F: Metal Physics, 10*(5), L123–L127. DOI:10.1088/0305-4608/10/5/001.

15 Deutz, J., Dederichs, P.H., & Zeller, R. (1981). Local density of states of impurities in Al. *Journal of Physics F: Metal Physics, 11*(9), 1787–1800. DOI:10.1088/0305-4608/11/9/008.

16 Müller, C., Blau, W., & Ziesche, P. (1983). Local partial DOS and experimental Al K spectra of transition metal aluminides. Charge transfer trend. *Phys. Stat. Sol. (b),* 116(2), 561–573. DOI:10.1002/pssb.2221160218.

17 Morinaga, M., Nasu, S., Adachi, H., Saito, J., & Yukawa, N. (1991). Alloying effect on the electronic structure of aluminium. *Journal of Physics: Condensed Matter, 3*(35), 6817–6828. DOI:10.1088/0953-8984/3/35/011.

18 Singh, P.P. (1991). First-principles calculations of the electronic properties of 3*d* transition-metal impurities in Al. *Journal of Physics: Condensed Matter, 3*(19), 3285–3300. DOI:10.1088/0953-8984/3/19/007.

19 Singh, P.P. (1991). Self-consistent electronic structure of 3*d*-transition-metal impurities in aluminum using the recursion method. *Phys. Rev. B, 43*(5), 3975–3985. DOI:10.1103/physrevb.43.3975.

20 Smiryagin, A.P., Smiryagina, N.A., & Belova, A.V. (1974). *Promyshlennye tsvetnye metally i splavy. Spravochnik [Industrial Non-Ferrous Metals and Alloys. Handbook]*. Moscow: Metallurgiia [in Russian].

21 Gall, D. (2016). Electron mean free path in elemental metals. *Journal of Applied Physics, 119*(8), 085101. DOI:10.1063/1.4942216.

22 Fisher, M. (2017). *In situ* manufacturing of polymer nanocomposites for energetic applications. *DSIAC Journal, 4*(1), 4–10. https://dsiac.org/articles/in-situ-manufacturing-of-polymer-nanocomposites-for-energetic-applications/ (accessed 11 September 2024).

23 Kelarakis, A. (2024). In situ generation of nanoparticles on and within polymeric materials. Polymers, 16, 1611. DOI: 10.3390/polym16111611**.**

24 Khomsky, D.I. (1985). Redkozemelnye soedineniia s promezhutochnoi valentnostiu: spektroskopicheskie issledovaniia [Rare earth compounds with intermediate valence: spectroscopic studies]. *Spektroskopiia kristallov — Crystal spectroscopy.* A.A. Kaplyansky (Ed.). Leningrad: Nauka [in Russian].

25 Khomsky, D.I. (1987). *Neobychnye elektrony v kristallakh. (Promezhutochnaia valentnost i tiazhelye fermiony) [Unusual Electrons in Crystals (Intermediate Valence and Heavy Fermions)]*. Moscow: Znanie [in Russian].

26 (1982). Aviatsionnye materialy. Spravochnik v deviati tomakh. Tom 4. Aliuminievye i berillievye splavy. Chast I. Deformiruemye aliuminievye splavy i splavy na osnove berilliia. Kniga 1 [Aviation materials. Handbook in nine volumes. Vol. 4, Aluminium and Beryllium Alloys. Part I, Wrought Aluminium and Beryllium Base Alloys, Book 1]. VIAM; ONTI. Moscow [in Russian].

27 Varich, N.I., Burov, L.M., & Kolesnichenko, K.Ye. (1967). Vliianie tretego komponenta na sostoianie tverdogo rastvora v sisteme Al–Cr, poluchennogo pri bolshikh skorostiakh okhlazhdeniia [The influence of the third component on the state of the solid solution in the Al–Cr system obtained at high cooling rates]. *Izvestiia vuzov. Seriia Tsvetnaia metallurgiia — News. Non-Ferrous Metallurgy, 3,* 111–114 [in Russian].

28 Itin, V.I., & Naiborodenko, Yu.S. (1989). *Vysokotemperaturnyi sintez intermetallicheskikh soedinenii [High-temperature synthesis of intermetallic compounds].* Tomsk: Izdatelstvo Tomskogo universiteta [in Russian].

29 Podergin, V.A., Neronov, V.A., Yarovoy, V.D., & Malanov, M.D. (1975). Sintez aliuminidov nekotorykh perekhodnykh metallov [Synthesis of aluminides of some transition metals]. *Combustion processes in chemical engineering and metallurgy.* A.G. Merzhanov (Ed.). Chernogolovka [in Russian].

30 Pismenskaya, E.B. (2000). Vysokotemperaturnyi sintez intermetallicheskikh soedinenii v rezhime dinamicheskogo teplovogo vzryva [High-temperature synthesis of intermetallic compounds in the dynamic thermal explosion mode]. *Extended abstract of candidate's thesis*. Chernogolovka [in Russian].

31 Company ADVANCED POWDER TECHNOLOGIES LLC (APT). Retrieved from http://www.nanosized-powders.com/ (accessed 11 September 2024).

Information about the authors

Kamil Moldosanov (corresponding author) — Leading engineer, Kyrgyz-Russian Slavic University named after B.N. Yeltsin, Kiyevskaya street, 44, 720000, Bishkek, Kyrgyzstan; *e-mail: altair1964@yandex.ru*

Valery Lelevkin — Doctor of physical and mathematical sciences, Professor, Kyrgyz-Russian Slavic University named after B.N. Yeltsin, Kiyevskaya street, 44, 720000, Bishkek, Kyrgyzstan; *e-mail: lelevkin44@mail.ru*

Article
https://doi.org/10.31489/2024PH4/83-91
UDC 535.377+544.541

Received: 15.05.2024
Accepted: 22.08.2024

S.V. Nikiforov[1*], D.V. Ananchenko[1], T.V. Shtang[1], A.F. Nikiforov[1],
V.M. Lisitsyn[2], M.G. Golkovski[3]

[1]*Ural Federal University, Yekaterinburg, Russia*
[2]*National Research Tomsk Polytechnic University, Tomsk, Russia*
[3]*Budker Institute of Nuclear Physics, SB RAS, Novosibirsk, Russia*
*(*Corresponding author's e-mail: s.v.nikiforov@urfu.ru)*

Synthesis, luminescent and dosimetric properties of ultrafine oxide ceramics for high-dose dosimetry of ionizing radiation

Thermoluminescent and dosimetric properties of ultrafine alumina and zirconia ceramics exposed to high-dose pulsed electron beam (130 keV, 1.5 kGy per one pulse) were studied. To synthesize ceramics with different sizes of crystallites, the authors sintered nanopowder compacts in air in an electric furnace at T=700-1700 °C, and exposed them to high-energy electrons (1.4 MeV) with high power density. It was found that ceramics annealing at T>1000 °C greatly increases crystallite sizes, which correlates with a significant growth of intensity of thermoluminescent peaks. Maximum thermoluminescent response is present in the ceramics that were obtained with an electron-beam method. This is due to formation of radiation-induced trapping and luminescence centers during synthesis. Analysis of dose dependences of thermoluminescence of the irradiated α-Al_2O_3 и ZrO_2 ceramics showed that these dependences are predominantly sublinear. Unlike their single-crystalline modifications, alumina-based ceramics have anomalous fading, which value increases as crystallites grow in size. The presence of the intensive isolated peak of thermoluminescence and sublinear character of the majority of dose dependences prove usability of the oxide ceramics synthesized in this work for measuring high doses of pulsed electron beams (unities-tens of kGy). Alumina-based ceramics require correction of thermoluminescent response by a fading value.

Keywords: aluminum oxide, zirconium oxide, ultrafine ceramics, thermoluminescence, electron-beam synthesis, crystallite size, dose characteristics, fading.

Introduction

Phosphors based on wide-gap oxide dielectrics (Al_2O_3, MgO, BeO, ZrO_2, etc.) have found applications in different fields of science and engineering. Many of them are used in micro-, nano-, and opto-electronic devices [1–3], in measuring devices for different physical quantities, for instance in scintillators and luminescent dosimeters [4, 5]. Nanostructured modifications of oxide materials, e.g. ultrafine ceramics with 50–500 nm nanoparticles, are a separate class of oxide materials.

Nanostructured phosphors have a number of characteristics which make mechanisms of formation of their luminescent properties under radiation significantly different from those of single-crystalline materials. Due to efficient annihilation of radiation defects on the boundaries of nanoparticles, nanomaterials are more radiation-resistant than the current bulk analogs [6] and retain their characteristics when exposed to intensive radiation. They can be used as dielectric integrated-circuit substrates which are employed at NPPs and in space, and as vacuum windows, lenses, mirrors for plasma diagnostics in fusion energy. Nanostructured ceramics are promising materials for high-dose (over 10 Gy) dosimetry of ionizing radiations, which relies on the effects of thermoluminescence (TL) and optically stimulated luminescence [4]. High doses of ionizing radiations are currently used in radiation technologies and academic research to sterilize food and medical instruments, purify sewage water, in brachytherapy, to modify properties of composite materials, metals and alloys, as well as for spectroscopy of intrinsic and impurity defects in semi-conductors and dielectrics [7].

High radiation resistance results in less effective generation of radiation defects in the exposed ultrafine ceramics with smaller grain size, which significantly affects the fundamental TL characteristics of the materials. The latter include TL response (the intensity of the maximum of TL peak and its light sum under exposure to a "test" dose), its dependence on the dose of ionizing radiation (dose characteristic), and the loss of the accumulated light sum while stored (fading). Possible applications of the material in TL dosimetry depend on these characteristics, since this requires high TL response, dose characteristic that is the closest to the linear one, and low fading. Thus, determining mechanisms of dose effects (formation of TL response in the studied phosphor, its dependence on a dose and storage time) is an important academic and practical task.

The purpose of this work is to synthesize and study the features and mechanisms of the processes of formation of luminescent and dosimetric properties in irradiated ultrafine ceramics based on wide-gap oxide dielectrics.

Experimental

Ultrafine ceramics of aluminum and zirconium oxides were studied in the paper. They were produced by using two methods from nanopowders (PLASMOTERM, Moscow, Russia) with 60–120 nm crystallites and impurity concentrations not higher than 0.5 ppm. The first method was based on annealing of the compacts which had been made by cold uniaxial pressing of the nanopowders under 100–120 MPa. The compacts were 5 mm in diameter and 1 mm thick. The compacts were annealed in air in muffle furnace General Therm LHT 04.1800 (S). The annealing temperature was varied within the range of T=700-1700 °C to change the sizes of nanoparticles.

Alongside with the traditional method of sintering ceramics by annealing them in a furnace, another method was used — electron-beam synthesis [8]. This method employs sintering of powders in the field of high-power flux of high-energy electrons (1.4 MeV) for less than 1 s. In the method not only heat processes, but also ionization ones are very important in synthesizing ceramics in a beam of fast electrons. These processes cause electron excitations to split into primary products of radiolysis and reactions between them.

X-ray diffraction analysis of the samples was carried out with Rigaku MiniFlex 600 diffractometer. To excite TL, the samples were exposed to pulsed electron beams (130 keV, 2 ns, 60 A cm^{-2}) from RADAN-EXPERT accelerator. The electron energy was much lower than the threshold energy for defect formation in the oxides (400 keV and higher) [9]. When such exposure is used, only changes in charge state of the present trapping and luminescence centers are observed. The exposure dose was varied by changing a number of pulses during irradiation. One pulse gave the value of the 1.5 kGy absorbed dose. TL curves of the ceramic samples were measured in the 50–400 °C range at linear heating rate of 2 K s^{-1}. FEU-130 photomultiplier tube (the maximum spectral sensitivity at 400–420 nm) was used to register TL.

Results and Discussion

Phase compositions of alumina and zirconia ceramics annealed at different temperatures were determined with X-ray diffraction analysis. The results show that all the samples of Al_2O_3 completely (100 %) consist of alpha-phase [10]. Zirconia ceramics entirely consist of monoclinic phase [11]. In addition, as the annealing temperature grows, the phase compositions of the ceramics do not change.

Scherrer equation was used to find the dependence of the crystallite size on ceramics annealing temperature on the base of analysis of half-width of diffraction reflections. In addition, results of SEM-image analysis were used [10]. The obtained dependences are shown in Figure 1. It can be seen that the crystallite sizes started growing when the annealing temperature increased above 1300 °C in Al_2O_3 samples. In the ceramics annealed at the maximum temperature (1700 °C), a mean grain size could not be determined due to almost complete absence of grain structure in the SEM-image of the sample surface. No significant changes in the crystallite sizes were observed in ZrO_2 ceramics annealed at T=700-1000 °C. Further increasing annealing temperature makes the grain grow to the value of order of 500 nm.

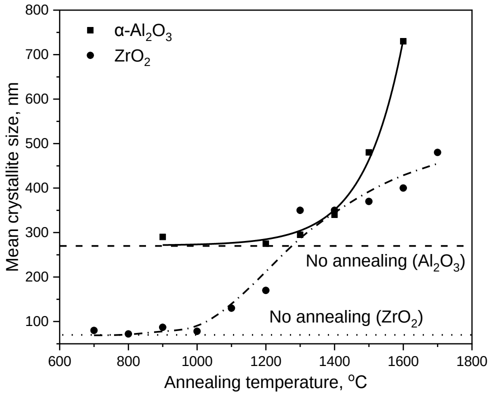

Figure 1. Dependence of the crystallite size in alumina and zirconia ceramics on the annealing temperature

Scherrer equation was also used to find the crystallite size in ZrO_2 ceramics synthesized with the electron-beam method. The resulting value (order of 100 nm) is nearly the same as the size of crystallites in the precursor powder taking into account the measurement error. In the samples synthesized in a flux of fast electrons, in spite of high temperatures, efficiency of crystallization significantly decreases in comparison with that of the samples traditionally annealed in furnace. Due to this fact, the initial size of crystallites is retained. This can be explained by a much shorter period of sintering of nanopowder in a fast electron beam, which is typical of other radiation methods of ceramic synthesis [12].

TL curves of alumina ceramics obtained at different annealing temperatures are shown in Figure 2a. It can be seen that all TL curves feature an isolated peak at 170 ^{o}C. It is noteworthy that this peak is close in the temperature position to the dosimetric TL peak in anion-defective α-Al_2O_3 single crystals which are used in TL dosimetry [13].

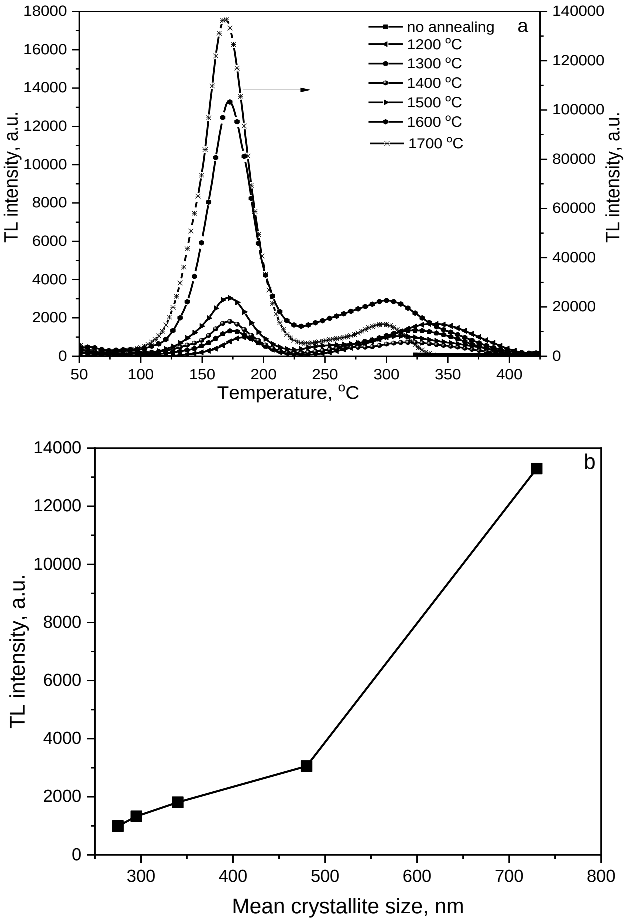

Figure 2. TL curves of α-Al2O3 ceramics annealed at different temperatures and exposed to a pulsed electron beam with 15 kGy dose (a) and dependence of TL peak intensity at 170 oC on the crystallite size (b)

Figure 2b shows dependence of TL peak intensity at 170 ^{o}C on the crystallite size. As it can be seen, growing grain size increases TL intensity. The most intensive rise of the intensity is observed when the crystallite are larger than 500 nm.

Figure 3a features TL curves of ZrO_2 ceramics exposed to a test dose of a pulsed electron beam (15 kGy). TL peak at 120 ^{o}C is seen in all the samples. A less intensive peak at 210 ^{o}C is also found in the ceramics synthesized with the electron-beam method. Figure 3b shows a dependence of the TL maximum intensity in the peak at 120 ^{o}C on the crystallite size. It can be seen that growing grain size increases TL intensity like in the alumina-based ceramics. The fastest growth is observed when the crystallites are bigger than 350 nm. The maximum TL intensity in the 120 ^{o}C peak is found in the ceramics synthesized with the electron-beam method. This can be due to formation of radiation defects during the synthesis. The defects are either charge carrier traps or luminescence centers.

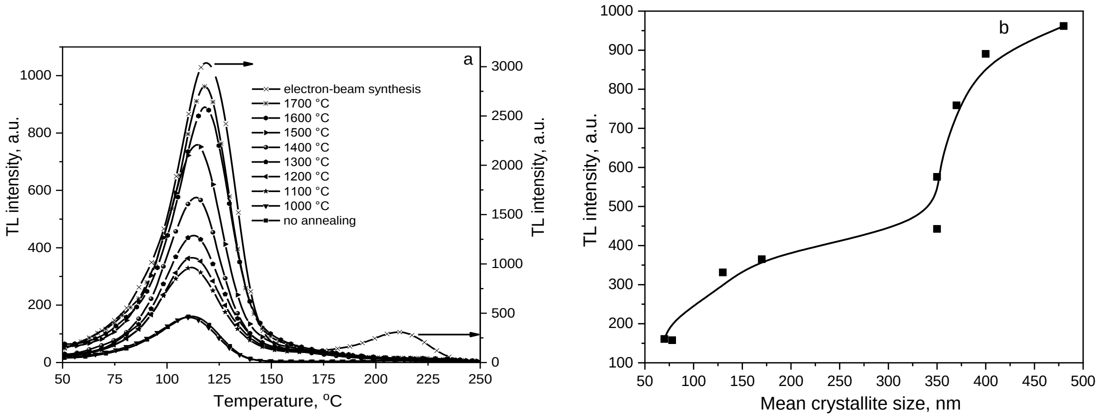

Figure 3. TL curves of ZrO_2 ceramics synthesized under different conditions, after exposure to a test dose of a pulsed electron beam (15 kGy) (a) and dependence of TL peak intensity at 120 °C on the crystallite size (b)

The effect of TL response drop with decreasing crystallite size had been observed earlier by other authors [14–16]. Ref. [17], which reviews literature data, shows that the reported effect is a common characteristic for many TL materials. Physical nature of the effect of dropping TL yield with decreasing crystallite size has not been well grounded yet and requires further studies. Increasing possibility of non-radiative transitions when nanoparticles lessen in size due to, for instance, localized transitions of electrons and holes between trapping and luminescence centers may be one of the reasons for the reported effect. Other possible causes of TL intensity drop may include decreasing concentration of traps, growing of the surface-to-volume ratio with decreasing crystallite size [17].

We studied dose dependences of TL intensity of dosimetric peaks of the ceramics (at 170 °C for aluminum oxide and at 120 °C for zirconium oxide). The obtained dependences were approximated with linear functions in different ranges of the changing dose. Slope angles of the dependences were values of nonlinearity coefficient *k*. Approximation results are given in Table.

Table

Approximation results of dose dependences of TL peaks in the ceramics synthesized under different conditions

No.	Type of samples	Dose range, kGy	Non-linearity coefficient
1	Al_2O_3 (1700 °C)	1.5-15	1.0
2	Al_2O_3 (1700 °C)	15-75	0.3
3	Al_2O_3 (1600 °C)	1.5-150	0.49
4	Al_2O_3 (1500 °C)	1.5-15	0.62
5	Al_2O_3 (1500 °C)	15-150	0.22
6	Al_2O_3 (1400 °C)	1.5-7.5	0.58
7	Al_2O_3 (1400 °C)	7.5-45	0.34
8	ZrO_2 (electron-beam synthesis)	1.5-7.5	0.84
9	ZrO_2 (1700 °C)	1.5-15	0.79
10	ZrO_2 (1600 °C)	1.5-15	0.51
11	ZrO_2 (1500 °C)	1.5-15	0.49
12	ZrO_2 (1400 °C)	1.5-7.5	0.89

It can be seen that the majority of dose dependences are sublinear ($k<1$), the only exception is Al_2O_3 ceramics synthesized at 1700 °C. In these ceramics, TL dependence on the dose is close to a linear one ($k=1$) in the 1.5–15 kGy range. The maximum range of the registered doses in which k=const is found in the alumina samples that were synthesized at 1600 °C. In these samples $k=0.49$ when the dose is changed by two orders of magnitude (from 1.5 to 150 kGy). It is noteworthy that according to the data from Table, there is not any noticeable correlation of non-linear coefficients and crystallite sizes in the ceramics under study. Sublinear character of dose dependences may be due to the competition in trapping charge carriers between different defects [18, 19]. The presence of such defects is more likely in nanostructured materials in comparison with bulk analogs.

In addition, we studied TL fading in alumina and zirconia ceramics. The samples were irradiated at room temperature with a 15 kGy dose and kept at this temperature in darkness for a set period of time. After this, the remaining TL was measured. The results show that unlike single-crystalline aluminum oxide, the samples of Al_2O_3 ceramics have significant fading. Maximum losses of dosimetric information (up to 60 % for one hour) are observed in the samples with the largest size of the grains annealed at 1600 °C. When the annealing temperature and nanoparticle size decrease, fading becomes less pronounced. At T=1400 °C, its value does not exceed 30 % per hour (Fig. 4).

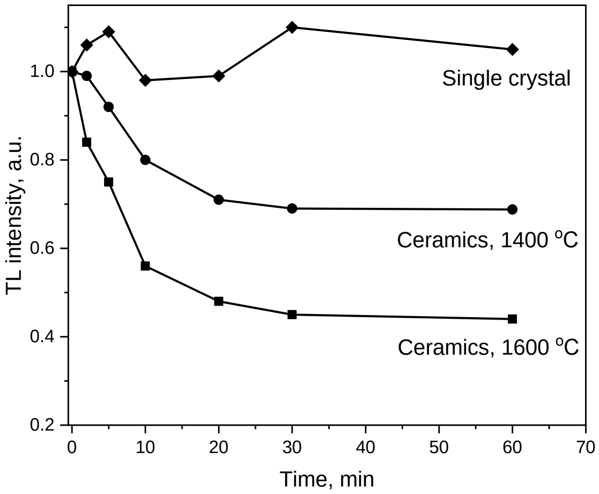

Figure 4. Fading of TL peak at 170 °C of α-Al_2O_3 ceramics synthesized by annealing at different temperatures

Examples of both decreasing fading when nanoparticle sizes grow and increasing one are available in literature [15, 16]. The effect of quantum tunneling may be a reason for anomalous TL fading in the samples [20]. In [20], computer simulation of the effect showed that both decrease and increase in intensity of tunneling recombination with growing grain size is possible at certain parameters of the nanomaterial (nanocrystal radius, tunneling length, initial mean distance between electrons and positive ions). Moreover, the intensity rise may serve as a reason for TL fading growth when crystallites become bigger in size, as it was observed in our experiments (Fig. 4).

Unlike alumina ceramics, noticeable decrease in TL intensity in the peak at 120 °C is not observed when the exposed ceramic ZrO_2 samples are kept for one hour. While its value accidentally changes within 10–15 %, which is comparable with an exposure dose error. The absence of anomalous fading may imply an insignificant role of quantum-mechanical tunneling and localized transitions of charge carriers in the formation of TL at 120 °C in the studied ZrO_2 ceramics.

Conclusions

In this work, samples of α-Al_2O_3 and monoclinic ZrO_2 ceramics were obtained by static annealing of nanopowder compacts. The samples were synthesized in air in a 700–1700 °C temperature range. Scanning electron microscopy and X-ray diffraction analysis were used to find that high-temperature annealing does not affect phase composition. However, it results in a significant growth of crystallite sizes. In ZrO_2 ceramics synthesized with the electron-beam method, the nanoparticle size is almost the same as the size of crystallites in the initial nanopowder. It was revealed that intensities of TL peaks grow with increasing grain size in the studied samples.

Dose dependences of TL in the samples of the ultrafine ceramics are predominantly sublinear. For aluminum oxide ceramics, unlike single crystals, the effect of anomalous TL fading which is presumably due to the presence of tunneling recombination and localized transitions typical of nanostructured materials was determined. Moreover, the value of anomalous TL fading increases with growing crystallite sizes.

The obtained sublinear dose dependences of TL show that the synthesized oxide ceramics are promising materials for TL dosimetry of high-dose (1–100 kGy) pulsed electron beams, which are used in radiation technologies and academic research. For aluminum oxide ceramics, due to significant TL fading, dosimetric information should be read out immediately after the end of exposure or special methods for correction of the readings from TL detectors should be used.

Acknowledgments

This work was supported by the Minobrnauki of Russia Federation, research project no. FEUZ-2023-0014

References

1 Dobrovinskaya E.R. Sapphire: material, manufacturing, applications / E.R. Dobrovinskaya, L.A. Lytvynov, V. Pishchik. — Springer Science & Business Media, 2009. — 493 p. DOI: 10.1007/978-0-387-85695-7

2 O'Connor R. Degradation and breakdown characteristics of thin MgO dielectric layers / R. O'Connor, G. Hughes, P. Casey, S.B. Newcomb // Journal of Applied Physics. — 2010. — Vol. 107, No. 2. — P. 024501. DOI: 10.1063/1.3265434

3 Yum J.H. A study of highly crystalline novel beryllium oxide film using atomic layer deposition / J.H. Yum, T. Akyol, M. Lei, D.A. Ferrer, T.W. Hudnall, M. Downer, C.W. Bielawski, G. Bersuker, J.C. Lee, S.K. Banerjee // Journal of Crystal Growth. — 2011. — Vol. 334, No. 1. — P. 126–133. — DOI: 10.1016/j.jcrysgro.2011.08.040

4 Yukihara E.G. Optically stimulated luminescence: fundamentals and applications / E.G. Yukihara, S.W.S. McKeever. — John Wiley & Sons, 2011. — 384 p. DOI:10.1002/9780470977064

5 Kato T. Optical, scintillation and dosimeter properties of MgO transparent ceramic and single crystal / T. Kato, G. Okada, T. Yanagida // Ceramics International. — 2016. — Vol. 42, No. 5. — C. 5617–5622. DOI: 10.1016/j.ceramint.2015.12.070

6 Andrievskii R.A. Radiation stability of nanomaterials / R.A. Andrievskii // Nanotechnologies in Russia. — 2011. — Vol. 6, No. 5. — P. 357–369. DOI: 10.1134/s1995078011030037

7 Mehnert R. Electron beams in research and technology / R. Mehnert // Nuclear Instruments and Methods in Physics Research Section B: Beam Interactions with Materials and Atoms. — 1995. — Vol. 105, No. 1–4. — P. 348–358. DOI: 10.1016/0168-583X(95)00634-6

8 Lisitsyn, V. The Optimization of Radiation Synthesis Modes for YAG: Ce Ceramics / V. Lisitsyn, D. Mussakhanov, A. Tulegenova, E. Kaneva, L. Lisitsyna, M. Golkovski, A. Zhunusbekov // Materials. — 2023. — Vol. 16, No. 8. — P. 3158. DOI: 10.3390/ma16083158

9 Kotomin E.A. Radiation-induced point defects in simple oxides / E.A. Kotomin, A.I. Popov // Nuclear Instruments and Methods in Physics Research Section B: Beam Interactions with Materials and Atoms. — 1998. — Vol. 141, No. 1–4. — P. 1–15. DOI: 10.1016/S0168-583X(98)00079-2

10 Nikiforov S.V. The effect of annealing tem-perature on the change in the structure, luminescent and dosimetric properties of ultrafine α-Al_2O_3 ceramics / S.V. Nikiforov, D.V. Ananchenko, G.R. Ramazanova, T.V. Shtang, A.V. Ishchenko, G.A. Yakovlev // Radiation Measurements. — 2023. — Vol. 166. — P. 106981. DOI: 10.1016/j.radmeas.2023.106981

11 Nikiforov S. Thermoluminescent and Dosimetric Properties of Zirconium Dioxide Ceramics Irradiated with High Doses of Pulsed Electron Beam / S. Nikiforov, A. Dauletbekova, M. Gerasimov, Y. Kasatkina, O. Denisova, V. Lisitsyn, M. Golkovski, A. Akylbekova, A. -D. Bazarbek, A. Akilbekov, A.I. Popov // Crystals. — 2023. — Vol. 13, No. 11. — P. 1585. DOI: 10.3390/cryst13111585

12 Ghyngazov S.A. Radiation-Thermal Sintering of Zirconia Powder Compacts Under Conditions of Bilateral Heating Using Beams of Low-Energy Electrons / S.A. Ghyngazov, T.S. Frangulyan, A.V. Chernyavskii, A.K. Goreev, E.P. Naiden // Russian Physics Journal. — 2015. — Vol. 58, No. 2. — P. 188–191. DOI: 10.1007/s11182-015-0480-2

13 Akselrod M.S. Highly Sensitive Thermoluminescent Anion-Defect Alpha-Al_2O_3: C Single Crystal Detectors / M.S. Akselrod, V.S. Kortov, D.J. Kravetsky, V.I. Gotlib // Radiation Protection Dosimetry. — 1990. — Vol. 33, No. 1–4. — P. 119–122. DOI: 10.1093/rpd/33.1-4.119

14 Salah N. Thermoluminescence of nanocrystalline LiF: Mg, Cu, P / N. Salah, P.D. Sahare, A.A. Rupasov // Journal of Luminescence. — 2007. — Vol. 124. — P. 357–364. DOI: 10.1016/j.jlumin.2006.04.004

15 Aboelezz E. Nano-barium–strontium sulfate as a new thermoluminescence dosimeter / E. Aboelezz, M.A. Sharaf, G.M. Hassan, A. El-Khodary // Journal of Luminescence. — 2015. — Vol. 166. — P. 156–161. DOI: 10.1016/j.jlumin.2015.05.026

16 Altunal V. Effect of sintering temperature on dosimetric properties of BeO ceramic pellets synthesized using precipitation method / V. Altunal, V. Guckan, A. Ozdemir, A. Sotelo, Z. Yegingil // Nuclear Instruments and Methods in Physics Research B. — 2019. — Vol. 441. — P. 46–55. DOI: 10.1016/j.nimb.2018.12.036

17 Tsoutsoumanos E. Nanostructured TLDs: Studying the impact of crystalline size on the Thermoluminescence glow-curve shape and electron trapping parameters / E. Tsoutsoumanos, M. Saleh, P.G. Konstantinidis, V. Altunal, P.D. Sahare, Z. Yengigil, T. Karakasidis, G. Kitis, G.S. Polymeris // Radiat. Phys. Chem. — 2023. — Vol. 212. — P. 111067. DOI: 10.1016/j.radphyschem.2023.111067

18 Lawless J.L. Sublinear dose dependence of thermoluminescence and optically stimulated lumines-cence prior to the approach to saturation level / J.L. Lawless, R. Chen, V. Pagonis // Radiation Measurements. — 2009. — Vol. 44. — P. 606–610. DOI: 10.1016/j.radmeas.2009.03.003

19 Nikiforov S.V. Sublinear dose dependence of thermoluminescence as a result of competi-tion between electron and hole trapping centers / S.V. Nikiforov, V. Pagonis, A.S. Merezhnikov // Radiation Measurements. — 2017. — Vol. 105. — P. 54–61. DOI: 10.1016/j.radmeas.2017.08.003

20 Pagonis V. The effect of crystal size on tunneling phenomena in luminescent nano-dosimetric materials / V. Pagonis, S. Bernier, F.M.S. Vieira, S. Steele // Nuclear Instruments and Methods in Physics Research B. — 2017. — Vol. 412. — P. 198–206. DOI: 10.1016/j.nimb.2017.09.016

21

С.В. Никифоров, Д.В. Ананченко, Т.В. Штанг, А.Ф. Никифоров,
В.М. Лисицин, М.Г. Голковский

Иондаушы сәулеленудің жоғары дозалы дозиметриясына арналған аса жұқа оксидті керамиканың синтезі, люминесцентті және дозиметриялық қасиеттері

Жоғары дозалы импульсті электронды сәулемен (130 кВ, импульсқа 1,5 кГр) сәулеленген алюминий және цирконий оксидтеріне негізделген ультра жұқа керамиканың термолюминесценттік және дозиметрлік қасиеттері зерттелді. Кристаллит өлшемдері әртүрлі керамикаларды синтездеу үшін наноұнтақтардан жасалған компакттарды ауада T = 700-1700 °C температурада электр пешінде агломерациялау, сондай-ақ оларды жоғары қуат тығыздығы бар жоғары энергиялы электрондармен (1,4 МэВ) сәулелендіру қолданылды. Керамиканың T>1000 °C күйдіруі термолюминесценттік шыңдардың қарқындылығының айтарлықтай өсуімен корреляциялық кристаллиттер мөлшерінің айтарлықтай ұлғаюына әкелетіні анықталды. Электрондық сәуле әдісімен өндірілген керамика максималды термолюминесценттік реакцияға ие, бұл синтез кезінде радиацияның әсерінен түсіру және люминесценция орталықтарының пайда болуымен байланысты. Сәулеленген a-Al_2O_3 және ZrO_2 керамикасының термолюминесценциясының дозаға тәуелділіктерін талдау олардың басым сублинарлық сипатын анықтады. Алюминий оксиді негізіндегі керамика үшін, монокристалды модификациядан айырмашылығы, кристаллит өлшемі ұлғайған сайын шамасы арта түсетін аномальды термолюминесцентті федингтің болуы анықталды. Интенсивті оқшауланған термолюминесценция шыңының болуы және көптеген дозаға тәуелділіктердің субсызықтық сипаты импульстік электронды сәулелердің жоғары дозаларын (бірнешеден ондаған кГр) өлшеу үшін осы жұмыста синтезделген оксид керамикасының болашағын дәлелдейді. Бұл жағдайда алюминий оксиді негізіндегі керамика үшін фединг мөлшеріне термолюминесцентті реакцияны түзету қажет.

Кілт сөздер: алюминий оксиді, цирконий оксиді, ультра жұқа керамика, термолюминесценция, электронды сәуленің синтезі, кристаллит мөлшері, доза сипаттамалары, фединг.

С.В. Никифоров, Д.В. Ананченко, Т.В. Штанг, А.Ф. Никифоров,
В.М. Лисицин, М.Г. Голковский

Синтез, люминесцентные и дозиметрические свойства сверхтонкой оксидной керамики для высокодозной дозиметрии ионизирующего излучения

Исследованы термолюминесцентные и дозиметрические свойства ультрадисперсных керамик на основе оксидов алюминия и циркония, облученных высокодозным импульсным электронным пучком (130 кэВ, 1,5 кГр на один импульс). Для синтеза керамик с различным размером кристаллитов использовалось спекание компактов, изготовленных из нанопорошков, на воздухе в электрической печи при T=700–1700 оС, а также их облучение высокоэнергетическими электронами (1,4 МэВ) с высокой плотностью мощности. Установлено, что отжиг керамик при T>1000 ^{o}С приводит к существенному росту размера кристаллитов, что коррелирует со значительным увеличением интенсивности термолюминесцентных пиков. Максимальным термолюминесцентным откликом обладают керамики, полученные электронно-лучевым методом, что связано с образованием радиационно-индуцированных центров захвата и свечения при синтезе. Анализ дозовых зависимостей термолюминесценции облученных керамик α-Al_2O_3 и ZrO_2 выявил их преимущественно сублинейный характер. Для керамик на основе оксида алюминия, в отличие от монокристаллической модификации, установлено наличие аномального термолюминесцентного фединга, величина которого увеличивается с ростом размера кристаллитов. Наличие интенсивного изолированного пика термолюминесценции и сублинейный характер большинства дозовых зависимостей доказывают перспективность синтезированных в настоящей работе оксидных керамик для измерения высоких доз импульсных электронных пучков (единиц — десятки кГр). При этом для керамик на основе оксида алюминия требуется коррекция термолюминесцентного отклика на величину фединга.

Ключевые слова: оксид алюминия, оксид циркония, сверхтонкая керамика, термолюминесценция, электронно-лучевой синтез, размер кристаллитов, дозовые характеристики, фединг.

References

1 Dobrovinskaya, E.R., Lytvynov, L.A., & Pishchik, V. (2009). *Sapphire: material, manufacturing, applications*. Springer Science & Business Media.

2 O'Connor, R., Hughes, G., Casey, P., & Newcomb, S.B. (2010). Degradation and breakdown characteristics of thin MgO dielectric layers. *Journal of Applied Physics*, *107* (2), 024501.https://doi.org/10.1063/1.3265434

3 Yum, J.H., Akyol, T., Lei, M., Ferrer, D.A., Hudnall, T.W, Downer, M., Bielawski, C.W., Bersuker, G., Lee, J.C., & Banerjee, S.K. (2011). A study of highly crystalline novel beryllium oxide film using atomic layer deposition. *Journal of Crystal Growth*, *334* (1), 126–133. https://doi.org/10.1016/j.jcrysgro.2011.08.040

4 Yukihara, E.G., & McKeever, S.W.S. (2011). *Optically stimulated luminescence: fundamentals and applications*. John Wiley & Sons.

5 Kato, T., Okada, G., & Yanagida, T. (2016). Optical, scintillation and dosimeter properties of MgO transparent ceramic and single crystal. *Ceramics International*, *42* (5), 5617–5622. https://doi.org/10.1016/j.ceramint.2015.12.070

6 Andrievskii, R.A. (2011). Radiation stability of nanomaterials. *Nanotechnologies in Russia*, *6* (5), 357–369. https://doi.org/10.1134/s1995078011030037

7 Mehnert, R. (1995). Electron beams in research and technology. *Nuclear Instruments and Methods in Physics Research Section B: Beam Interactions with Materials and Atoms*, *105* (1–4), 348–358. https://doi.org/10.1016/0168-583X(95)00634-6

8 Lisitsyn, V., Mussakhanov, D., Tulegenova, A., Kaneva, E., Lisitsyna, L., Golkovski, M., & Zhunusbekov, A. (2023). The Optimization of Radiation Synthesis Modes for YAG: Ce Ceramics. *Materials*, *16* (8), 3158. https://doi.org/10.3390/ma16083158

9 Kotomin, E.A., & Popov, A.I. (1998). Radiation-induced point defects in simple oxides. *Nuclear Instruments and Methods in Physics Research Section B: Beam Interactions with Materials and Atoms*, *141* (1–4), 1–15. https://doi.org/10.1016/S0168-583X(98)00079-2

10 Nikiforov, S.V., Ananchenko, D.V., Ramazanova, G.R., Shtang, T.V., Ishchenko, A.V., & Yakovlev, G.A. (2023). The effect of annealing tem-perature on the change in the structure, luminescent and dosimetric properties of ultrafine α-Al_2O_3 ceramics. *Radiation Measurements*, 166, 106981. https://doi.org/10.1016/j.radmeas.2023.106981

11 Nikiforov, S., Dauletbekova, A., Gerasimov, M., Kasatkina, Y., Denisova, O., Lisitsyn, V., Golkovski, M., Akylbekova, A., Bazarbek, A. -D., Akilbekov, A., & Popov, A.I. (2023). Thermoluminescent and Dosimetric Properties of Zirconium Dioxide Ceramics Irradiated with High Doses of Pulsed Electron Beam. *Crystals*, *13* (11), 1585. https://doi.org/10.3390/cryst13111585

12 Ghyngazov, S.A., Frangulyan, T.S., Chernyavskii, A.V., Goreev, A.K., & Naiden, E.P. (2015). Radiation-Thermal Sintering of Zirconia Powder Compacts Under Conditions of Bilateral Heating Using Beams of Low-Energy Electrons. *Russian Physics Journal*, *58* (2), 188–191. https://doi.org/10.1007/s11182-015-0480-2

13 Akselrod, M.S., Kortov, V.S., Kravetsky, D.J., & Gotlib, V.I. (1990). Highly Sensitive Thermoluminescent Anion-Defect Alpha-Al_2O_3: C Single Crystal Detectors. *Radiation Protection Dosimetry*, *33* (1–4), 119–122. https://doi.org/10.1093/rpd/33.1-4.119

14 Salah, N., Sahare, P.D., & Rupasov, A.A. (2007). Thermoluminescence of nanocrystalline LiF: Mg, Cu, P. *Journal of Luminescence*, *124*, 357–364. https://doi.org/10.1016/j.jlumin.2006.04.004

15 Aboelezz, E., Sharaf, M.A., Hassan, G.M., & El-Khodary, A. (2015). Nano-barium–strontium sulfate as a new thermoluminescence dosimeter. *Journal of Luminescence*, *166*, 156–161. DOI: 10.1016/j.jlumin.2015.05.026

16 Altunal, V., Guckan, V., Ozdemir, A., Sotelo, A., & Yegingil, Z. (2019). Effect of sintering temperature on dosimetric properties of BeO ceramic pellets synthesized using precipitation method. *Nuclear Instruments and Methods in Physics Research B*, *441*, 46–55. https://doi.org/10.1016/j.nimb.2018.12.036

17 Tsoutsoumanos, E., Saleh, M., Konstantinidis, P.G., Altunal, V., Sahare, P.D., Yengigil, Z., Karakasidis, T., Kitis, G., & Polymeris, G.S. (2023). Nanostructured TLDs: Studying the impact of crystalline size on the Thermoluminescence glow-curve shape and electron trapping parameters. *Radiat. Phys. Chem*, *212*, 111067. https://doi.org/10.1016/j.radphyschem.2023.111067

18 Lawless, J.L., Chen, R., & Pagonis, V. (2009). Sublinear dose dependence of thermoluminescence and optically stimulated lumines-cence prior to the approach to saturation level. *Radiation Measurements*, *44*, 606–610. https://doi.org/10.1016/j.radmeas.2009.03.003

19 Nikiforov, S.V., Pagonis, V., & Merezhnikov, A.S. (2017). Sublinear dose dependence of thermoluminescence as a result of competition between electron and hole trapping centers. *Radiation Measurements*, *105*, 54–61. https://doi.org/10.1016/j.radmeas.2017.08.003

20 Pagonis, V., Bernier, S., Vieira, F.M.S., & Steele, S. (2017). The effect of crystal size on tunneling phenomena in luminescent nano-dosimetric materials. *Nuclear Instruments and Methods in Physics Research B, 412*, 198–206. https://doi.org/10.1016/j.nimb.2017.09.016

Information about the authors

Sergey Nikiforov (corresponding author) — Doctor of physical and mathematical sciences, Head of Chair, Department of Physical Techniques and Devices for Quality Control, Ural Federal University, Mira street 21, 620002, Yekaterinburg, Russia; *e-mail: s.v.nikiforov@urfu.ru*. https://orcid.org/0000-0001-7797-8267

Daria Ananchenko — Senior lecturer, Junior researcher, Department of Physical Techniques and Devices for Quality Control, Ural Federal University, Mira street 21, 620002, Yekaterinburg, Russia; *e-mail: d.v.ananchenko@urfu.ru*. https://orcid.org/0000-0002-1998-8405

Tatiana Shtang — Candidate of physical and mathematical sciences, Associate professor, Department of Physical Techniques and Devices for Quality Control, Ural Federal University, Mira street 21, 620002, Yekaterinburg, Russia; *e-mail: t.v.shtang@urfu.ru*. https://orcid.org/0000-0002-6454-4870

Alexander Nikiforov — Doctor of chemical sciences, Professor, Department of Radiochemistry and Applied Ecology, Ural Federal University, Mira street 21, 620002, Yekaterinburg, Russia; *e-mail*: *a.f.nikiforov@urfu.ru*

Victor Lisitsyn — Doctor of physical and mathematical sciences, Professor, Department of Materials Science, Engineering School, National Research Tomsk Polytechnic University, Lenin Avenue, 30, 634034, Tomsk, Russia; *e-mail: lisitsyn@tpu.ru*. https://orcid.org/0000-0002-2075-4796

Michael Golkovski — Candidate of physical and mathematical sciences, Senior research fellow, Budker Institute of Nuclear Physics, SB RAS, Academician Lavrentiev Avenue, 11, 630090, Novosibirsk, Russia; *e-mail: golkovski@mail.ru*. https://orcid.org/0000-0003-4399-444X

Article
https://doi.org/10.31489/2024PH4/92-97
UDC 535.37

Received: 30.05.2024
Accepted: 05.08.2024

V.I. Oleshko[*], Zixuan Li

The National Research Tomsk Polytechnic University，Tomsk，Russia
([*]Corresponding author's e-mail: oleshko@tpu.ru)

Obtaining and studying the luminescent properties of zinc oxide synthesized in a stream of high-energy electrons

For the first time, zinc oxide samples were obtained by a method based on irradiation of nominally pure zinc with a stream of high-energy electrons with an energy of 1.4 MeV and a power density of 7 kW/cm^2 in atmospheric air. The morphology of the synthesized substance was studied by transmission electron and optical microscopy. Particles of ultrafine zinc oxide in the form of needles were found at a distance (1–3) cm from the irradiation zone, with average lengths and diameters of 150 and 10 nm, respectively. Ultrafine samples are characterized by the presence of a hexagonal wurtzite structure. By optical microscopy, ZnO whisker microstructures with a diameter of ~ 1 μm and a length of 50–100 μm were detected in the irradiation zone. The photoluminescence spectrum of all samples is represented by one narrow exciton band with a maximum at λ = 380 nm and a decay time of τ < 13 ns in the absence of other bands due to intrinsic and impurity defects, which indicates the high crystalline perfection of the synthesized crystals.

Keywords: zinc oxide, radiation synthesis, nano- and microstructures, transmission electron microscopy, photoluminescence.

Introduction

Adding Zinc oxide is of scientific and practical interest due to its unique properties: wide band gap (~ 3.3 eV at 300 K), high exciton binding energy (60 MeV) and high radiation resistance. In this regard, ZnO-based materials synthesized by various methods are of interest for the creation of UV light-emitting devices, registration of gamma quanta and X-ray radiation [1–3]. Recently, special attention has been paid to highly dispersed forms of ZnO nanocrystals and thin films. Due to their improved physical and chemical properties, nanostructures have become attractive materials in the field of nanoelectronics, optoelectronics, energy and biomedicine [4–6]. Zinc oxide is a promising material for the creation of semiconductor lasers in the UV and blue ranges operating at room temperature [7]. Various methods are used to produce thin films of zinc oxide and nanostructures of other materials: molecular beam epitaxy, hydrothermal, pulsed laser spraying, magnetron deposition, chemical vapor deposition [8–11]. The literature data indicate a strong influence of the synthesis method and the presence of impurities on the luminescent characteristics of zinc oxide nanocrystals. Special attention is paid to the development of high-performance, economical and safe technologies for the production of nanopowders, thin films and multicomponent ceramics, which include electron beam and laser [11, 12]. The purpose of this work is to elucidate the possibility of radiation synthesis of ZnO nanocrystals using a powerful electron beam with energy of 1.4 MeV and a power density of 6–10 kW/cm^2 released into the air at atmospheric pressure.

Experimental

For the synthesis of ZnO, samples of pure (99.9 %) zinc in the form of granules were used, which were placed in specially prepared cells in a copper plate (crucible), measuring 40×100×10 mm, with a diameter of 8 mm and a depth of 4 mm and irradiated with an electron flux with an energy of 1.4 MeV and a power density of (6–10) kW/cm^2 generated by the ELV-6 accelerator (BINP, Novosibirsk). The crucible moved at a speed of 1 cm/s relative to an electron beam with a cross section of 1 cm^2. Thus, the surface of Zn was irradiated for 1 s. The characteristics of products deposited on a copper substrate were studied by transmission electron microscopy (TEM) on a JEOL JEM-2100F electron microscope by employees of the Scientific and Educational Innovation Center "Nanomaterials and Nanotechnology" TPU (ESNPT).

In addition to TEM, luminescent analysis of the synthesized material was applied. The source of excitation of pulsed photoluminescence (PPL) was a nitrogen laser (λ = 337.1 nm; τ = 10 ns). The PPL spectra and luminescence kinetics were recorded using the "point–by-point spectrum" method using the MDR-23 monochromator, PMTs -84 and the Tektronix DPO-3034 oscilloscope.

Results and Discussion

Zinc irradiation led to the formation of a white powder located both on the irradiated zinc surface (Fig. 1, a, zone 1) and on the surface of the copper plate (Fig. 1, a-b, zone 2), at a distance of up to 10 mm from the irradiation zone.

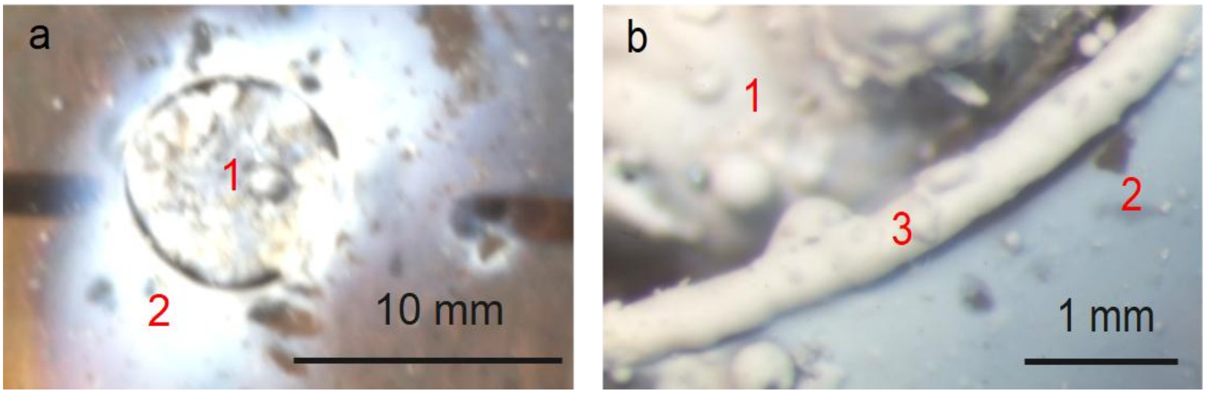

Figure 1, a-b. Photographs of a white powder formed on the surface of Zn (zone 1) and on the surface of a copper plate at a distance of up to 10 mm from the irradiation zone (zone 2).

Zone 2 was formed as a result of the effect of the supply ventilation air flow on the evaporation products formed near the irradiated zinc surface. The powder layer formed away from the irradiation zone (zone 2) was easily removed by mechanical cleaning, while the white layer, tens to hundreds of microns thick, formed on the irradiated zinc surface (zone 1) had good adhesion. At the periphery of the copper cylindrical cell, a thicker layer was formed (Fig. 1, b, zone 3), in the form of a roller.

Filamentous formations (whiskers) with a diameter of 1 μm and a length of 50–100 microns were found inside the copper cell after irradiation with an electron beam on the surface of microcrystals (Fig. 2, a-b)

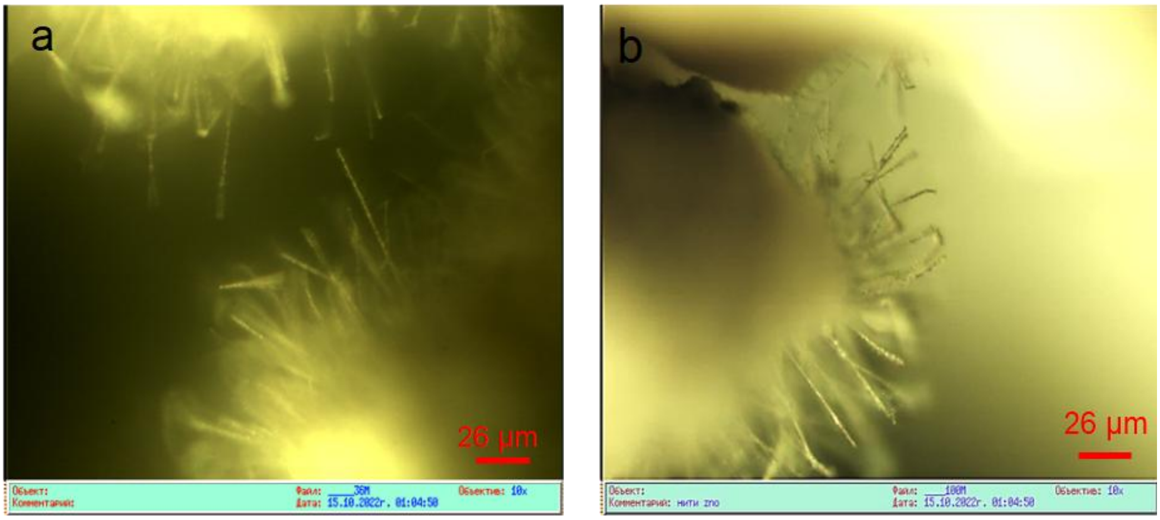

Figure 2, a-b. Image of an ensemble of filamentous structures formed on the surface of microcrystals synthesized inside a copper cell.

Figure 3a shows a high-resolution photograph (HRTEM image) of white powder nanocrystals formed on the surface of a copper plate at a distance of 10 mm from the irradiation zone, and Figure 3b shows an electronogram (SEAD image) on which several diffraction rings are observed.

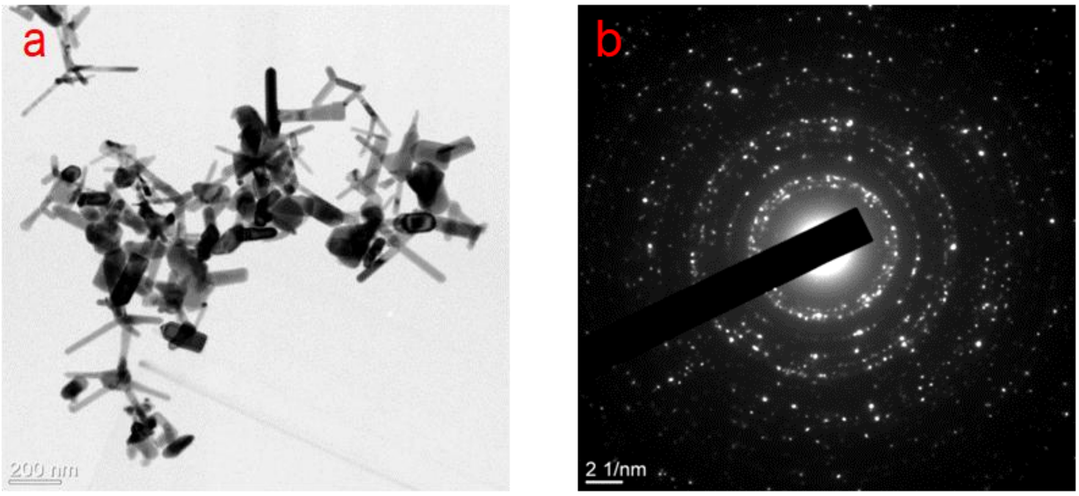

Figure 3 a — TEM — image of ultrafine ZnO powder; b — electron diffraction from the same region.

The calculation of the rings radii (r) and the corresponding interplanar distances d (Å) is given in Table. and indicates that the white powder is zinc oxide with a hexagonal wurtzite structure.

Table

Calculation of the radius of the rings and the corresponding interplanar distances

No.	1/2r	1/r	r	d(Å)	h	k	l
1	7.0588	3.5294	0.284	2.84	1	0	0
2	7.647	3.5294	0.2615	2.61	0	0	2
3	8.0672	4.033	0.2479	2.47	1	0	1
4	10.420	5.210	0.191	1.91	1	0	2
5	12.268	6.134	0.163	1.63	1	1	0

The analysis of synthesized ZnO was additionally carried out by the luminescent method. The PPL spectrum and the kinetics of luminescence of zinc oxide are shown in Figure 4, a, b.

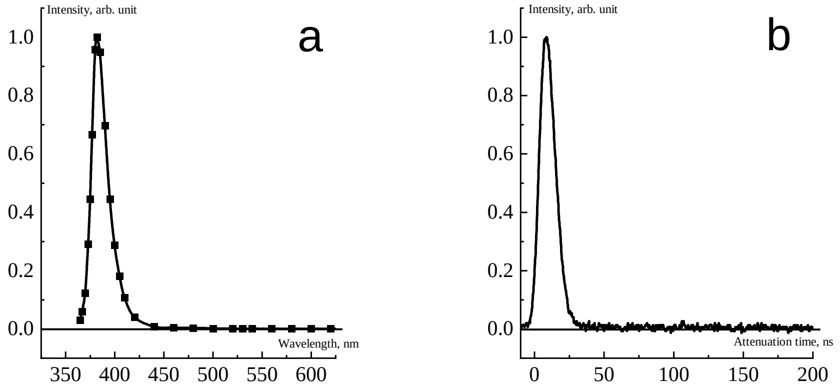

Figure 4. a — PPL spectrum; b — photoluminescence kinetics of synthesized ZnO

It can be seen that in the PPL spectrum there is one exciton band with a maximum at λ =380 nm with a decay time of $\tau \leq 13$ ns in the absence of other bands due to intrinsic and impurity defects, which indicates the high crystalline perfection of the synthesized nanocrystals.

The revealed features of the process of formation of ZnO filamentous structures correspond to the model representation of the classical Vapor–liquid–solid (VLS) mechanism by Givargizov-Chernov [13]. According to the model, the process of forming filamentous structures begins with the formation of an ensemble of metal droplets, in this case zinc, whose molecules condense on a copper substrate. Subsequently, oxygen vapor molecules from atmospheric air enter the drop, where they react with zinc and form a supersaturated liquid solution. Zinc oxide crystals fall out of the solution. A similar mechanism of growth of filamentous crystals was observed earlier by the authors of [14] when growing CdS on a SiC substrate.

Acknowledgements

The results were obtained using the equipment of the Central Research and Development Center of the ESNPT TPU supported by the project of the Ministry of Education and Science of the Russian Federation No. 075-15-2021-710. The samples were irradiated using the ELV-6 electronic accelerator (BINP, Novosibirsk).

Conclusions

For the first time, a technique for the synthesis of zinc oxide nanocrystals by irradiating nominally pure (99.9 %) zinc with an electron beam with an energy of 1.4 MeV and a density of 7 kW/cm^2 released into the air at atmospheric pressure was proposed and implemented. It was found that the ZnO PPL spectrum consists of a single exciton band in the absence of bands associated with impurities and defects. The implementation of electron beam technological processes in atmospheric pressure air opens up new possibilities for obtaining high-crystalline zinc oxide nanocrystals.

This work was performed within the framework of the Program of Strategic Academic Leadership “Priority 2030”.

References

1 Özgür Ü. A comprehensive review of ZnO materials and devices / Ü. Özgür, Ya. I. Alivov, C. Liu, A. Teke, M.A. Reshchikov, S. Doğan, V. Avrutin, S. -J. Cho, H. Morkoç // J. Appl. Phys. — 2005. — Vol. 98, No. 4. — 041301. https://doi.org/10.1063/1.1992666.

2 Klingshirn C. ZnO: Material, Physics and Applications. / C. Klingshirn // ChemPhysChem. — 2007. — Vol. 8. — P. 782–803. https://doi.org/10.1002/cphc.200700002.

3 Sharma D. A review on ZnO: Fundamental properties and applications. / D. Sharma, S. Shukla, K. Sharma, V. Kumar // Materials Today: Proceedings. — 2022. — Vol. 49. — P. 3028–3035. https://doi.org/10.1016/j.matpr.2020.10.238.

4 Willander M. Zinc Oxide Nanorod Based Photonic Devices: Recent Progress in Growth, Light Emitting Diodes and Lasers / M. Willander, O. Nur, Q.X. Zhao et al. // Nanotechnology. — 2009. — Vol. 20, No. 33. — 332001. DOI 10.1088/0957-4484/20/33/332001.

5 Wang Z. L. Novel nanostructures of ZnO for nanoscale photonics, optoelectronics, piezoelectricity, and sensing. / Z.L. Wang // Appl. Phys. Mater. Sci. Process, — 2007. — Vol. 88. — P. 7–15. https://doi.org/10.1007/s00339-007-3942-8.

6 Thapa D. Achieving highly-enhanced UV photoluminescence and its origin in ZnO nanocrystalline films. / Dinesh Thapa, Jesse Huso, John L. Morrison, и et al. // Optical Materials — 2016. — Vol. 58. — P. 382–389. https://doi.org/10.1016/j.optmat.2016.05.008.

7 Ополченцев А.М. УФ люминесценция и лазерная генерация в ансамблях микрокристаллов оксида цинка с медью / А.М. Ополченцев, Л.А. Задорожная, Ч.М. Брискина, В.М. Маркушев, А.П. Тарасов, А.Э. Муслимов, В.М. Каневский // Оптика и спектроскопия — 2018. — Т. 125, № 4. — С. 501–506. https://doi.org/10.21883/OS.2018.10.46702.142-18.

8 Курбанов С.С. Фотолюминесцентные свойства нанородов ZnO, синтезированных различными методами / С.С. Курбанов, Ш.З. Уролов, З.Ш. Шаймарданов, Х.Д. Чо, Т.В. Канг // ФТП. — 2018. — Т. 52, № 7. — С. 757–762. https://doi.org/10.21883/FTP.2018.07.46048.8673.

9 Бутова В.В. Синтез наночастиц оксида цинка, покрытых оксидом кремния / В.В. Бутова, В.А. Поляков, Е.А. Ерофеева, Ч. Ли, М.А. Солдатов, А.В. Солдатов // Докл. РАН. Химия, науки о материалах. — 2020. — Т. 492, № 1. — С. 5–9. DOI: 10.31857/S268695352003005X.

10 Карпов И.В. Плазмохимический реактор на основе импульсного дугового разряда низкого давления для синтеза нанопорошков / И.В. Карпов, А.В. Ушаков, А.А. Лепешев, Л.Ю. Федоров // Журн. техн. физики. — 2017. — Т. 87, № 1. — С. 140–145. https://doi.org/10.21883/JTF.2017.01.44031.1851.

11 Жерихин А.Н. Лазерное напыление пленок ZnO на кремниевые и сапфировые подложки / А.Н. Жерихин, А.И. Худобенко, Р.Т. Вилльямс, Д. Вилкинсон, К.Б. Усер, Г. Хионг, В.В. Воронов // Квантовая электроника. — 2003. — Т. 33, № 33. — С. 975–980. https://doi.org/10.1070/QE2003v033n11ABEH002533.

12 Патент RU № 2426625 РФ. Способ получения ультрадисперсного порошка висмута. Опубл. БИ. 2011. № 23. Толочко Б.П., Антохин Е.И., Юхин Ю.М. и др.

13 Гиваргизов Е.И. Рост нитевидных и пластичных кристаллов из пара / Е.И. Гиваргизов. — М.: Наука; Гл. ред. физ.-мат. лит., 1977. — 303 с.

14 Беляев А.П. Формирование нитевидных кристаллов сульфида кадмия методом вакуумного испарения и конденсации в квазизамкнутом объеме / А.П. Беляев, В.В. Антипов, В.П. Рубец // ФТП. — 2016. — Т. 50, № 3. — С. 420–422. https://doi.org/10.1134/S1063782616030027.

В.И. Олешко, Цзысюань Ли

Жоғары энергиялы электрондар ағынында синтезделген мырыш оксидінің люминесцентті қасиеттерін алу және зерттеу

Алғаш рет мырыш оксидінің сынамалары номиналды таза мырышты атмосфералық ауада энергиясы 1,4 Мэв және қуат тығыздығы 7 квт/см2 жоғары энергиялы электрондар ағынымен сәулелендіруге негізделген әдіспен алынды. Синтезделген заттың морфологиясы трансмиссиялық электронды және оптикалық микроскопия арқылы зерттелді. Инелер түріндегі ультра жұқа мырыш оксидінің бөлшектері сәулелену аймағынан (1-3) см қашықтықта, орташа ұзындығы мен диаметрі сәйкесінше 150 және 10 нм болатын. Ультра жұқа үлгілер алтыбұрышты вурцит құрылымының болуымен сипатталады. Оптикалық микроскопия арқылы сәулелену аймағында диаметрі ~ 1 мкм және ұзындығы 50-100 мкм болатын ZnO вискерлі микроқұрылымдары анықталды. Барлық үлгілердің фотолюминесценция спектрі максимумы $\lambda = 380$ нм және ыдырау уақыты τ болатын бір тар экситон диапазонымен ұсынылған. $\tau < 13$ нс ішкі және қоспалық ақауларға байланысты басқа жолақтар болмаған кезде, бұл синтезделген кристалдардың жоғары кристалды жетілуін көрсетеді.

Кілт сөздер: мырыш оксиді, радиациялық синтез, нано- және микроқұрылымдар, трансмиссиялық электронды микроскопия, фотолюминесценция.

В.И. Олешко, Цзысюань Ли

Получение и изучение люминесцентных свойств оксида цинка, синтезированного в потоке электронов высокой энергии

Впервые получены образцы оксида цинка методом, основанным на облучении номинально чистого цинка потоком высокоэнергетических электронов с энергией 1,4 МэВ и плотностью мощности 7 кВт/см^2 в атмосферном воздухе. Морфология синтезированного вещества исследовалась методами просвечивающей электронной и оптической микроскопии. На расстоянии (1–3) см от зоны облучения обнаружены частицы ультрадисперсного оксида цинка в форме игл, средние значения длины и диаметров составляют 150 и 10 нм соответственно. Для ультрадисперсных образцов характерно наличие гексагональной вюрцит структуры. Методом оптической микроскопии в зоне облучения обнаружены вискерные микроструктуры ZnO диаметром ~ 1 мкм и длиной 50–100 мкм. Спектр фотолюминесценции всех образцов представлен одной узкой экситонной полосой с максимумом при λ=380 нм и временем затухания $\tau < 13$ нс при отсутствии других полос, обусловленных собственными и примесными дефектами, что свидетельствует о высоком кристаллическом совершенстве синтезированных кристаллов.

Ключевые слова: оксид цинка, радиационный синтез, нано- и микроструктуры, просвечивающая электронная микроскопия, фотолюминесценция.

References

1 Özgür, Ü., Alivov, Ya. I., Liu, C., Teke, A., Reshchikov, M.A., Doğan, S., Avrutin, V., Morkoç, & S. -J. Cho (2005). A comprehensive review of ZnO materials and devices. J. *Appl. Phys, 98*(4), 041301. https://doi.org/10.1063/1.1992666.

2 Klingshirn, C. (2007). ZnO: Material, Physics and Applications, *ChemPhysChem, 8,* 782–803. https://doi.org/10.1002/cphc.200700002.

3 Sharma, D., Shukla, S., Sharma, K., & Kumar, V. (2022). A review on ZnO: Fundamental properties and applications. *Materials Today: Proceedings, 49,* 3028–3035. https://doi.org/10.1016/j.matpr.2020.10.238.

4 Willander, M. et al. (2009). *Zinc Oxide Nanorod Based Photonic Devices: Recent Progress in Growth, Light Emitting Diodes and Lasers. Nanotechnology, 20*(33), 332001. DOI 10.1088/0957-4484/20/33/332001.

5 Wang, Z. L. (2007). Novel nanostructures of ZnO for nanoscale photonics, optoelectronics, piezoelectricity, and sensing, *Appl. Phys. Mater. Sci. Process, 88*, 7–15. https://doi.org/10.1007/s00339-007-3942-8.

6 Thapa, D. et al. (2016). Achieving highly-enhanced UV photoluminescence and its origin in ZnO nanocrystalline films. *Optical Materials, 58,* 382–389. https://doi.org/10.1016/j.optmat.2016.05.008.

7 Opolchentsev, A.M., Zadopozhnaia, L.A., Briskina, Ch.M., Markushev, V.M., Tarasov, A.P., Muslimov, A.E., & Kanevsky, V.M. (2018). UF liuminestsentsiia i lazernaia generatsiia v ansambliakh mikrokristallov oksida tsinka s mediu [UV luminescence and laser generation in ensembles of zinc oxide microcrystals with copper]. *Optika i spektroskopiia — Optics and Spectroscopy, 125*(4), 501–506. https://doi.org/10.21883/OS.2018.10.46702.142-18 [in Russian].

8 Kurbanov, S.S., Urolov, Sh.Z., Shaimardanov, Z.Sh., Cho, H.D., & Kang, T.V. (2018). Fotoliuminestsentnye svoistva nanorodov ZnO, sintezirovannykh razlichnymi metodami [Photoluminescent properties of nano-genera of ZnO synthesized by various methods]. *Semiconductor Physics and Engineering, 52*(7), 757–762. https://doi.org/10.21883/FTP.2018.07.46048.8673 [in Russian].

9 Butova, V.V., Poliakov, V.A., Erofeeva, Ye.A., Li, Ch., Soldatov, M.A., & Soldatov, A.V. (2020). Sintez nanochastits oksida tsinka, pokrytykh oksidom kremniia [Synthesis of zinc oxide nanoparticles coated with silicon oxide]. *Doklady Rossiiskoi akademii nauk. Khimiia, nauki o materialakh — Reports of the Russian Academy of Sciences. Chemistry, Materials Sciences, 492*(1), 5–9. DOI: 10.31857/S268695352003005X [in Russian].

10 Karpov, I.V., Ushakov, A.V., Lepeshev, A.A., & Fedorov, L.Yu. (2017). Plazmokhimicheskii reaktor na osnove impulsnogo dugovogo razriada nizkogo davleniia dlia sinteza nanoporoshkov [A plasma chemical reactor based on a low-pressure pulsed arc discharge for the synthesis of nanopowders]. *Zhurnal tekhnicheskoi fiziki — Journal of Technical Physics, 87*(1), 140–145. https://doi.org/10.21883/JTF.2017.01.44031.1851 [in Russian].

11 Zherikhin, A.N., Hudobenko, A.I., Villiams, R.T., Vilkinson, D., User, K.B., Hiong, G. & Voronov, V.V. (2003). Lazernoe napylenie plenok ZnO na kremnievye i sapfirovye podlozhki [Laser deposition of ZnO films on silicon and sapphire substrates]. *Kvantovaia elektronika — Quantum Electronics, 33*(11), 975–980. https://doi.org/10.1070/QE2003v033n11ABEH002533 [in Russian].

12 Tolochko, B.P., Antokhin, Ye.I., Yukhin, Yu.M. & et al. (2011). Patent RU № 2426625 RF. Sposob polucheniia ultradispersnogo poroshka vismuta [Patent RU No. 2426625 RF. Method for producing ultrafine bismuth powder] [in Russian].

13 Givargizov, E.I. (1977*). Rost nitevidnykh i plastichnykh kristallov iz para [The growth of filamentous and plastic crystals from steam]*. Moscow: Nauka [in Russian].

14 Belyaev, A.P., Antipov, V.V., & Rubets, V.P. (2016). Formirovanie nitevidnykh kristallov sulfida kadmiia vakuumnogo ispareniia i kondensatsii v kvazizamknutom obeme [Formation of filamentous nanocrystals of cadmium sulfide by vacuum evaporation and condensation in a quasi-closed volume]. *Semiconductor Physics and Engineering, 50*(3), 420–422. https://doi.org/10.1134/S1063782616030027 [in Russian].

Information about the authors

Vladimir Oleshko (corresponding author) — Doctor of physical and mathematical sciences, Professor, The National Research Tomsk Polytechnic University, Tomsk, Russia; e-mail: *oleshko@tpu.ru*; https://orcid.org/0000-0003-0675-3591

Zixuan Li — Researcher, The National Research Tomsk Polytechnic University, Tomsk, Russia; e-mail*: li8633@yandex.ru*; https://orcid.org/0000-0001-8315-028X

Article
https://doi.org/10.31489/2024PH4/98-104
UDC 538.9

Received: 05.06.2024
Accepted: 05.08.2024

O.A. Shkoda[*]

Tomsk Scientific Center, Siberian Branch, Russian Academy of Sciences, Tomsk, Russia
([*]E-mail: O.Shkoda@dsm.tsc.ru)

Clarification of the state diagram of “Metal 1-Metal 2” systems by analyzing the “cloud” of data of combustion parameters of “Metal 1-Metal 2-Nitrogen” SHS systems

The combustion of the “Metal 1 — Metal 2 — Nitrogen” systems in the layer-by-layer mode of self-propagating high-temperature synthesis was studied. A large amount of experimental data was obtained by changing the initial synthesis parameters. As a result, a “cloud” of data was obtained, and not a single curve. Since self-consistency of many factors that ensure the propagation of the combustion wave occurs in this system, the structure of the “cloud” of data obeys strict laws characteristic of dissipative structures of nonequilibrium nonlinear systems. Variations in the initial data made it possible to obtain changes in the combustion parameters in a wide range. The combustion parameters reflect the properties of the solid-liquid medium that is formed in the chemical reaction zone in the combustion wave. The combustion temperature is between the “liquidus” and “solidus” temperatures of the corresponding “Metal 1-Metal 2” binary phase diagrams, where titanium, molybdenum, tungsten, and aluminum were used as the Metal. The resulting data “clouds” were compared with the corresponding phase diagrams of state.

It has been established that the shape and outline of the “cloud” of date for combustion parameters coincide with the shape and outline of the region bounded by the liquidus and solidus lines of the binary phase diagrams of the state “Metal 1 — Metal 2”. Clarification in the phase diagrams of state has been carried out. The other arrangement of the liquidus and solidus lines on the melting diagrams of aluminum-tungsten and aluminum-titanium is proposed.

Keywords: self-propagating high-temperature synthesis, degree of conversion, phase diagram, nitrides, data “cloud”, nonequilibrium system.

Introduction

The development of modern technology is associated with the development and production of materials that are able to operate in various extreme conditions. One of such materials are compounds of metals with nitrogen. Of important interest are metal nitrides, which have many useful properties, such as dielectric, semiconductor, chemical stability in various aggressive environments and other specific properties.

These properties of materials allow their use for products in microelectronics, laser technology, to work in contact with metal melts at high temperatures. Ternary systems “Metal 1-Metal 2-Nitrogen” exhibit unique properties characteristic of metals and ceramics [1–4]. Some compounds based on ternary systems belong to MAX-phases with a special layered nanolaminate structure, which allows them to exhibit both metallic and ceramic properties [5–7].

Self-propagating high-temperature synthesis (SHS) is a method for the production of metal nitrides, which makes it possible to obtain materials with the necessary different properties [2, 3]. However, the mechanism of formation of these compounds in the combustion wave is not fully understood, as well as the state diagrams of the systems used, which makes this work relevant.

The peculiarity of filtration synthesis is in the strong dependence of the composition of products and combustion parameters on pressure, composition of the gas medium, on the diameter of the briquette, its permeability. The way of gas reagent entering the combustion zone is important: spontaneous filtration (in which the combustion zone plays the role of a pump that sucks gas). The afterburning process also plays an important role in filtration synthesis. Due to the high temperatures that develop in the combustion zone, it can happen that the combustion temperature exceeds the melting point of the fusion products. The intermediates melt and the permeability of the sample is reduced. The gaseous reactant saturates only the layers of the sample on the surface by reaction diffusion, while the inner part of the sample often remains underreacted [8–10]. The nature of the temperature interval between the solidus temperature and the liquidus temperature (Liquidus-Solidus “L-S”) affects the mode of combustion, the completeness of conversion, the maximum temperature and the rate of combustion in this case. LS-melt means a two-phase suspension that occurs in the Liquidus-Solidus temperature interval (“L-S”).

It was noted in [10] that it is possible to construct a hypothetical diagram of state of the “Ti-Me-B” ternary system through the analysis of combustion parameters of the “Ti-Me-B” ternary system. Both in [10] and in this paper the idea that combustion parameters reflect the properties of the solid-liquid medium formed in the chemical reaction zone of the combustion wave, with the combustion temperature lying between the temperatures “L” and “S” of the corresponding double phase diagrams “Metal 1 — Metal 2”. By changing the initial synthesis parameters (composition, density, dispersity of powders, etc.), the properties of the medium (viscosity, the size of solid particles in suspension, the rate of nitrogen supply, etc.) also change.

For filtration combustion of three-component systems, such variation of initial parameters results in a “cloud” of data rather than a separate curve of dependence. The self-consistency of many factors in the system that provide propagation of the combustion wave occurs, and the structure of the data “cloud” obeys strict laws that are characteristic for dissipative structures of nonequilibrium linear systems. Different properties of the environment cause different types of formation of intermediate, unstable nitrides. Nanoscale suspension particles are the centers of chemical reactions of nitriding in a solid-liquid medium in which nitrogen is continuously supplied [9–14].

In [7, 13], devoted to the filtration combustion of a mixture of two metals in nitrogen, it was noted that all combustion parameters at appropriate scales are located within the “L-S” region of the melting diagram “Metal 1 — Metal 2”. The task arose to check to what extent the envelopes of the “cloud” lines of these combustion parameters of the ternary system “Metal 1 — Metal — Nitrogen” repeat the course of the liquidus and solidus lines of the double system “Metal 1 — Metal 2”. The systems “Ti-W” and “Ti-Mo”, having accurately constructed phase diagrams in coordinates “temperature-composition”, were chosen for verification. “Ti-Al” and “W-Al” were chosen as the diagrams that need to clarify the positions of the liquidus and solidus lines.

Experimental

Metal powders were used as initial components for synthesis: titanium of PTM grade; aluminum of ASD-4 grade of technical purity; finely dispersed molybdenum and tungsten (less than 10 μm). Gaseous nitrogen of high purity with oxygen content less than 0,001 % was used. The mixture of powders in the amount of 16 g was poured into cylindrical cups with a diameter of 20 mm and a height of more than 30 mm. The cups were made of well-permeable filter paper. Combustion was initiated by a tungsten spiral through an igniting tablet. The composition of the tablet was selected so that a combustion wave with a maximum temperature between the “L” and “S” temperature of the systems was formed. The cups were placed on a special stand, which was transferred to the reactor, which was a constant pressure unit with a volume of 3 liters. A constant nitrogen pressure of 20 atm was maintained in the reactor.

The amount of nitrogen assimilated during combustion was determined by weighing the sample before and after combustion with an accuracy of ±0.005 g. The maximum combustion temperature was measured by the thermocouple method using tungsten-rhenium thermocouples. The temperature data were recorded using a computer in the form of thermograms. Diffractograms were taken from the final synthesized combustion products on a “Drone-2” apparatus.

The completeness of conversion was determined as follows. For the case where the leading component is titanium, the completeness of transformation was calculated as the ratio of the percentage-weight content of nitrogen in titanium mononitrides of the final product to the percentage-weight content of nitrogen in stoichiometric titanium mononitride $TiN_{1,00}$:

$$\eta'=\eta_{Ti}=[N_c\cdot 100\ \%/(N_c+Ti_c)]/22{,}63\ \%.$$

Similarly, for the case where the leading component in the combustion wave is aluminum:

$$\eta''=\eta_{Al}=[N_c\cdot 100\ \%/(N_c+Al_c)]/34{,}17\ \%.$$

Here N_c is the amount of assimilated nitrogen (in grams) during SHS synthesis (calculated by weighing the sample before and after combustion with an accuracy of ±0.005 g), Ti_c and Al_c are the amounts of titanium and aluminum in the initial mixture (in grams, respectively).

The difference between η_{Ti} and η_{Al} is determined by the different stoichiometric nitrogen content: in titanium mononitride — 22.63 % wt. % and in aluminum mononitride — 34.17 % wt. %, and by the different contents of titanium and aluminum in the initial mixture. If both aluminum and titanium are nitrided to form mononitrides simultaneously, the completeness of the transformation is calculated by the following formula:

$$\eta''' = [\alpha N_c\cdot 100\ \%/(\alpha N_c+Ti_c)]/22{,}63\ \% + [\beta N_c\cdot 100\ \%/(\beta N_c+Al_c)]/34{,}17\ \%\ \text{or}$$

$$\eta''' = [\alpha N_c \cdot 4{,}419/(\alpha N_c+Ti_c)] + [\beta N_c \cdot 2{,}926/(\beta N_c+Al_c)] \text{ or}$$

$$\eta'''_{TiN+AlN}=\alpha\cdot\eta'+\beta\cdot\eta''.$$

Here α and β are the fraction of titanium and aluminum in the mixture, respectively. In arriving at this formula, we were guided by the fact that titanium and aluminum have almost equal enthalpies and nitrogen is distributed between them according to the initial composition.

Results and Discussion

The limiting factor in filtration combustion is the problem of gas delivery to the nitriding reaction site. The porosity structure of the medium is of great importance for the kinetics. If a large amount of liquid appears in the reaction zone, combustion stops due to the impossibility of gas penetration to the reaction site. In such cases, inert additives are used to lower the combustion temperature.

The composition of the synthesized product depends on the initial ratio of components. Up to 40 weight % Ti the product consists of aluminum mononitride, Al3Ti phase and pure aluminum. The diffractograms record clear, well-formed AlN peaks. In the range of 40 to 60 weight % Ti, the following are found: aluminum mononitride, titanium mononitride, TiAl phase and pure aluminum. At the ratio from 60 weight%Ti and above in the synthesized product are found: titanium mononitride, Ti3Al phase, αTi, and also, here are found small peaks of MAH phases Ti2AlN, Ti4AlN3. The diffractogram shows high broadened peaks, from which peaks of titanium mononitride, Ti3Al, αTi intermetallide with aluminum dissolved in it, emerge. Any traces of aluminum mononitride are absent [7].

An equilibrium suspension consisting of particles of solid solutions or compounds is formed when two different metals are heated above the solidus temperature. A vortex motion that entrains nitrogen gas and delivers it to the reaction site is easily formed in such a heterogeneous medium at high temperatures. In this case, the melt in any quantity is not an obstacle to the penetration of gas to the reaction centers, which are solid particles in the “L-S”-melt.

Figure 1, a shows two combined diagrams: a part of the phase diagram “Mo-Ti” and a “cloud” of values of the degree of conversion η. It can be seen that the enveloping “cloud” completely repeats the solidus and liquidus lines. Inside the cloud, the η data are located along the lines that repeat the course of the liquidus curve. Figure 1, b shows the superposition of the state diagram for the “W-Ti” systems and the “cloud” of η data taken from the combustion analysis of the “W-Ti-N” system. The lower envelope coincided exactly with the course of the solidus line. The upper envelope partially coincided with the liquidus line, the rest of the data repeat its course. Complete filling of the “L-S” space did not occur, apparently, solid suspension particles of the required size were not formed at high combustion temperatures [13–16].

“Cloud” data of maximum combustion temperatures (Tmax) are plotted on the fusibility diagram of the “Mo-Ti” system (Fig. 2, a). The presence of two “clouds” of Tmax data can be seen. The lower cloud completely coincides with the “L-S” space. The second cloud, which is located above the “L” line, is the result of “flare afterburning”, when the gaseous part of the product, consisting of suboxides, burns in the form of flares, outside the combustion wave [9]. The data inside the second “cloud” also lie on curves repeating the course of the liquidus line. Figure 2, b shows a “cloud” of combustion rate (Uc) data. If the combustion rate (Uc) data are plotted in a mirror-hyperbolic reflection, this “cloud” of data coincides completely with the “L-S” region, as does the transformation completeness (η) data. This suggests that the relationship between the combustion rate (Uc) and the degree of transformation (η) is proportional to ~1/1-η, in contrast to the cases of single metal combustion in nitrogen, for which this relationship is defined as ~1/η [12].

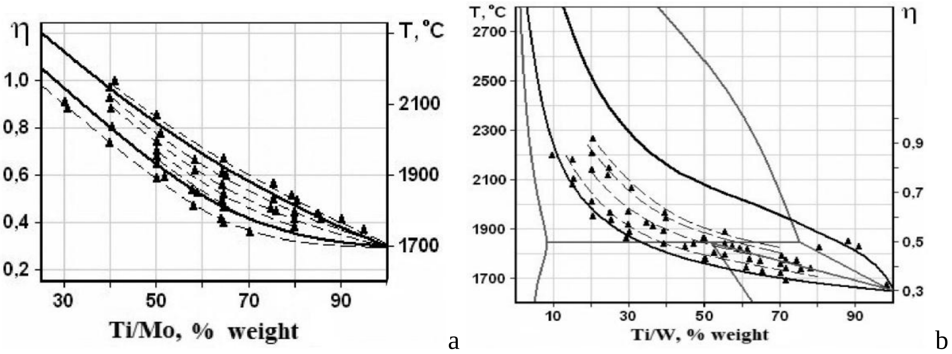

Fig. 1. a — Combined melting diagram of “Ti-Mo” with “cloud” data of the degree of conversion η,
b — Combined melting diagram of “Ti-W” with “cloud” data of the degree of conversion η.

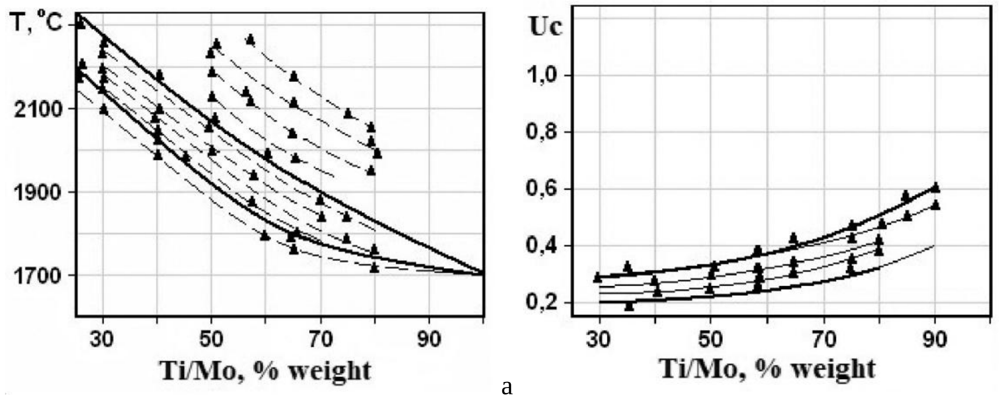

a b

Fig. 2. a — Combined melting diagram of “Ti-Mo” with “clouds” of maximum temperature (Tmax) data,
b — “Cloud” of combustion velocity (Uc) data for the “Ti-Mo-N” system.

All analyses of the combined graphs allowed us to assume a more correct position of the liquidus line, peritectic horizontals and solidus lines for the phase diagrams of state of the systems “Al-Ti” and “Al-W”. Experimental data of completeness of transformation (η) for these systems in certain concentration limits were located in the regions of known diagrams, where there is no solid-liquid melting zone, which according to the assumed mechanism of phase formation in the combustion wave cannot be. Therefore, we propose another variant of the melting diagram section, which is shown in Figure 3 (a, b) and Figure 4.

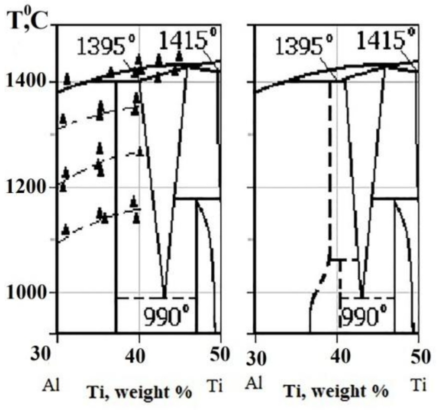

a b

Fig. 3. “Al-Ti” combined melting diagram with “cloud” of degree of transformation data (η): a) known; b) proposed.

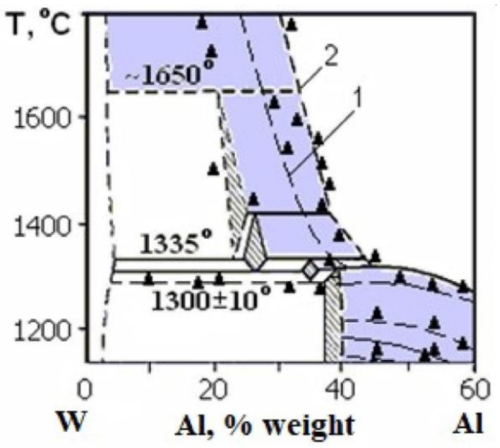

Fig. 4. “Al-W” fusibility diagram with “cloud” of conversion degree data (η): curve 1 — known, curve 2 — proposed.

The proposed changes result in a diagram with the presence of a high-temperature phase β-Al_3Ti, in addition to α-Al_3Ti, for the “Ti-Al” system. The modified melting diagram of “W-Al” differs from the previous one by the shift of the liquidus line towards increasing Al concentration starting from the temperature ~1310 ºC.

Conclusions

A different arrangement of liquidus and solidus lines in the melting diagrams of “W-Al” and “Ti-Al” is proposed. It is shown that the shape and outline of “clouds” of these combustion parameters of SHS system “Metal 1 — Metal — Nitrogen” repeat the area of the zone between “L” and “S” of double diagrams “Metal 1 — Metal 2”.

It is revealed that the relationship between UG and η for “Metal 1 — Metal — Nitrogen” SHS systems is determined by the formula: Uc~1/1-η (or η~1/1/1-Uc).

Acknowledgment

The blessed memory of Raskolenko Larisa G. whose ideas are the basis of this work.

References

1 Ivanovskii A.L. Ternary carbides and nitrides based on transition metals and subgroup IIIB, IVB elements: electronic structure and chemical bonding / A.L. Ivanovskii // Russian Chemical Reviews. — 1996. — 65(6). — P. 461–478 https://doi.org/10.1070/RC1996v065n06ABEH000299

2 Алдушин А.П. О некоторых особенностях горения конденсированных систем с тугоплавкими продуктами реакции / А.П. Алдушин, А.Г. Мержанов, Б.И. Чайкин // Докл. АН СССР. — 1972. — Вып. 204 (5). — С. 1139–1142.

3 Shugurov A.R. Microstructure and Mechanical Properties of Ti–Al–Ta–N Coatings Alloyed with Si / A.R. Shugurov, E.D. Kuzminov, Y.A. Garanin, et al. // Russ. Phys. J. — 2023. — 65. — 1762–1767. https://doi.org/10.1007/s11182-023-02828-0

4 Savchuk M.V. Influence of Conditions of the Electric Arc Discharge Burning on the Size of Microdroplet Fraction in a Nitride Coating / M.V. Savchuk, V.V. Denisov, Y.A. Denisova, et al. // Russ. Phys. J. — 2022. — 64. — P. 2155–2161. https://doi.org/10.1007/s11182-022-02568-7

5 Grenadyorov A.S. Energy Flux at the Substrate During Dual Magnetron Sputtering of TiAlN Coating / A.S. Grenadyorov, A.N. Zakharov, V.O. Oskirko, et al. // Russ. Phys. J. — 2023. — 65. — 1825–1831. https://doi.org/10.1007/s11182-023-02837-z

6 Low I.M. MAX Phases and Ultra-High Temperature Ceramics for Extreme Environments / I. M. Low, Y. Sakka, C.F. Hu. — IGI Global. Copyright. 2013. — 679p. https://doi.org/10.4018/978-1-4666-4066-5

7 Shkoda O.A. Iinfluence of Ti and Al content on self-propagating high-temperature synthesis of Ti-Al-N systems / O.A. Shkoda // Russian Physics Journal. — 2023. — 66(9). — P. 934–939. https://doi.org/10.1007/s11182-023-03026-8

8 Chlubny L. Influence of Nitrogen Pressure on ShS synthesis of Ti2AlN Powders / L. Chlubny, J. Lis, M.M. Bućko // Ceramic Engineering and Science Proceedings, Materials for Extreme Environments: Ultrahigh Temperature Ceramics and Nanolaminated Ternary Carbides and Nitrides. — 2015. — P. 251-260. https://doi.org/10.1002/9781119211747

9 Raskolenko L.G. Combustion in the Me1-Me2-N2 system: Unconventional macrostructure of combustion products / L.G. Raskolenko, O.A. Shkoda // Int. J Self-Propag. High-Temp. Synth. — 2013. — 22. — P. 84–87. https://doi.org/10.3103/S1061386213020076

10 Круглова Н.В. Самораспространяющийся высокотемпературный синтез на основе титана и сплавов III, VI, VIII групп с азотом / Н.В. Круглова, Л.Г. Расколенко, Ю.М. Максимов // Известия вузов. Цветная металлургия. —2002. — № 2. — С. 56–59.

11 Raskolenko L.G. Construction of a Hypothetical Ti-B Diagram by Analysis of Com-bustion Product of Three-Component System / L.G. Raskolenko, Yu.M. Maksimov, O.K. Lepakova // Journal of Material Synthesis and Processering. — 1995. — 3.

12 Maksimov Y.M. Combustion of vanadium-iron alloys in nitrogen / Y.M. Maksimov, M.K. Ziatdinov, A.G. Merzhanov, et al. // Combust Explos Shock Waves. — 1984. — 20. — P. 487–492 https://doi.org/10.1007/BF00782233

13 Hansen M. Compounds of Bianory Alloy / M. Hansen, K. Anherko. — New York. K., 1958.

14 Shkoda O.A. Connection of the Combustion Process of SHS System Ti-Co-N with the State Diagram / O.A. Shkoda // 7th International Congress on Energy Fluxes and Radiation Effects (EFRE). — 2020. — P. 1232–1235. Tomsk. Russia. doi: 10.1109/EFRE47760.2020.9242011. https://www.researchgate.net/publication/345763319_Connection_of_the_Combustion_Process_of_SHS_System_Ti-Co-N_with_the_State_Diagram

15 Barsoum M.W. Synthesis of Ti4AlN3 and phase equilibria in the Ti-Al-N system / M.W. Barsoum, T. El-Raghy, A. Procopio // Metall Mater Trans A. — 2000. — 31. — P. 373–378. https://doi.org/10.1007/s11661-000-0273-1

16 Samsonov G.V. Refractory compounds / G.V. Samsonov, I.M. Vinnuzkii. — Moscow: Metalurgiia. — 1976. — 560 p.

О.А. Шкода

«Металл 1–металл 2–азот» СВС жүйелерінің жану параметрлері туралы деректердің «бұлтын» талдау арқылы «металл 1-металл 2» жүйелерінің балқыту диаграммасын нақтылау мүмкіндігі туралы

«Металл 1–металл 2–азот» жүйелеріне өздігінен таралатын жоғары температуралық синтездің қабат-қабат режимінде жануы бойынша зерттеу жүргізілді. Бастапқы синтез параметрлерін өзгерту арқылы тәжірибелік мәліметтердің үлкен көлемі алынды. Құрамы, тығыздығы, ұнтақтардың дисперсиясы және басқалары сияқты синтездің бастапқы параметрлерін өзгерту арқылы ортаның қасиеттері де өзгереді, мысалы, тұтқырлық, суспензиядағы қатты бөлшектердің мөлшері, азотпен қамтамасыз ету жылдамдығы және т.б. Үш компонентті жүйелерді фильтрациялық жану үшін аталған бастапқы параметрлерді өзгерту нәтижесінде жеке қисық емес, деректердің «бұлты» алынды. Бұл жүйеде жану толқынының таралуын қамтамасыз ететін көптеген факторлардың өзіндік сәйкестігі болғандықтан, деректер «бұлтының» құрылымы тепе-теңдіксіз сызықты емес жүйелердің диссипативті құрылымдарына тән қатаң заңдарға бағынады. Бастапқы деректердің өзгеруі жану параметрлерінің кең ауқымдағы өзгерістерін алуға мүмкіндік берді. Жану параметрлері жану толқынындағы химиялық реакциялар аймағында түзілетін қатты-сұйық ортаның қасиеттерін көрсетеді. Бұл жағдайда жану температурасы титан, молибден, вольфрам және алюминий металдар ретінде пайдаланылған «металл 1-металл 2» сәйкес қос фазалы диаграммаларының «сұйықтық» және «қатты» температуралары арасында болады. Алынған деректер «бұлттары» сәйкес фазалық диаграммалармен салыстырылды. Бұл жану параметрлерінің «бұлтының» пішіні мен контуры «металл 1-металл 2» күйінің қос фазалық диаграммаларының ликвидус және солидус сызықтарымен шектелген аймақтың пішіні мен контурымен сәйкес келетіні анықталды. Фазалық диаграммалар нақтыланды. Алюминий-вольфрам және алюминий-титан балқитын диаграммаларындағы ликвидус пен солидус сызықтарының басқаша орналасуы ұсынылды. Өздігінен таралатын жоғары температуралық синтездің қабат-қабат режиміндегі «металл 1-металл 2-азот» жүйелері үшін жану жылдамдығы мен конверсия дәрежесі арасындағы байланыс формуласы анықталды.

Кілт сөздер: өздігінен таралатын жоғары температуралық синтез, түрлену дәрежесі, фазалық диаграмма, нитридтер, деректер бұлты, тепе-теңдік емес жүйе.

О.А. Шкода

О возможности уточнения диаграммы плавкости систем «металл 1–металл 2» через анализ «облака» данных параметров горения СВС систем «металл 1–метал 2–азот»

Проведено исследование горения систем «металл 1–металл 2–азот» в послойном режиме самораспространяющегося высокотемпературного синтеза. Меняя начальные параметры синтеза, получено большое количество экспериментальных данных. Варьируя начальные параметры синтеза, такие как состав, плотность, дисперсность порошков и другие, меняются и свойства среды, такие как вязкость, размер твердых частиц в суспензии, скорость поступления азота и т.д. Для фильтрационного горения трёхкомпонентных систем в результате варьирования перечисленных исходных параметров получено «облако» данных, а не отдельно взятая кривая. Поскольку в этой системе происходит самосогласование многих факторов, обеспечивающих распространение волны горения, то строение «облака» данных подчиняется строгим законам, характерным для диссипативних структур неравновесных нелинейных систем. Вариации исходных данных позволили получить изменения в параметрах горения в большом диапазоне. Параметры горения отражают свойства твердожидкой среды, которая образуется в зоне химических реакций в волне горения. Температура горения при этом находится между температурами «ликвидус» и «солидус» соответствующих двойных фазовых диаграмм «металл 1–металл 2», где в качестве металла использовались титан, молибден, вольфрам, алюминий. Полученные «облака» данных были сопоставлены с соответствующими фазовыми диаграммами состояния. Установлено, что форма и очертание «облака» данных параметров горения совпадают с формой и очертанием области, ограниченной линиями ликвидус и солидус двойных фазовых диаграмм состояния «металл 1–металл 2». Проведено уточнение в фазовых диаграммах состояния. Предложено иное расположение линий ликвидус и солидус в диаграммах плавкости «алюминий–вольфрам» и «алюминий–титан». Определена формула соотношения между скоростью горения и степенью превращения для систем «металл 1–металл 2–азот» при послойном режиме самораспространяющегося высокотемпературного синтеза.

Ключевые слова: самораспространяющийся высокотемпературный синтез, степень превращения, диаграмма состояния, нитриды, «облако» данных, неравновесная система.

References

1 Ivanovskii, A.L. (1996). Ternary carbides and nitrides based on transition metals and subgroup IIIB, IVB elements: electronic structure and chemical bonding. *Russian Chemical Reviews, 65*(6), 461–478 https://doi.org/10.1070/RC1996v065n06ABEH000299

2 Aldushin, A.P., Merzhanov, A.G., & Chaikin, B.I. (1972). O nekotorykh osobennostiakh goreniia kondensirovannykh system s tugoplavkimi produktami reaktsii [On some features of combustion of condensed systems with refractory reaction products]. *Doklady Akademii nauk SSSR — Reports of the USSR Academy of Sciences, 204* (5), 1139–1142 [in Russian].

3 Shugurov, A.R., Kuzminov, E.D., Garanin, Y.A. et al. (2023). Microstructure and Mechanical Properties of Ti–Al–Ta–N Coatings Alloyed with Si. *Russ. Phys. J*, 65, 1762–1767. https://doi.org/10.1007/s11182-023-02828-0

4 Savchuk, M.V., Denisov, V.V., Denisova, Y.A. et al. (2022). Influence of Conditions of the Electric Arc Discharge Burning on the Size of Microdroplet Fraction in a Nitride Coating. *Russ. Phys. J*, 64, 2155–2161. https://doi.org/10.1007/s11182-022-02568-7

5 Grenadyorov, A.S., Zakharov, A.N., Oskirko, V.O. et al. (2023). Energy Flux at the Substrate During Dual Magnetron Sputtering of TiAlN Coating. *Russ. Phys. J*, 65, 1825–1831. https://doi.org/10.1007/s11182-023-02837-z

6 Low, I. M., Sakka, Y., Hu, C. F. (2013). MAX Phases and Ultra-High Temperature Ceramics for Extreme Environments. *IGI Global*. Copyright, 679p. https://doi.org/10.4018/978-1-4666-4066-5

7 Shkoda, O.A. (2023). Iinfluence of Ti and Al content on self-propagating high-temperature synthesis of Ti-Al-N systems, *Russian Physics Journal*, *66*(9) 934–939. https://doi.org/10.1007/s11182-023-03026-8

8 Chlubny, L., Lis, J., & Bućko, M.M. (2015). Influence of Nitrogen Pressure on ShS synthesis of Ti2AlN Powders. *Ceramic Engineering and Science Proceedings, Materials for Extreme Environments: Ultrahigh Temperature Ceramics and Nanolaminated Ternary Carbides and Nitrides*, 251-260. https://doi.org/10.1002/9781119211747

9 Raskolenko, L.G. & Shkoda, O.A. (2013). Combustion in the Me1-Me2-N2 system: Unconventional macrostructure of combustion products. *Int. J Self-Propag. High-Temp. Synth*., 22, 84–87. https://doi.org/10.3103/S1061386213020076

10 Kruglova, N.V., Raskolenko, L.G., & Maksimov, Yu. M., (2002). Samorasprostraniaiushchiisia vysokotemperaturnyi sintez na osnove titana i splavov III, VI, VIII grupp s azotom [Self-propagating high-temperature synthesis of three-component systems on basis of titanium and alloys of III, VI, VIII groups with nitrogen]. *Izvestiia vusov. Tsvetnaia metallurgiia — News of Universities, Non-ferrous metallurgy,* 2, 56–59 [in Russian].

11 Raskolenko, L. G., Maksimov, Yu. M., & Lepakova, O. K., (1995). Construction of a Hypothetical Ti-B Diagram by Analysis of Com-bustion Product of Three-Component System. *Journal of Material Synthesis and Processering,* 3.

12 Maksimov, Y.M., Ziatdinov, M.K., Merzhanov, A.G. et al. (1984). Combustion of vanadium-iron alloys in nitrogen. *Combust Explos Shock Waves,* 20, 487–492 https://doi.org/10.1007/BF00782233

13 Hansen, M. & Anherko K. (1958). *Compounds of Bianory Alloy*. New York.

14 Shkoda, O.A. (2020). Connection of the Combustion Process of SHS System Ti-Co-N with the State Diagram. *7th International Congress on Energy Fluxes and Radiation Effects (EFRE),* 1232–1235. Tomsk. Russia. doi: 10.1109/EFRE47760.2020.9242011, https://www.researchgate.net/publication/345763319_Connection_of_the_Combustion_Process_of_SHS_System_Ti-Co-N_with_the_State_Diagram

15 Barsoum, M.W., El-Raghy, T., & Procopio, A. (2000). Synthesis of Ti4AlN3 and phase equilibria in the Ti-Al-N system. *Metall Mater Trans A*, 31, 373–378. https://doi.org/10.1007/s11661-000-0273-1

16 Samsonov G.V. & Vinnuzkii I.M. (1976). *Refractory compounds.* Moscow: Metalurgiia, 560.

Information about the authors

Shkoda Olga Aleksandrovna — Candidate of technical sciences, senior research officer, Tomsk Scientific Center of the Siberian Branch of the Russian academy of Sciences, Tomsk, Russia; e-mail: *O.Shkoda@dsm.tsc.ru*. ORCID ID: https://orcid.org/0000-0002-6068-4817

Article
https://doi.org/10.31489/2024PH4/105-113
UDC 537.527.9; 537.53

Received: 20.06.2024
Accepted: 08.08.2024

V.F. Tarasenko[*], D.V. Beloplotov, D.A. Sorokin, A.N. Panchenko

Institute of High Current Electronics SB RAS, Tomsk, Russia
([*]*Corresponding author's e-mail: VFT@loi.hcei.tsc.ru*)

Fast particles and metal vapors from electrodes with small radii of curvature during nanosecond discharges in gases

In gaps with a non-uniform electric field, the high electric fields (>1 MV/cm) are achieved with a short voltage pulse front, which are enhanced by the accumulation of positive ions at the cathode and the formation of plasma. Based on the known experimental and theoretical studies of vacuum discharge, we hypothesized that the mechanism of destructive mechanical stresses in the surface layer of electrodes should also take place during nanosecond breakdown in gases. In this paper, the radiation of diffuse discharge plasma formed between two electrodes with a small radius of curvature was investigated when the discharge gaps were filled with air, nitrogen, argon, and helium at atmospheric pressure. With a nanosecond voltage pulse duration and energy inputs into the gas of <1 mJ/cm3, the tracks of particles emitted from bright spots on the electrodes, including those at a right angle to their surface, were recorded. It is shown that the length of the tracks depends on the polarity of the electrode and that at low energy inputs in the air the tracks end with a brighter glow region. It is established that the greatest radiation intensity during discharges in four different gases (air, nitrogen, argon and helium) are found in tracks that are formed in the air. From this result, as well as from the recorded duration of track glow pulses in hundreds of microseconds, it follows that the increase in the brightness of the radiation of the ends of the tracks during propagation in the air is determined by the heating of the electrode material during the interaction of the emitted particles with oxygen.

Keywords: tip-to-tip gap, nanosecond pulses, diffuse discharge, particle tracks.

Introduction

It is known that erosion of the electrode surface occurs during the formation of bright spots on the electrodes due to explosive emission of electrons as a result of breakdown processes [1]. The formation of craters on the cathode surface in vacuum and gas-filled gaps has been recorded in many studies, see, for example [1–3] and references in these publications. During nanosecond discharges in gaps filled with various gases, damage on the cathode surface, including crater-shaped damage, in the region of bright spots before a spark channel formation is also observed [4–6]. Erosion of the electrode surface is explained by the heating of microheterogeneities due to an increase in current density in local areas to the melting temperature and rapid (explosive) evaporation of these microheterogeneities [1]. As a result, a cloud of dense plasma is formed on the surface of the electrodes with negative polarity before formation of a spark channel. In works [7, 8], devoted to the study of the mechanism of vacuum breakdown at high electric field strengths, it was established that one of the reasons limiting the electrical strength of a vacuum insulation is the effect of a strong electric field on the mechanical properties of the electrode surface. Calculations carried out in [8] showed that even in the unheated region, the size of which significantly exceeds the size of the explosive emission center, the cathode material is also exposed to destructive mechanical stresses. In this case, the primary appearance of the cathode spot during discharge in a vacuum and the formation of plasma near the electrode surface lead to multiple local destructions of its relatively smooth surface, including those at the periphery of the cathode spot.

Based on experimental and theoretical studies of breakdown in a vacuum, described by the authors of articles [7, 8]), in works [9, 10] it was suggested that the mechanism associated with the occurrence of destructive mechanical stresses should also take place during nanosecond breakdown in gases between electrodes with a small radius of curvature. Photographing the discharge with a high (up to 1.7 μm) spatial resolution in [9, 10] showed that thin luminous tracks (TLT) of particles appear in the interelectrode gap in both spark and diffuse discharges, moving along various trajectories. Shooting with a highly sensitive ICCD camera made it possible to establish that particles at a minimum distance from the electrodes are recorded with a delay of more than 1 μs, and their speed depends on the track diameter and is as high as ~ 40 m/s [9–11]. This speed is significantly less than the plasma expansion speed during explosive emission in a vacuum (~ 20 km/s), as well as the speed of a liquid metal jet at the cathode (~ 0.4 km/s) [12].

The results obtained in [9–11] aroused great interest and showed the need to continue studying the conditions for the appearance of TLT from electrodes. Attention to the observation of tracks is due to the lack of data on the registration of TLT during nanosecond diffuse discharges in a non-uniform electric field, see, for example, [13–17]. Note that during a spark discharge, a number of studies reported observation of the scattering of particles from the electrodes [8, 18], as well as the production of small-sized particles [19]. In addition, in [20], it was shown that tip erosion is observed during a corona discharge during generation of a series of Trichel pulses.

The aim of this work to study possibility of the appearance of tracks and define their shape under the conditions of a diffuse discharge in air, nitrogen, argon and helium, formed with small energy inputs.

Experimental setup and methods

The studies were performed using setup similar to that described in [9–11]. Schematic diagram of the setup is shown in Figure 1.

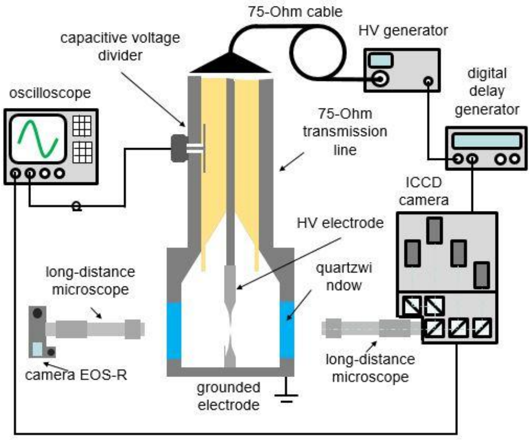

Figure 1. Block diagram of the experimental setup for studying particle tracks.

Voltage pulses from various high-voltage generators (HV), which are described in detail in [21], were fed to the input of the discharge chamber transmission line via a coaxial cable. The generators had positive or negative polarity. Minimum energy inputs into the discharge plasma were achieved using a positive polarity generator GIN-10 with a voltage pulse duration $\tau_{0.5} \approx 1$ ns (FWHM) and its rise time of $\tau_{0.1\text{–}0.9} \approx 0.7$ ns. The amplitude of the incident voltage wave in the transmission line was 11.6 kV. The energy in the pulse did not exceed 1.2 mJ. In the idle mode, the voltage across the gap doubled. Oscillograms of the incident and reflected from the gap waves of the voltage pulses and current through the gap are shown in Figure 2.

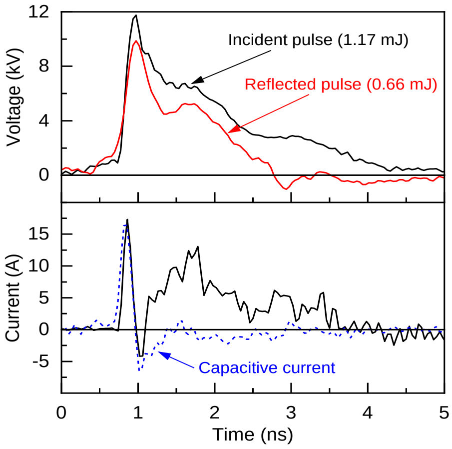

Figure 2. Oscillograms of the pulses of the incident and reflected voltage wave, as well as the current through the gap of the total and capacitive (dashed line).

The wave impedance of the transmission line with a built-in shunt was 75 Ohm. The resistance of the shunt was 8.7 mOhm. This shunt made it possible to record voltage waves incident on the gap and reflected from it, as well as to restore the voltage pulses reflected from the generator. The current through the gap was measured by a current shunt assembled from thin-film SMD resistors (Vishay Intertechnology), which was installed near the grounded electrode. The shunt resistance was 30 mOhm.

The radiative characteristics of the nanosecond discharge were recorded from the area between the electrodes, which were made from sections of sewing needles with a base diameter of 0.75 mm. The length of the needles was ~ 5.5 mm, and the rounding radii were ≈ 35 μm. Due to the low energy in the voltage pulse, the shape of the electrodes did not change significantly from pulse to pulse. We have not used before this generator to study particle tracks. The gap between the needles was 4 mm. Due to the lack of matching of the resistances of the gas-discharge, generator and transmission line, voltage pulses were reflected from the gap and from the generator. As a result, voltage pulses reflected from the generator returned to the gap with the opposite polarity. When using the GIN-10 generator, this delay was 22 ns. The main part of the energy was usually deposited in the discharge plasma during the first voltage pulse from the generator. Similar excitation modes of the diffuse discharge with other generators are described in detail in [9–11].

Waveforms of the incident wave of voltage and current pulses through the gap from the GIN-50-1 generator with the pulse duration of 13 ns are shown in Figure 3.

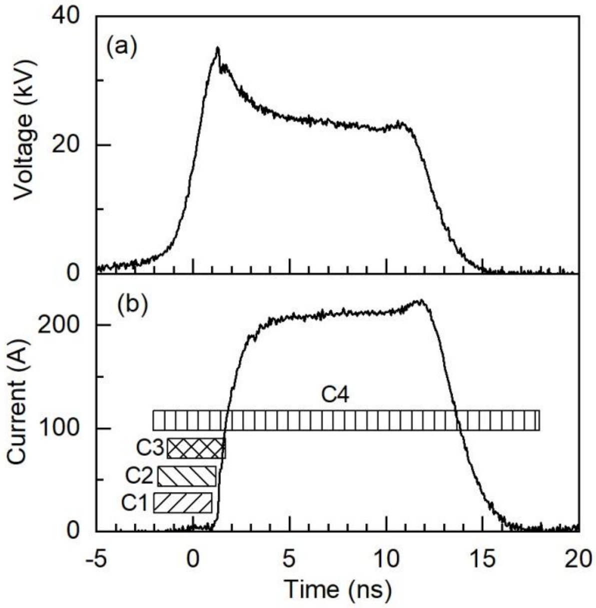

Figure 3. Waveforms of the voltage pulse on the gap and the current through the gap.
Generator GIN-50-1. Rectangles C1, C2, C3 and C4 show the time of photographing the discharge plasma on different channels of the ICCD camera.

The maximum voltage pulse amplitude at the idle reached 50 kV. The maximum energy input into the discharge plasma during the first incident pulse were achieved due to the increase in the voltage pulse duration with this generator. The positive polarity voltage pulse duration of this generator at half-height was $\tau_{0.5} \approx 13$ ns and its front was $\tau_{0.1–0.9} \approx 4$ ns.

The signals from the shunts were recorded by a Tektronix MSO64B oscilloscope (8 GHz, sampling frequency 20 samples/ns). The discharge plasma glow images were taken with a Canon EOS 2000D SLR camera (24.7 MP pixel count, 22.3×14.9 mm matrix size, 3.72 μm pixel size), which was equipped with a K2 DistaMax long-focus microscope (Infinity Photo-Optical Company) with a CF-3 lens. The microscope in this configuration provided a magnification of 3.56 with a maximum resolution of 1.7 μm. The camera exposure time was usually 0.5 s, and the sensitivity was 40000 ISO. In addition, a four-frame ICCD camera HSFC PRO with frame duration of 3 ns was used to photograph the discharge. This ICCD camera and generators could be switched on with an accuracy of about 10 ps. This made it possible to record changes in the plasma glow during the discharge over a time of tens of picoseconds. The shaded rectangles show the switching time of individual frames of the ICCD camera are shown in Figure 3. An HR2000+ES spectrometer with a 13 light guide (range 200–1150 nm; optical resolution ≈ 0.9 nm) with a known spectral sensitivity was used to measure the discharge emission spectra. The discharge chamber had two side windows made of KU-1. Photographing the discharge and measuring the emission spectra were carried out in the absence of extraneous lighting.

The gas discharge chamber was evacuated by a forevacuum pump and filled with atmospheric air with a relative humidity of 23 %, or nitrogen, argon, helium. The studies were carried out at a pressure of ≈ 760 Torr.

Results and Discussion

With the GIN-10 generator, the studies of discharge glow in air, nitrogen, argon and helium were carried out at minimum energy inputs, which in our conditions were determined by the short duration of the voltage pulse (~ 1 ns at half-height) and its amplitude (~ 11.6 kV in the incident wave). In addition, similarly to [9–11], the studies were carried out at energy inputs with higher energy inputs by 5 times or more with the GIN-50-1 generator and generators providing negative polarity of the voltage pulses. Breakdown of the gap filled with air, nitrogen or argon at pressure of 760 Torr with the GIN-10 generator was usually observed at a voltage pulse amplitude close to the maximum. Due to short rise time duration of the voltage pulse, a peak of the capacitive current was stably evident on the oscillogram of the current through the gap, which exceeded in its amplitude the conduction current, Figure 2. The energy, deposited into the gas in the first voltage pulse from the generator, in air was about 0.5 mJ and changed slightly (~ 10 %) from pulse to pulse.

As is known, before the breakdown of the gas-filled gap, the idle mode is realized, the resistance of the discharge plasma decreases due to development of the ionization processes in the gas. If forming a diffuse discharge with optimal voltage on the gap, a matched mode can be realized for some time, in which the plasma resistance in the gap is equal to the resistance of the generator transmission line. However, in the case of nanosecond voltage pulse, the process of matched energy input usually takes only a part of the voltage pulse duration. For these reasons, it is impossible to achieve complete matching of the discharge plasma resistance and the GIN-10 generator impedance. Figure 2 shows oscillograms of voltage and current pulses in the gap filled with atmospheric air, which consisted of capacitive current and conduction current. Photographs of the discharge plasma glow in air and nitrogen under conditions of track appearance at low energy inputs are shown in Figure 4 and Figure 5, respectively.

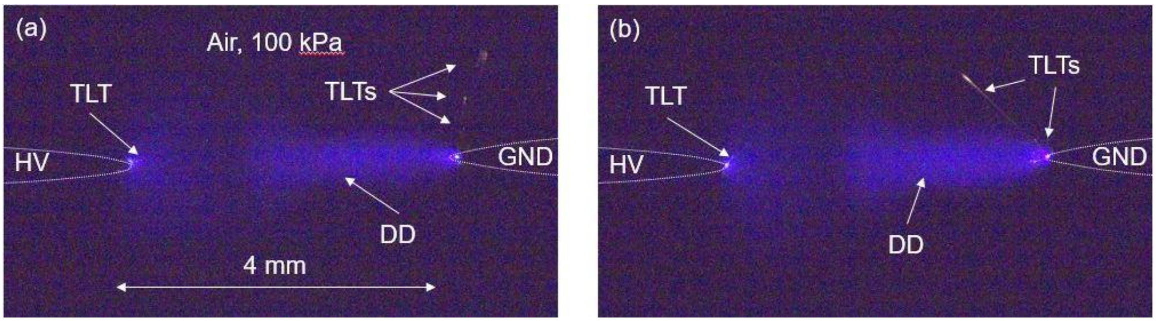

Figure 4. Photographs of the integral discharge glow in air, obtained for one voltage pulse for two different switches of the GIN-10 generator, (a) and (b). HV — high-voltage electrode, TLT — thin luminous tracks, DD diffuse discharge, GND — grounded electrode.

The discharge mode with the formation of a diffuse discharge and TLT in air for two different voltage pulses is shown in Figure 4. Tracks are visible at both electrodes, and the TLT with the greatest length were recorded at the grounded electrode, which had a negative polarity when arriving the first voltage pulse. A feature of the glow of tracks in air at low energy inputs was the greatest intensity at their end. When the energy inputs are increased to >5 mJ, see also works [9–11], most tracks in air and argon had approximately the same glow brightness along their length.

When the discharge was formed in nitrogen or in helium, in contrast to the discharge in air, the intensity of the track radiation was maximum at the bright spots on the electrodes and slowly decreased with distance from the spots, see Figure 5.

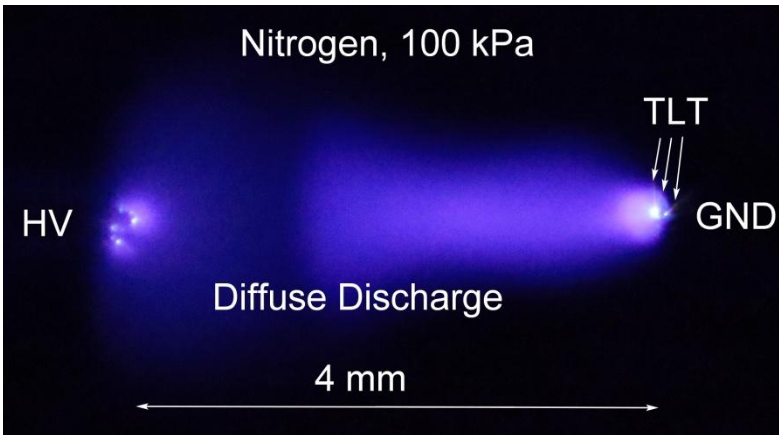

Figure 5. Photographs of the integral discharge glow in nitrogen, obtained for one voltage pulse of the GIN-10 generator. HV — high-voltage electrode, TLT — thin luminous tracks, GND — grounded electrode.

Moreover, the TLT in nitrogen had higher glow brightness than in helium, but lower than in air. It was not possible to register particle tracks in argon with the GIN-10 generator. However, TLT were observed with the GIN-50-1 generator at higher energy inputs and in [9] with the GIN-55-01 generator, when the gas pressure was decreased.

The dynamics of the formation of a diffuse discharge before the gap is closed by a spark channel is shown in Figure 6.

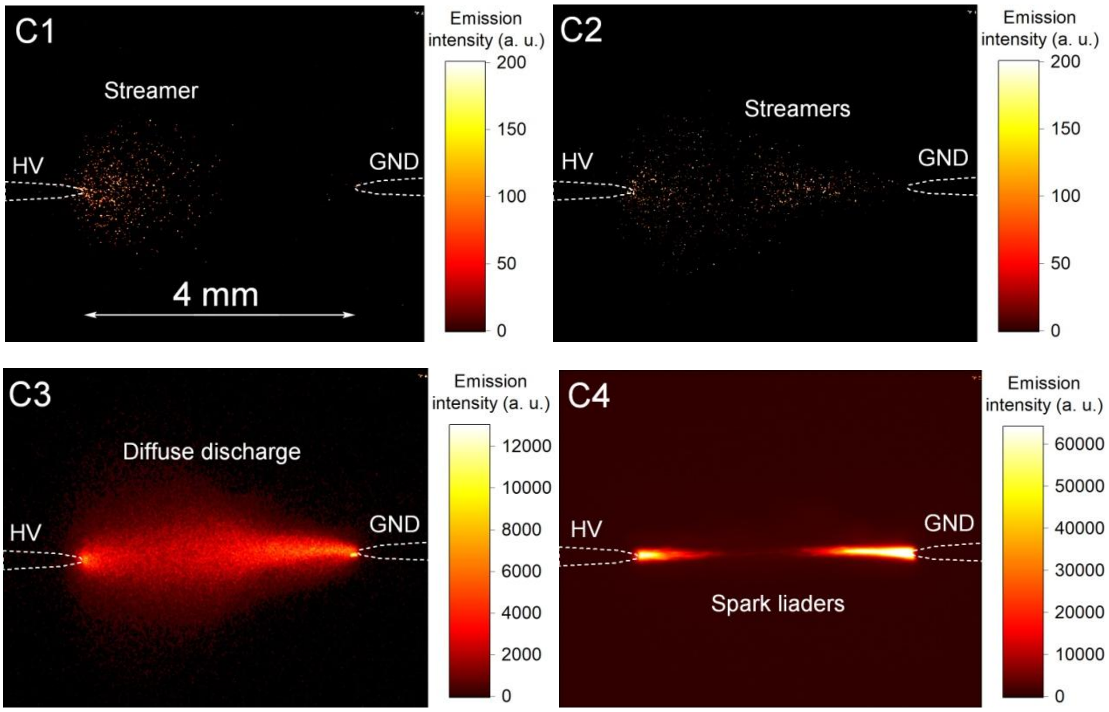

Figure 6. Images of the discharge in air obtained with the ICCD camera for the first voltage pulse from the GIN-50-1 generator, which is shown in Figure 3, where individual frames of the ICCD camera are shown as shaded rectangles. HV is the high-voltage electrode, GND is the grounded electrode.

The dynamics of the formation of the first spherical streamers is described in detail in [22, 23]. Figure 6 demonstrates the appearance of the first spherical streamer at the high-voltage electrode. Then the second streamer is formed at the grounded electrode. The streamers collide, and a diffuse discharge is formed in the gap, see frame C3, as well as the integral photographs in Figure 4 and Figure 5. When the voltage pulse duration and (or) its amplitude are increased, spark leaders grow from the electrodes. In this case, see frame C4, it can close the gap and forms a spark channel as expected, see, for example, [6, 9]).

As expected with HR2000+ES spectrometer, the bands of the second positive system (2^+) of molecular nitrogen dominated in the emission spectra during diffuse discharge stage in air and nitrogen, which is due to the high electric field strength across the gap during its breakdown by the voltage pulse with sub-nanosecond rise timed. The spectral density of the radiation energy of the main bands of the 2^+ nitrogen system was several orders of magnitude greater than that of the bands of the first positive (1^+) nitrogen system. It was not possible to register the emission spectra of the TLTs under these conditions. The difficulties in registering the emission spectra of the tracks can be explained by their thermal nature and, accordingly, by the large width of the emission spectra of the TLT. The emission of tracks during the expansion of particles from the electrodes is also affected by the high temperature of the bright plasma spots on the electrodes. These spots are known to be formed due to the explosive emission of electrons [1]. It follows from the data obtained that both processes take place during the heating of the particles that form the tracks. In nitrogen, see Figure 5, and helium, the brightness of the tracks decreased with distance from the electrodes, while in air it was maximal at the end of the tracks, see Figure 4. Apparently, particles from the electrodes can also be heated during collisions with molecules and gas atoms, but this process is less effective.

The studies performed support the hypothesis put forward in [9, 10]. The observed TLTs are traces of hot metal particles that fly out of the electrode surface in the area of its contact with dense plasma. Initially, plasma is formed during heating and thermal explosion of microinhomogeneities due to an increase in the current density in these places. The plasma created strengthens the electric field on the electrode surface. When the energy input is low, the tracks were found to have a greater length when initiated from an electrode with negative polarity. Note, that in our experiments the greatest electric field strength was achieved on the high-voltage electrode upon arrival of the first pulse from the generator. The grounded electrode was surrounded by the walls of the discharge chamber, which weakened the electric field at the tip, see Figure 1. However, the tracks were mainly generated from this electrode and spread over large distances.

Conclusions

In this paper, we study the formation of thin luminous tracks in the gap with electrodes having a small radius of curvature in diffuse discharge in air, nitrogen, argon, helium at low energy inputs into the gas. It was found that TLTs are formed mainly from the negative polarity electrode and their length becomes shorter with decreasing energy inputs into the discharge plasma. It was shown that the ends of the tracks have the greatest brightness in air, which can be explained by their additional heating during the oxidation of particles that start from the electrodes. The intensity of track radiation in nitrogen and helium is maximal near bright spots on the electrodes and decreases with distance from them, which indicates a decrease in the temperature of the particles, forming the tracks. TLTs in discharge in argon could not be registered, when energy input is low.

This research was performed within the framework of the State assignment of the IHCE SB RAS, project No. FWRM-2021-0014.

References

1 Бугаев С.П. Взрывная эмиссия электронов / С.П. Бугаев, Е.А. Литвинов, Г.А. Месяц, Д.И. Проскуровский // Успехи физических наук. — 1975. — Вып. 115. — № 1. — С. 101–120.

2 Beilis I. Plasma and Spot Phenomena in Electrical Arcs; Springer Series on Atomic, Optical and Plasma Physics / I. Beilis — Cham Switzerland: Springer, 2020. — Vol. 113. — P. 255–283. https://doi.org/10.1007/978-3-030-44747-2.

3 Korsbäck A. Statistics of vacuum electrical breakdown clustering and the induction of follow-up breakdowns / A. Korsbäck, F. Djurabekova, W. Wuensch // AIP Adv. — 2022. — Vol. 12. — Art. № 115317. https://doi.org/10.1063/5.0111677.

4 Королев Ю.Д. Наносекундный газовый разряд в неоднородном поле со взрывными процессами на электродах / Ю.Д. Королев, В.А. Кузьмин, Г.А. Месяц // ЖТФ. — 1980. — 50. — № 4. — С. 699–704.

5 Almazova K.I. Investigation of plasma properties in the phase of the radial expansion of spark channel in the pin-to-plate geometry / K.I. Almazova, A.N. Belonogov, V.V. Borovkov, Z.R. Khalikova, G.B. Ragimkhanov, D.V. Tereshonok, A.A. Trenkin // Plasma Sources Sci. Technol. — 2021. — Vol. 30. — Art. № 095020. https://doi.org/10.1088/1361-6595/aba8cc.

6 Lomaev M. Nano-and Microparticles of Carbon as a Tool for Determining the Uniformity of a Diffuse Discharge Exposure / M. Lomaev, V. Tarasenko, M. Shulepov, D. Beloplotov, D. Sorokin // Surfaces. — 2023. — Vol. 6. — P. 40–52. https://doi.org/10.3390/surfaces6010004

7 Nefedtsev E.V. Position of erosion marks on the surface of single-crystal and coarse-grained cathodes after a short-pulse vacuum spark / E.V. Nefedtsev, S.A. Onischenko // In Proceedings of the 2020 29th International Symposium on Discharges and Electrical Insulation in Vacuum (ISDEIV). — Padova, Italy. — P. 23–26. https://doi.org/10.1109/isdeiv46977.2021.9586987.

8 Нефедцев Е. Модификация материала катода вокруг центров взрывной электронной эмиссии в искровой стадии вакуумного пробоя / Е. Нефедцев, С. Онищенко // Письма в ЖТФ. — 2022. — 48. — № 22. — С. 33–35.

9 Tarasenko V.F. Thin luminous tracks of particles released from electrodes with a small radius of curvature in pulsed nanosecond discharges in air and argon / V.F. Tarasenko, D.V. Beloplotov, A.N. Panchenko, D.A. Sorokin // Surfaces. — 2023. — Vol. 6, No. 2. — P. 214–226. https://doi.org/10.3390/surfaces6020014.

10 Тарасенко В.Ф. Тонкие светящиеся треки при наносекундном разряде в неоднородном электрическом поле / В.Ф. Тарасенко, Д.В. Белоплотов, М.И. Ломаев, А.Н. Панченко, Д.А. Сорокин // Успехи прикладной физики. — 2023. — 11. — № 4. — С. 312–319.

11 Tarasenko V. F. Formation of diffuse and spark discharges between two needle electrodes with the scattering of particles / V.F. Tarasenko, D.V. Beloplotov, A.N. Panchenko, D.A. Sorokin // Plasma Sci. Technol. — 2024. — Vol. 26. — Art. № 094003. https://doi.org/10.1088/2058-6272/ad34aa.

12 Mesyats G.A. Pulsed power / G.A. Mesyats. — New York: Springer Science & Business Media, 2007. — 568 p.

13 Tardiveau P. Diffuse mode and diffuse-to-filamentary transition in a high pressure nanosecond scale corona discharge under high voltage / P. Tardiveau, N. Moreau, S. Bentaleb, C. Postel, S. Pasquiers // J. Phys. D Appl. Phys. — 2009. — Vol. 42. — Art. № 175202. https://doi.org/10.1088/0022-3727/42/17/175202.

14 Pai D.Z. Nanosecond repetitively pulsed discharges in air at atmospheric pressure — the spark regime / D.Z. Pai, D.A. Lacoste, C.O. Laux // Plasma Sources Sci. Technol. — 2010. — Vol. 19. – Art. № 065015. DOI: 10.1088/0963-0252/19/6/065015

15 Starikovskiy Andrey. Streamer breakdown development in undercritical electric field / Andrey Starikovskiy, Andrey Nikipelov, Aleksandr Rakitin // IEEE Transactions on Plasma Science. — 2011. — Vol. 39, No. 11. — P. 2606–2607. DOI: 10.1109/TPS.2011.2160740.

16 Xin Y. Plasma in aqueous methanol: Influence of plasma initiation mechanism on hydrogen production / Y. Xin, Q. Wang, J. Sun, B. Sun // Applied Energy. — 2022. — Vol. 325. — Art. № 119892. https://doi.org/10.1016/j.apenergy.2022.119892.

17 Zhang B. Streamer-to-filament transition in pulsed nanosecond atmospheric pressure discharge: 2D numerical modeling / B. Zhang, Y. Zhu, X. Zhang, N. Popov, T. Orrière, D.Z. Pai, S.M. Starikovskaia // Plasma Sources Sci. and Technol. — 2023. — Vol. 32. — Art. № 115014. DOI: 10.1088/1361-6595/ad085c. hal04267618.

18 Roth C. Generation of Ultrafine Particles by Spark Discharging Aerosol / C. Roth, G.A. Ferron, E. Karg, B. Lentner, G. Schumann, S. Takenaka, J. Heyder // Science and Technol. — 2004. — Vol. 38, No. 3. — P. 228–235. https://doi.org/10.1080/02786820490247632.

19 Tabrizi N.S. Generation of nanoparticles by spark discharge / N.S. Tabrizi, M. Ullmann, V.A. Vons, U. Lafont, A. Schmidt-Ott // J. of Nanoparticle Research. — 2009. — Vol. 11. — P. 315–332. DOI: 10.1007/s11051-008-9407-y.

20 Асиновский Э.И. Амплитудно-частотные характеристики импульсов Тричела и поведение катодного пятна в отрицательном коронном разряде / Э.И. Асиновский, А.А. Петров, И.С. Самойлов // Письма в ЖЭТФ. — 2007. — 86. — № 5–6. — С. 354–356.

21 Efanov V.M. Ultra-Wideband, Short Pulse Electromagnetics / V.M. Efanov, M.V. Efanov, A.V. Komashko, A.V. Kriklenko, P.M. Yarin, S.V. Zazoulin // New York, USA: Springer, 2010. — P. 301–305.

22 Тарасенко В.Ф. Формирование широких стримеров при субнаносекундных разрядах в воздухе атмосферного давления / В.Ф. Тарасенко, Г.В. Найдис, Д.В. Белоплотов, И.Д. Костыря, Н.Ю. Бабаева // Физика плазмы. — 2018. — 44. — №. 8. — С. 652–660.

23 Белоплотов Д. В. Формирование стримеров шаровой формы при субнаносекундном пробое газов высокого давления в неоднородном электрическом поле / Д.В. Белоплотов, В.Ф. Тарасенко, Д.А. Сорокин, М.И. Ломаев // Письма в ЖЭТФ. — 2017. — Т. 106. — № 10. — С. 627–632.

В.Ф. Тарасенко, Д.В. Белоплотов, Д.А. Сорокин, А.Н. Панченко

Газдардағы наносекундтық разрядтар кезінде қисықтық радиусы аз электродтардан жылдам бөлшектер мен металл булары

Біркелкі емес электр өрісі бар саңылауларда жоғары электр өрістеріне (>1 МВ/см) қысқа кернеу импульсі арқылы қол жеткізіледі, олар катодта оң иондардың жиналуымен және плазманың түзілуімен күшейеді. Вакуумдық разрядтың белгілі эксперименттік және теориялық зерттеулеріне сүйене отырып, біз электродтардың беткі қабатындағы деструктивті механикалық кернеулердің механизмі газдардың наносекундтық ыдырауы кезінде де жүруі керек деген болжам жасадық. Мақалада атмосфералық қысым кезінде разрядтық саңылаулар ауамен, азотпен, аргонмен және гелиймен толтырылған кезде қисықтық радиусы аз екі электрод арасында пайда болған диффузиялық разрядты плазманың сәулеленуі зерттелді. Наносекундтық кернеу импульсінің ұзақтығы және газға түсетін энергия мөлшері <1 мДж/см^3 болған кезде электродтардағы жарқын дақтардан, соның ішінде олардың бетіне тік бұрышта орналасқан бөлшектердің іздері тіркелді. Жолдардың ұзындығы электродтың полярлығына байланысты екендігі және ауадағы төмен энергия кірістері кезінде жолдар жарқыраған аймақпен аяқталатыны көрсетілген. Төрт түрлі газдағы (ауа, азот, аргон және гелий) разрядтар кезінде сәулеленудің ең жоғары қарқындылығы ауада түзілетін жолдарда болатыны анықталды. Осы нәтижеден, сондай-ақ жүздеген микросекундтық тректердің жарқыл импульстарының тіркелген ұзақтығынан ауада таралу кезінде трек ұштарының сәулелену жарықтығының жоғарылауы ұшатын бөлшектердің оттегімен әрекеттесуі кезінде электрод материалының қызуымен анықталады.

Кілт сөздер: ұшынан ұшына дейінгі саңылау, наносекундтық импульстар, диффузиялық разряд, бөлшектердің іздері.

В.Ф. Тарасенко, Д.В. Белоплотов, Д.А. Сорокин, А.Н. Панченко

Быстрые частицы и пары металлов с электродов, имеющих малые радиусы кривизны, при наносекундных разрядах в газах

В промежутках с неоднородным электрическим полем при коротком фронте импульса напряжения достигаются высокие электрические поля (>1 MV/cm), которые усиливаются за счёт накопления у катода положительных ионов и образования плазмы. На основании известных экспериментальных и теоретических исследований вакуумного разряда нами было высказано предположение, что механизм разрушающих механических напряжений в поверхностном слое электродов должен иметь место и при наносекундном пробое в газах. В статье при заполнении разрядных промежутков воздухом, азотом, аргоном и гелием атмосферного давления исследовано излучение плазмы диффузного разряда, формируемой между двумя электродами с малым радиусом кривизны. При наносекундной длительности импульса напряжения и энерговкладах в газ <1 mJ/cm^3 зарегистрированы треки частиц, вылетающих из ярких пятен на электродах, в том числе под прямым углом к их поверхности. Показано, что длина треков зависит от полярности электрода, и, что при малых энерговкладах в воздухе треки заканчиваются более яркой областью свечения. Установлено, что наибольшую интенсивность излучения при разрядах в четырёх различных газах (воздух, азот, аргон и гелий) имеют треки, которые формируются в воздухе. Из этого результата, а также из зарегистрированной длительности импульсов свечения треков в сотни микросекунд следует, что усиление яркости излучения окончаний треков при распространении в воздухе определяется нагревом материала электрода при взаимодействии вылетающих частиц с кислородом.

Ключевые слова: промежуток остриё–остриё, диффузный разряд, треки частиц.

References

1 Bugaev, S.P., Litvinov, E.A., Mesyats, G.A., & Proskurovskii, D.I. (1975). Vzryvnaia emissiia elektronov [Explosive emission of electrons]. *Uspekhi fizicheskikh nauk — Soviet Physics Uspekhi, 18*(1), 51–63 [in Russian].

2 Beilis, I. (2020). Plasma and Spot Phenomena in Electrical Arcs; Springer Series on Atomic, Optical and Plasma Physics. Cham Switzerland: Springer, 113, 255–283.

3 Korsbäck, A., Djurabekova, F., & Wuensch, W. (2022). Statistics of vacuum electrical breakdown clustering and the induction of follow-up breakdowns. *AIP Adv., 12.* Art. № 115317.

4 Korolev, Yu.D., Kuzmin, V.A., & Mesiats, G.A. (1980). Nanosekundnyi gazovyi razriad v neodnorodnom pole so vzryvnymi protsessami na elektrodakh [Nanosecond Gas Discharge in an Inhomogeneous Field with Explosive Processes on the Electrodes]. *Zhurnal tekhnologicheskoi fiziki — Technol. Phys. Lett., 50,* 699–704 [in Russian].

5 Almazova, K.I., Belonogov, A.N., Borovkov, Z.R., Khalikova, V.V., Ragimkhanov, G.B., Tereshonok, D.V., & Trenkin, A.A. (2021). Investigation of plasma properties in the phase of the radial expansion of spark channel in the pin-to-plate geometry. *Plasma Sources Sci. Technol., 30,* Art. № 095020.

6 Lomaev, M., Tarasenko, V., Shulepov, M., Beloplotov, D., & Sorokin, D. (2023). Nano-and Microparticles of Carbon as a Tool for Determining the Uniformity of a Diffuse Discharge Exposure. *Surfaces, 6,* 40–52.

7 Nefedtsev, E.V., & Onischenko, S.A. (2021). Position of erosion marks on the surface of single-crystal and coarse-grained cathodes after a short-pulse vacuum spark. *In Proceedings of the 2020 29th International Symposium on Discharges and Electrical Insulation in Vacuum (ISDEIV).* Padova, Italy, 23–26.

8 Nefedtsev, E.V., & Onischenko, S.A. (2022). Modifikatsiia materiala katoda vokrug tsentrov vzryvnoi elektronnoi emissii v iskrovoi stadii vakuumnogo proboia [Modification of the Cathode Material around the Explosive Electron Emission Centers in the Spark Stage of Vacuum Breakdown]. *Pisma v Zhurnal tekhnologicheskoi fiziki — Technol. Phys. Lett., 48,* 69–71 [in Russian].

9 Tarasenko, V.F., Beloplotov, D.V., Panchenko, A.N., & Sorokin, D.A. (2023). Thin luminous tracks of particles released from electrodes with a small radius of curvature in pulsed nanosecond discharges in air and argon. *Surfaces, 6*(2), 214–226.

10 Tarasenko, V.F., Beloplotov, D.V., Lomaev, M.I., Panchenko, A.N., & Sorokin, D.A. (2023). Tonkie svetiashchiesia treki pri nanosekundnom razriade v neodnorodnom elektricheskom pole [Thin luminous tracks during a nanosecond discharge in a nonuniform electric field]. *Uspekhi prikladnoi fiziki — Advances in Applied Physics, 11*(4), 312–319 [in Russian].

11 Tarasenko, V.F., Beloplotov, D.V., Panchenko, A.N., & Sorokin, D.A. (2024). Formation of diffuse and spark discharges between two needle electrodes with the scattering of particles. *Plasma Sci. Technol.*, *26*, Art. № 094003.

12 Mesyats, G.A. (2007). *Pulsed power*. New York: Springer Science & Business Media, 568.

13 Tardiveau, P., Moreau, N., Bentaleb, S., Postel, C., & Pasquiers, S. (2009). Diffuse mode and diffuse-to-filamentary transition in a high-pressure nanosecond scale corona discharge under high voltage. *J. Phys. D Appl. Phys*., *42*, Art. № 175202.

14 Pai, D.Z., Lacoste, D.A., & Laux, C.O. (2010). Nanosecond repetitively pulsed discharges in air at atmospheric pressure — the spark regime. *Plasma Sources Sci. Technol., 19*, Art. № 065015.

15 Starikovskiy, Andrey, Nikipelov, Andrey, & Rakitin, Aleksandr. (2011). Streamer breakdown development in undercritical electric field. *IEEE Transactions on Plasma Science, 39*(11) 2606–2607.

16 Xin, Y., Wang, Q., Sun, J., & Sun, B. (2022). Plasma in aqueous methanol: Influence of plasma initiation mechanism on hydrogen production. *Applied Energy*, *325*, Art. № 119892.

17 Zhang, B., Zhu, Y., Zhang, X., Popov, N., Orrière, T., Pai, D.Z., & Starikovskaia, S.M. (2023). Streamer-to-filament transition in pulsed nanosecond atmospheric pressure discharge: 2D numerical modeling. Plasma *Sources Science and Technology*, *32*, Art. № 115014.

18 Roth, C., Ferron, G.A., Karg, E., Lentner, B., Schumann, G., Takenaka, S., & Heyder J. (2004). Generation of Ultrafine Particles by Spark Discharging Aerosol. *Science and Technology, 38*(3), 228–235.

19 Tabrizi, N.S., Ullmann, M., Vons, V.A., Lafont U., & Schmidt-Ott, A. (2009). Generation of nanoparticles by spark discharge. *J. of Nanoparticle Research. 11*, 315–332.

20 Asinovskii, É.I., Petrov, A.A., & Samoylov, I.S. (2007). Amplitudno-chastotnye kharakteristiki impulsov Trichela i povedenie katodnogo piatna v otritsatelnom koronnom razriade [Frequency response characteristics of Trichel pulses and the behavior of the cathode spot in a negative corona discharge]. *Pisma v ZhETF — JETP Letters, 86*(5–6), 354–356 [in Russian].

21 Efanov, V.M., Efanov, M.V., Komashko, A.V., Kriklenko, A.V., Yarin, P.M., & Zazoulin, S.V. (2010). Ultra-Wideband, Short Pulse Electromagnetics. New York, USA: Springer, 301–305.

22 Tarasenko, V.F., Naidis, G.V., Beloplotov, D.V., Kostyrya, I.D., & Babaeva, N.Yu. (2018). Formirovanie shirokikh strimerov pri subnanosekundnykh razriadakh v vozdukhe atmosfernogo davleniia [Formation of Wide Streamers during a Subnanosecond Discharge in Atmospheric-Pressure Air]. *Fizika plazmy — Plasma Physics Reports, 44*(8), 652–660 [in Russian].

23 Beloplotov, D.V., Tarasenko, V.F., Sorokin, D.A., & Lomaev, M.I. (2017). Formirovanie strimerov sharovoi formy pri subnanosekundnom probe gazov vysokogo davleniia v neodnorodnom elektricheskom pole [Formation of ball streamers at a subnanosecond breakdown of gases at a high pressure in a nonuniform electric field]. *Pisma v ZhETF — JETP Letters, 106*(10), 627–632 [in Russian].

Information about the authors

Victor Tarasenko (corresponding author) — Professor, Doctor of physical and mathematical sciences, Chief researcher, Institute of High Current Electronics, Siberian branch, Russian Academy of Science, Tomsk 634055, Russia; e-mail*: VFT@loi.hcei.tsc.ru*; ORCID ID: https://orcid.org/0000-0001-5706-3211

Dmitry Beloplotov — Candidate of physical and mathematical sciences, Senior researcher, Institute of High Current Electronics, Siberian branch, Russian Academy of Science, Tomsk 634055, Russia; e-mail: *rffbdim@loi.hcei.tsc.ru*; ORCID ID: https://orcid.org/0000-0001-7807-2520

Dmitry Sorokin — Candidate of physical and mathematical sciences, Head of Laboratory, Institute of High Current Electronics, Siberian branch, Russian Academy of Science, Tomsk 634055, Russia; e-mail: *SDmA-70@loi.hcei.tsc.ru*; ORCID ID: https://orcid.org/0000-0002-6884-2525

Alexei Panchenko — Doctor of physical and mathematical sciences, Senior researcher, Institute of High Current Electronics, Siberian branch, Russian Academy of Science, Tomsk 634055, Russia; e-mail: *alexei@loi.hcei.tsc.ru*; ORCID ID: https://orcid.org/0000-0002-1701-3874

Article
https://doi.org/10.31489/2024PH4/114-122
UDC: 535.37

Received: 17.06.2024
Accepted: 19.08.2024

A.T. Tulegenova[1, 2*], G.Zh. Nogaibekova[1, 3], I.A. Saidazimov[3],
S.S. Vilchinskaya[3], A.A. Markhabayeva[1, 2]

[1]*Institute of Applied Science & Information Technology, Almaty, Kazakhstan*
[2]*Al-Farabi Kazakh National University, Almaty, Kazakhstan*
[3]*National Research Tomsk Polytechnic University, Tomsk, Russia*
([*]Corresponding author's e-mail: tulegenova.aida@gmail.com)

Spectral Characteristics of Photoluminescence Synthesized in the Field of Radiation YAGG Phosphors with Different Al/Ga Ratio

In the study the results of luminescence spectra investigating and excitation of ceramics luminescence with different Al/Ga ratios, synthesized by irradiating a mixture of initial materials with different prehistories were presented. Mixtures of oxides powders with stoichiometric composition corresponding to $Y_3Al_xGa_{5-x}O_{12}$: Ce, where x ranged from 0 to 5, were prepared for synthesis. All initial materials had a purity of no less than analytical grade. The synthesis was carried out under the influence of an electron beam with an energy of 1.4 MeV and a power density of 20 kW/cm^2. The yield of the synthesis reaction, the ratio of the sample mass to the mixture, was 90–95 %. Research has shown that decreasing the Al/Ga ratio results in a shift of the luminescence band towards the short-wavelength region of the spectrum. Additionally, the excitation spectrum changes. As the Al/Ga ratio decreases, the excitation band shifts towards the long-wavelength region around 350 nm. The characteristics of luminescence are influenced by the prehistory of the initial materials.

Keywords: Al/Ga ratio; luminescence; radiation synthesis; high-energy electron beam.

Introduction

Materials based on metal oxides have found wide application in electronics, photonics, optics, laser technology, dosimetry [1–4] due to the variety of functional properties possible for practical use. They are used in the form of crystals, ceramics, films, powders. Most often these materials are complex in composition. Materials are characterized by high resistance of their functional properties to external influences: temperature, radiation, and aggressive media. The range of such materials is very wide and continues to grow.

The main obstacle in expanding the range of possible applications is the complexity of their synthesis. The most widespread method is thermal synthesis, using which many materials with a variety of functional properties have been obtained [5]. However, the thermal synthesis methods of refractory materials are complicated, characterized by the duration of the process, as a rule of thumb for a few dozen hours. This restrains the possibility of expanding the range of materials, optimization of processes in order to increase the main functional characteristics. Less common are such synthesis methods as sol-gel [6], co-precipitation [7] and similar [8]. The main disadvantage of all these methods is the duration of the process, the need to use additional substances to facilitate synthesis, which must be discarded at the final stages of synthesis.

Combustion, flame heating methods allow to accelerate the synthesis process considerably [9, 10]. However, they require complicated procedures for purification from additionally introduced substances. The methods of pulse flame sintering [11, 12], which have been spreading in recent years, are universal, fast, but do not exclude the necessity of purification from additionally used substances. It is difficult to obtain voluminous materials with these methods.

The radiation method of synthesis by direct impact of powerful flux of high-energy electrons on the mixture of stoichiometric composition seems promising. The method was first implemented in 2017 [13, 14]. Radiation method allows to provide synthesis of ceramics in time less than 1 s without using any substances to facilitate the process. The main features and examples of synthesis are described in [15–17].

At present, in the formation period of the radiation synthesis method, it is urgent to prove the possibility of its implementation for obtaining multicomponent materials from powders of refractory monocomponent metal oxides. The confirmation of obtaining such a material can be the correspondence of its properties to the obtained materials properties by other methods. The synthesis of activated yttrium-aluminium-gallium garnets (YAGG), whose structural and luminescent properties are well studied, is of interest. The present work involves the synthesis of YAGG: Ce ceramics under different modes of radiation exposure, the study of luminescent properties and comparison with the available information on the properties of materials of similar composition were obtained by other methods used.

Ceramic synthesis

The synthesis of ceramics was carried out by direct impact of a powerful electron beam with an energy of 1.4 MeV on the mixture in a massive copper crucible using the UNU ‘Stand ELV-6’ of the INP SB RAS. The synthesis of $Y_3(Al_xGa_{1-x})_5O_{12}$: Ce ceramics with different Al/Ga ratios in the composition was carried out by electron fluxes with the energy of 1.4 MeV. The electron beam had a diameter at the mixture surface of 1 cm, scanned in the transverse direction of the crucible with an amplitude of 5 cm and a frequency of 50 Hz. During synthesis, the crucible with internal dimensions of 10x5 cm^2 was stretched relative to the scanning electron beam at a speed of 1cm/s. As a result of synthesis in the crucible samples were formed in the form of plates with the crucible dimensions. The total time of electron flux impact on the mixture treated surface of crucible was 10s. The synthesis of ceramics was realized only due to the radiation energy flux, only from the mixture materials, without additives of other materials facilitating the process.

Powder mixtures of Y_2O_3, Al_2O_3, Ga_2O_3 oxides in stoichiometric ratio were prepared for synthesis, Ce_2O_3 was added for activation in the amount of 0.5 % from the total mass of the mixture. All the initial powders were obtained from Hebei Suoyi New Material Technology Co., Ltd. (K1, K6, K7, K8) and Chemreactiv (F800, ITO). The mixtures compositions are shown in Table 1. The activator was added in the amount of 0.5 % of the mixture mass of the main components. The initial powders had purity degree not lower than 99.95, close distribution of particle sizes of powders. Sample numbers in the table means their number in the accounting system adopted by the authors. All experiments of ceramics synthesis were carried out using electron fluxes with energy 1.4 MeV, power density 20kW/cm^2.

Table 1

Description of samples and initial mixture composition

№	Sample, Initial mixture composition description	Yield% Weight M_m / M_o
630	$Y_3Al_5O_{12}$: Ce- Al_2O_3(43 %) (F800), Y_2O_3(57 %)(ИТО), Ce_2O_3 (0.5 %)(К1)	90,1
631	$Y_3Al_4GaO_{12}$: Ce — Al_2O_3 (32 %) (F800), Y_2O_3 (53 %)(ИТО), Ga_2O_3 (15 %)(К8), Ce_2O_3 (0.5 %)(К1)	94,5
632	$Y_3Al_3Ga_2O_{12}$: Ce- Al_2O_3 (28.5 %) (F800), Y_2O_3 (50 %)(ИТО), Ga_2O_3 (27.5 %)(К8), Ce_2O_3 (0.5 %)(К1)	96,6
633	$Y_3Al_2Ga_3O_{12}$: Ce-Al_2O_3 (14 %) (F800), Y_2O_3 (47 %)(ИТО), Ga_2O_3 (39 %)(К8), Ce_2O_3 (0.5 %)(К1)	97,4
634	$Y_3Al_1Ga_4O_{12}$: Ce -Al_2O_3 (6.7 %) (F800), Y_2O_3 (44.3 %)(ИТО), Ga_2O_3 (49 %)(К8), Ce_2O_3 (0.5 %)(К1)	97,4
635	$Y_3Ga_5O_{12}$: Ce -Y_2O_3 (42 %)(ИТО), Ga_2O_3 (58 %)(К8), Ce_2O_3 (0.5 %)(К1)	97,7
636	$Y_3Al_5O_{12}$: Ce -Al_2O_3 (43 %) (К7), Y_2O_3 (57 %)(К6), Ce_2O_3 (0.5 %)(К1), Ce_2O_3 (0.5 %)(К1)	96,5
637	$Y_3Al_4GaO_{12}$: Ce -Al_2O_3 (32 %)(К7), Y_2O_3 (53 %)(К6), Ga_2O_3 (15 %) (К8), Ce_2O_3 (0.5 %)(К1)	96,3
638	$Y_3Al_3Ga_2O_{12}$: Ce- Al_2O_3(К7) (28.5 %) (К7), Y_2O_3 (50 %)(К6), Ga_2O_3 (27.5 %)(К8), Ce_2O_3 (0.5 %)(К1)	96,3
639	$Y_3Al_2Ga_3O_{12}$: Ce -Al_2O_3 (14 %)(К7), Y_2O_3 (47 %)(К6), Ga_2O_3 (39 %)(К8), Ce_2O_3 (0.5 %)(К1)	97,2
640	$Y_3AlGa_4O_{12}$: Ce -Al_2O_3 (6.7 %)(К7) (К7), Y_2O_3 (44.3 %)(К6), Ga_2O_3 (49 %)(К8), Ce_2O_3 (0.5 %)(К1)	96,6
641	$Y_3Ga_5O_{12}$: Ce+ Y_2O_3 (42 %)(К6), Ga_2O_3 (58 %)(К8), Ce_2O_3 (0.5 %)(К1)	94,4

As shown in the table, the synthesis was carried out using initial materials from different manufacturers to check the validity of obtained samples.

Figure 1 shows photos of typical synthesized samples in crucibles. $Y_3Al_5O_{12}$: Ce ceramics have a characteristic bright yellow color. The color changes when Ga is introduced instead of Al.

$Y_3Al_3Ga_2O_{12}$: Ce- Al_2O_3 (28.5 %) (F800), Y_2O_3 (50 %)(ITO), Ga_2O_3 (27.5 %), Ce_2O_3 (0.5 %)(К1)

$Y_3Al_3Ga_2O_{12}$: Ce- Al_2O_3(К7) (28.5 %) (К7), Y_2O_3 (50 %)(К6), Ga_2O_3 (27.5 %), — Ce_2O_3 (0.5 %)(К1)

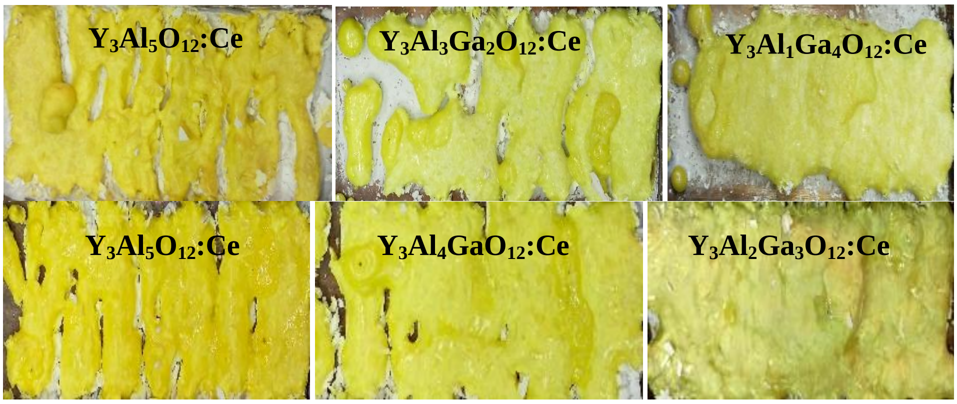

Figure 1. Photo of typical synthesized samples in crucibles

Table 1 shows the values of synthesis reaction yield. In this article we understand the synthesis reaction yield as the ratio of the synthesized sample mass to the mass of the mixture used. The mass of the obtained ceramic samples is in the range of 44–58 g. One of the reasons for the difference may be the poorly controlled process of pressing the mixture in the crucible during its leveling before synthesis and the crucibles size used. The mixture amount in the crucible was such that the electron flux did not reach the crucible bottom. The remainder of the mixture could be used in further experiments. It should be emphasized that to date the authors have succeeded in selecting initial materials that provide ceramics with a high yield of 90 to 97 %.

Spectral properties of luminescence

Excitation and luminescence spectra were measured using a Cary 5000 UV-Vis-NIR spectrophotometer. The measurements were performed as follows. Three small ceramic samples were spun off from different areas of each synthesized plate. The excitation and luminescence spectra of each were measured. In the measurements, the excitation flux was directed to the outer surface of the sample, which was facing the incoming electron flux during synthesis. Each sample was then crushed mechanically to powder. The powders were poured into cuvettes, and the excitation and luminescence spectra of each were measured. An example of excitation and luminescence spectra measurements results is shown in Figure 2. The excitation (a) and luminescence (b) spectra of ceramics (630-1, 630-2, 630-3) and their powders (630P-1, 630P-2, 630P-3) are shown. The difference in the luminescence spectra of the ceramic samples and their powders is clearly visible. The difference of luminescence spectra of samples of the same ceramics taken from one and the same plate, ceramics and complete coincidence of spectra of powders from them draws attention.

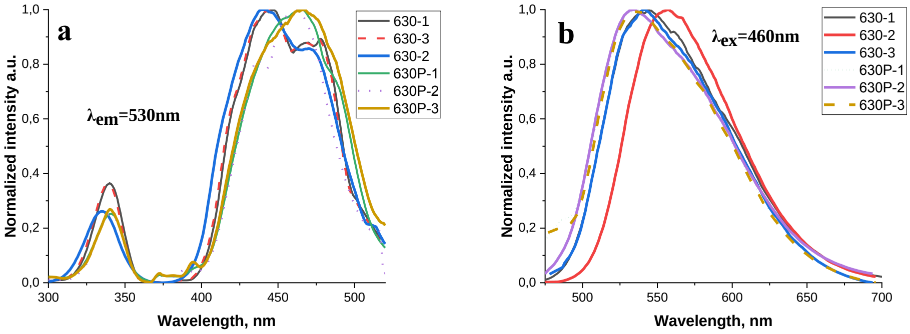

Figure 2. Excitation spectra (a) of ceramics (630-1, 630-2, 630-3)
and their powders (630P-1, 630P-2, 630P-3) and luminescence (b).

Clearly, the powders exhibit averaged characteristics of the excitation and luminescence spectra of the entire sample material. The excitation of ceramic samples by UV radiation occurs only in the near-surface region. Therefore, the contribution of surface luminescence to the integral is minimal. Considering this, only the results of the spectral characteristics of the powdered materials are presented below.

In Figure 3, the excitation spectra of luminescence at the maxima of the luminescence bands and the luminescence spectra under UV excitation at 340 and 445 nm for the powders from samples 632 and 638 are presented. The ceramic samples 632 and 638 have the same composition: $Y_3Al_3Ga_2O_{12}$: Ce, but were synthesized from initial materials with different histories. Sample 632 was synthesized from powders of Al_2O_3 (F800), Y_2O_3 (ITO), Ga_2O_3 (K8), and Ce_2O_3 (0.5 %) (K1). Sample 638 was synthesized from powders of Al_2O_3 (F800), Y_2O_3 (ITO), Ga_2O_3 (K8), and Ce_2O_3 (0.5%) (K1). Sample 638 was synthesized from powders of Al_2O_3 (K7), Y_2O_3 (50%) (K6), Ga_2O_3 (K8), and Ce_2O_3 (0.5%) (K1). The results of the measurements show that the origin of the selected initial powders for synthesis does not affect the position of the luminescence spectra bands.

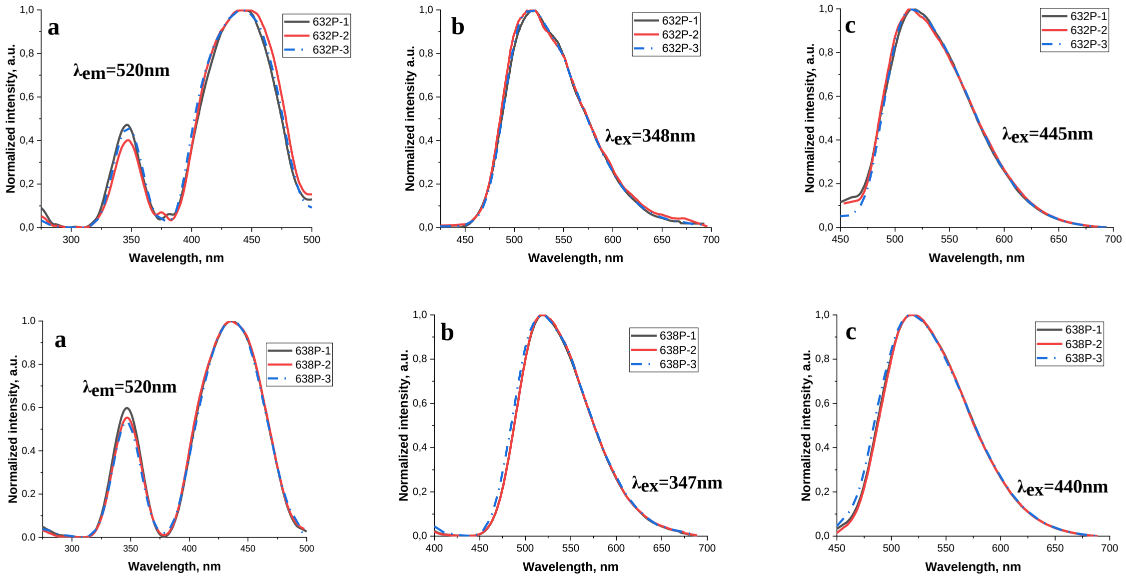

Figure 3. Excitation (a) and luminescence (b, c) spectra of powders 632 and 638

Note that the excitation and luminescence spectra of the powders do not depend on the part of the plate from which the sample was taken for measurements. This means that the luminescent properties are uniform throughout the entire plate. We emphasize that this conclusion holds well for all studies of 12 ceramic compositions.

Figure 4 shows the luminescence spectra of powders from ceramics 630–634 and 636–540 upon excitation by UV radiation in the region of 450, 350 and 220 nm. The luminescence spectra of ceramics 635 and 641 are not shown. Their luminescence is weak and could not be measured correctly by the spectrophotometer used. The luminescence of the powders clearly depends on the Al/Ga ratio in the composition. With a change in this ratio, a shift in the luminescence band and its shape occurs.

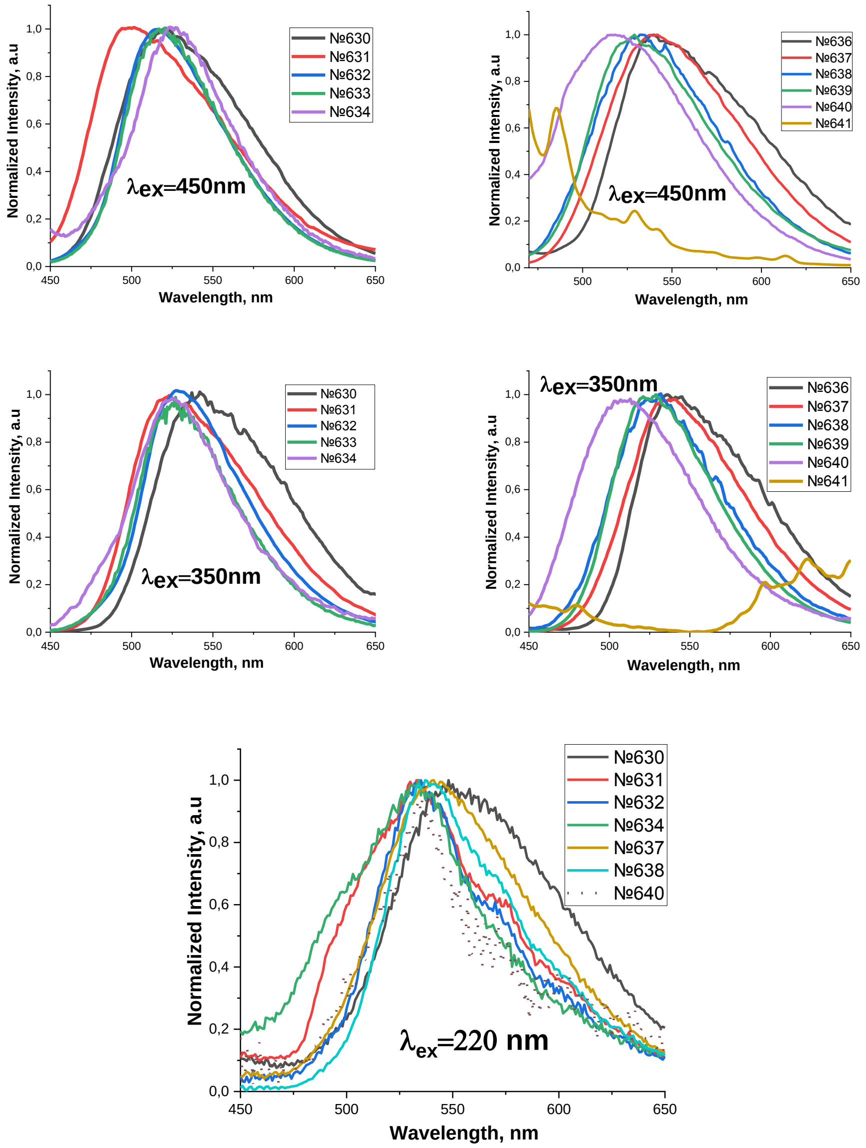

Figure 4. Luminescence spectra of powders from ceramics 630–634 and 636–540 upon excitation by UV radiation in the region of 450, 350 and 220 nm

Quantitative comparison of spectral characteristics: band positions and their half-widths are summarized in Table 2. We have intentionally provided this extensive information in table form, but not in the compact form of graphs. We believe that quantitative information in table form is more important.

Table 2

Spectral characteristics of luminescence

Initial materials for synthesis		ITO, F800, K1					K6, K7, K1				
No. Sample		630	631	632	633	634	636	637	638	639	640
Ratio Al/Ga		5/0	4/1	3/2	2/3	1/4	5/0	4/1	3/2	2/3	1/4
λ_{ex}=450 nm	λ_{em} nm	521	501	516	521	525	540	540	534	529	517
	ΔE, eV	0,416	0,444	0,331	0,313	0,321	0,375	0,368	0,356	0,35	0,412
λ_{ex}=340 nm	λ_{em} nm	543	525	530	529	525	537	540	532	530	510
	ΔE, eV	0,382	0,389	0,306	0,296	0,314	0,363	0,356	0,466	0,328	0,404
λ_{ex}=220 nm	λ_{em} nm	549	535	534	-	535	-	541	537	-	535
	ΔE, eV	0,381	0,375	0,29		0,389		0,354	0,288		0,245

It follows from the results presented in Figure 4 and Table 2 that with a change in the Al/Ga ratio in the ceramic composition, there is a shift in the band position and in their half-width. It is significant that the bandshapes and their position generally do not depend on the wavelength of UV excitation. We emphasize that the studies results of the luminescence spectra dependence on the Al/Ga ratio in the ceramic composition are in good agreement with the regularities obtained in [18] in the crystals grown study by the thermal method. This means that the ceramic samples obtained by us by the radiation express method from Y_2O_3, Al_2O_3, Ga_2O_3, Ce_2O_3 powders have the same crystalline structure as those obtained by the thermal method.

For luminescent materials, not only qualitative and spectral properties are important. Information on quantitative properties is no less necessary: the value of the luminescence flux. The most correct way to assess this value are measurements of energetic (or light) brightness. Brightness is the value of the radiation flux from a unit of the emitter surface in a single solid angle.

The luminescence brightness of the phosphor depends on the excitation conditions and the direction of measurement. However, with an unchanged mutual arrangement of all excitation sources, sample, brightness meter and unchanged excitation modes, it is possible to measure the relative brightness of a series of samples. Moreover, it can be shown that when these conditions are met, the brightness of the surfaces when changing the spectra in the range of 520–545 nm, the measurement error does not exceed 5–7 %. When the specified conditions are met, the brightness of the powder surfaces is proportional to the luminous fluxes of the samples.

During photoexcitation, the brightness value reflects the probability of energy transfer to the luminescence center. In the study of luminescence dependence YAGG: Ce ceramics on the Al/Ga ratio in its ceramic composition, relative brightness measurements are of interest.

To measure relative brightness values, a stand was created based on the CS-200 brightness meter with a constant mutual placement of all stand elements. Samples in cuvettes were placed strictly in the same place. Measurements of relative brightness values of samples were performed relative to the brightness of the SDL 4000 phosphor. Standard LED modules with radiation in the range of 450 and 340 nm were used as excitation sources.

Measurement results of relative brightness values $L_{отн} = L_{cer}/L_{SDL}$, where L_{cer}, L_{SDL} — brightness of the ceramics and the standard are shown in Figure 5 in the form of histograms.

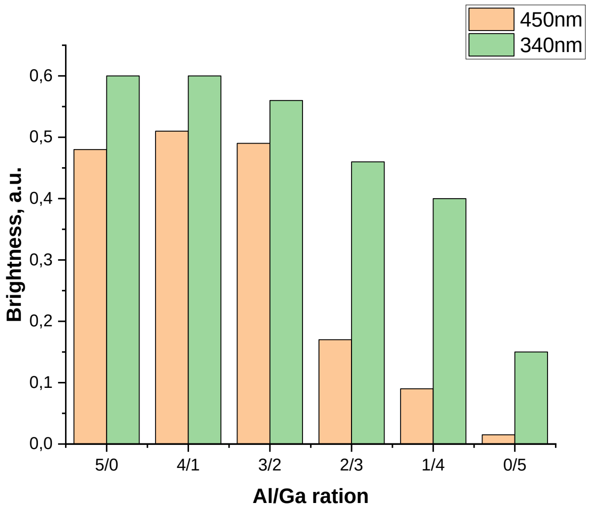

Figure 5. Dependence of relative brightness of ceramic samples on Al/Ga ratio

The dependence of the relative brightness of ceramic samples on the Al/Ga ratio under excitation in the 450 nm region qualitatively corresponds to the regularity given in [18]. With a decrease in the Al/Ga ratio, the width of the forbidden band decreases 5d the level of the Ce ion appears near the bottom of the conduction zone, passes into the conduction zone. The probability of radiative transition decreases sharply [19].

The difference of this pattern from that measured under excitation by radiation in the 340 nm region seems unexpected. Among the most probable reasons, in our opinion, is the following. The two excitation bands at λmac=460 and 340 nm are due to transitions $4F_{5/2}\rightarrow 5D_0$, $5D_1$, the broad luminescence band at λmac=520 and 580 nm is due to transitions $5D_0\rightarrow 4F_{5/2}$, $4F_{7/2}$ in Ce ions [20]. It is known that modification (so doping) affects the electronic structure of the luminescence centers [21, 22]. The position of 5d levels relative to 4f and cleavage changes with the change in the structure of the environment [23]. This manifests itself in a change in the appearance of the excitation and luminescence spectra and possibly leads to a change in the probability of radiative transitions.

Conclusion

We emphasize that the study results of the luminescence spectra dependence on the Al/Ga ratio in the composition of ceramics correspond well to the regularities obtained in [Zorenko, 2012 or 2014] when studying crystals grown by the thermal method. This indicates that the ceramic samples obtained by the radiation express method have the same crystal structure as the crystals grown by traditional thermal approaches. These results confirm the versatility and reliability of the radiation method of synthesis, opening new horizons for further research in the field of luminescence and creation of high-quality materials.

Funding

This research was funded by the Science Committee of the Ministry of Science and Higher Education of the Republic of Kazakhstan (Grant No. AP 19577213).

This research was funded by the Russian Science Foundation of the Russian Federation. (Grant No. 23-73-00108).

References

1 Auffray, D.E., Bourret-Courchesne, E., Dorenbos, P., Lecoq, P., Nikl, M., Vasil'ev, A.N., Yoshikawa, A., & Zhu, R. -Y. (2018). Needs Trends and Advances in Inorganic Scintillators. *IEEE Transactions on Nuclear Science, 65*(8), 1977–1997 https://doi.org/10.1109/TNS.2018.2840160.

2 Xia, Z., & Meijerink, A. (2017). Ce3+-Doped Garnet Phosphors: Composition Modification, Luminescence Properties and Applications. *Chem. Soc. Rev.,* 46, 275–299 https://doi.org/10.1039/C6CS00551A.

3 Zhu, D., Nikl, M., Chewpraditkul, W., & Li, J. (2022). Development and prospects of garnet ceramic scintillators: A review. *J. Adv. Ceram*., 11, 1825–1848 http://dx.doi.org/10.1007/s40145-022-0660-9.

4 Retivov, V., Dubov, V., Komendo, I., Karpyuk, P., Kuznetsova, D., Sokolov, P., Talochka, Y., & Korzhik, M. (2022). Compositionally disordered crystalline compounds for next generation of radiation detectors. *Nanomaterials*, 12, 4295 http://dx.doi.org/10.3390/nano12234295.

5 Sarukura, N., Nawata, T., Ishibashi, H., Ishii, M., & Fukuda, T. (2015). Czochralski Growth of Oxides and Fluorides. *Handbook of Crystal Growth*, 131–168. https://doi.org/10.1016/B978-0-444-63303-3.00004-3.

6 Viciute, E., Raudonyte-Svirbutaviciene, R., Zarkov, A., & Kareiva, A. (2020). Ga-Substituted Cobalt-Chromium Spinels as Ceramic Pigments Produced by Sol–Gel Synthesis. *Crystals*, 10, 1078. https://doi.org/10.3390/cryst10121078.

7 Dai, P., Cheng, J., Shen, L., Qian, Q., Guo, G., Zhang, X., & Bao, N. (2017). Photoluminescence properties of YAG: Ce3+, Pr3+ nano-sized phosphors synthesized by a modified co-precipitation method. *Journal of Rare Earths, 35*(4), 341–346. https://doi.org/10.1016/S1002-0721(17)60917-7.

8 Kyoung, H., Hyun Jeong, Y. (2009). Synthesis, Crystal Growth, and Photoluminescence Properties of YAG: Eu3+ Phosphors by High-Energy Ball Milling and Solid-State Reaction. *The Journal of Physical Chemistry C.*, 114, 226–230 http://dx.doi.org/10.1021/jp908903t

9 Ohyama, J., Zhu, C., Saito, G., Haga, M., Nomura, T., Sakaguchi, N., & Akiyama, T. (2018). Combustion Synthesis of YAG Phosphors via the Thermite Reaction of Aluminum. *J. Rare Earths*, 36, 248–256. https://doi.org/10.1016/j.jre.2017.06.014.

10 McDonald, K., & Schweitzer, G. S. (2018). Synthesis of GAGG: Ce3+ powder for ceramics using mechanochemical and solution combustion methods. *J. Am. Ceram. Soc.*, 101, 3837–3849.

11 Wu, J., Wu, X., Gao, Y., & Yan, Z. (2024). Innovations in Electric Current-Assisted Sintering for SOFC: A Review of Advances in Flash Sintering and Ultrafast High-Temperature Sintering. *Appl. Sci.*, 14, 3953. https://doi.org/10.3390/app14103953.

12 Le Godec, Y., & Le Floch, S. (2023). Recent Developments of High-Pressure Spark Plasma Sintering: An Overview of Current Applications, Challenges, and Future Directions. *Materials*, 16, 997. https://doi.org/10.3390/ma16030997.

13 Lisitsyn, V.M., Golkovsky, M.G., Musakhanov, D.A., Tulegenova, A.T., Abdullin, K.A., & Aitzhanov, M.B. (2018). YAG based phosphors synthesized in a field of radiation. IOP Conf. Series: *Journal of Physics: Conf. Series*, 1115, 052007. https://doi.org/10.1088/1742-6596/1115/5/052007.

14 Lisitsyn, V., Lisitsyna, L., Dauletbekova, A., Golkovskii, M., Karipbayev, Zh., Musakhanov, D., Akilbekov, A., Zdorovets, M., Kozlovskiy, A., & Polisadova, E. (2018). Luminescence of the tungsten-activated MgF2 ceramics synthesized under the electron

beam. *Nuclear Instruments and Methods in Physics Research Section B: Beam Interactions with Materials and Atoms*, 435, 263–267. https://doi.org/10.1016/j.nimb.2017.11.012.

15 Lisitsyn, V., Tulegenova, A., Mussakhanov, D., & Gritsenko, G. (2023). Radiation Synthesis of High-Temperature Wide-Bandgap Ceramics. *Micromachines*, 14, 2193. https://doi.org/10.3390/mi14122193.

16 Lisitsyn, V., Tulegenova, A., Kaneva, E., & Mussakhanov, D. (2023). Express Synthesis of YAG Ceramics in the High-Energy Electrons Flow Field. *Materials*, 16, 1057. https://doi.org/10.3390/ma1603105.

17 Lisitsyn, V., Mussakhanov, D., Tulegenova, A., Kaneva, E., Lisitsyna, L., Golkovski, M., & Zhunusbekov, A. (2023). The Optimization of Radiation Synthesis Modes for YAG Ceramics. *Materials*, 16, 3158. https://doi.org/10.3390/ma16083158.

18 Zorenko, Yu., Zorenko, T., Malinowski, P., Sidletskiy, O., & Neicheva, S. (2014). Luminescent properties of Y3Al5-xGaxO12: Ce crystals. *Journal of Luminescence*, 156, 102–107. https://doi.org/10.1016/j.jlumin.2014.07.011.

19 Dorenbos, P. (2013). Electronic structure and optical properties of the lanthanide activated RE3(Al1-xGax)5O12 (RE=Gd, Y, Lu) garnet compounds. *Journal of Luminescence*, 134 https://doi.org/10.1016/j.jlumin.2012.08.028

20 Dorenbos, P. (2002). 5d-level energies of Ce3+ and the crystalline environment. IV. Aluminates and "simple" oxides. *Journal of Luminescence*, 99, 283–299 https://doi.org/10.1016/S0022-2313(02)00347-2

21 Yang, H.S., & Kim, Y.S. (2008). Energy transfer-based spectral properties of Tb-, Pr-, or Sm-codoped YAG nanocrystalline phosphors. *Journal of Luminescence*, 128, 1570–1576 http://dx.doi.org/10.1016/j.jlumin.2008.03.003

22 Yang, H.S., Lee, D.K., & Kim, Y.S. (2009). Spectra variations of nano-sized Y3Al5O12: Ce phosphors via codoping/substitution and their white LED characteristics. *Mater. Chem. Phys.*, 114, 665–669 http://dx.doi.org/10.1016/j.matchemphys.2008.10.019 A

23 Ha, H., Yang, S., & Park, S. (2024). Photoluminescence Spectra Correlations with Structural Distortion in Eu3+- and Ce3+-Doped Y3Al5-2x(Mg, Ge)xO12 (x = 0, 1, 2) Garnet Phosphors. *Materials*, 17, 2445. https://doi.org/10.3390/ma17102445.

А.Т. Тулегенова, Г.Ж. Ногайбекова, И.А. Сайдазимов, С.С. Вильчинская, А.А. Мархабаева

Әр түрлі Al/Ga қатынасы бар YAGG сәулелену өрісінде синтезделген люминофордың фотолюминесценциясының спектрлік сипаттамалары

Мақалада әртүрлі бастапқы материалдардың қоспасын сәулелендіру арқылы синтезделген әртүрлі Al/Ga қатынасы бар керамиканың люминесценция және қозу спектрлерін зерттеу нәтижелері келтірілген. Синтез үшін $Y_3Al_xGa_{5-x}O_{12}$: Ce стехиометриялық құрамы бар оксид ұнтақтарының қоспалары дайындалды, мұндағы x 0-ден 5-ке дейін өзгереді. Барлық бастапқы материалдар аналитикалық материалдардан төмен емес тазалыққа ие болды. Синтез энергиясы 1,4 МэВ және қуат тығыздығы 20 кВт/см^2 болатын электронды сәуленің әсерінен жүргізілді. Синтез реакциясының шығымы — үлгінің массасының қоспаның массасына қатынасы — 90–95% құрады. Зерттеулер көрсеткендей, Al/Ga қатынасының төмендеуі люминесценция жолағының спектрдің қысқа толқынды аймағына ауысуына әкеледі. Сонымен қатар, қозу спектрі де өзгереді. Al/Ga қатынасы төмендеген кезде қозу жолағы шамамен 350 нм ұзын толқынды аймаққа ауысады. Люминесценцияның сипаттамаларына бастапқы материалдардың тарихы әсер етеді.

Кілт сөздер: Al/Ga қатынасы, люминесценция, радиациялық синтез, жоғары энергиялы электронды сәуле.

А.Т. Тулегенова, Г.Ж. Ногайбекова, И.А. Сайдазимов, С.С. Вильчинская, А.А. Мархабаева

Спектральные характеристики фотолюминесценции синтезированных в поле радиации YAGG люминофоров с различным соотношением Al/Ga

В статье представлены результаты исследования спектров люминесценции и возбуждения люминесценции керамики с различным соотношением Al/Ga, синтезированной путем облучения смеси исходных материалов с различной предысторией. Для синтеза были подготовлены смеси порошков оксидов со стехиометрическим составом, соответствующим $Y_3Al_xGa_{5-x}O_{12}$: Ce, где x варьируется от 0 до 5. Все исходные материалы имели чистоту не ниже аналитической. Синтез проводился под воздействием электронного пучка с энергией 1,4 МэВ и плотностью мощности 20 кВт/см^2. Выход реакции синтеза — отношение массы образца к массе смеси — составил 90–95 %. Исследования показали, что уменьшение соотношения Al/Ga приводит к смещению полосы люминесценции в коротковолновую область спектра. Кроме того, изменяется спектр возбуждения. При уменьшении соотношения Al/Ga полоса возбуждения смещается в длинноволновую область около 350 нм. На характеристики люминесценции влияет предыстория исходных материалов.

Ключевые слова: соотношение Al/Ga, люминесценция, радиационный синтез, высокоэнергетический электронный пучок.

Information about the authors

Aida Tulegenova (corresponding author) — Candidate of physical and mathematical sciences, Acting assistant professor, Institute of Applied Science & Information Technology, al-Farabi Kazakh National University, Almaty, Kazakhstan; e-mail: *tulegenova.aida@gmail.com*; https://orcid.org/0000-0002-5701-6674

Gulnur Nogaibekova — Master of science, Senior lecturer, Institute of Applied Science & Information Technology, National Research Tomsk Polytechnic University, Tomsk, Russia; e-mail: *zheniskyzy_nur@mail.ru*; https://orcid.org/0009-0008-8688-4279

Ibrokhimkhon Saidazimov — Master of science, National Research Tomsk Polytechnic University, Lenin ave., 30, 634050, Tomsk, Russia; e-mail: *ias121@tpu.ru*

Svetlana Vilchinskaya — Candidate of physical and mathematical sciences, Associate Professor, National Research Tomsk Polytechnic University, Lenin ave., 30, 634050, Tomsk, Russia; e-mail: *svetvil@tpu.ru*; https://orcid.org/0000-0002-1251-3773

Aiymkul Markhabayeva — PhD, Acting assistant professor, Institute of Applied Science & Information Technology, al-Farabi Kazakh National University, Almaty, Kazakhstan; e-mail: *aiko_marx@mail.ru*; https://orcid.org/0000-0002-0657-422X

Article
https://doi.org/10.31489/2024PH4/123-132
UDC 535.015

Received: 00.00.2024
Accepted: 00.00.2024

A.A. Zvekov[1*], A.V. Kalenskii[1], A.V. Ivanov[1], A.P. Borovikova[1], D.R. Nurmuhametov[2]

[1]*Kemerovo State University, Kemerovo, Russia*
[2]*Federal Research Center of Coal and Coal Chemistry SB RAS, Kemerovo, Russia*
(**Corresponding author's e-mail: aazvekov@yandex.ru)*

Non-linear optic properties of colloids prepared by metal targets' laser ablation in dimethylsulfoxide

A set of colloids on the base of aluminum, nickel, and zinc was prepared by their targets' ablation in dimethylsulfoxide medium. The samples were characterized with UV-vis spectroscopy, transmission electron microscopy, and dynamic light scattering methods. The substantial non-linear attenuation was observed with z-scan techniques using pulsed neodymium laser (532 nm, 14 ns). The transmittance of the samples diminishes when the light intensity increases. The photoacoustic signal amplitude rises with the energy density increasing according to the sublinear law. The dependencies of the attenuation linear coefficient and pressure generation efficiency on the pulse energy density were described with power laws with a threshold of the effect and the parameters were estimated. We found out that the dependencies' parameters change when the colloids were diluted. The pear pressure was determined using ferrocene as a calibration standard. It is shown that the values of peak pressure could not be explained in terms of thermal expansion of the substance. The results are discussed in terms of the non-linear attenuation mechanism concerned on the substance evaporation leading to vapor bubbles formation around the nanoparticles.

Keywords: ablation, dimethylsulfoxide, non-linear light attenuation, photoacoustic spectroscopy, laser irradiation.

Introduction

Non-linear light attenuation poses an important place among the non-linear optics phenomena because it can be used in the intensity selection devices. Colloid metals and systems based on them performs significant dependence of the transmittance on the energy density of the pulsed [1] or power density of the continuous wave laser irradiation [2]. Numerous results were obtained in that way that make it possible to solve applied problems.

Silver nanoparticles were obtained by metal target in ethanol ablation and their influence on the curcumin dye fluorescence and nonlinear light absorption was studied [3]. The authors found out that fluorescence intensity increases linearly and normalized transmittance in focus decreases almost linearly with silver nanoparticles concentration increasing while the fluorescence decay time remains unchanged. The silver nanoparticles coated with silica are able to shift the nonlinear attenuation of methylene blue depending on the dye to nanoparticles concentrations ratio [4]. At low ratio the bleaching is observed changed to absorption increasing at the high ones. The effect is discussed as increasing in the triplet state absorption cross section of the dye. Gold and platinum nanoparticles were prepared with laser ablation synthesis as well as the respective bimetallic nanoparticles with laser molding of nanoparticles [5]. These nanoparticles show significant non-linear absorption and refraction and they are heated efficiently with stationary laser at the wavelength 403 nm. The silver coated gold nanoparticles were synthesized in [6] by metals reduction with Jatoba extract. The light absorption of prepared colloid was tested with thermal lens techniques. The boron- Antimony -europium glasses containing silver nanoparticles whose non-linear absorption and refraction coefficients are linearly dependent on silver content were prepared in [7]. It was shown in [8] that commercial silver and zinc nanopartciles performs significant non-linear light attenuation at the wavelength 1550 nm.

At the same time, the definite mechanisms of non-linear attenuation of light remain unclear in many cases that lead to insufficiently predictable results when the sample parameters are changed. The concentration of metal nanoparticles influence is seldom discussed as well as the effects accompanying the non-linear attenuation of laser beams. Thermalization always accompanies the absorption of laser irradiation [9], so their study as photoacoustic effect [10] or themal lensing [6] can give essential information on the absorption features.

The aim of the work is to study the non-linear light attenuation and accompanying effects in the model metal colloids prepared with laser ablation method.

The main tasks are:

1. Preparation of the colloids on the aluminum, nickel, and zinc base with ablation method.
2. Research into optic characteristics and photoacoustic response of these colloids varying the laser light intensity and solution concentration.
3. Results description with empiric models and discussion.

We used ablation products of aluminum, zinc, and nickel in dimethylsulfoxide (DMSO) as experimental samples. The methods of noble metal nanoparticles synthesis with ablation under the layer of water or organic solvents are descried in [10–12]. Aluminum nanoparticles formed by metal ablation in chloroform and carbon tetrachloride showing pronounced non-linear attenuation were prepared in [13]. One of the problems in the ablation under solvent layer approach is byproducts formation. Utilization of solvents less reactive than water is one of the ways to inhibit formation of the oxides. Increasing in viscosity of the solvent hiders the sedimentation. From that point of view, utilization of DMSO which is more viscose than water is able to be beneficial in the products properties. At the same time DMSO decomposition could give additional byproducts such as carbon [14], sulfides or oxides. Silver sulfide forms in the case of silver ablation in DMSO, for instance [15].

Experimental section

Synthesis of the nanoparticles, z-scan and photoacoustic measurements were done with YAG-Nd laser Solar LQ929 operated in the Q-switch mode with pulse duration full width at half maximum 14 ns. A round 8 mm aperture was used for cutting the peripheral part of the beam central part of the beam, so the intensity fallen on the sample was almost uniform in the spot.

Colloids were synthesized by pulsed irradiation with main wavelength of YAG-Nd laser of metal targets sink in DMSO in a beaker. The pulses frequency was 10 Hz. The solvent was agitated with magnetic stirrer during the irradiation. Horizontal laser beam was focused on the vertical target with a lens having focus length 5 cm so the spark at the target surface was pronounced. The energy of the beam was taken as 50 mJ initially with subsequent increasing as the turbidity of the solution hindered the ablation. The beaker was placed on the table with variable height which allowed us to shift the point of the beam action on the target surface. The turbid yellow-to-gray colloid solution formed as a result of laser pulsed irradiation of the target. Aluminum concentration estimated by the target mass losses was 196 μg/ml. Tough partial sedimentation of the solid was observed after the storage the colloid could be homogenized with ultrasonification. The colloidal products of zinc and nickel targets were prepared the same way. The concentration of metals in DMSO were estimated at 102 μg/ml and 100 μg/ml in the cases of zinc and nickel respectively. The photoacoustic and dynamic light scattering measurements were conducted with colloids diluted 12.5 times that did not suffer from sedimentation.

The samples were characterized with transmission electron microscopy (TEM) using electron microscope JEOL-2100. Dynamic light scattering was done with Malvern Zetasizer Nano ZS (Malvern Instruments). The UV-vis spectra of the colloids were measured with the spectrophotometer Shimadzu UV-3600.

The photoacoustic effect and laser beam attenuation by colloid ablation products was studied on the facility based on YAG-Nd laser operating in the Q-switch mode (pulse duration 14 ns, wavelength 532 nm). The cuvette filled with colloid solution was placed on the stage that could be moved along the optical rail. In the case of photoacoustic measurements the cuvette thickness was 2 cm and the sample was situated at the lens focus (*f*=25 см). The beam diameter in the focal plane was estimated at 485 μm. The pulse energy varied with the neutral light filters placed on the beam path. The photoacoustic signal was measured with a sensor on the PZT ceramics whose aluminum “acoustic delay” sinks in the colloid from the top at the center or near the front glass of the cuvette. The voltage generated by the acoustic sensor when it received the acoustic wave was transferred to the resistance of the oscilloscope. We used ferrocene solution in DMSO (5 mg/ml) as a standard.

The photoacoustic signals were processed as follows. The noises were eliminated with the moving average approach. This method has an essential drawback that is diminishing of the maximum and minimum values in the absolute scale. For that reason, we approximated the signal near these points with parabolic functions determining the extreme values. The dispersion and confidence interval at the confidence probability level 95 % were calculated for each extreme value.

The non-linear attenuation was studied with open aperture z-scan method using the same facility by moving the sample stage along the optic rail. We did not dilute the colloidal solutions in the case using the cuvette with sample thickness 1 cm. The energy of the laser pulse was determined with OPHIR Photonics detector. The beam radius at the sample surface was determined by the spot diameter left on the photofilm situated in front of the cuvette. The radii were approximated with Raleigh equation; the radius in the focus was estimated as 263 μm and the confocal distance as 1.43 cm. The measurements of the transmittance and photoacoustic signal were done 5 times for each conditions used.

Results

TEM images of the aluminum and nickel ablation products in DMSO show metal nanoparticles free or covered by substance with lower density (Fig. 1).

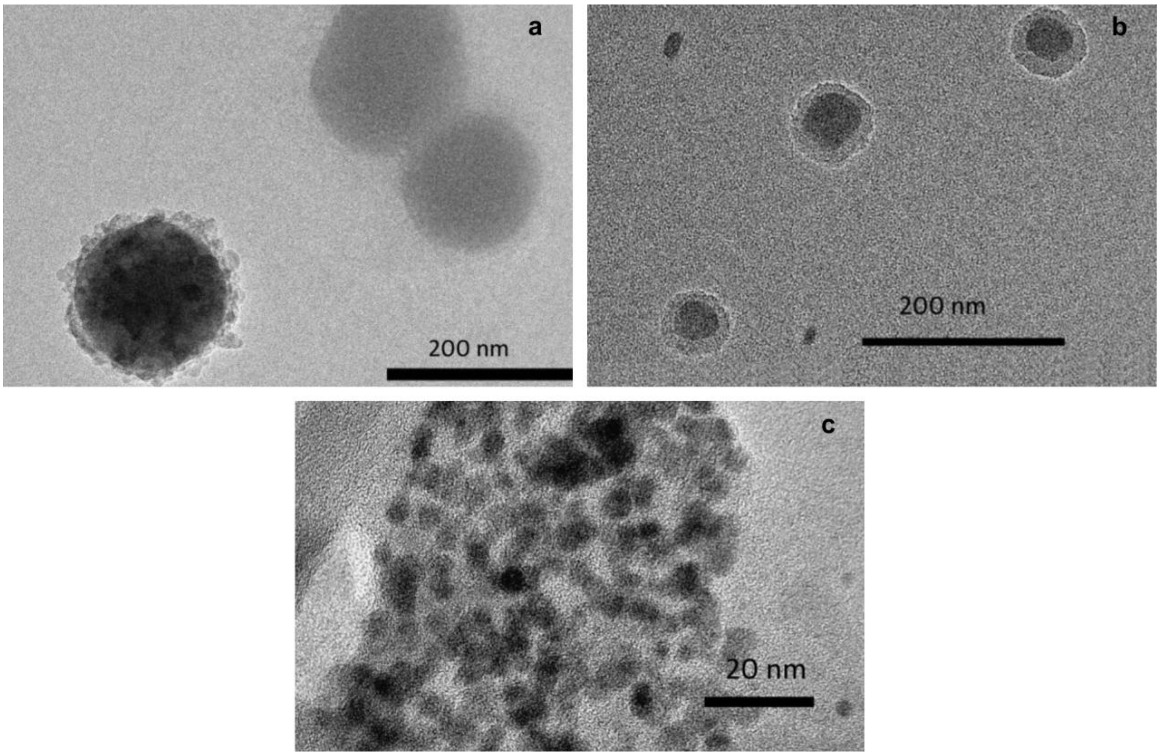

Figure 1. TEM images of aluminum (a), nickel (b), and zinc (c) colloid ablation products in DMSO.

In the aluminum case small particles with interplane distance about 0.6 nm were found, which is close to interplane distance for one of the carbon forms [16]. TEM images of sinc ablation products show agglomerates of extremely fine nanoparticles.

The optical attenuation spectra of the systems studied are presented in Figure 2 (cuvette thickness was 1 cm).

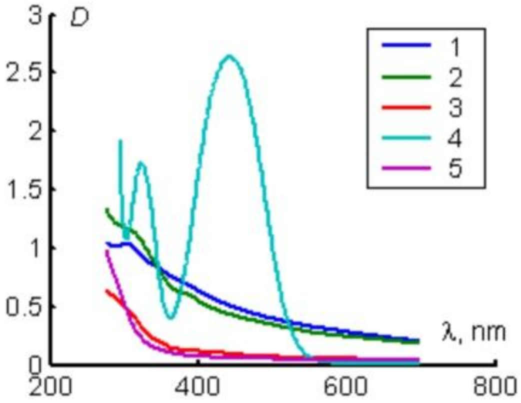

Figure 2. Attenuation spectra of zinc (1), nickel (2) and aluminum (3 diluted 10 times), and ferrocene in DMSO

The significant background level in the high wavelength area is observed that can be linked with carbon particles formation of metal particles covered with carbon shell [14]. The sulfide formation, spectrum of which is affected significantly by the stochiometry [17], while absorption maximum is situated near 300 nm [18], is possible in the zinc case. Nickel can also produce sulfides and oxides as ablation byproducts.

The dynamic light scattering results are presented in Table 1.

Table 1

Particle sized determined with dynamic light scattering

№	Target	Particles size, nm			
		By *I*	Rel. peak area, %	By *N*	Rel. peak area, %
1	Zn	1.1±0.4 340±210	18.0 82.0	0.8±0.2	100
	Zn (US)	500±100	100	480±110	100
2	Ni	170±36 500±100	4.6 95.4	164±39 460±100	16.1 83.9
	Ni (US)	265±80 530±500	97.4 2.6	240±80	100.0
3	Al	58±11 200±50	12.3 87.7	47±10 190±50	96.9 3.1

The aluminum ablation products are nanoparticles with typical diameter 47 nm and their agglomerates of the size about 190 nm. The dymanic aggregation or sedimentation were not found in the aluminum ablation products' case. Zinc ablation products have typical size 1 nm, though these small particles are strongly agglomerated. The agglomerate size in the nickel case is 460 nm. Both zinc and nickel ablation products agglomeration extent is changed by ultrasonification that evidences the unstability of these colloids.

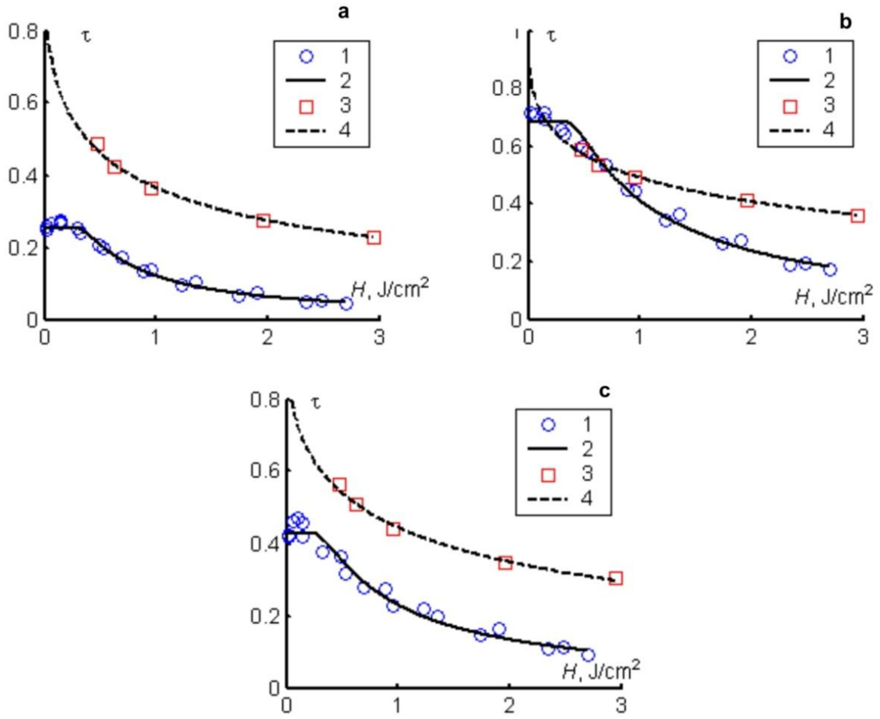

Figure 3. The trasmittance dependence of aluminum (a), nickel (b), and zinc (c) colloid ablation products on the pulse energy density measured for initial samples in 1 cm cuvette (1) and diluted in 12.5 times in 2 cm cuvette (3) with their approximation (2, 4).

Figure 3 presents the transmittance of the colloids of the laser beam at the wavelength 532 nm versus its energy density. The energy density was corrected by the beam reflectance at the cuvette wall taking into account. The data were measured with z-scan method and as additional information found in the photoacoustic experiments. The increasing in the laser pulse energy density makes the transmittance decrease for both three systems studied. We assumed the power law dependence of the attenuation linear coefficient on the energy density with some effect threshold H_c one arrives at the following equation for transmittance:

$$\mu = \mu_0 \cdot \begin{cases} 1, H < H_c, \\ \left(H/H_c\right)^n, H \geq H_c \end{cases}, \tag{1}$$

where μ_0 is the attenuation linear coefficient in the Beer's law range (linear range), n is the power value, and H is incident energy density. Using the following transmittance dependence on the energy density was derived:

$$\tau = \begin{cases} \exp\left(-\mu_0 l\right), H_0 \leq H_c, \\ \frac{H_c}{H_0} \exp\left[-\mu_0 l + \frac{1}{n} \cdot \left(1 - \left(\frac{H_c}{H_0}\right)^n\right)\right], H_c < H_0 \leq H_c \cdot \left(1 - n\mu_0 l\right)^{1/n}, \\ \left[1 + n\mu_0 l \cdot \left(\frac{H_0}{H_c}\right)^n\right]^{-1/n}, H_0 > H_c \cdot \left(1 - n\mu_0 l\right)^{1/n} \end{cases} \tag{2}$$

where $H_0 = H_{inc} \cdot (1 — \rho_{cell})$ is energy density on the front boundary of the sample which is the incident one corrected by the cell wall reflection ($\rho_{cell} \approx 10$ %).

The approximation results are shown in Figure 3 at the sample thickness 1 cm (initial concentration) with solid lines. The respective variable parameters are presented in Table 2. In the aluminum ablation product case the attenuation coefficient in the Beer's law range found with spectrophotometrical approach and extrapolated in the z-scan measurements coincide. The spectrophotometry gives 1.9 higher the linear attenuation coefficient in the Beer's limit than z-scan results' extrapolations in the nickel case, while for zinc ablation products the difference is about 5 %. This discrepancy evidences the instability of the colloids and changing of their properties during the storage, agreeing with the conclusion of the ultrasonification influence on the average aggregates size estimated with dynamic light scattering.

The transmission coefficients of the colloid ablation products 12.5 times diluted in the cuvette with 2 cm thickness are shown in Figure 3. These results were obtained along with the photoacoustic data, so the linear range was not reached, as the photoacoustic signal was too low in it. For that reason, the linear attenuation coefficient in the Beer's range was taken as the determined in the z-scan measurement divided by the dilution coefficient. The approximated dependencies are presented as dashed curves in Figure 3; the respective parameters determined could be found in Table 2. The comparison of the parameters determined in z-scan and photoacoustic experiments revealed that the critical energy density of the non-linear attenuation decreases by order of magnitude and power n decreases in 2-3 times for diluted solutions. The power n is a strong parameter, while critical energy density depends on the linear absorption coefficient in the Beer's range. The colloid ablation products of nickel and zinc targets are rather instable, so the critical energy densities for such colloids could vary in 0.5–2 times. Nonetheless, the conclusion on the critical energy density diminishing after the dilution is valid for every system studied.

The typical photoacoustic signal read with an oscilloscope is shown in Figure 4. The nickel target ablation product was used when this curve was measured; the sensor was situated in front of the cuvette; the energy density was 0.47 J/cm^2.

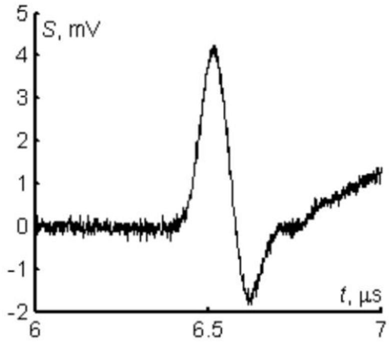

Figure 4. The typical photoacoustic signal

The first maximum on the photoacoustic curve is concerned on the compression wave due to the substance expansion in the irradiated zone. The maximum amplitude is linked with the linear absorption coefficient and energy density of the pulse. The ferrocene does not luminescence at all, so the thermal yield in its case is 1, and pressure amplitude could be estimated as (3):

$$p = \frac{\mu_a \rho c_s^2 \beta H_0}{a c_p} \int_{x_0}^{x_0+a} \exp(-\mu_a x) dx = \frac{\rho c_s^2 \beta H \cdot \exp(-\mu_a x_0)}{a c_p} \cdot [1 - \exp(-\mu_a a)], \qquad (3)$$

where μ_a = 0.48 cm^{-1} is linear absorption coefficient of the ferrocene solution, *l* is cuvette thickness (2 cm), *a* is effective layer thickness forming the pressure wave influencing the sensor, *w* is radius of the laser beam at the cuvette center, c_p = 2.15 J/(cm^{3}K) is volumic heat capacity of DMSO, ρ =1.0955 g/cm^3 is density of DMSO, β = 8.8·10^{-4} K^{-1} is thermal expansion coefficient of DMSO [19]. The starting integration point was taken as 0, or (*l* — *a*)/2, or (*l* — *a*) depending on the sensor position at the front, center or rear point of the cuvette.

The photoacoustic signals measured at the lowest energy density value for ferrocene solution locating the sensor at the front, center, rear points of the cuvette gave us valuer of *a* parameter. The respective amplitudes were 1.36, 1.63, and 1.04 mV that gives the area value *a*= 1.1 cm at the experimental ferrocene solution linear absorption coefficient 0.48 cm^{-1}.

The amplitude of the photoacoustic signal dependences on the energy density of the laser pulse at the sensor position in the front and center points of the cuvette are shown in Figure 5.

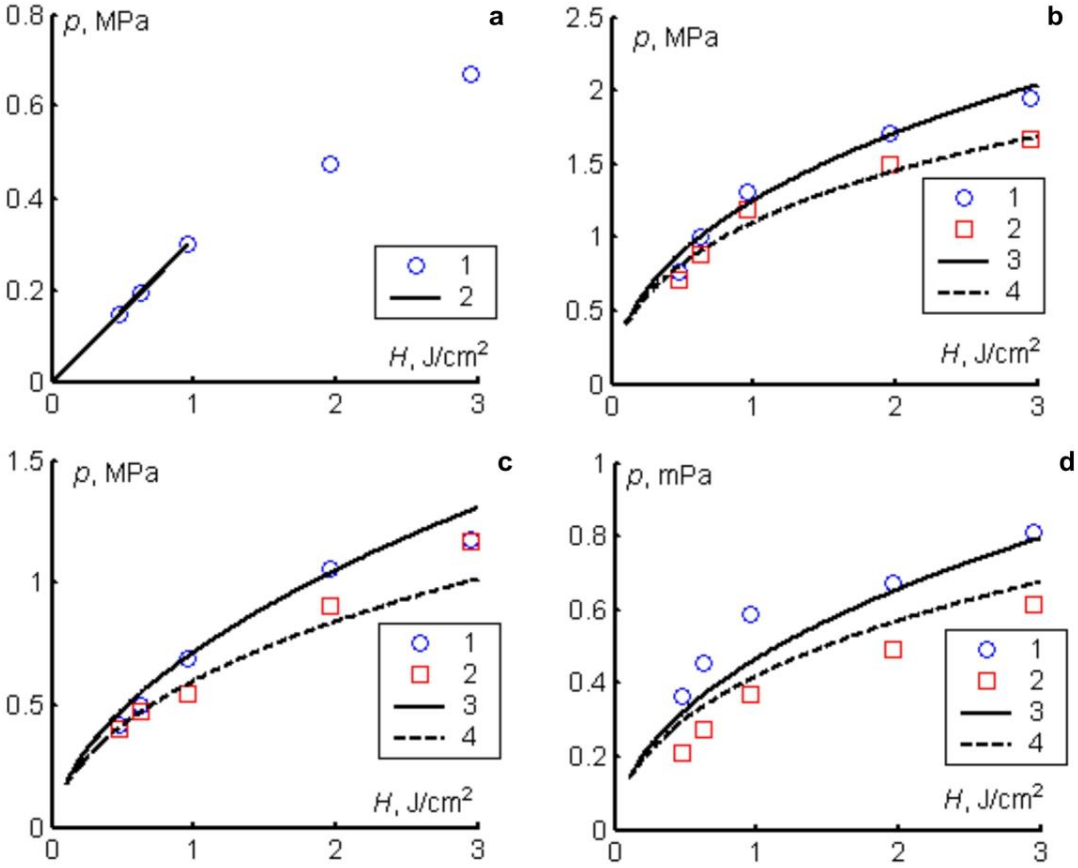

Figure 5. The photoacoustic signal amplitude dependence on the pulse energy density in the cases of ferrocene (a) and colloid ablation products of aluminum (b), nickel (c), and zinc (d) targets. On the “a” part 1 is experiment and 2 is linear approximation, while on others 1 and 2 are experimental data and 3 and 4 are approximation using model (5).

The dependence is linear up to 1 J/cm^2 in the ferrocene case. The sublinear character at higher energy densities arises due to optical breakdown on the bubbles and uncontrolled impurities. The photoacoustic signal amplitude dependence on the energy density is substantially sublinear in the cases of colloid obtained with metal targets' ablation in the entire studied range. The linear type of the dependence at low energy densities allowed us to estimate the calibration coefficient linking pressure and signal amplitudes at 101 kPa/mV.

We approximated the photoacoustic signal amplitude in the studied colloids case as:

$$p = \int_{x_0}^{x_0+a} \eta(x)\frac{dH(x)}{dx}dx = \int_{H(x_0)}^{H(x_0+a)} \eta(H)dH. \tag{4}$$

Equation (4) assumes that the transformation of the laser energy into the pressure wave has the efficiency η. The transformation is sensible in the range with *a* width only. In the linear range η = const. We assumed, that the efficiency is a power function of the energy density in the attenuation becomes non-linear ($H > H_c$) $\eta = \eta_b \cdot \left(H/H_b\right)^{-m}$, where H_b is "basic" energy density value taken as 0.2 J/cm^2, so $\eta = \eta_b$, if $H = H_c$.

The linear absorption range is not reached in the case of photoacoustic measurements; the energy density falling inside the cuvette is described with the lowest part of the formula (2). Having taken the integral in (4) one gets:

$$p = \frac{\eta_b H_b}{1-m} \cdot \left[\left(\frac{H(x_0)}{H_b} \right)^{1-m} - \left(\frac{H(x_0+a)}{H_b} \right)^{1-m} \right]. \tag{5}$$

The approximation results of the experimental dependencies of photoacoustic response amplitude on energy density of the laser pulse are shown in Figure 5; the approximation parameters are presented in Table 2.

Table 2

Approximation parameters for μ(*H*) and η(*H*) dependencies

sample source	μ, cm^{-1} (spectrophotometry)	z-scan			photoacoustics			
		μ, cm^{-1}	*n*	H_c, mJ/cm^2	*n*	H_c, mJ/cm^2	η_b, cm^{-1}	*m*
Al	1.37	1.34	1.79	288	0.47	22.9	9.71	0.94
Ni	0.692	0.379	1.41	336	0.39	1.21	4.06	0.75
Zn	0.811	0.849	0.902	241	0.47	14.3	4.39	0.91

Discussion

The experimental dependencies of the transmittance on the pulse energy density in the case of colloid ablation products evidence the substantially non-linear light attenuation. The simple model based on the energetic threshold describes the results well (Fig. 3). An interesting feature is this threshold decreasing as a dilution result. The power value in the respective law is not a positive integer number, which decreases with dilution. The dependence of the equation (1) parameters on the colloid concentration observed cannot arise if the laser light absorption centers act independently. The threshold of non-linear attenuation H_c decreasing after dilution is reasonable if the interaction becomes weaker with the distance between centers increasing.

One discerns the influences of the optic properties and absorbed energy transformation. The efficiency parameter could be written as $\eta(H) = \mu_a\gamma$. In the case of solids thermal expansion the dimensionless parameter γ is known as Grüneisen parameter that can be estimated as $\rho c_s^2\beta/c_p$. The respective value for DMSO is 0.99 [19] which is close to typical value about 1 for most of the substances. In the low energy density range the value of η is higher than 1. For instance, at H =150 mJ/cm^2 the efficiency value is 12.7, 5.04, and 5.70 cm^{-1} for colloid obtained with aluminum, zinc, and nickel targets' ablation respectively. Estimating the linear absorption coefficient roughly as the attenuation one, we may estimate the respective values for γ as 39, 22, and 23 respectively for the same samples. The attenuation is the sum of absorption and scattering processes, so real γ should be even higher. So high values could be reached, if the substance undergoes phase transitions accompanied by significant expansion, such as evaporation and sublimation. These considerations agree with the parameters H_c and *n* of the equation (1) decreasing after dilution. The decreasing in concentration means increasing of the average solvent volume containing one light absorbing center. The typical acoustic relaxation time of the excited area is $w/c_s \approx 160$ ns, which is an order of magnitude higher than the pulse duration. On the other hand, estimating the typical concentration of nanoparticles using average diameter, one founds the acoustic relaxation time between nanoparticles about 1 ns. Thus, the irradiation zone cannot increase its volume significantly during the pulse, so pressure increasing due to gases formation has to be linked with the respective solvent contraction. In the pressure range experimentally estimated the 12.5 times dilution has led to pressure drop in the system 12.5 times at the same gas phase volume. The pressure increasing shifts the evaporation and sublimation equilibrium toward the condensed phase formation. This way, the decreasing in H_c after dilution agrees with the phase transitions influence on the qualitative level. Formation of the gas phase around the light absorbing centers leads to the increasing in their scattering cross section that agrees with transmittance decreasing when the energy density of the laser pulse increases (Fig. 3).

The influence of the nanoparticles' concentration is seldom discussed as the parameter influencing the non-linear light attenuation. The effects discussed have some similarities with laser initiation of the secondary explosives doped with metal nanoparticles. It was shown in [20] that the minimal energy density is achieved for the nanoparticles' concentration providing the maximum of pressure measured with photoacoustic techniques in the under threshold mode. The gas phase formation is highly endothermic becoming a fast means of the energy dissipation. If the pressure increases when the nanoparticles are heated with the laser pulse, this increasing inhibits the sublimation and evaporation, making the temperature in the reaction hot-spots increase and threshold energy density of explosion decrease [20].

In the case of zinc target ablation products and photoacoustic sensor position near the front of the cuvette the pressure values vary in the vide range. The pressure amplitude on the energy density dependence for both sensor positions is poorer than in the aluminum and nickel cases. We suggest that in the zinc case the optic breakdown begins at the front of the cuvette. The zinc sulfide colloids are able to self-focus the laser beams [21] that increase the effective energy density. The breakdown is a probabilistic event that can explain high dispersion of the pressure amplitudes. Stronger laser light attenuation in the breakdown area making the pressure increase in the front area decreases it in the middle one hindering the description of both curves with one set of parameters.

Conclusion

Metal targets ablation in the liquid medium allows one to obtain colloid with strong non-linear light attenuation. In the present paper we proved that photoacoustic data are important for the nature of the non-linear absorption detection. The photoacoustic results and influence of the concentration on the non-linear absorption parameters exclude such mechanisms of non-linear absorption as two-photon and two-step absorption. At the same time, the formation of the gas phase due to heating and subsequent evaporation and sublimation of the matter qualitatively agrees with the effects observed.

References

1 Ganeev, R.A. (2019). Characterization of the Optical Nonlinearities of Silver and Gold Nanoparticles. *Optics and Spectroscopy*, 127, 487–507. https://doi.org/10.1134/S0030400X19090108

2 Majles Ara, M.H., Dehghani, Z., Sahraei, R., Daneshfar, A., Javadi, & Z., Divsar, F. (2012). Diffraction patterns and nonlinear optical properties of gold nanoparticles. *Journal of Quantitative Spectroscopy & Radiative Transfer*, 113, 366–372. https://doi.org/10.1016/j.jqsrt.2011.12.006

3 Fathima, R., Mujeeb, A. (2021). Plasmon enhanced linear and nonlinear optical properties of natural curcumin dye with silver nanoparticles. *Dyes and Pigments*, 189, 109256. https://doi.org/10.1016/j.dyepig.2021.109256

4 Ovchinnikov, O.V., Smirnov, M.S., Chevychelova, T.A., Zvyagin, A.I., & Selyukov, A.S. (2022). Nonlinear absorption enhancement of Methylene Blue in the presence of Au/SiO2 core/shell nanoparticles. *Dyes and Pigments*, 197, 109829. https://doi.org/10.1016/j.dyepig.2021.109829

5 Fathima, R., & Mujeeb, A. (2021). Enhanced nonlinear and thermo optical properties of laser synthesized surfactant-free Au-Pt bimetallic nanoparticles. *Journal of Molecular Liquids*, 343, 117711. https://doi.org/10.1016/j.molliq.2021.117711

6 Silva-Silva, T.P., Silva, A.A., Oliveira, M.Ch.D., Souza, P.R., Silva-Filho, E.C., Garcia, H.A., Costa, J.C.S., & Santos, F.E.P. (2023). Biosynthesis of Ag@Au bimetallic nanoparticles from Hymenaea courbaril extract (Jatoba) and nonlinear optics properties. *Journal of Molecular Liquids*, 389, 122641. https://doi.org/10.1016/j.molliq.2023.122641

7 Al–Ghamdi, H., Aloraini, D.A., Almuqrin, A.H., Jagannath, G., & Sayyed, M.I. (2024). Nanosecond nonlinear optical properties of oxide glasses embedded with plasmonic nanoparticles at the spectral excitation near to surface plasmon resonance. *Physica B*, 678, 415756. https://doi.org/10.1016/j.physb.2024.415756

8 Guzman-Barraza, A., Ortega-Mendoza, J.G., Padilla-Vivanco, A., Arroyo Carrasco, M.L., Silva-Gonzalez, N.R., Zaca-Moran, P., & García Ramírez, E.V. (2024). Characterization of the nonlinear optical properties of Zn and Ag nanoparticles using light at 1550 nm. *Results in Optics*, 14, 100590. https://doi.org/10.1016/j.rio.2023.100590

9 Gusev, V.E., & Karabutov, A.A. (1992). *Laser Optoacoustics*. N.Y. American Institute of Physics, 296 p.

10 Bialkowski, S.E., Astrath, N.G.C., & Proskurnin, M.A. (2019). *Photothermal Spectroscopy Methods*. John Wiley & Sons, 512 p.

11 Amendola, V., Polizzi, S., & Meneghetti, M. (2006). Laser Ablation Synthesis of Gold Nanoparticles in Organic Solvents. *Journal of Physical Chemistry B*, 110, 7232–7237. https://doi.org/10.1021/jp0605092

12 Bozon-Verduraz, F, Brayner, R., Voronov, V.V., Kirichenko, N.A., Simakin, A.V., & Shafeev, G.A. (2003). Production of nanoparticles by laser-induced ablation of metals in liquids. *Quantum Electronics*, 33, 714–720. https://doi.org/10.1070/QE2003v033n08ABEH002484

13 Podagatlapalli, G.K., Hamad, S., Sreedhar, S., Tewari, S.P., & Rao, S.V. (2012). Fabrication and characterization of aluminum nanostructures and nanoparticles obtained using femtosecond ablation technique. *Chemical Physics Letters*, 530, 93–97. https://doi.org/10.1016/j.cplett.2012.01.081

14 Shiju, E., Siji, N.N.K, Narayana, R.D., & Chandrasekharan, K. (2020). Enhanced nonlinear absorption and efficient power limiting action of Au/Ag@ graphite core-shell nanostructure synthesized by laser ablation. *Nano Express*, 1, 030026. https://doi.org/10.1088/2632-959X/abca0f

15 Aleali, H., Sarkhosh, L., Karimzadeh, R., & Mansour, N. (2011). Optical limiting response of Ag2S nanoparticles synthesized by laser ablation of silver target in DMSO. *Phys. Status Solidi B*, 248(3), 680–685. https://doi.org/10.1002/pssb.201046107http://database.iem.ac.ru/mincryst/rus/index.php

16 Wang, G., Huang, B., Li, Zh., Lou, Z., Wang, Z., Dai, Y., & Whangbo, M.H. (2015). Synthesis and characterization of ZnS with controlled amount of S vacancies for photocatalytic H2 production under visible light. *Scientific Reports*, 5, 8544. https://doi.org/10.1038/srep08544

17 Dehghani, Z., Nazerdeylami, S., Saievar-Iranizad, E., & Majles Ara, M.H. (2011). Synthesis and investigation of nonlinear optical properties of semiconductor ZnS nanoparticles. *Journal of Physics and Chemistry of Solids*, 72, 1008–1010. https://doi.org/10.1016/j.jpcs.2011.05.005

18 Watcher (Ed.) (1998). *Kirk-Othmer Encyclopedia of Chemical Technology* (Vol. 23, 4th edition). John Wiley & Sons. 107-108.

19 Aduev, B.P., Nurmukhametov, D.R., Zvekov, A.A., Nikitin, A.P., & Kalenskii, A.V. (2016). Laser initiation of petn-based composites with additives of ultrafine aluminium particles. *Combustion, Explosion, and Shock Waves, 52*(6), 713–718. https://doi.org/10.1134/S0010508216060113

20 Ganesha Krishna, V.S., & Mahesha, M.G. (2022). “ZnS, an excellent material in photonics” — A review based on Z-scan study. *Physica B*, 628, 413628. https://doi.org/10.1016/j.physb.2021.413628

А.А. Звеков, А.В. Каленский, А.В. Иванов, А.П. Боровикова, Д.Р. Нурмухаметов

Диметилсульфоксидтегі металл нысандарының лазерлік абляциясымен дайындалған коллоидтардың сызықтық емес оптикалық қасиеттері

Алюминий, никель және мырыш негізіндегі коллоидты ерітінділер диметилсульфоксид ортасында тиісті металл нысандарын абляциялау арқылы алынды. Үлгілер ультракүлгін УК-*вис* спектроскопиясы, трансмиссиялық электронды микроскопия және динамикалық жарық шашырау әдістерімен зерттелді. Импульсті неодим лазерін (532 нм, 14 нс) қолдана отырып, z-сканерлеу әдістерімен айтарлықтай сызықтық емес әлсіреу байқалды. Жарық қарқындылығы жоғарылаған сайын үлгілердің өткізгіштігі төмендейді. Оптоакустикалық сигналдың амплитудасы сәулелену қарқындылығының жоғарылауымен сызықтық түрде өсті. Ферроцен ерітіндісін стандарт ретінде қолдану абсолютті бірліктердегі қысым амплитудасының шамаларын алуға мүмкіндік берді. Оптоакустикалық сигналдың өткізгіштігі мен амплитудасының импульстік энергия тығыздығына тәуелділігін сипаттау үшін әсер ету шегі бар қуат заңдары қолданылды. Коллоидты ерітінділерді сұйылту кезінде өзгеретін тәуелділік параметрлері бағаланды. Шың қысымының шамалары қыздырылған кезде үлгінің сызықтық кеңеюін қарастыратын классикалық оптоакустикалық эффект теориясының бөлігі ретінде түсіндіруге болмайтындығы көрсетілген. Нәтижелерді талқылау үшін заттың булануына және оларды қыздыру кезінде нанобөлшектердің айналасында бу көпіршіктерінің пайда болуына негізделген сызықтық емес әлсіреу механизмі тартылады, ол сапалы деңгейде оптоакустикалық сигнал амплитудасының энергия тығыздығына субсызықтық тәуелділігіне сәйкес келеді.

Кілт сөздер: абляция, диметилсульфоксид, жарықтың сызықты емес әлсіреуі, фотоакустикалық спектроскопия, лазерлік сәулелену.

А.А. Звеков, А.В. Каленский, А.В. Иванов, А.П. Боровикова, Д.Р. Нурмухаметов

Нелинейные оптические свойства коллоидных продуктов абляции металлических мишеней в диметилсульфоксиде

Коллоидные растворы на основе алюминия, никеля и цинка были получены абляцией соответствующих металлических мишеней в среде диметилсульфоксида. Образцы были исследованы методами УФ-*вис* спектроскопии, просвечивающей электронной микроскопии и динамического рассеяния света. Существенное нелинейное ослабление излучения неодимового лазера (532 нм, 14 нс) было обнаружено методом *z*-сканирования, причем наблюдалось падение пропускания при приближении к фокусу. Амплитуда оптоакустического сигнала увеличивалась сублинейно при росте интенсивности излучения. Применение раствора ферроцена в качестве стандарта позволило получить величины амплитуды давления в абсолютных единицах. Для описания зависимостей коэффициента пропускания и амплитуды оптоакустического сигнала от плотности энергии импульса использовались степенные законы с порогом появления эффекта. Были оценены параметры зависимостей, которые изменяются при разбавлении коллоидных растворов. Показано, что величины пикового давления не могут быть интерпретированы в рамках классической теории оптоакустического эффекта, рассматривающей линейное расширение образца при нагревании. Для обсуждения результатов привлекается механизм нелинейного ослабления, основанный на испарении вещества и формировании пузырьков паров вокруг наночастиц при их нагреве, который на качественном уровне согласуется с сублинейной зависимостью амплитуды оптоакустического сигнала от плотности энергии.

Ключевые слова: абляция, диметилсульфоксид, нелинейное ослабление, фотоакустическая спектроскопия, лазерное излучение.

Information about the authors

Alexander Zvekov (corresponding author) — Doctor of physical and math science, Professor, Department of Solid State Chemistry and Material Science, Kemerovo State University, Krasnaya st., 6, 650000, Kemerovo, Russia; *e-mail*: *zvekovaa@gmail.com*, https://orcid.org/0000-0002-2941-9783

Alexander Kalenskii — Doctor of physical and math science, Head of the Department of Solid State Chemistry and Material Science, Kemerovo State University, Krasnaya st., 6, 650000, Kemerovo, Russia; *e-mail: kalenskyav@gmail.com*; https://orcid.org/0000-0002-6658-0787

Alexey Ivanov — 3rd year PhD student, Kemerovo State University, Krasnaya st., 6, 650000, Kemerovo, Russia; e-mail: *alecs-2004@yandex.ru*

Anastasia Borovikova — Candidate of physical and math science, Head of the Scientific and Innovation Office, Kemerovo State University, Krasnaya st., 6, 650000, Kemerovo, Russia; e-mail: *science@kemsu.ru*, https://orcid.org/0000-0002-4987-3406

Denis Nurmuhametov — Doctor of physical and math science, Head of the Institute of coal Chemistry and Material Science, Federal Research Center of Coal and Coal Chemistry SB RAS, Sovetsky av., 18, 650000, Kemerovo, Russia; e-mail: *ndr999@gmail.com*

Article
https://doi.org/10.31489/2024PH4/133-142
UDC: 666.215.4

Received: 03.06.2024
Accepted: 14.08.2024

Vladimir P. Tsipilev[1*], Vladimir I. Oleshko[1], Alexey N. Yakovlev[2], Vladislav A. Ovchinnikov[3],
Ilya Yu. Zykov[1], Egor V. Forat[1], Ibrokhimkhon A. Saidazimov[1], Tatiana V. Grechkina[1]

[1]National Research Tomsk Polytechnic University
[2]T.F. Gorbachev State Technical University
[3]LLC "Saber interactive SGS"
([*]Corresponding author's e-mail: tsipilev@tpu.ru)

Laser initiaion of PETN-based composites with nano-sized absorbing additives of carbon and aluminum under conditions of various volume compression

The energy thresholds and the kinetics of explosive decomposition of pentaerythritol tetranitrate (PETN) and its composites induced by the laser pulse (λ_0 = 1064 nm; $\tau_и$ = 12 ns) in dependence on the concentration of absorbing additives and different volume compression within the range from 40 to 600 MPa are experimentally studied. The sensitivity of pure PETN and its composites increases along with the volume compression value. For low pressures (less than 200 MPa) with the increase of additives concentration the sensitivity of mixtures to laser pulse exposure increases and for higher pressures (more than 300 MPa) — it decreases. Such behavior is explained from the perspective of both diffuse light scattering and the thermal micro-spot model of initiating the transparent explosive components (the "hot spot" model), according to which the reactive capacity of hot spots is determined by their heat reserve, their concentration and the scale of gas dynamic unloading in the neighboring to hot spots pores and through the sample surface pressed by the input window (the area of low pressures), as well as by the heat conducting unloading of hot spots in the explosive components matrix and the covering glass (the area of high pressures).

Keywords: PETN, laser pulse initiation, nano-sized particles, optical breakdown, hot spots.

Introduction

The goal of this work is to identify the combined effect of absorbing nano-sized additives and volume compression pressure on the energy thresholds of pulsed laser initiation of pentaerythritol tetranitrate (PETN) and to improve model concepts of the mechanism of laser initiation of explosive decomposition of composites based on PETN powders. The objectives of the study included determining the value of spatial illumination in the sample volume at different concentrations of absorbing additives (up to 1 % by weight) and different compression pressures (from $2.5 \cdot 10^7$ Pa to $4 \cdot 10^8$ Pa), determining the coupling coefficient between spatial illumination and surface illumination specified by the laser beam, obtaining experimental dependencies of the energy thresholds of initiation of explosive decomposition of mixtures, developing and describing the mechanisms of explosive decomposition of PETN.

The studies of the laser pulse ignition of the secondary explosive components are conducted since the 60s of the previous century [1–6]. However, until now the united opinion about the initiation mechanisms has not been formed. The main cause for this is the absence of the unified methodology of research conducted by different research teams which is discussed in [6]. The most informative direction of research to discover the ignition mechanisms is the experiments of the impact of the volume compression pressure on the ignition energy thresholds. The pioneering experiments in this direction were described in [2], where the volume compression of powders of PETN, hexogen and octogen was achieved by the positioning of the samples into metallic compression mold with the transparent input window placed into the hydraulic press. In the experiments there was used the compression pressure of the input window from 10 MPa (0.1 kbar) to 2000 MPa (20 kbar). At that, with the compression pressure increase there was observed the monotonous increase of sensitivity (the ignition threshold decrease). Thus, with the laser pulse irradiation with the pulse duration of 40 ns on the wave length of 1064 nm the threshold energy density comprised about 600 J/cm^2 under the pressure of 10 MPa, while under the pressure of 2000 MPa — it is about 20 mJ/cm^2, that is, it decreased approximately in 30000 times.

The studies of PETN mixtures with absorbing additives were conducted in [3–5], where it was demonstrated that with introduction of additives the ignition energy decrease is recorded and it depends on the additive material. The maximum decrease of energy was discovered in [3, 4] with introduction of aluminum particles with the size of 2 μm.

In the study [6] there were measured the ignition thresholds for pure PETN with the dispersion of 6000 cm^2/g and PETN with additives of carbon nanopowder particles (the typical size of the particles is 75 nm) with the additives' concentration from 0.1 % to 1 % on the mass. The compression pressure of the input window (the plexiglass thickness 5 mm) did not change and was $1.76 \cdot 10^8$ Pa (1.76 kbar) with the laser beam diameter equal to 0.6 mm. It was demonstrated that with the increase of additives concentration the threshold energy (the energy density) decreases monotonically. Thus, under zero concentration (pure PETN) the threshold energy comprises 6.5 mJ (the threshold energy density 2.3 J/cm^2), under the concentration 0.1 %C — 2.4 mJ (0.85 J/cm^2); under the concentration 0.5 %C — 1.8 mJ (0.64 J/cm^2); under 1 %C — 1.3 mJ (0.46 J/cm^2). It was discovered that the sensitivity under 1 % additive of carbon nanopowder increases in 5 times in comparison with the PETN sensitivity which does not contain additives. In [7] there was sufficiently detailed study of the PETN behavior with additives of coarse particles of different metals (the size 20–100 μm) and with the additives of aluminum fine particles (the average size is about 1 μm) in dependence on their concentration (up to 10 % on the mass). The specifics of the methods of the experiments were the low density of mixture (less than 1 g/cm^3) and the input window (the sheet glass) tightly pressed to the surface avoiding the pressuring force. There were obtained the dependences of the ignition thresholds on the irregularities' concentrations. In both cases the minimum of the ignition threshold was discovered under certain values of concentration. The similar results were obtained in the studies [8-9], but under high densities of PETN mixtures with nano-sized aluminum particles (1.75 g/cm^3).

In the study [10] there was investigated PETN with the additives of aluminum nano-sized particles from 0 to 1.0 of the weight percentage under different pressures of the input window. At that, the typical size of the particles comprised 140 nm with the aluminum content in the particle about 90 %. In these experiments the quantities of mixture powders were preliminary pressed under the pressure of 1800 MPa, while the compression pressure of the input window was changed from 17 MPa up to 288 MPa with the side lever press. It was demonstrated that with the compression pressure increase and increase of additives concentration the ignition thresholds are decreasing monotonically, at that in the area of low pressures the additives decrease the thresholds in more than 3 times, while in the area of high pressures — in only 1.4 times.

Some different results were obtained earlier in the study [11] on PETN with carbon nanopowder additives (75 nm) under the compression pressures from 200 to 600 MPa avoiding the preliminary pressing. The concentration of carbon particles changed from 0 to 1.0 of the weight percentage. In the area of low pressures (about 200 MPa) there was discovered the sensitivity increase approximately in 1.85 times in the mixture with one percentage of carbon nanopowder in comparison with pure PETN. However, in the area of high pressures (about 600 MPa) 1 % mixture turned out to be less sensitive (there was observed the threshold increase in comparison with pure PETN in 1.37 times).

It is evident that the impact of the sensitivity increase in the area of low pressures with the concentration growth is dependent on the energy localization of the laser pulse on the absorbing additives and formation of supplementary hot spots distributed throughout the sample volume. Introduction of the additives leads to hot spots concentration in comparison with concentration of hot spots formed in self-generating defects in pure samples. This conclusion is trivial and does not require any proof; however, based on the given contradictory data [7–9, 11] it is difficult to explain the decrease of additives efficiency under high compression pressure. To solve this problem, it is necessary to conduct the research of impact of carbon nanopowder and aluminum participles concentration on the behavior of mixture compositions in the same interaction conditions. It requires the measurements for different composites performed using the same set-up which constitutes the goal of this study.

Experiment

The measurements of the ignition thresholds under different compression pressure of the input window. The measurements were performed within the compression pressure range from 40 to 600 MPa. Pure PETN and PETN with nano-sized carbon and aluminum particles were under investigation. The substance quantities with the weight of 10 mg were positioned into the metallic compression mold with the diameter of d_n = 1.15 mm, and were located in the hydraulic press and pressed against the input window. The sheet glass with the thickness of 10 mm was used as the input window. The kinetic characteristics of the decomposition process were determined with the photomultiplier H5773 Hamamatsu with the time resolution about 1 ns and the force wave detector on the piezoelectric ceramic PZT-19 with the time resolution about 10 ns. Figure 1 represents the obtained by us results (with consideration of [11, 12]) the experimental dependences of the PETN energy ignition threshold on the compression pressure of the input window under different concentrations (in the weight percentage) of carbon nanopowder particles (the curves 1–4) and aluminum (the curve 5). At that, the typical size of carbon and aluminum nanopowder particles was 75 nm and 140 nm respectively. It is highlighted that with the pressure increase of the pure PETN powder sensitivity increases not monotonically but there is observed the rapid leap of the sensitivity under the pressures exceeding 200 MPa. The quality of mixtures behavior remains the same as of pure PETN. The ignition threshold decreases under low compression pressures of the input window with the additives' concentration increase. While under the pressure of 100 MPa the threshold decreases in 5 times. With the pressure increase the additives' impact decreases and under the pressures exceeding the break-down point of PETN crystals the impact becomes unperformed. Under the pressures higher than $3 \cdot 10^8$ Pa their impact becomes negative (Fig. 1, the curves 1–5); that is, with the additives concentration increase the threshold increases and under the pressure of 600 MPa it reaches the value of 100 mJ/cm^{2}and 60 mJ/cm^2 against 50 mJ/cm^2 for pure PETN.

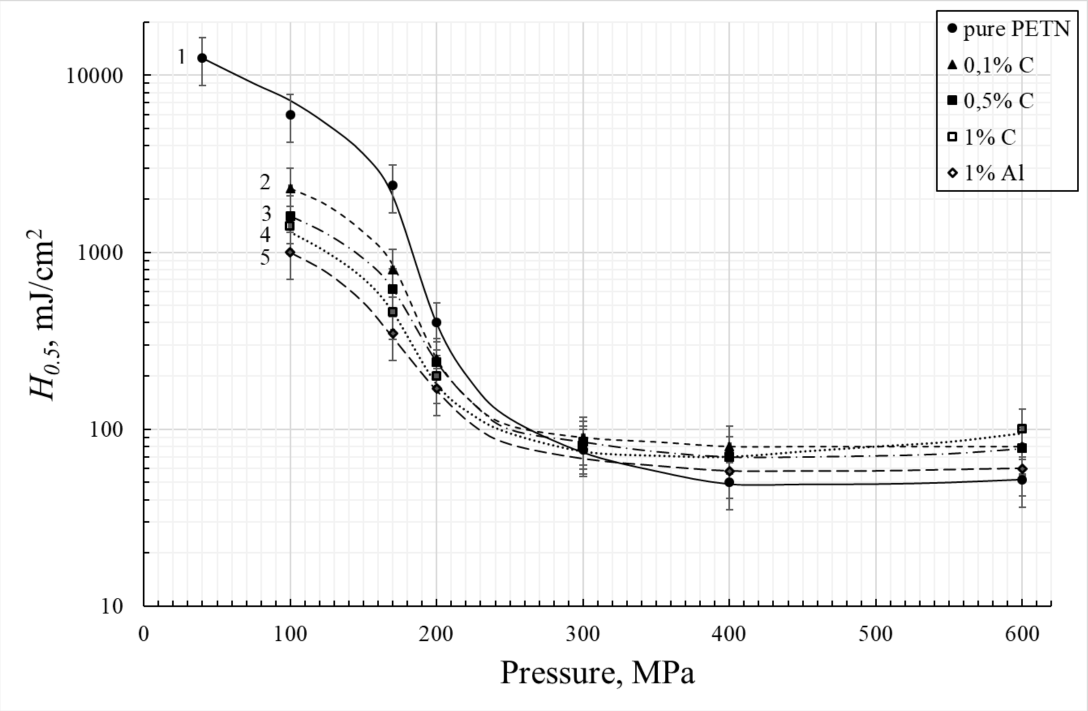

Figure 1. Dependence of PETN ignition energy threshold on the pressure P with different concentrations of carbon nanopowder and aluminium additives. Pure undoped PETN (1); with additives 0.1 % of carbon nanopowder (2); with additives 0.5 % of carbon nanopowder (3); 1 % of carbon nanopowder (4); PETN with additives 1 % of aluminium (5).

PETN with aluminium additives (the typical size 140 nm) was studied in less detail and only with the maximum concentration of additives, that is, with the same weight coefficient, following the hypothesis that in the area of low compression pressures with this concentration it is possible to obtain significant decrease of the threshold. In fact, the threshold decrease under the compression pressure of 100 MPa comprised 6 volumes (please see the curve 5). It should be mentioned that the ignition thresholds for the mixture with aluminium additives are slightly lower than the thresholds for the mixture with carbon nanopowder additives. Thus, under the pressure 100 MPa the ignition energy threshold density for the ignition of PETN with aluminium additives comprised 1050 mJ/cm^2 against 1400 mJ/cm^2 for PETN with carbon nanopowder additives. In the area of 300 MPa this ratio comprised 82 and 80 mJ/cm^2, correspondingly. Certain measurement data with carbon nanopowder additives is given in Table 1. In Table 2 there is given the data on the ignition thresholds for PETN mixture with aluminium additives obtained in the study [10] under slightly different conditions comparing to our experiments (samples were pre-pressed), which are partly used by us in discussion of the results. It is evident that in the area of high compression pressures of the input window the mixture porosity in our experiments and in the experiments from [10] is minimal that is the experimental conditions are almost similar while the thresholds are of near value. In the area of low pressures the mixture porosity in the experiments of [10] still remains minimal while in our experiments it is maximum. It is possible to suggest that the ignition thresholds are determined by the mixture porosity and explain high ignition thresholds in our experiments (1050 mJ/cm^2) in comparison with low thresholds obtained in the study [10] (100 mJ/cm^2).

Table 1

The ignition thresholds of PETN $H_{0,5}$ (mJ/cm^2) with carbon nanopowder additives under different volume compression pressure (the compression pressure for the input window)

P, MPa	C, %				Al, %
	0.0	0.1	0.5	1.0	1.0
40	12000±3000	–	–	–	–
100	6000±1700	2300±800	1600±400	1400±200	1000±150
170	2299±700	849±200	640±160	460±110	300±100
200	370±150	250±100	210±70	200±50	200±30
300	80±20	80±15	75±15	82±12	80±10
400	50±10	80±10	-	73±10	62±10
600	55±10	80±15	-	100±20	60±10

Table 2

The ignition thresholds for PETN H0,5 (mJ/cm2) with the additives Al, obtained in the study [10] on the samples preliminary pressed up to 1800 MPa under different compression pressures of the input window

P, МПа	Al,%			
	0,0	0,1	0,5	1,0
17	2700	900	450	400
120	320	150	80	80
288	70	50	50	50

The kinetics of the explosive decomposition is given in Figure 2. Earlier we have demonstrated in [12], that for pure PETN the kinetics of the explosive decomposition are characterized by greater length of the induction period. In this respect, the interest represents the comparison of the kinetics of the mixture composites decomposition with the kinetics of pure PETN decomposition. With this objective Figure 2 provides the kinetics of the explosive decomposition of the composites under study. Comparison of Figure 2 with the pictures from the study [12] points to the quality conformity of the kinetics of the explosive decomposition in both cases. In particular, it is evident that under the threshold levels impact there is always observed the ignition delay in PETN composites containing carbon nanopowder and aluminium, that is, there is the induction period. The delay length depends on the compression pressure of the input window, laser spot size, and the mixture concentration and reaches 60 μs under certain conditions (please see Fig. 2 *a*, *b*, *c*); it can also exceed the length of the laser pulse in 4 orders of value. With multiple orders exceeding of the threshold levels the delay effects become shorter up to the values of microseconds.

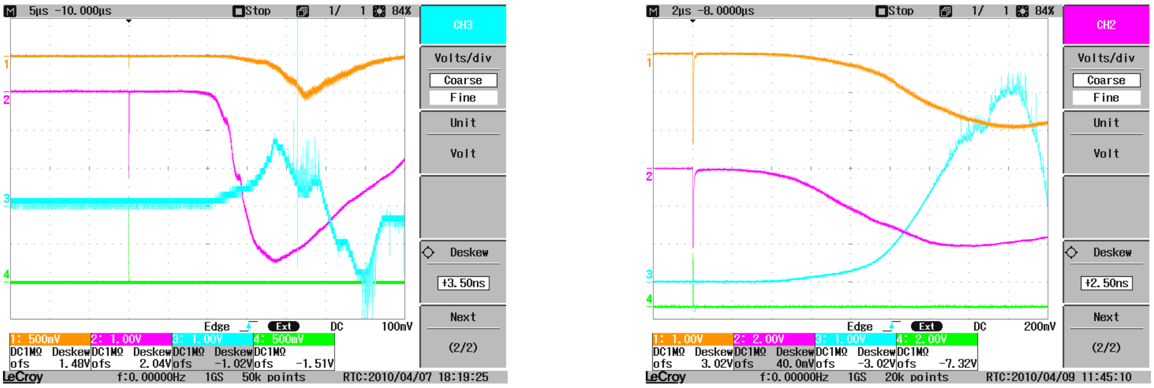

a) б)

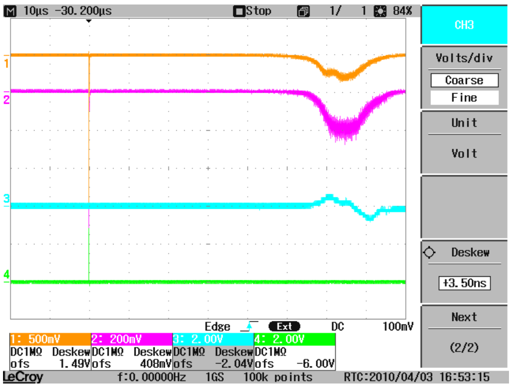

Fig. 2. Oscillograms of the process of explosive decomposition of PETN with additives 0.1 % of carbon nanopowder (a, b) and 0.1 % aluminium (c). 1 — laser pulse duration τ = 12 ns; 2 — the light signal of explosive decomposition in the radiation zones; 3 — the same at the all-round view; 4 — the pressure pulse registered by the acoustic transducer. λ0 = 1064 nm. d_n = 1.15 mm. H = 300 mJ/cm2, P = 200 MPa (a); H = 80 mJ/cm2, P = 300 MPa (b); H = 50 mJ/cm2P = 600 MPa. (c).

в)

Discussion of Results

Despite the differences in optical and thermo-physical properties of these additives (carbon nanopowder and *Al*), their impact is the same from the quantitative perspective, in particular, the additives concentration increase leads to the sensitivity increase (please see Fig. 1). This is especially evident in the areas of low compression pressure. Such behavior of the curves is determined by a number of factors. We will analyze these factors from the standpoint of heating the absorbing additives, the formation of thermal micro hot spots in their volume and surroundings.

One of these factors is strong change of optical properties of powders under pressures exceeding the material breaking down point (visually observed is contrast darkening of the mixture with its high compression pressure). The optical characteristics change under different concentrations of additives of carbon nanopowder and aluminium and different volume compression pressure of PETN powder were measured by us in separate experiments. There were experimentally determined the diffuse-reflection factors for the pressed tablets with the thickness h = 2 mm and based on their values there was determined the distribution of spatial luminance through the sample volume, using the Monte Carlo method. It was demonstrated that the spatial luminance E_0 in the volume of pressed powders may significantly increase the luminance E_n of the sample surface. It should be noted that spatial illumination (the saturation of a point in space with light) determines the heating temperature of the “hot spot”. Table 3 gives the values of relative increase of the spatial illuminance $F_0 = E_0/E_n$ in the near-surface layer in comparison with the illuminance on its surface defined by the incident laser beam.

The estimated value F_0^{max} for PETN with the dispersion 6000 cm^2/g under different compression pressures P and different concentrations of absorbing nano-sized additives γ the weight percentage. The layer thickness h = 2 mm (semi-infinite layer from the optical perspective)

Table 3

γ, %	$P = 2{,}5\cdot10^7$ Pa		$P = 10^8$ Pa		$P = 2\cdot10^8$ Pa		$P = 4\cdot10^8$ Pa	
	Al	*C*	*Al*	*C*	*Al*	*C*	*Al*	*C*
0,0	8,9	8,9	8,9	8,9	7,8	7,8	6,46	6,46
0,05	8,5	5,6	7,0	3,7	5,9	3,2	4,6	2,7
0,11	7,5	4,1	5,1	2,7	4,1	2,6	3,0	2,4
0,25	5,0	2,9	3,6	1,7	2,6	1,5	2,0	1,4
0,33	4,4	2,5	3,1	1,5	2,4	1,4	1,9	1,2
0,5	3,6	2,0	2,5	1,4	2,1	1,3	1,5	1,2
0,66	3,2	1,8	2,3	1,2	1,9	1,2	1,5	1,1
1,0	2,9	1,5	2,0	1,2	1,5	1,1	1,4	1,02

The data from Table 3 informs that the luminance in the powder volume decreases with increase of concentration of absorbing additives and the compression pressure increase. From the perspective of micro hot spots ignition mechanism [6, 11, 12] and hot spots formation separately this factor does not explain the sensitivity increase with the increase of pressure and concentration as decrease in the spatial luminance, on the contrary, is to lead to lesser heating of hot spots, hindering the ignition process and the threshold increase. The experiment shows the opposite, so it is necessary to take into account the heating of the matrix.

The second, in our opinion, key factor is the following. In the area of low (for example, 100 MPa) volume compression pressures (the area of high values for the ignition threshold, H_{05} = 6 J/cm^2) the mixture porosity is high. The temperature of heat micro hot spots may reach tens of thousands Kelvin degree, due to this, the intensive gasification of PETN takes place in the vicinity of hot spots. In such situation the interest represents the processes of heat averaging through the illuminated sample and formation of high temperature macro hot spot capable of igniting the explosive decomposition.

When evaluating the heating temperature for irregularities as well as the temperature for energy material matrix heating with different additives concentration, it is necessary to take into consideration the relative cross-section of particles absorption k (λ_0, R_0, N_0, N_p) and the luminance increase coefficient $F_{max}(R_\partial, h, \gamma)$ in the vicinity of the absorbing center. Thus, with the impact on the surface of the thick (semi-infinite layer from the optical perspective) tablet of pure PETN by the neodymium laser beam (λ_0 = 1064 nm; τ_p =10 ns) the temperature of single irregularity T_p in approximation of the adiabatic heating conditions comprises:

$$T_c \sim T_н + 3HkF_0/(4c_1\rho_1R_0) \qquad (1)$$

(where H — the laser pulse energy density; $c_1\rho_1$ — the particle thermal capacity; R_0 — the particle radius, T_0 — the initial temperature),

while the temperature for the matrix heating T_m of PETN

$$T_м \sim T_н + \mu HF_0/c_2\rho_2 \qquad (2)$$

(where μ — the index of absorption ($\mu = k\pi R_0^2 n$); $c_2\rho_2$ — the thermal capacity of energy material; n — the particles concentration ($n = 3\cdot10^{-2}\rho_2\gamma/4\rho_1\,\pi R_0^3$); γ — the additives weight percentage).

For clarity, we present the calculated dependences of the heating temperature of the hot spots and matrix and their distribution over the depth of the sample at a laser energy density of 100 mJ/cm^2 under adiabatic heating conditions (see Fig. 3). From (1) and (2) it is clear that the heating temperature is directly related to the coefficient F_0, which was calculated by the Monte Carlo method in three different ways [13], giving slightly different results. In this work, taking into account the importance of F_0 and the accuracy of its determination, the Monte Carlo algorithms were improved, and the F_0 values were obtained more reliable. Taking into account the duration of the laser pulse, the temperature values will be significantly less than the estimates from (1) and (2). Modeling and numerical calculation of the problem of heating a single spherical absorbing particle (carbon, aluminum) of different radii at different durations of the laser pulse in a transparent scattering medium are described in detail in the article [14–16]. Using the results of [14], the data of Table 1 and Table 3, we will estimate the heating temperatures of the hot spot in the region of low and high pressures of volume compression of the samples. The calculation data are shown in Figure 3.

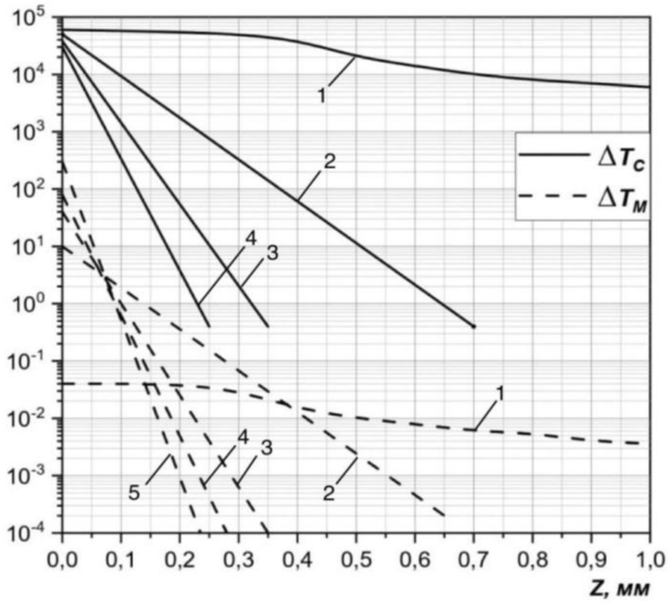

Fig. 3. Calculated dependence of the heating temperature of carbon nanopowder inclusions ΔTc (solid curves) and the heating temperature of PETN matrix ΔTм (dashed curves) along the layer depth z on the weight percentage of carbon nanopowder additives γ. Radiation wavelength λ0 = 1064 nm; h → ∞. Relative particle absorption cross section k = 1.5. Weight percentage of carbon (C) nanopowder additives γ.= 0.0 % (1); 0.1 % (2); 0.5 % (3); 1 % (4); 10 % (5). The energy density on the surface (Hs= 100 mJ/cm2) is close to the threshold value.

Let's consider the initiation mechanism in the low pressure region (about 100 MPa). Here the samples have high porosity and high initiation thresholds (from 1 to 6 J/cm^2). It can be assumed that possible gas-dynamic unloading from the hot spot volume will significantly reduce their temperature, however, the addition of impurities from the standpoint of the initiation process from the hot spot volume cannot explain their effect on the threshold reduction observed in the experiments. From Figure 3 it is evident that the temperature in the hot spot volume decreases with increasing concentration of additives and this should lead to an increase in the threshold, but this contradicts the experimental results. Ignition due to heating the matrix and averaging on the mechanism of heat transfer is not realized as the averaging time $\tau = d_n^2/\alpha$, where $\alpha = 6{,}77\cdot10^{-4}$ cm^2/s [16] comprises about 10 s which exceeds the maximum time for ignition delay observed in the experiment, in 5 orders of the value (Fig. 2).

However, in the areas of low volume compression pressures, another mechanism for heating hot spots is feasible. The possibility of ignition from its volume and impact of the irregularities concentration in this process will be considered further. Each PETN microcrystal is surrounded by pores in which gas break-through in the neighboring pores takes place. With the minimum expansion velocity of gas v_n (about 1 km/s) in the time of laser pulse the gases break-through will comprise the distance from hot spot up to 100 μm, which significantly exceeds the average distances between hot spots (with irregularities concentrations of 1 %, the average distance equals to 0.4 μm). Thus, during the laser impact each hot spot may receive additional energy from the neighboring hot spots. At that, the greater irregularities concentration is, the greater number of hot spots will give additional energy into the considered hot spot and the more its heating will be as well as the better conditions for ignition will be. In this mode, the temperature averaging is possible on the volume limited by the crosswise size of the laser spot on the samples surface and by the light penetration depth. The time of this averaging comprises the volume of $d_n/v_n \approx 10^{-6}$s. The averaging on this mechanism may lead to formation of reactive capable hot spot with the heat reserve necessary for development of explosion decomposition of the total mass of the sample. The higher the additives concentration is, the higher the heat reserve in hot spot is, the higher its reactive capacity and the lower the ignition threshold which was observed in experiment.

The necessary additional energy reserve in macro hot spot may be formed in the following way. In the vicinity of hot spots after the laser impact completion along with gasification the reaction of decomposition takes place in the gaseous phase with great energy production and growth of heat micro hot spots. Due to this, the average temperature of macro hot spot is determined not only by heat reserved by a hot spot as a result of laser-induced heating and of heating from micro hot spots, in the vicinity of which the chemical reaction of decomposition took place and heat storage of which increased in many times.

Let's consider the initiation mechanism in the high pressures region (more than 300 MPa). In this mode, the initiation thresholds are about 0.1 J/cm^2, pores are practically absent, gasification in the vicinity of the hot spot is difficult due to their relatively low temperature, the vapor pressure is insufficient to destroy the heating element matrix and break through gases into cracks. For the most, unloading of thermal micro hot spots has thermal conductivity nature. At that, the typical heat transit during the laser pulse comprises about $3\cdot10^{-6}$cm, which is much less than the average distance between the particles of carbon nanopowder and aluminium (for carbon nanopowder with the concentration 1 % this distance comprises about $3\cdot10^{-5}$cm, while for aluminium it is about $3.8\cdot10^{-5}$ cm). With the irregularities concentration 0.1 % the distances between the particles will be greater in approximately 2.15 times. Taking this into consideration it is possible to think that hot spots development takes place without the neighboring particles impact, that is the collective impact is absent in this situation. Due to this, the ignition process develops in the vicinity of single particle and is determined only by its temperature and initial heat reserve in micro hot spot which decrease with the particles concentration increase. This, with the collective impact absent, is to lead to increase of the ignition threshold and it is observed in the experiment under the pressure more than 300 MPa (please see Fig. 1).

It is necessary to point out that this conclusion is made without considering the heating of the explosive components matrix in dependence on absorbing irregularities concentration. However, it is obvious that with the maximum concentration of carbon nanopowder particles (in the experiment up to 1 %) the matrix temperature according to (2) does not exceed 350 K, while in aluminium composite it may be even less. Considering the minimum temperature of PETN self-ignition comprises 515 K [17–19], it is possible to state that under the conditions of heating the near surface layer of the matrix up to the temperature 350 K PETN ignition is known to be impossible. Further to that, it is also possible to neglect the matrix heating impact on hot spots reactive capacity due to the difference in their temperatures almost in 3 orders of value as well as due to long (about 10 s) time of heating the illuminated volume in comparison with the experimentally measured time of the ignition delay (tens of μs, see Fig. 2).

Important from our perspective result is to be mentioned; it goes from comparison of the experimental data on carbon nanopowder particles and *Al* impact on the quantitative and qualitative levels. It is obvious that the mixture with aluminium additives is more sensitive than the mixture with carbon nanopowder particles that is in the vicinity of aluminium particles there are formed more reactive capable hot spots. However, the computing simulation and calculation of carbon nanopowder and *Al* particles heating in PETN matrix in [14] demonstrates that heat reserve in the hot spot with heating carbon nanopowder particle located in PETN matrix exceeds the heat reserves in the vicinity of aluminium one. And this is due to the fact that the relative cross-section of carbon particles has a value of $k = 1.5$, and of aluminum — $k = 0.2$. To explain this phenomenon in the area of high pressures it is necessary along with understanding the heating of carbon nanopowder and aluminium particles due to absorption to engage the understanding about the possibility to form hot spots as a result of optical breakdown and localization of the laser pulse energy in the vicinity of particles. In case of realization of the optical breakdown in the vicinity of the absorbing metal and dielectric particles the hot spots parameters (temperature, heat reserve) are in weak dependence on the particle material and determined by the matrix properties. As it goes from here the ignition thresholds for PETN mixtures with carbon nanopowder and PETN with aluminium are to be near in their values. In the experiment there is observed higher sensitivity of PETN with additives of aluminium, and possibly, with higher concentration of free electrons in aluminium, their thermal emission under the laser heating of aluminium particles and, consequently, with lower threshold of optical breakdown.

Conclusions

In general, the behavior of PETN and composites based on it is easily described from the standpoint of the thermal focal theory of ignition by an external pulse. It can be argued that laser action leads to the formation of reactive hot spots as a result of optical micro breakdowns in the vicinity of intrinsic or introduced absorbing inhomogeneities.

In the low-pressure region of volume compression, the initiation process occurs from a macro hot spot limited by the diameter of the laser beam on the sample surface and the depth of light penetration, the temperature of which and its reactivity are proportional to the concentration of absorbing impurities. The macro hot spot is created by the breakthrough of gases from the volume of the micro hot spot into the surrounding pores. Unloading of the macro hot spot through the irradiated surface (interface), which occurs mainly during the induction period, determines the high level of initiation thresholds.

In the region of high values of input window pressing pressures, the initiation process occurs from the volume of the micro hot spot, the temperature of which and reactivity decrease with increasing concentration due to the decrease in spatial illumination and, consequently, the energy thresholds of initiation grow, i.e. the effect of absorbing additives is negative. The absence of pores excludes the possibility of gas breakthrough and rapid gas-dynamic formation of a reactive macro hot spot. Gas-dynamic unloading in this mode is insignificant, which determines the low level of initiation thresholds.

The indicated patterns and features must be taken into account in theoretical and experimental studies of the sensitivity of mixed compositions, as well as explosives containing their own optical inhomogeneities, to the action of laser pulsed radiation.

This work was performed within the framework of the Program of Strategic Academic Leadership “Priority 2030”.

References

1 Brish, A. A., Galeev, I. A., & Zaitsev, B. N. (1966). Detonation excitation of condensed explosives by radiation of an optical quantum generator. *Combustion, Explosion, and Shock Waves, 2* (3), 132.

2 Karabanov, Yu. F., Afanasiev, G.T., & Bobolev, V.K. (1977). Ignition of solid secondary explosives by a short laser pulse, Collection Combustion of condensed systems, Chernogolovka, 5–8.

3 Aleksandrov, V. E., Dolgolaptev, A. V., Ioffe, V. B., Kovalchuk, V. M., Levin, B. V., & Obraztsov, A. P. (1983). Investigation of the ignition features of condensed media with absorbing additives with a concentrated supply of radiant energy. *Combustion, Explosion, and Shock Waves, 19* (4), 19–20.

4 Ioffe, V. B., Dolgolaptev, A.V., Alexandrov, V. E., & Obraztsov, A. P. (1985). Ignition of aluminum-containing condensed systems by laser monopulse radiation. *Combustion, Explosion, and Shock Waves, 21* (3), 51.

5 Ng, W. L., Field, J. E., & Hauser, H. M. (1986). Thermal, fracture, and laser-induced decomposition of pentaerythritol tetranitrate. *Journal of applied physics, 59* (12), 3945–3952.

6 Aleksandrov, E. I., Voznyuk, A. G., & Tsipilev, V. P. (1989). Influence of absorbing impurities on the ignition of explosives by laser radiation. *Combustion, Explosion, and Shock Waves*, 51, 3–9.

7 Tarzhanov, V. I., Sdobnov, V. I., Zinchenko, A. D. Y., & Pogrebov, A. I. (2017). Laser initiation of low-density mixtures of PETN with metal additives. *Combustion, Explosion, and Shock Waves*, 53, 229–235.

8 Aduev, B. P., Nurmukhametov, D. R., Zvekov, A. A., Nikitin, A. P., & Kalenskii, A. V. E. (2016). Laser initiation of PETN-based composites with additives of ultrafine aluminium particles. *Combustion, Explosion, and Shock Waves*, 52, 713–718.

9 Aduev, B. P., & Nurmukhametov, D. R. (2011). The influence of added aluminum nanoparticles on the sensitivity of pentaerythritol tetranitrate to laser irradiation. *Russian Journal of Physical Chemistry B*, 5, 290–292.

10 Aduev, B. P., Nurmukhametov, D. R., Belokurov, G. M., Zvekov, A. A., & Nelyubina, N. V. (2019). Laser initiation of petn with inclusions of aluminum nanoparticles under static pressure. *Combustion, Explosion, and Shock Waves*, 55, 237–243.

11 Skripin, A. S., Ovchinnikov, V. A., Tsipilev, V. P., & Yakovlev, A. N. (2012). Dependence of explosion initiation threshold of petn with absorptive additives on the uniform compression pressure of the sample. *News of higher educational institutions. Physics, 55*(11-3), 217–218.

12 Tsipilev, V. P., Morozova, E. Yu., & Skripin, A. S. (2010). Laser initiation of PETN powders under conditions of volumetric compression. *Bulletin of the Tomsk Polytechnic University. Energy, 317* (4), 149–155.

13 Yakovlev, A. N. (2023). Patterns and features of laser and electron beam pulse initiation of energetic materials of various classes. *Doctoral dissertation*.

14 Murastov, G., Tsipilev, V., Ovchinnikov, V., & Yakovlev, A. (2017, April). About laser heat absorbing impurities in the transparence matrix of pentaerythritol tetranitrate. In *Journal of Physics: Conference Series, 830* (1), 012155. IOP Publishing.

15 McPeak, K. M., Jayanti, S. V., Kress, S. J., Meyer, S., Iotti, S., Rossinelli, A., & Norris, D. J. (2015). Plasmonic films can easily be better: rules and recipes. *ACS photonics, 2* (3), 326–333.

16 Larruquert, J. I., Rodríguez-de Marcos, L. V., Méndez, J. A., Martin, P. J., & Bendavid, A. (2013). High reflectance ta-C coatings in the extreme ultraviolet. *Optics express, 21* (23), 27537–27549.

17 Belyaev, A. F. (1968). *Combustion, detonation and operation of the explosion of condensed systems*. Science.

18 Bowden, F. (1962). *Fast reactions in solids*. Moscow: Foreign Literature Publishing House.

19 Orlova, E. Yu. (1973). *Chemistry and technology of high explosives*. Leningrad, Chemistry.

В.П. Ципилев, В.И. Олешко, А.Н. Яковлев, В.А. Овчинников, И. Ю. Зыков,
Е.В. Форат, И.А. Сайдазимов, Т.В. Гречкина

Жан-жақты қысудың әртүрлі қысымдары жағдайында көміртекті қара және алюминийдің наноөлшемді сіңіргіш қоспалары бар лазерлік инициацияға негізделген композиттер

Лазерлік импульстік әсерде ($\lambda0$ = 1064 нм; және τ= 12 нс) 40-тан 600 МПа-ға дейінгі диапазондағы әртүрлі көлемді ұнтақты қысу қысымдарындағы (мөлдір кіріс терезесінің қысу қысымы) сіңіргіш қоспалардың концентрациясына байланысты оның негізіндегі қыздыру элементі мен композиттердің жарылғыш ыдырауының энергетикалық шектері мен кинетикалық сипаттамалары эксперименталды түрде зерттелді. Таза қыздыру элементі мен оның негізіндегі композиттер үшін көлемді қысу қысымының жоғарылауымен сезімталдық тұтастай жоғарылайды, бірақ монотонды емес. Сонымен қатар төмен қысым аймағында (200 МПа-дан аз), қоспалар концентрациясының жоғарылауымен аралас композициялардың лазерлік импульстік әсеріне сезімталдығы жоғарылайды, ал жоғары қысым аймағында (300 МПа-дан жоғары) ол төмендейді. Бұл тәртіпті авторлар диффузиялық жарық шашырауын мөлдір ВВ инициациясының микроошақтық жылу моделі («ыстық нүктелер» моделі (ЫН)) тұрғысынан да түсіндіреді; осыған сәйкес «ыстық нүктелердің» реактивтілік қабілеттілігі олардың көлеміндегі жылу қорымен, олардың концентрациясымен, КТ-ға жақын тіректерге газдинамикалық түсіру және үлгінің кіріс саңылауының басылған беті (төмен қысым аймағы), сондай-ақ ВВ матрицасына және жабын шыныға (жоғары қысым аймағы) ГТ жылу өткізгіштік түсіру арқылы анықталады.

Кілт сөздер: қыздыру элементі, лазерлік импульсті инициация, наноөлшемді бөлшектер, оптикалық сыну, ыстық нүктелер (ЫН).

В.П. Ципилев, В.И. Олешко, А.Н. Яковлев, В.А. Овчинников, И.Ю. Зыков,
Е.В. Форат, И.А. Сайдазимов, Т.В. Гречкина

Лазерное инициирование композитов на основе тэна с наноразмерными поглощающими добавками сажи и алюминия в условиях различных давлений объемного сжатия

Экспериментально исследованы энергетические пороги и кинетические характеристики взрывного разложения тэна и композитов на его основе при лазерном импульсном воздействии (λ_0 = 1064 нм; $\tau_и$ = 12 нс) в зависимости от концентрации поглощающих добавок при различных давлениях объемного сжатия порошков (давлениях прижатия прозрачного входного окна) в диапазоне от 40 до 600 МПа. Показано, что для чистого тэна и композитов на его основе с ростом давления объемного сжатия чувствительность, в целом, увеличивается, но не монотонно. При этом в области малых давлений (менее 200 МПа) с возрастанием концентрации добавок чувствительность смесевых составов к лазерному импульсному воздействию увеличивается, а в области больших (более 300 МПа) — уменьшается. Такое поведение объясняется авторами с позиций как диффузного светорассеяния, так и с позиций тепловой микроочаговой модели инициирования прозрачных ВВ (модель «горячих точек» (ГТ)), согласно которой реакционная способность «горячих точек» определяется запасом тепла в их объеме, их концентрацией, газодинамической разгрузкой в близлежащие к ГТ поры и через прижатую входным окном поверхность образца (область малых давлений), а также теплопроводностной разгрузкой ГТ в матрицу ВВ и покровное стекло (область высоких давлений).

Ключевые слова: тэн, лазерное импульсное инициирование, наноразмерные частицы, оптический пробой, горячие точки.

Information about the authors

Vladimir P. Tsipilev (corresponding author) — Professor, Doctor of physical and mathematical sciences, Consulting professor, National Research Tomsk Polytechnic University, Lenin Avenue, 30, 634050, Tomsk, Russian Federation; e-mail: *tsipilev@tpu.ru*; https://orcid.org/0000-0003-1568-5279; https://www.scopus.com/authid/detail.uri? authorId=12241632500

Vladimir I. Oleshko — Doctor of physical and mathematical sciences, Professor, National Research Tomsk Polytechnic University, Lenin Avenue, 30, 634050, Tomsk, Russian Federation; email*: oleshko@tpu.ru*; https://orcid.org/0000-0003-0675-3591

Alexey N. Yakovlev — Associate professor, Doctor of technical sciences, Rector, T.F. Gorbachev State Technical University, Vesennaya Street, 28, 650000, Kemerovo, Russian Federation; e-mail: yakovlevan@kuzstu.ru; https://orcid.org/0000-0002-0539-151X

Vladislav A. Ovchinnikov — Game developer, LLC “Saber interactive SGS”, Engels Avenue, 33, 194156, Saint Petersburg, Russian Federation; e-mail: *vladislavovchin@mail.ru*; https://orcid.org/0009-0000-1177-3939

Ilya Yu. Zykov — Candidate of physical and mathematical sciences, Associate professor, National Research Tomsk Polytechnic University, Lenin Avenue, 30, 634050, Tomsk, Russian Federation; e-mail: *zykov@tpu.ru*; https://elibrary.ru/author_profile.asp? id=176738; https://www.scopus.com/authid/detail.uri? authorId=57188734965

Egor V. Forat — Candidate of physical and mathematical sciences, Associate professor, National Research Tomsk Polytechnic University, Lenin Avenue, 30, 634050, Tomsk, Russian Federation; e-mail: *forat@tpu.ru*; https://orcid.org/0000-0002-7692-4774

Ibrokhimkhon A. Saidazimov — Engineer, National Research Tomsk Polytechnic University, Lenin Avenue, 30, 634050, Tomsk, Russian Federation; e-mail: *ias121@tpu.ru*

Tatiana V. Grechkina — Candidate of physical and mathematical sciences, Associate professor, National Research Tomsk Polytechnic University, Lenin Avenue, 30, 634050, Tomsk, Russian Federation; e-mail: *greta_tv@tpu.ru;* https://orcid.org/0000-0003-1323-9208

.

Article
https://doi.org/10.31489/2024PH4/143-155
UDC 535.8, 543.4

Received: 22.05.2024
Accepted: 08.08.2024

L.A. Lisitsyna[1*], G.K. Alpyssova[2], D.A. Mussakhanov[3]

[1]*Tomsk State University of Architecture and Building, Tomsk, Russia;*
[2]*Karaganda Buketov University, Karaganda, Kazakhstan;*
[3]*L.B. Gumilyov Eurasian National University, Astana, Kazakhstan*
([*]Corresponding author's e-mail: *lisitsyna@mail.ru*)

Optical characteristics of tungsten trioxide luminescence in different matrices

The comparative research using time-resolved spectroscopy of the optical characteristics of an emission in two types phosphors: natural phosphors: ZnWO4, CdWO4, microcrystalline WO3, and artificial once: wide band gap dielectrics LiF, MgF2и BaF2 doped with tungsten trioxide were presented. Both single crystals and ceramic samples obtained in the process of high-speed radiation synthesis in air under a flux of 1.5 MeV electrons were studied. It has been established that the spectral-kinetic characteristics of the studied materials luminescence are the similarity in dielectrics, where WO3 is present as a dopant; in semiconductors (MeWO4), where tungsten trioxide is present as WO62– oxyanion and in crystal lattice of tungsten trioxide binary component. It is found that tungsten trioxide, being doped in dielectric, forms a subband of impurity states in the dielectric band gap, due to which, of spatial separation of electron-hole impurity pairs becomes possible upon optical excitation of the dielectric.

Keywords: radiation synthesis; natural phosphors, artificial phosphors, luminescence, time-resolved spectroscopy, emission center, subband.

Introduction

The wide practical use of transition metal oxides MeO (Me: W, Ti, Fe), double oxides AMeO (A: Cd, Mg, Ca, Zn), oxyfluorides AMeOF is due to the manifestation of amazing electrical, magnetic, optical properties of such materials. Their superior chemical stability, high catalytic activity, molecular and electronic flexibility are sufficient to make this material suitable for a wide range of applications including photocatalysis for water purification from contaminants, gas sensors, solar cells in electrochromic, photochromic, photoelectrochromic devices [1–7].

Among polyvalent metal oxides, tungsten trioxide WO_3 is considered to be one of the most important gas sensing materials in the world, being sensitive to many different gas species, like O_3, CO, NO, H_2S, and CH_4. Among double oxides $MeWO_4$ wolframite $ZnWO_4$ is a promising candidate in photocatalysis for the photodegradation of chemical contaminants. It has proved to be an efficient photocatalyst under both ultraviolet and visible light irradiation, or being doped with different ions, or by forming a heterostructure with different compounds such as ZnO, TiO_2, WO_3, and others. $ZnWO_4$-based catalysts have been explored toward inorganic and organic molecules [8–10].

In general, the catalysis process starts with the creation under the light irradiation of electrons (e) in the conduction band (CB) and holes (h) in the valence band (VB) of the catalyst. Holes in the VB are strongly oxidizing, while electrons in the CB are strongly reducing. The free charges, reaching the catalyst surface, are involved in the creation of free radicals, consumed in the processes of decomposition, mineralization, and oxidation of various pollutants. The efficiency of catalysis depends, in particular, on the number of charge carriers in the CB and VB, which is kept constant if spatial charge separation can be achieved or decreases, as a result, of the e-h pairs recombination.

In the present work the radiative recombination of electron-hole pairs in the materials used in catalysis is investigated. The relevance of such studies is obvious since it is free charge carriers that determine the efficiency of the realized catalytic processes.

The study of optical properties of phosphors has been carried out for several decades, however, at present; there is no consensus on the nature of the luminescence center even in the well-studied natural phosphors $MeWO_4$. According to [11–14], emission centers (EC) are octahedral oxyanion WO_6^{2-}, as components of the undisturbed crystal lattice. The luminescence spectrum presents a monoband at 2.6 eV belonging to spin-forbidden $^3T_{1u} \rightarrow {}^1A_{1g}$ triplet singlet electron transition in self-trapped excitons (STE) and is an intrinsic (fundamental) property of the crystal lattice.

An alternative interpretation of the EC nature was reported in [15, 16], where the light output in band at 2.6 eV is due to strong influence of external factors, complex technology of sample preparation, low degree of the original materials purity, high level of lattice imperfection caused by inability to maintain the specified level and defect type of the devices components. Within this concept, both the emission and excitation spectra of the emission in band at 2.6 eV belong to extrinsic defects of lattice deficit-oxygen centers WO_{6-x}. The luminescence of such material is not fundamental, and the crystal lattice is only an intermediary in the light energy transition to the local impurity center.

Obviously, without knowing the nature of the EC, there is no chance to influence on the efficiency recombination of the free charges created by the action of light in material. The lack of a unified view on the nature of emission centers, as well as the on influence of external factors on the magnitude of the light output, is obstacles to expanding the scope of practical application of these advanced materials. From the generally accepted point of view, parameters of the emission transition, such as light output, emission region, decay time of emission, excitation spectrum are determined by not only the structure of EC but also properties of matrix.

The present study is a comparative research of the optical characteristics of the W-O emission centers in in six types of phosphors: natural ones ($ZnWO_4$, $CdWO_4$crystals, WO_3 ceramics micro-powder) which are widely used in catalysis and artificial ones (wide-band gap dielectrics: LiF, MgF_2 and BaF_2, doped with tungsten trioxide). The studies were carried out using time-resolved spectrometry with nanosecond time resolution.

The aim of such comparison investigation is to figure out the nature of ECs and effect of the phosphorus matrixes on the properties of tungsten-oxygen emission centers.

Materials and research methods

In the present work, the emission properties of W-O complexes either in the form of dopant or as a component of the crystal structure were the objects of research. The wide-band dielectrics of different morphology: LiF crystal and ceramics MeF_2 (Me: Mg, Ba), doped with WO_3 (so called artificial phosphors) presented the first group of materials. The natural scintillators, the so-called self-activating materials: crystals and ceramics $MeWO_4$ (Me: Zn, Cd,) and microcrystalline ceramics powder WO_3 presented the second one.

Natural phosphors of $ZnWO_4$ and $CdWO_4$ were grown by the Czochralski method at the Institute for Single Crystals (Kharkov). The tungsten trioxide was present in the form of oxyanion WO_6^{2-}. The phosphors belong to semiconductors with a band gap not exceeding 5 eV and possess high radiation resistance and high light output.

Artificial phosphor LiF doped with tungsten trioxide WO_3 with a concentration up to 1 wt.% was grown by the Czochralski method at the State Optical Institute (Sankt Petersburg). The MgF_2 and BaF_2 doped with tungsten trioxide were synthesized under a high-energy electron beam with an ELV-6 electron accelerator created at the G.I. Budker Institute of Nuclear Physics (Novosibirsk). The maximum content of the dopant in ceramics samples was 0.5 wt. % due to the high volatility of tungsten hexafluoride WF_6.

Microcrystalline WO_3 powder was supplied by Hebei Suoy New Material Technology Co., Ltd (China) with a purity of not less than 99.5 %.

The method of synthesis by using a flux of 1.4 MeV electrons was developed, applied and described by us in [17–21]. A charge consisting of a mixture of powders with different composition and components ratio was placed in a copper solid crucible. A beam of electrons with a diameter of about 2 mm was scanned along the surface of the charge with a frequency of 50 Hz using electromagnets; the crucible with the charge was displaced relative to the beam at a rate of 1 cm/s. The duration of the radiation pulse was 2 ms, the estimated value of the synthesis temperature was ~1500 C.

Radiation-chemical processes of interaction of environmental components with the open surface of the molten charge start with the formation by electron pulses of free (non-localized) electrons (e) and holes (h) (electron-hole plasma) for a time not more than 10^{-15} s from the onset moment of the radiation pulse. Normally, the formation of a new near-order (phase transition) was initiated by an external parameter — the temperature. In the express synthesis method used, phase formation takes place in dielectric materials containing short-lived radiolysis products of high concentration (10^{22} cm^{-3}) during the radiation pulse (2 ms) with a significant time delay in temperature rise. Apparently, in such extreme conditions the phase formation was initiated by quantum fluctuations of charge density in electric and magnetic fields of electron-hole plasma. Formation of the crystalline phase occurs during the action of the radiation pulses (≤ 2 ms) and subsequent annealing of ceramics at 700 C in air.

The repeatability of spectral-kinetic characteristics of synthesized materials, as well as the properties similarity of crystalline and synthesized materials of the same chemical composition testify to the possibility of using the express method developed by us for practical purposes. Its main advantages include high-speed synthesis in air without supplying thermal energy from outside, possibility of obtaining ceramics in the form of crystallites with sizes depending on radiation field parameters.

The initial imperfection of research materials was evaluated by the absorption spectra in the range of 13–3 eV with a vacuum monochromator-based spectrometer at 300 K.

Natural phosphors $ZnWO_4$ and $CdWO_4$ regardless of morphology (ceramic, crystal) reveal transparency boundaries in the form of a threshold of about 4 eV. It is assumed to be located in the region of the Urbach "tail" and refers to the absorption transition of self-trapped excitons (STE) in WO_6^{2-} oxyanion [22–27]. The band gap E_g in these materials is determined in the range from 3.2 to 4.5 eV.

The lattice structure of the binary compound WO_3 was corner-sharing WO_6 octahedron units that are capable of forming clusters of different sizes [28, 29]. These clusters are considered to be connected to each other by W-O-W or hydrogen bonds, the latter due to incorporated water. The value of the band gap depends on the degree of the anionic sublattice imperfection and is determined in the range E_g=3.25–2.7 eV. The latter value belongs to the formation with the chemical formula (WO_3 nH_2O).

Pure wide band gap crystals LiF (E_g=13.6 eV), MgF_2 (E_g=12.4 eV) and BaF_2 (E_g=10.6 eV), grown in a fluorinating atmosphere, were transparent in the $E<E_g$ region. In the LiF crystal, the WO_3 doping is accompanied by a shift of the transparency boundary towards lower energies up to 4 eV with increasing tungsten trioxide content in the lattice (Fig. 1 (a)). The absorption coefficient at 8 eV reaches the value of 100 cm^{-1}, which indicates a high level of initial lattice imperfection of the doped crystals.

Crystals $ZnWO_4$, $CdWO_4$ and ceramics samples BaF_2-WO_3 and MgF_2-WO_3 opaque in the E>3.9 eV.

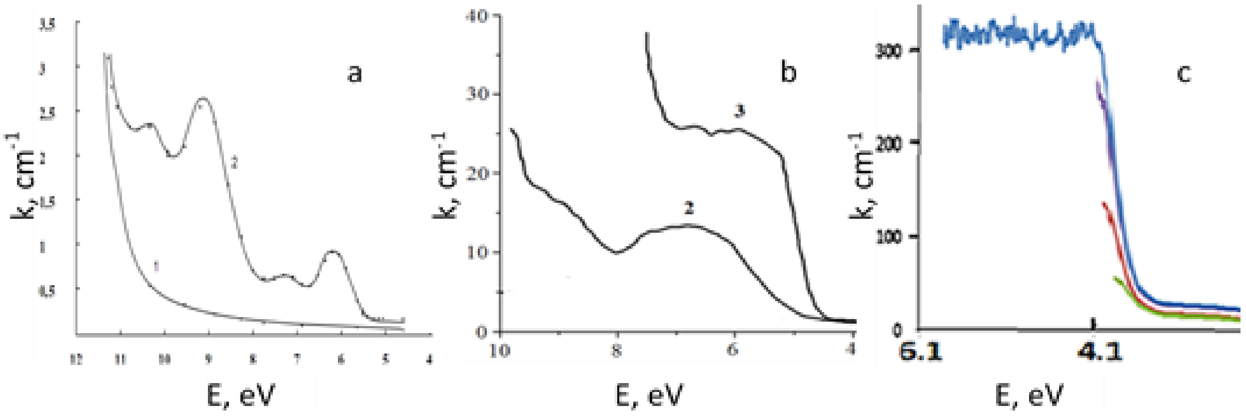

Figure 1. Absorption spectra of LiF crystals (a)(b). (a): non-doped (1), doped with WO_3 0.1 wt. % (2); (b): 0.2 wt. % (2); 0.3 wt. % (3). (c): absorption spectra of $ZnWO_4$ crystals.

All investigated materials under the action of light flux luminesced in the spectral range of 2.9–2.5 eV. The luminescence spectra were measured using two crossed MDR-204 monochromators equipped with a Hamamatsu R928 PMT for radiation detection. The integral characteristics of the luminescence were measured using an AvaSpec-2048 USB2.0 high-precision fiber optic spectrometer. Spectral-kinetic parameters of photoluminescence (PhL) and cathodoluminescence (CL) in crystals were studied in the time interval of 1.10^{-8}–1.10^{-3} s after the end of a single excitation pulse in the temperature range of 15–300 K.

Emission spectra and decay kinetics of PhL and CL were recorded on a LeGroy-WP-6030a oscilloscope.

The excitation spectra of the emission were measured in the interval of 6–1 eV at 300 K in a steady state mode with a hydrogen lamp as a source and were measured by the Agilent Cary Eclipse spectrofluorimeter.

The emission of phosphors was investigated under two types of excitation: $E_{ex}\approx E_g$ (1) and $E_{ex}>>E_g$ (2), where E_g is the band gap of the binary component WO_3.

The first condition was realized when PhL was excited by the fourth harmonic of Nd-laser (photon energy of 4.66 eV, pulse duration is 5 ns). The second condition was realized at excitation of luminescence by a pulse of 250 keV electrons with a duration of 10 ns. In both cases, researched materials luminesced in the region of 3.0–2.5 eV.

The surface structure of the synthesized samples was investigated using a scanning electron microscope Mira 3 (TESCAN). If the examined samples were dielectrics, they were coated with a conductive carbon layer using a Quorum Q150R ES sputtering system. The investigation was conducted at an accelerating voltage of 25 kV.

As an example, Figure 2 shows a picture of as-synthesized under the influence of an electron beam E=1.4 MeV, P=18 kW/cm^2 $ZnWO_4$ ceramics in the crucible and SEM images of its sample surfaces. On the surface of $ZnWO_4$ samples upon increasing the image resolution, a porous microstructure with elongated elements ranging in size from 7 to 20 μm and a thickness of approximately 7 μm are observed.

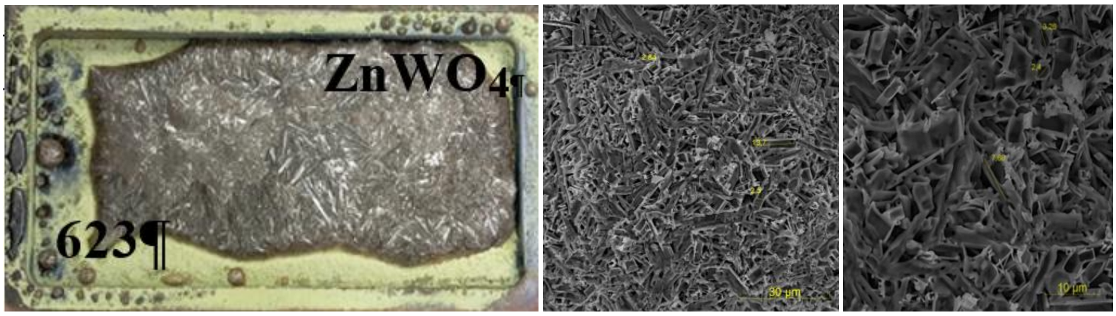

Figure 2. A picture of as-synthesized ceramics $ZnWO_4$ being in the crucible and SEM images of the surface of this ceramic sample.

X-ray diffraction patterns were collected using a Bruker D8 ADVANCE diffractometer (AXS, Berlin, Germany) equipped with a scintillation detector in step-scan mode over a diffraction angle range 2θ of 10 to 90° and CuKα radiation as the source. Sample identification utilized the Powder Diffraction File (PDF-2) database (ICDD, 2007), and indexing was performed using the EVA software (Bruker, 2007).

Figure 3 shows XRD spectra of synthesized ZnWO4 (a), and MgF2 doped with WO3 (b) samples.

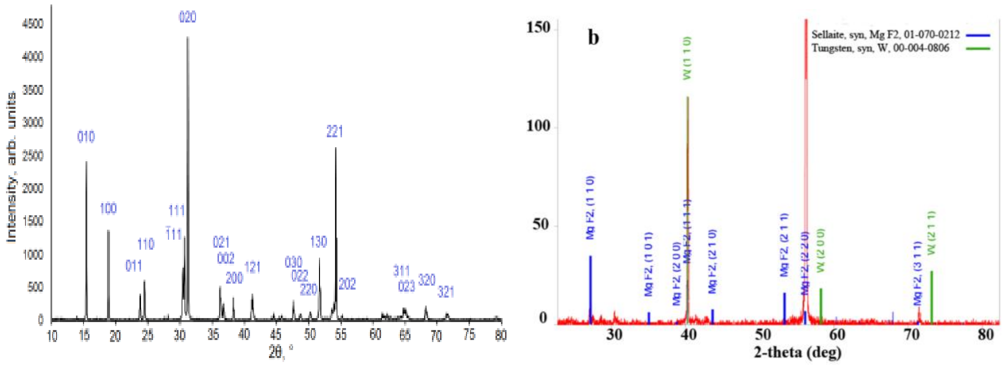

Figure 3. XRD patterns of $ZnWO_4$ ceramics sample (a) and MgF_2 doped with WO_3 (b)

Every synthesized ceramics $ZnWO_4$, $CdWO_4$, MgF_2 and BaF_2 are found to have a high degree of crystallinity, their elements composition is close to stoichiometric, and parameters similar to those ones in single crystals.

Results and Discussion

As it was previously shown [30, 31], in LiF dielectric doped with transition metal oxides (Me: Ti, Fe, W), emission in the region of 3–2.6 eV (Fig.4 (a)) occurs inertia-free with respect to a nanosecond excitation laser pulse (4.6 eV) or electron pulse (250 keV). The luminescence decay kinetics has two components: ns and μs at 270 K (Fig.4 (b)). The intensities ratio of the short and long components in band maximum is determined by the degree overlap of the bands at 3.0 and 2.6 eV.

The spectrum of the ns component is independent of the oxide type and is a band with a maximum at 3.0 eV and FWHM of 0.6–0.7 eV. The spectrum of the μs component is a monoband in the region of 2.8–2.5 eV, whose maximum position depends on the oxide type (Fig. 4 (a)).

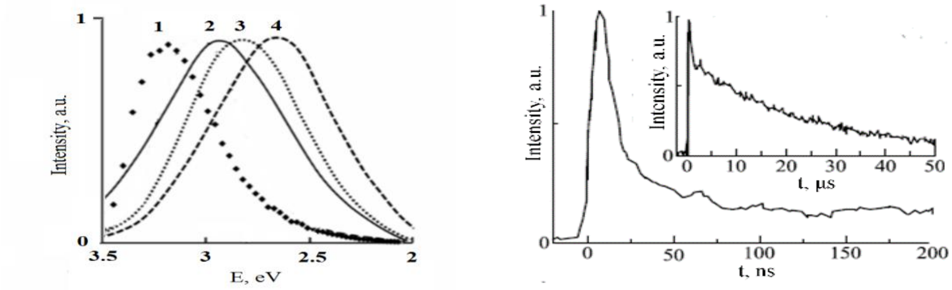

Fig. 4 (a): PhL spectra, excited by laser pulse (4.6 eV) in LiF crystals, doped with Fe_2O_3 (1, 2), TiO_2 (1, 3), WO_3 (1, 4), measured with 10 ns (1) and μs delay (2–4) relative to the end of the excitation pulse at 270 K (the spectra are normalized); (b): PhL decay kinetics at 2.6 eV in the crystal LiF-WO_3, measured with ns and μs delay (on the insert).

Below we will mainly describe the optical properties of tungsten trioxide in different matrixes.

As it turned out, luminescence at 2.6 eV can be excited in quite different materials: in dielectrics, not only LiF, but also MgF_2 and BaF_2, doped with WO_3; in natural phosphors $ZnWO_4$, $CdWO_4$, where tungsten trioxide is a structural component of the lattice; and in binary compound WO_3 (Fig. 5 (a)).

Figure 5 also shows the excitation spectra of emission at 2.6 eV in the studied materials in the range 3.8–6.2 eV.In all spectra there are thresholds in the region of 3.8–4 eV. Due to the presence of a small amount of dopant, we were able to measure the long-wavelength edge of the spectrum in the region >4 eV and establish the presence of three well-resolved bands at 6.2; 5.5 and 5 eV in spectrum of BaF_2 ceramics doped with 0.04 wt. % WO_3 (Fig. 5 (c)).

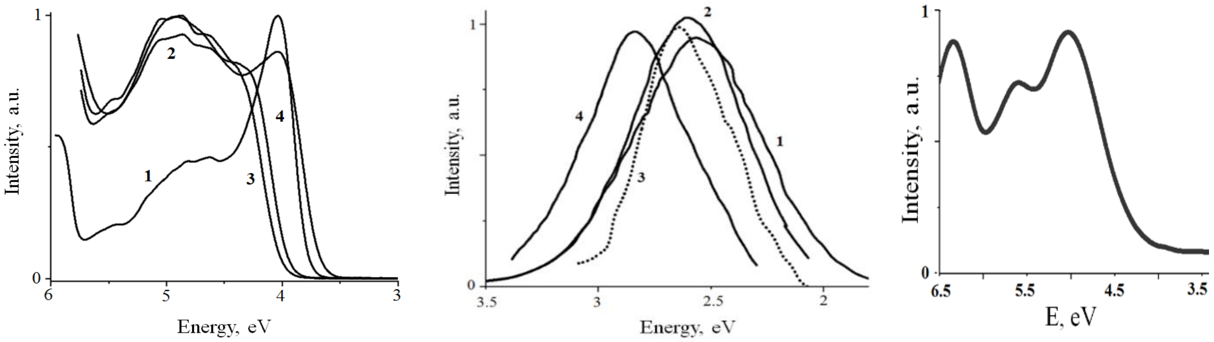

Figure 5 (a): PhL spectra, excited by laser pulse (4.6 eV) of $ZnWO_4$ ceramics samples (1); MgF_2-WO_3 (2), CL spectrum of binary compound WO_3 (3); BaF_2-WO_3 (4). (b): excitation spectra of emission at 2.6 eV in ceramics: $ZnWO_4$ (1), BaF_2-WO_3 (2), $CdWO_4$ (3) and MgF_2-WO_3 (4); (c): excitation spectrum of emission at 2.6 eV in BaF_2 ceramics doped with 0.01 wt. % WO_3.

Attempts to evaluate the role of the lattice cation in the organization of the energy structure of the EC led to the following conclusions.

It is known that at photoexcitation in the region ≥4 eV in double oxides AWO (A: Zn, Mg, Ca, Cd), which are n-type semiconductors with a band gap width of 3–5 eV, a luminescence in the region of 2.4–2.8 eV occurs; the lattice cation practically does not affect the spectral position and band half-width of the luminescence.

It turns out that this conclusion can be extended to materials of other chemical composition, provided that they contain W-O complex. So, in the double oxide Li2WO4 and in the Li2W0.95 Mo0.05 O4 system at low temperature (4.2 and 10 K, respectively), the spectrum of an intrinsic luminescence of the tetrahedral WO4 complex excited at about 5 eV consists of a band at 2.5 eV and FWHM 0.6 eV [32, 33]

In the most studied oxyfluoride K3WO3F3, belonging to the double oxides AWO6-xFx (A: K, Rb), emission at 2.6 eV with spectral and kinetic parameters similar to those in the spectrum of natural phosphorus ZnWO4 have been found [34].

Thus, the experimental data carried out by us and known from the literature confirm the calculations of theorists and indicate a minor influence of lattice cation on the formation of VB and CB in studied $MeWO_4$ semiconductor materials. Band structure of materials was formed by oxyanion orbitals. The VB top was formed by 2p states of oxygen; the bottom of the CB was formed by vacant 5d states of the polyvalent ion W. The value of the minimum energy required to excite the intrinsic luminescence in the materials is not less than E_g (3.2–4.5 eV).

Another parameter that allows estimating the degree of connection between the EC and the matrix lattice is the Stokes shift (E_{ss}). E_{ss} carries information about the value of energy losses for relaxation of the crystal lattice of the matrix in the location area of the excited EC. According to our results, the value of E_{ss} does not depend on the lattice type and is equal to 1.5–1.3 eV for EC with emission transition at 2.6 eV. Since the same value of E_{ss} is determined and in nanocrystalline powder WO_3, it becomes obvious that in this case E_{ss} does not reflect the elastic properties of the matrix containing the EC but characterizes the energy losses inside the tungsten oxide during its excitation.

In search of structure-sensitive characteristics of the luminescence, we have investigated the emission decay at 2.6 eV in various materials. It was found that in LiF matrix the emission decay time constant in the series of Fe, Ti, W oxides is equal to 180, 60 and 25 μs at 270 K and increases by a few orders of magnitude when temperature decreases. Figure 6 (a) (curves 1, 2) shows the temperature dependence of the luminescence decay time of impurity oxide centers TiO_2 and WO_3 in the LiF matrix. For the WO_3 the luminescence decay time in the low temperature region is different in ZnWO4 and LiF -WO_3 (Fig. 6 (a) (curves 2, 3)). However, it is not clear whether the lattice type or the energy position of the impurity in the lattice affects the probability of a radiative transition in the low temperature region.

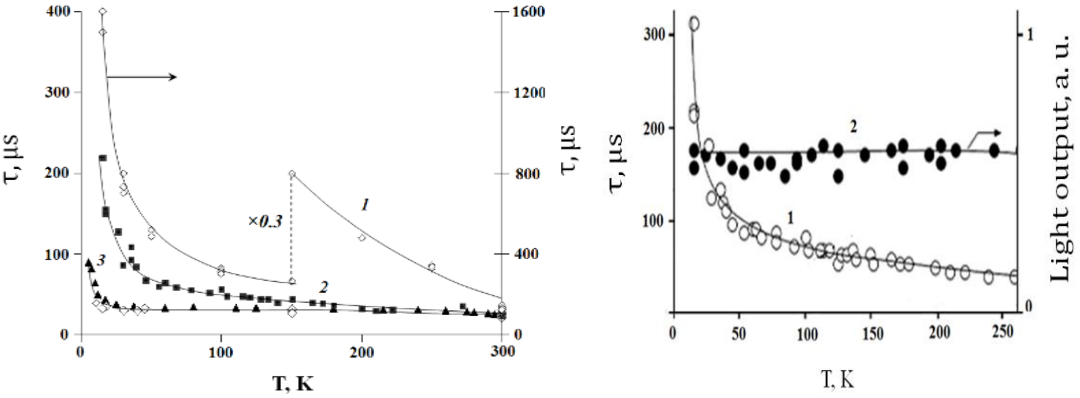

Figure 6 (a): temperature dependence of the decay time constants of PhL at 2.6 eV in LiF crystals, doped with TiO2 (1), WO3 (2), and in ceramic semiconductor ZnWO4 (3).
(In curve (3, a) black triangles are data from [35], rhombuses are data from the present studies). (b): temperature dependence of time decay constant (1), light output at 2. 6 eV (2) in LiF-WO3 crystal.

The kinetics of emission decay over time after the end of nanosecond pulse excitation splits up into three branches with different decay components and can be expressed by three exponentials:

$$J(t)=\sum A_i \exp(-t/\tau_i),$$

where A_i and τ_i are the amplitude intensity and the decay time constant of the corresponding decay time component.

Decay time constants at 270 K have the following values: τ_1=0.2 μs, τ_2= (3−4) μs and τ_3=18−20 in MgF_2-WO_3 and BaF_2-WO_3 ceramics samples, 25−35 μs in Zn and Cd tungstate ceramic samples and in LiF-WO_3 crystals. It should be noted that this peculiarity in the energy structure of luminescence centers (three-component attenuation process) is an inherent property of the emission transition at 2.6 eV and is preserved in different types of crystal lattice: in the face-centered cubic lattice (LiF), wolframite ($ZnWO_4$), rutile (MgF_2) and in the fluorite lattice (BaF_2).

The fundamental properties of the ES also include the existence of an anomalous temperature dependence of the emission decay at 2.6 eV in the low temperature region. In $MeWO_4$ semiconductors in the temperature range $5–400^0$ K there are two temperature regions with different temperature dependence of the light output in the band at 2.6 eV. In the high-temperature region ($T>250^0$ K) — in the region of temperature luminescence quenching — the decrease of light output with rising T ($I_3\tau_3=f(T)$) is due to increasing probability of thermal transition of the luminescence center from the excited to the ground state accompanied with phonons emission. In the low-temperature region ($5–100^0$ K) in a narrow temperature range, an increasing probability of the radiative transition is observed with a constant value of light output ($I_3\tau_3\neq f(T)$). This effect is observed in the range of 4–15 K in $ZnWO_4$ crystals, in $CdWO_4$ crystals in the region of 8–20 K, and in $CaWO_4$ in the range of 10–40 K [36–38].

We found a similar effect in LiF-WO_3 and LiF-TiO_2 systems, but in a wider temperature range of 15–150 K [39, 40]. The details of the anomalous temperature dependence of the luminescence parameters at 2.6 eV in the LiF-WO_3 crystal are presented in Figure 6 (b) (Temperature quenching of luminescence in the 2.6 eV band in this material starts at T> 250 K [36, 38, 41]). For mathematical description of the observed effects, a three-level energy model emission center consisting of ground level and splitted excited level, which lower sublevel is metastable, were proposed in [38, 42].

Thus, the above-described properties of the emission at 2.6 eV in six types of phosphors indicate the absence of a connection between tungsten trioxide and the matrix and the absence of a matrix effect on the parameters of various processes: absorption, excitation and photoluminescence with the participation of this oxide.

The minimum value of photon energy required to excite the emission at 2.6 eV in $ZnWO_4$ and $CdWO_4$ is about 4.1 eV and coincides with the transparency border these materials. In binary compound WO_3 the energy of about 3.6–2.7 eV is required to excite the luminescence at 2.6 eV. According to [43–45], emission in this material is a result of electron-hole recombination.

It has been established that in natural phosphors the excitation spectrum of luminescence at 2.5–2.7 eV represents an energy continuum in the range of 4–30 eV (the range of fundamental absorption). For example, in $CdWO_4$ 2.5 eV emission excited in the region of 4.5–7 eV is the result of recombination of genetically linked electron-hole pairs in the form of molecular oxyanion self-trapped excitons. In the region of higher energies photons create free electrons and holes. During subsequent electron-hole recombination, part of the released energy is transferred to EC to excite 2.5 eV emission. The similar processes occur in $ZnWO_4$ and $CaWO_4$ [12, 46–48]. The authors estimated the absorption coefficient in the region of fundamental absorption of 5–30 eV and confirmed the correlation between these two processes: emission excitation at 2.6 eV and the value of the absorbed energy. Consequently, the presented two types of spectra (excitation and absorption) belong to the fundamental properties of natural phosphors with tungsten trioxide as the oxyanion WO_6^{2-}.

Based on our earlier studies, the introduction tungsten oxide or oxides of transition metals Fe or Ti in LiF crystal is accompanied by a loss of transparency in a wide range of 4–12 eV. The absorption spectrum of LiF crystal doped with WO_3 is a group of overlapping bands in the range of 5–12 eV (Fig. 1 (a)). It means that the oxide of polyvalent metal forms wide energy subband of the absorption states in the dielectric band gap. In this case in LiF-WO_3 under light irradiation the following sequence of events is possible.

- Due to the large width, the subband of absorbed states of dopant (Fig. 1 (a)) located close to bottom of the dielectric CB or even overlapped one.
- Photogenerated exited electron (e) of dopant transits to CB leaving a hole on the dopant ion.
- The lifetime of such free electron in the CB becomes indefinitely large, first, due to absence of a hole (h) in the VB of the dielectric, second, low probability of e-h recombination on dopant, concentration of which is not more than 1 wt.%.

Conclusion

The characteristics of PhL and CL in semiconductors $ZnWO_4$, $CdWO_4$, binary compound WO_3 and in WO_3 doped dielectric matrixes LiF, MgF_2 and BaF_2 both in single crystals and in ceramic samples were investigated using time-resolved spectrometry methods.

The similarity of spectral-kinetic parameters of emission in the region of 2.9–2.5 eV excited in all investigated materials has been established.

The parameters values of the studied emission at 300 K are given below:

1. the spectral position of the emission band peak is at 2.5−2.8 eV;

2. FWHM of emission band is 0.5−0.75 eV;
3. emission decay time is 18−30 μs;
4. three-component character of luminescence decay at 2.6 eV and coincidence of time decay constants of components in different matrixes;
5. splitting of the upper excited energy level of the luminescence center;
6. the value of the minimum energy of excitation emission at 2.6 eV is about 3.8–4.1 eV in all investigated materials;
7. the Stokes shift value of emission center is 1.5–1.3 eV;
8. no impact of the lattice cation on the optical properties of tungsten trioxide.
9. the absorption spectrum of the LiF dielectric doped with WO_3 is a set of overlapping bands in the range of 4–12 eV, which indicates the formation of a subband of absorption levels of the dopant in the forbidden band of the dielectric.

The independence of the parameters of the observed emission from the properties of the matrices in which the radiative center is located allows us to attribute the radiative transition at 2.6 eV to an interband transition in the crystal structure of the binary compound WO_3, and the characteristics of the transition — to fundamental ones.

It is found that tungsten trioxide being doped in dielectric, forms a subband of impurity states in the dielectric band gap due to which of spatial separation of electron-hole impurity pairs becomes possible upon optical excitation of the dielectric.

References

1 Xu, H. BN nanosheets modified WO3 photocatalysts for enhancing photocatalytic properties under visible light irradiation / H. Xu, L. Liu, Y.H. Song, L.Y. Huang, Y.P. Li, Z.G. Chen, Q. Zhang, H.M. Li // J. Alloy. Compd. — 2016. — Vol. 660. — P. 48–54.

2 Xie, G. Gas sensing characteristics of WO3 vacuum deposited thin films / G. Xie, J.Yu, X. Chen, Y.Jiang // Sens. Actuators B Chem. — 2007. — Vol. 123. — P. 909–914.

3 Georg, A. Mechanism of the gasochromic coloration of porous WO3 films / A. Georg, W. Graf, R. Neumann, V. Wittwer // Solid State Ion. — 2000. — Vol. 127. — P. 319–328.

4 Hoˇcevar, M.; Cubic WO3 stabilized by inclusion of Ti: Applicable in photochromic glazing / M. Hoˇcevar, U.O. Krašovec // Sol. Energy Mater. Sol. Cells. — 2016. — Vol. 154. — P. 57–64.

5 Zhang, J.C. Preparation of ultra-thin and high-quality WO3 / J. C Zhang, C.W. Shi, J.J. Chen, Y.Q. Wang, M.Q. Li // J. Solid State Chem. — 2016. — Vol. 238. — P. 223–228.

6 Granqvist, C.G. Electrochromic tungsten oxide films: Review of Progress 1993–1998 // Sol. Energy Mater. Sol. Cells. — 2000. — Vol. 60. — P. 201–262.

7 Krašovec, U.O. Performance of a solid-state photoelectrochromic device / U.O. Krašovec, A. Georg, V. Wittwer, J. Luther, M. Topiˇc // Sol. Energy Mater. Sol. Cells. — 2004. — Vol. 84. — P. 369–380.

8 Fominsky, V. Yu. Properties of thin tungsten oxide films formed by ion-plasma and laser deposition methods / V.Yu. Fominsky, S.N. Grigoriev, R.I. Zomanov, V.V. Zuev, V.V. Grigoriev // Phys. and Tech. of Semiconductors. — 2012. — Vol. 46. — P. 416–424.

9 de Macedo O.B. Zinc tungstate: a review on its application as heterogeneous photocatalyst / O. B de Macedo, A. L. M. de Oliveira, I. M. G. dos Santos // Cerâmica. — 2022. — Vol. 68. — P. 294–315. http://dx.doi.org/10.1590/0366-69132022683873265

10 Mariappan, K. Fabrication of ZnWO4/Carbon Black Nanocomposites Modified Glassy Carbon Electrode for Enhanced Electrochemical Determination of Ciprofloxacin in Environmental Water Samples / K. Mariappan, S. Alagarsamy, S. -M. Chen, S. Sakthinathan // Materials. — 2023. — Vol. 16. — P. 741–754. https://doi.org/10.3390/

11 Nagirnyi, V. Energy transfer in ZnWO4 and CdWO4 scintillators / V. Nagirnyi, E. Feldbach, L. Jonsson, M. Kirm, A. Kotlov, A. Luschik, V. Nefedov, B. Zadneprovski // NIM A. — 2002. — Vol. 486. — P. 395–398.

12 Rzhevskaya, O.V. Optical and luminescent properties of single crystals CdWO4 and CdWO4: Mo / O.V. Rzhevskaya, D.A. Spassky, V.N. Kolobanov, V.V. Mikhailin, L.L. Nagornaya, I.A. Tupitsyna, B.I. Zadneprovsky // Opt. Spectr. — 2008. — Vol. 104. — P. 407–414.

13 Ovechkin, AE. Pulsed cathode luminescence of CdWO4 and ZnWO4 crystals / A.E. Ovechkin, L.V. Viktorov, L.L. Nagornaya // J. Appl. Spektroskopii. — 1988. — Vol. 48. — P. 396–401.

14 Kraus, H. Feasibility study of a ZnWO4 scintillator for exploiting materials signature in cryogenic WIMP dark matter searches / H. Kraus, V.B. Mikhailik, Y. Ramachers, D. Day, K.B. Hutton, J. Telfer // Phys. Letter D. — 2005. — Vol. 610. — P. 37–44.

15 Watterich, A. Coloration, impurities and non-local charge-compensation in ZnWO4 / A. Watterich, O.R. Gillianm, L.A. Kappers // Sol. St. Commun. — 1993. — Vol. 88. — P. 619–621.

16 Lammers, M. J.J. The luminescence of cadmium tungstate (CdWO4) / M. J. J Lammers, G. Blasse, D.S. Robertson // Phys. Stat. Sol. (a). — 1981. — Vol. 63. — P. 569–572.

17 Lisitsyn, V. Luminescence of the tungsten-activated MgF2 ceramics synthesized under the electron beam / V. Lisitsyn, L. Lisitsyna, A. Dauletbekova, M. Golkovski, Zh. Karipbayev, D. Musakhanov, A. Akilbekov, M. Zdorovets, A. Kozlovskiy, E. Polisadova. // NIM B. — 2018. — Vol. 435. — P. 263–267. https://doi.org/10.1016/j.nimb.2017.11.012

18 Лисицына Л.А. Оптическая керамика MgF_2 / Л.А. Лисицына, Р.Н. Сулеймен, Д.А. Мусаханов // Изв. вузов. Физика. — 2021. — Т. 64(1). — С. 64–70. DOI: 10.17223/00213411/64/1/64.

19 Lisitsyn, V. Radiation Synthesis of High-Temperature Wide-Bandgap Ceramics. / V. Lisitsyn, A. Tulegenova, M. Golkovski, E. Polisadova, L. Lisitsyna, D. Mussakhanov, G. Alpyssova // Micromachines. — 2023. — Vol. 14. — P. 2193. https://doi.org/10.3390/ mi14122193

20 Lisitsyn, V. Efficiency Dependence of Radiation-Assisted Ceramic Synthesis Based on Metal Oxides and Fluorides on Initial Powder Particle Sizes / V. Lisitsyn, E. Polisadova, L. Lisitsyna, A. Tulegenova, I. Denisov, M. Golkovski // Photonics. — 2023. — Vol. 10. — P. 1084. https://doi.org/10.3390/ photonics10101084

21 Lisitsyn, V. Nanodefects in YAG: Ce-Based Phosphor Microcrystals / V. Lisitsyn, L. Lisitsyna, A. Tulegenova Y. Ju, E. Polisadova, E. Lipatov, V. Vaganov // Crystals — 2019. — Vol. 9. — 476 (1–18). doi:10.3390/cryst9090476

22 Ovechkin, A.E. Luminescence of ZnWO4 and CdWO4 crystals / A.E. Ovechkin, V.D. Ryzhikov, G. Tamulaitis, A. Žukauskas // Phys. Stat. Sol. (a). — 1987. — Vol. 103. — P. 285–290.

23 Mikhailik, V.B. Cryogenic scintillators in searches for extremely rare events / V.B. Mikhailik, H. Kraus // J. Phys. D. – 2006. — Vol. 39. No. 6. — P. 1181–1191. DOI 10.1088/0022-3727/39/6/026.

24 Itoh, M. Photo-stimulated luminescence and photo induced infrared absorption in ZnWO4 / M. Itoh, T. Katagiri, T. Aoki, V. Fujita // Rad. Measur. — 2007. — Vol. 42. — P. 545–548.

25 Nagirnyi, V. Separation of excitonic and electron-hole process in metal tungstate / V. Nagirnyi, M. Kirm, A. Kotlov, A. Lushchik, L. Jonsson // J. Lumin. — 2003. — Vol. 102–103. — 597603.

26 Grigorjeva, L. Luminescence and transient absorption in ZnWO4 and ZnWO4-Fe crystals / L. Grigorjeva, D. Millers, S. Chernov, V. Pankratov, A. Watterich // Rad. Measur. — 2001. — Vol. 33. — P. 645–648.

27 Chernov, S. Luminescence spectra and decay kinetics in ZnWO4 and CdWO4 crystals / S. Chernov, L. Grigorjeva, D. Millers, A. Watterich // Phys. Stat. Sol. B. — 2004. — Vol. 241. — P. 1945–1948.

28 Figueiredo, Nuno M. Au-WO3 Nanocomposite Coatings for Localized Surface Plasmon Resonance Sensing / Nuno M. Figueiredo, F. Vaz, L. Cunha, A. Cavaleiro // Materials. — 2020. — Vol. 13. — P. 246. doi:10.3390/ma13010246.

29 Aslam, I. A novel Z-schemeWO3/CdWO4 photocatalyst with enhanced visible-light photocatalytic activity for the degradation of organic pollutants / I. Aslam, Ch. Cao, M. Tanveer, M.H. Farooq, W.S. Khan, M. Tahir, F. Idrees, S. Khalid // Royal Soc. Chem., RSC Advances. — 2014. — P. 6019–6026.

30 Баринова О.П. Исследование оптических свойств и низкотемпературной люминесценции монокристаллов в системе Li_2MoO_4–Li_2WO_4 / О.П. Баринова, С.В. Кирсанова, В.Н. Колобанов, В.В. Михайлин, Д.А. Спасский // Журн. Перспективные материалы. — 2008. — Т. 4. — С. 34–39. https://bib-pubdb1.desy.de/record/85859/files/Barinova_Kirsanova_Perspective_Mat.pdf

31 Lisitsyna, L.A. Composition Nanodefects in Doped Lithium Fluoride Crystals / L.A. Lisitsyna, V.M. Lisitsyn // Phys. Sol. State. — 2013. — Vol. 55. — P. 2297–2303.

32 Dauletbekova, A. Radiation transformation of the oxygen- containing impurity in LiF crystals doped with different polyvalent cations / A. Dauletbekova., L. Lisitsyna, V. Korepanov, V. Lisitsyn, L. Trefilova, R. Kassymkanova // Phys. Stat. Sol. C. — 2013. — Vol. 10. — P. 263–267.

33 Blasse, G. Luminescence of U6+ -activated Li2WO4 / G. Blasse, G.P.M. Van den Heuvel // Phys. Stat. Sol. (a). — 1977. — Vol. 39. — P. K157–K160.

34 Kozlov, A. Luminescence spectroscopy of K3WO3F3 oxyfluoride crystals / A. Kozlov, V. Pustovarov // AIP Conf. Proceed. — 2016. — Vol. 1767. — P. 020037–020042.

35 Kraus, H. ZnWO4 scintillators for cryogenic dark matter experiments / H Kraus, F.A. Danevich, S. Henry, V.V. Kobychev, V.B. Mikhailik, V.M. Mokina, S.S. Nagorny, O.G. Polischuk, V.I. Tretyak // NIM A. — 2009. — Vol. 600. — P. 594–598.

36 Mikhailik, V.B. Luminescence of CaWO4, CaMoO4, and ZnWO4 scintillating crystals under different excitations / V.B. Mikhailik, H. Kraus, G. Miller, M.S. Mykhaylyk, D. Wahl // J. Appl. Phys. — 2005. — Vol. 97. — 083523 (1–8).

37 Nagirnyi, V. Luminescence study of pure and Fe- or Mo-doped ZnWO4 crystals /V. Nagirnyi, L. Jonsson, M, Kirm, A. Kotlov, A. Luschik, I. Martinson, A. Watterich, B Zadneprovski // Rad. Measure. — 2004. — Vol. 38. — P. 519–522.

38 Mikhailik, V.B. Performance of scintillation materials at cryogenic temperatures / V.B. Mikhailik, H. Kraus // Phys. Stat. Sol. B. — 2010. — Vol. 247. — P. 1583–1599. DOI 10.1002/pssb.200945500

39 Lisitsyna, L. Luminescence of MgF2-WO3 ceramics synthesized in flux of 1.5 MeV electron beam / L. Lisitsyna, A. Popov, Zh. Karipbayev, D. Mussakhanov, E. Feldbach // Opt. Mat. — 2022. — Vol. 133. 112999 (1–8). https://doi.org/10.1016/ j.optmat.2022.112999

40 Lisitsyna, L. Spectral and kinetic characteristics of the luminescence center in LiF-WO3 and ZnWO4 crystals / L. Lisitsyna, I A. Tupitsyna, L.N. Trefilova // IOP Conf. Series: Mat. Science and Engineering. — 2015. — Vol. 81. — P. 1–9.

41 Koerke, Cr. Excited- state absorption in ZnWO4 crystal / Cr. Koerke, A. Lempicki // J. Lumines. — 1994. — Vol. 59. — P. 33–37.

42 Van Loo, W. Liminescence decay of lead molybdate and lead tungstate — a descriptive model // J. Luminesc. — 1975. — Vol. 10. — P. 221–235.

43 He, T. Photochromic materials based on tungsten oxide /T. He, J. Yao // J. Mater. Chem. — 2007. — Vol. 17. — P. 4547–4557. DOI: 10.1039/b709380b

44 Bechinger, C. On the fundamental roleofoxygenforthephotochromiceffectof WO_3 / C. Bechinger, G. Oefinger, S. Herminghaus, P. Leiderer // J. Appl. Phys. — 1993. — Vol. 74. — P. 4527−4533.

45 Yan, J. Design of 3D WO3/h-BN nanocomposites for efficient visible-light-driven photocatalysis / J. Yan, J. Gu, X. Wang, Y. Fan, Y. Zhao, J. Lian, Y. Xu, Y. Song, H. Xu, H. Li // RSC Adv. — 2017. — Vol. 7. — 25160. DOI: 10.1039/c7ra02929b

46 Mikhailin, V.V. Study of optical and luminescent properties of some inorganic scintillators in the fundamental absorption region / V.V. Mikhailin, A.N. Belsky, I.A. Kamenskikh, V.N. Kolobanov, P.A. Orekhanov, I.N. Shpinkov, D.A. Spassky, A.N. Vasil'ev // Nucl. Instr. Meth. A. — 2002. — Vol. 486. — P. 367–373.

47 Kolobanov, V.N. Optical and luminescent properties of anisotropic tungstate crystals / V. N Kolobanov,. I.A. Kamenskikh, V.V. Mikhailin, I.N. Shpinkov, D.A. Spassky, B.I. Zadneprovsky, L.I. Potkin, G. Zimmerer // NIM A. — 2002. — Vol. 486. — P. 496–503.

48 Nagirnyi, V. Excitinic and recombination processes in CaWO4 and CdWO4 scintillators under synchrotron irradiation / V. Nagirnyi, E. Feldbach, L. Jonsson, M, Kirm, A. Luschik, Ch. Luschik, L.L. Nagornaya, V.D. Ryzhikov, F. Savikhin, G. Svensson, I.A. Tupitsina // Rad. Measur. — 1998. — Vol. 29. — P. 247–250.

Л.А. Лисицына, Г.К. Алпысова, Д.А. Мусаханов

Әртүрлі матрицалардағы вольфрам триоксиді люминесценциясының оптикалық сипаттамалары

Екі түрдегі люминофорлардағы сәулеленудің оптикалық сипаттамаларының рұқсат етілген уақыт бойынша спектроскопиясына салыстырмалы зерттеу ұсынылған, яғни: табиғи люминофорлар: $ZnWO_4$, $CdWO_4$, микрокристалды WO_3 және жасанды люминофорлар: кең аралықтағы диэлектриктер, LiF, MgF_2 және BaF_2 вольфрам триоксидімен легирленген. 1,5 МэВ электрон ағыны кезінде ауада жоғары жылдамдықты сәулелену синтезі процесінде алынған монокристалдар да, керамикалық үлгілер де зерттелді. Зерттелетін материалдардың люминесценциясының спектрлік және кинетикалық сипаттамалары диэлектриктердің қасиеттеріне ұқсас екендігі анықталды, мұнда WO_3 допант ретінде қатысады; жартылай өткізгіштерде вольфрам триоксиді WO_6^2 – оксианион түрінде және вольфрам триоксиді екілік компонентінің кристалдық торында болады. Вольфрам триоксиді диэлектрикте легирленген кезде диэлектриктің өту жолағында қоспа күйлерінің ішкі жолағын түзетіні дәлелденді, соның арқасында диэлектриктің оптикалық қозуы кезінде электронды-тесік қоспа жұптарының кеңістікте бөлінуі мүмкін болады.

Кілт сөздер: радиациялық синтез, табиғи фосфор, жасанды фосфор, люминесценция, уақыт-рұқсат етілген спектроскопия, жарқырау орталығы, ішкі жолақ.

Л.А. Лисицына, Г.К. Алпысова, Д.А. Мусаханов

Оптические характеристики люминесценции триоксида вольфрама в различных матрицах

Представлено сравнительное исследование с помощью время-разрешенной спектроскопии оптических характеристик излучения в двух типах люминофоров: природные люминофоры: ZnWO4, CdWO4, микрокристаллический WO3 и искусственные люминофоры: широкозонные диэлектрики, LiF, MgF2 и BaF2, легированные триоксидом вольфрама. Были исследованы как монокристаллы, так и керамические образцы, полученные в процессе высокоскоростного радиационного синтеза на воздухе под потоком электронов 1,5 МэВ. Установлено, что спектрально-кинетические характеристики люминесценции исследованных материалов имеют сходство со свойствами диэлектриков, где WO3 присутствует в качестве допанта; в полупроводниках, где триоксид вольфрама присутствует как WO62 — оксианион и в кристаллической решетке бинарного компонента триоксида вольфрама. Доказано, что триоксид вольфрама, будучи легированным в диэлектрике, образует в полосе пропускания диэлектрика подполосу примесных состояний, благодаря которой при оптическом возбуждении диэлектрика становится возможным пространственное разделение электронно-дырочных примесных пар.

Ключевые слова: радиационный синтез, природный люминофор, искусственный люминофор, люминесценция, время-разрешенная спектроскопия, центр свечения, подзона.

References

1 Xu, H., Liu, L., Song, Y.H., Huang, L.Y., Li, Y.P., Chen, Z.G., Zhang, Q., & Li, H.M. (2016). BN nanosheets modified WO3 photocatalysts for enhancing photocatalytic properties under visible light irradiation. *J. Alloy. Compd., 660*, 48–54. https://doi.org/10.1016/j.jallcom.2015.11.042

2 Xie, G., Yu, J., Chen, X., & Jiang, Y. (2007). Gas sensing characteristics of WO3 vacuum deposited thin films. *Sens. Actuators B Chem., 123*, 909–914. DOI: 10.1016/j.snb.2006.10.059

3 Georg, A., Graf, W., Neumann, R., & Wittwer, V. (2000). Mechanism of the gasochromic coloration of porous WO3 films. *Solid State Ion., 127*, 319–328. https://doi.org/10.1016/S0167-2738(99)00273-8

4 Hoˇcevar, M. & Krašovec, U.O. (2016). Cubic WO3 stabilized by inclusion of Ti: Applicable in photochromic glazing. *Sol. Energy Mater. Sol. Cells., 154*, 57–64. https://doi.org/10.1016/j.solmat.2016.04.041

5 Zhang, J.C., Shi, C.W., Chen, J.J., Wang, Y.Q., & Li, M.Q. (2016). Preparation of ultra-thin and high-quality WO3. *J. Solid State Chem., 238*, 223–228. https://doi.org/10.1016/j.jssc.2016.03.033

6 Granqvist, C.G. (2000). Electrochromic tungsten oxide films: Review of Progress 1993–1998. *Sol. Energy Mater. Sol. Cells., 60*, 201–262. https://doi.org/10.1016/S0927-0248(99)00088-4

7 Krašovec, U.O., Georg, A., Wittwer, V., Luther, J., & Topiˇc, M. (2004). Performance of a solid-state photoelectrochromic device. *Sol. Energy Mater. Sol. Cells., 84*, 369–380. https://doi.org/10.1016/j.solmat.2004.01.043

8 Fominski, V.Y., Grigoriev, S.N., Romanov, R.I., Zuev, V.V., & Grigoriev, V.V. (2012). Properties of tungsten oxide thin films formed by ion-plasma and laser deposition methods. *Phys. and Tech. of Semiconductors, 46*, 401–409. https://doi.org/10.1134/S1063782612030098

9 De Macedo, O.B., de Oliveira, A.L.M., & dos Santos, I.M.G. (2022). Zinc tungstate: a review on its application as heterogeneous photocatalyst. *Ceramica. 68*, 294–315. http://dx.doi.org/10.1590/0366-69132022683873265

10 Mariappan, K., Alagarsamy, S., Chen, S.M., & Sakthinathan, S. (2023). Fabrication of ZnWO4/Carbon Black Nanocomposites Modified Glassy Carbon Electrode for Enhanced Electrochemical Determination of Ciprofloxacin in Environmental Water Samples. *Materials, 16*, 741–754. https://doi.org/10.3390/.

11 Nagirnyi, V., Feldbach, E., Jonsson, L., Kirm, M., Kotlov, A., Luschik, A., Nefedov, V., & Zadneprovski, B. (2002). Energy transfer in ZnWO4 and CdWO4 scintillators. *NIM A., 486*, 395–398. DOI: 10.1016/S0168-9002(02)00740-4

12 Rzhevskaya, O.V., Spassky, D.A., Kolobanov, V.N., Mikhailin, V.V., Nagornaya, L.L., Tupitsyna, I.A., & Zadneprovsky, B.I. (2008). Optical and luminescent properties of single crystals CdWO4 and CdWO4: Mo. *Opt. Spectr., 104.*, 407–414. DOI: 10.1134/S0030400X08030090

13 Ovechkin, A.E., Viktorov, L.V., & Nagornaya, L.L. (1988). Pulsed cathode luminescence of CdWO4 and ZnWO4 crystals. *J. Appl. Spektroskopii, 48*, 396–401. https://doi.org/10.1007/BF00663290

14 Kraus, H., Mikhailik, V.B., Ramachers, Y., Day, D., Hutton, K.B., & Telfer, J. (2005). Feasibility study of a ZnWO4 scintillator for exploiting materials signature in cryogenic WIMP dark matter searches. *Phys. Letter D., 610*, 37–44. https://doi.org/10.1016/j.physletb.2005.01.095

15 Watterich, A., Gillianm, O.R., & Kappers, L.A. (1993). Coloration, impurities and non-local charge-compensation in ZnWO4. *Sol. St. Commun., 88*, 619–621. https://doi.org/10.1016/0038-1098(93)90063-S

16 Lammers, M.J.J., Blasse, G., & Robertson, D.S. (1981). The luminescence of cadmium tungstate (CdWO4). *Phys. Stat. Sol. (a)., 63*, 569–572. https://doi.org/10.1515/9783112501863-023

17 Lisitsyn, V., Lisitsyna, L., Dauletbekova, A., Golkovski, M., Karipbayev, Zh., Musakhanov, D., Akilbekov, A., Zdorovets, M., Kozlovskiy, A., & Polisadova, E. (2018). Luminescence of the tungsten-activated MgF2 ceramics synthesized under the electron beam. *NIM B., 435*, 263–267. https://doi.org/10.1016/j.nimb.2017.11.012.

18 Lisitsyna, L.A., Sulejmen, R.N., & Mussahanov, D.A. (2021). Opticheskaia keramika MgF$_2$ [Optical ceramics MgF2]. *Izvestiia vysshikh uchebnykh zavedenii. Fizika — News of higher educational institutions. Physics*, *64*(1), 64–70 [in Russian]. DOI: 10.17223/00213411/64/1/64.

19 Lisitsyn, V., Tulegenova, A., Golkovski, M., Polisadova, E., Lisitsyna, L., Mussakhanov, D., & Alpyssova, G. (2023). Radiation Synthesis of High-Temperature Wide-Bandgap Ceramics. *Micromachines, 14*, 2193. https://doi.org/10.3390/mi14122193.

20 Lisitsyn, V., Polisadova, E., Lisitsyna, L., Tulegenova, A., Denisov, I., & Golkovski, M. (2023). Efficiency Dependence of Radiation-Assisted Ceramic Synthesis Based on Metal Oxides and Fluorides on Initial Powder Particle Sizes. *Photonics, 10*, 1084. https://doi.org/10.3390/ photonics10101084.

21 Lisitsyn, V., Lisitsyna, L., Tulegenova, A., Ju Y., Polisadova, E., Lipatov, E., & Vaganov, V. (2019). Nanodefects in YAG:Ce-Based Phosphor Microcrystals. *Crystals, 9*, 476 (1–18). doi:10.3390/cryst9090476.

22 Ovechkin, A.E., Ryzhikov, V.D., Tamulaitis, G., & Žukauskas, A. (1987). Luminescence of ZnWO4 and CdWO4 crystals. *Phys. Stat. Sol. (a)., 103*, 285–290. https://doi.org/10.1002/pssa.2211030133

23 Mikhailik, V.B., & Kraus, H. (2006). Cryogenic scintillators in searches for extremely rare events. *J. Phys. D., 39*(6), 1181–1191. DOI 10.1088/0022-3727/39/6/026.

24 Itoh, M., Katagiri, T., Aoki, T., & Fujita, V. (2007). Photo-stimulated luminescence and photo induced infrared absorption in ZnWO4. *Rad. Measur., 42*, 545–548. DOI: 10.1016/j.radmeas.2007.01.049

25 Nagirnyi, V., Kirm, M., Kotlov, A., Lushchik, A., & Jonsson, L. (2003). Separation of excitonic and electron-hole process in metal tungstate. *J. Lumin.*, 102–103, 597603. https://doi.org/10.1016/S0022-2313(02)00596-3

26 Grigorjeva, L., Millers, D., Chernov, S., Pankratov, V., & Watterich, A. (2001). Luminescence and transient absorption in ZnWO4 and ZnWO4-Fe crystals. *Rad. Measur., 33,* 645–648. https://doi.org/10.1016/S1350-4487(01)00076-2

27 Chernov, S., Grigorjeva, L., Millers, D., & Watterich, A. (2004). Luminescence spectra and decay kinetics in ZnWO4 and CdWO4 crystals. *Phys. Stat. Sol. B.*, *241*, 1945–1948. DOI: 10.1002/pssb.200302015

28 Figueiredo, Nuno, M., Cunha, F. & Vaz, L.A. (2020). Cavaleiro Au-WO3 Nanocomposite Coatings for Localized Surface Plasmon Resonance Sensing. *Materials, 13*, 246. doi:10.3390/ma13010246.

29 Aslam, I., Cao, Ch., Tanveer, M., Farooq, M.H., Khan, W.S., Tahir, M., Idrees, F., & Khalid, S. (2014). A novel Z-scheme WO3/CdWO4 photocatalyst with enhanced visible-light photocatalytic activity for the degradation of organic pollutants. *Royal Soc. Chem., RSC Advances,* 6019–6026. https://doi.org/10.1039/C4RA15847D

30 Barinova, O.P., Kirsanova, S.V., Kolobanov, V.N., Mihajlin, V.V., & Spasskij, D.A. (2008). Issledovanie opticheskikh svoistv i nizkotemperaturnoi liuminestsentsii monokristallov v sisteme Li_2MoO_4–Li_2WO_4 [Study of optical properties and low-temperature luminescence of single crystals in the Li_2MoO4–Li_2WO4 system]. *Zhurnal Perspektivnye materialy — Journal of Perspective Materials, 4*(1), 34–39. https://bib-pubdb1.desy.de/record/85859/files/Barinova_Kirsanova_Perspective_Mat.pdf [in Russian].

31 Lisitsyna, L.A., & Lisitsyn, V.M. (2013). Composition Nanodefects in Doped Lithium Fluoride Crystals. *Phys. Sol. State,* 55, 2297–2303. DOI:10.1134/S1063783413110139

32 Dauletbekova, A., Lisitsyna, L., Korepanov, V., Lisitsyn, V., Trefilova, L., & Kassymkanova, R. (2013). Radiation transformation of the oxygen- containing impurity in LiF crystals doped with different polyvalent cations. *Phys. Stat. Sol. C., 10,* 263–267. DOI:10.1002/pssc.201200473

33 Blasse, G., & Van den Heuvel, G.P.M. (1977). Luminescence of U6+ -activated Li2WO4. *Phys. Stat. Sol. (a).*, 39, K157–K160. DOI:10.1002/pssa.2210390261

34 Kozlov, A., & Pustovarov, V. (2016). Luminescence spectroscopy of K3WO3F3 oxyfluoride crystals. *AIP Conf. Proceed*., *1767*, 020037–020042. DOI:10.1063/1.4962621

35 Kraus, H., Danevich, F.A., Henry, S., Kobychev, V.V., Mikhailik, V.B., Mokina, V.M., Nagorny, S.S., Polischuk, O.G., & Tretyak, V.I. (2009). ZnWO4 scintillators for cryogenic dark matter experiments. *NIM A., 600,* 594–598. DOI:10.1016/j.nima.2008.12.142

36 Mikhailik, V.B., Kraus, H., Miller, G., Mykhaylyk, M.S., & Wahl, D. (2005). Luminescence of CaWO4, CaMoO4, and ZnWO4 scintillating crystals under different excitations. *J. Appl. Phys.*, *97*, 083523 (1–8). https://doi.org/10.1063/1.1872198

37 Nagirnyi, V., Jonsson, L., Kirm, M., Kotlov, A., Luschik, A., Martinson, I., Watterich, A., & Zadneprovski, B. (2004). Luminescence study of pure and Fe- or Mo-doped ZnWO4 crystals. *Rad. Measure., 38,* 519–522. DOI:10.1016/j.radmeas.2004.01.024

38 Mikhailik, V.B., & Kraus, H. (2010). Performance of scintillation materials at cryogenic temperatures. *Phys. Stat. Sol. B., 247*, 1583–1599. DOI 10.1002/pssb.200945500.

39 Lisitsyna, L., Popov, A., Karipbayev, Zh., Mussakhanov, D., & Feldbach, E. (2022). Luminescence of MgF2-WO3 ceramics synthesized in flux of 1.5 MeV electron beam. *Opt. Mat.*, *133*, 112999 (1–8). https://doi.org/10.1016/j.optmat.2022.112999.

40 Lisitsyna, L., Tupitsyna, I.A., & Trefilova, L. (2015). Spectral and kinetic characteristics of the luminescence center in LiF-WO3 and ZnWO4 crystals. *IOP Conf. Series: Mat. Science and Engineering, 81*, 1–9. DOI:10.1088/1757-899X/81/1/012024

41 Koepke, Cz., & Lempicki, A. (1994). Excited- state absorption in ZnWO4 crystal. *J. Lumin., 59,* 33–37. https://doi.org/10.1016/0022-2313(94)90019-1

42 Van Loo, W. (1975). Liminescence decay of lead molybdate and lead tungstate - A descriptive model. *J. Lumin*., *10,* 221–235. https://doi.org/10.1016/0022-2313(75)90071-X

43 He, T., & Yao, J. (2007). Photochromic materials based on tungsten oxide. *J. Mater. Chem., 17,* 4547–4557. DOI: 10.1039/b709380b.

44 Bechinger, C., Oefinger, G., Herminghaus, S., & Leiderer, P. (1993). On the fundamental role of oxygen for the photochromic effect of WO_3. *J. Appl. Phys., 74,* 4527−4533. DOI:10.1063/1.354370

45 Yan, J., Gu, J., Wang, X., Fan, Y., Zhao, Y., Lian, J., Xu, Y., Song, Y., Xu, H., & Li, H. (2017). Design of 3D WO3/h-BN nanocomposites for efficient visible-light-driven photocatalysis. *RSC Adv., 7,* 25160. DOI: 10.1039/c7ra02929b.

46 Mikhailin, V.V., Belsky, A.N., Kamenskikh, I.A., Kolobanov, V.N., Orekhanov, P.A., Shpinkov, I.N., Spassky, D.A., & Vasil'ev, A.N. (2002). Study of optical and luminescent properties of some inorganic scintillators in the fundamental absorption region. *Nucl. Instr. Meth. A., 486,* 367–373. https://doi.org/10.1016/S0168-9002(02)00735-0

47 Kolobanov, V.N., Kamenskikh, I.A., Mikhailin, V.V., Shpinkov, I.N., Spassky, D.A., Zadneprovsky, B.I., Potkin, L.I., & Zimmerer, G. (2002). Optical and luminescent properties of anisotropic tungstate crystals. *NIM A., 486*, 496–503. doi:10.1016/S0168-9002(02)00760-X

48 Nagirnyi, V., Feldbach, E., Jonsson, L., Kirm, M., Luschik, A., Luschik, Ch., Nagornaya, L.L., Ryzhikov, V.D., Savikhin, F., Svensson, G., & Tupitsina, I.A. (1998). Excitonic and recombination processes in CaWO4 and CdWO4 scintillators under synchrotron irradiation. *Rad. Measur., 29,* 247–250. DOI:10.1016/S1350-4487(98)00017-1

Information about the authors

Liudmila A. Lisitsyna (corresponding author) — Doctor of physical and mathematical sciences, professor, Department of Physics, Chemistry and Theoretical Mechanics, Tomsk State University of Architecture and Building, Tomsk, Russia; e-mail: *lisitsyna@mail.ru*. SCOPUS Author ID: 6602905153

Gulnur K. Alpyssova — PhD, Department of Radiophysics and Electronics, Karaganda Buketov University, Karaganda, Kazakhstan; e-mail: *gulnur-0909@mail.ru*; SCOPUS Author ID: 57204979025, ORCID ID: 0000-0002-7164-2188

Dossymkhan A. Mussakhanov — Candidate of technical sciences, Department of Radio Engineering, Electronics and Telecommunications, L.N. Gumilyov Eurasian National University, Department of Radio Engineering, Electronics and Telecommunications, Astana, Kazakhstan. Author ID: 57197728253, ORCIDID:0000-0002-1823-2526.

Article
https://doi.org/10.31489/2024PH4/156-167
UDC 628.9.037

Received: 06.06.2024
Accepted: 09.08.2024

E.F. Polisadova, N.D. Tran

National Research Tomsk Polytechnic University, Tomsk, Russia
*(*Corresponding author's e -mail: elp@tpu.ru)*

Electron Beam-assisted Synthesists, Structure and Luminescent Properties Porous Ceramics of $MgAl_2O_4$ and $MgAlGaO_4$ Doped with Europium

Porous ceramics of $MgAl_2O_4$ (MAS) and $MgAlGaO_4$ (MAGS) doped with europium were synthesized by radiation method. Radiation synthesis was performed with high efficiency within less than 1 s using radiation energy and mixture materials with no additives or any other materials used to promote synthesis. The synthesis method using a high-energy electron beam makes it possible to obtain refractory materials with high productivity, flexibly control the technological conditions of the process, and, accordingly, synthesize materials with desired properties. The structural properties of synthesized porous ceramics were investigated by X-ray diffraction (XRD-7000S diffractometer, Shimadzu), SEM. Results have shown that, the synthesized MAS have cubic structure and are in crystalline spinel $MgAl_2O_4$, while the synthesized double spinel MAGS contains two main phase components, $MgAl_2O_4$ and $MgGa_2O_4$. To study the luminescence properties of MAS and MAGS synthesized spinel doped with europium, photoluminescence measurements were performed. The photoluminescence spectrum of excitation of Eu^{3+} ions in spinel was monitored at λ_{em} = 615 nm ($^5D_0 \rightarrow {}^7F_2$). The PLE shows the f→f transition in the configuration of Eu^{3+} ions (at 393 nm ($^7F_0 \rightarrow {}^5L_6$), 463 nm ($^7F_0 \rightarrow {}^5D_2$)). The excitation band at 330 nm and 260 nm is characteristic of the charge transition between Eu^{3+} and O^{2-} ions. The photoluminescence spectrum of the samples under excitation at 260 nm was studied. In the PL spectrum of spinel samples, the emission of Eu^{3+} ions are clearly visible. In the structure of the band with a maximum of 615, a peak is visible at 590 nm, characterized by the $^5D_0 \rightarrow {}^7F_1$ transition. In the PL spectrum of samples, a weak spectral band appears with a maximum at 535 nm, characteristic of the emission of Eu^{3+} ions with the $^5D_1$-$^7F_1$ transition. It is shown that the efficiency of radiation synthesis depends on the granulometric composition of the initial oxide powders.

Keywords: ceramic spinels, double spinel, Eu-doped, radiation synthesis, luminescence, MgAl2O4, MgAlGaO4.

Introduction

Materials with spinel structure are technologically significant materials in science and technology. Aluminum-magnesium spinel $MgAl_2O_4$ has high hardness, chemical stability, low electrical conductivity, resistance to temperature effects, spinel crystals are transparent in the visible and infrared wavelength ranges [1]. Due to the combination of optical, mechanical and thermal properties, aluminum-magnesium spinel is used in aviation and space technology, optical elements of optical and optoelectronic devices operating in extreme conditions, gas sensors, and active laser media are produced from it. Design of materials in the form of double spinels opens up great prospects. In [2, 3], theoretical methods showed that the double spinel structure is thermodynamically favorable for the mixed system $MgAl_2O_4$ + $MgGa_2O_4$, mixing of cations on different sublattices will occur at a relatively low temperature. Synthesis of such materials opens up new possibilities for designing materials with spinel structure and individual functionality.

The authors of [4] showed that double aluminum-gallium-magnesium spinel $MgAlGaO_4$ spinel has semiconductor properties and is a promising material for manufacturing short-wave LED and laser devices, photovoltaic solar cells. However, the technologies for synthesizing such materials are not developed. Synthesis of materials based on normal $MgAl_2O_4$ and inverse $MgGa_2O_4$ spinel is carried out by thermal [5] and sol-gel [6] methods. The methods are complex and labor-intensive. In [5, 6], it was shown that partial conversion occurs in inverse spinel $MgGa_2O_4$: Mg^{2+} and Ga^{3+} can occupy tetrahedral and octahedral positions, which facilitate the penetration of the dopant and changes the luminescent properties. In [5], it was shown that $MgGa_2O_4$ doped with Eu^{3+} ions has excellent luminescent properties in the "red" and "orange" regions of the spectrum, $MgGa_2O_4$: Mn^{2+} phosphors were successfully used as green emitters in night vision and data storage devices, and in [7], inverse spinel was proposed to be used as a self-activating phosphor. Europium-activated $MgAl_2O_4$ spinel is a promising heat-resistant phosphor [8]. The luminescent properties of double spinel $MgAlGaO_4$ have not yet been studied.

This paper considers the possibility of using a radiation method using a high-energy electron beam to synthesize ceramics based on $MgAl_2O_4$ and double spinel $MgAlGaO_4$. The synthesis method has been well tested on refractory oxide materials [9, 10]. The method is characterized by high synthesis speed and high efficiency.

Experimental

The radiation method of synthesis is based on the ability of high-energy particles to excite and destroy molecules of a substance, leading to the formation of new materials. For example, an electron penetrates a substance, causing ionization in it: the particle forms about 10 thousand particles of lower energy, these particles begin to break old chemical bonds and form new ones. Therefore, the use of the energy of an electron beam generated by an accelerator for the synthesis of ceramics from refractory inorganic materials is very promising and this method is used to synthesize spinel samples in our study. The synthesis of ceramics was carried out by direct action of an electron beam on the initial mixture of a given composition on the ELV6 electron accelerator at the facility UNU Stand ELV-6 at the Budker Institute of Nuclear Physics SB RAS [11]. High-energy electron beams with an electron energy of 1.4 MeV were used for synthesis. The resulting beam was extracted through a differential pumping system, had a Gaussian profile on the target surface with a spot area of 1 cm^2. The synthesis occurred when the threshold power density of the energy flow was exceeded, which was 30 kW/cm^2. For the synthesis process, a mixture of high-purity oxides MgO, Al_2O_3 and Ga_2O_3 in a stoichiometric ratio was prepared. Eu_2O_3 oxide was added to the mixture in an amount of 0.5 wt.%. The oxide mixture was stirred in a mixer for 2 hours, after which it was placed in a massive copper crucible measuring 100 × 50 × 10 mm. The crucible depth for the synthesis of a specific ceramic was selected based on the condition of complete absorption of the electron beam of a given energy by the mixture. The crucible was located under the accelerator outlet on a strong metal table. Synthesis proceeds in two different modes: “scanning” and “no scanning”. In the “no scanning” mode, the crucible displaces relative to the beam at a speed of 1 cm/s along the entire length of 100 mm. In the “scanning” mode, the beam scans in the transverse direction of the scanning beam. The beam cross section is 1 cm^2 in the plane of the crucible surface. The electron beam was scanned at a frequency of 50 Hz in the transverse direction of the crucible, while the crucible moved relative to the scanning beam at a speed of 1 cm/s.

The structure of the obtained samples was studied using an XRD-7000 X-ray diffractometer (Shimadzu, Japan). The morphology of the samples was studied using a Hitachi TM3030 scanning electron microscope CEM with a Bruker XFlash MIN SVE energy dispersive analysis system at an accelerating voltage of 15 kV. The dispersion of all starting materials was measured by laser diffraction on a Shimadzu SALD-7101 laser particle size analyzer.

Cathodoluminescence (CL) was measured using a pulsed electron beam from the GIN-600 accelerator as an excitation source. The electron pulse duration at half-width $t_{1/2}$ was 15 ns, the average energy of accelerated electrons E was 250 keV, and the electron beam power density was $j = 8$ — 300 mJ/cm^2. Cathodoluminescence oscillograms were recorded at a certain wavelength in the range of 250–1100 nm by an optical spectrometer consisting of an MDR-3 monochromator, an FEU-106 photomultiplier, and a four-channel 350 MHz LeCroy WR 6030A oscilloscope. The oscillograms were then converted into luminescence kinetic curves in order to determine the kinetic parameters of luminescence decay. The integral CL spectra were measured using an AvaSpec-2048 fiber-optic spectrometer (340–1100 nm) in a “time window” 1 ms. All measured data were corrected taking into account the spectral sensitivity of the optical path.

The photoluminescence (PL) and excitation spectra were measured using an Agilent Cary Eclipse fluorescence spectrophotometer. The spectrophotometer uses a high-performance R928 dual photomultiplier with a scanning speed of 24,000 nm/min, a pulsed xenon flash lamp with a frequency of 80 Hz is used, the spectral range of the spectrometer is from 190 to 1100 nm.

Results and Discussion

In this work, several samples of spinels, normal and double, were synthesized and studied using initial components with different dispersion and under different process conditions. Table 1 shows the compositions and designations of the samples and initial components.

The study of the structure of the synthesized radiation ceramics showed that the position of the diffraction peaks of the MgAl2O4 samples and their intensity completely correspond to the X-ray diffraction pattern of the reference sample of spinel $MgAl_2O_4$ from the PDF2 database (card 00-021-1152). The synthesized samples have a cubic structure belonging to the F3dm group with a lattice constant corresponding to the sample in the PDF2 database. In addition to the diffraction peaks corresponding to the reference sample of spinel, there is also a diffraction peak at $2\theta = 43.04$, attributed to the flat reflection (200) of the MgO phase. Clear diffraction peaks indicate good crystallinity of the synthesized $MgAl_2O_4$. Weak peaks of the MgO phase and the absence of peaks associated with Al_2O_3 indicate a sufficiently high purity of the obtained $MgAl_2O_4$. The average crystallite size of the synthesized samples is in the range of 500–600 nm.

Table 1

Ceramics synthesized by radiation method

Type spinel	Sample	Type powder			Composition	Power kW/cm^2	Sample weight, g.	Output %
		MgO	Al_2O_3	Ga_2O_3				
$MgAlGaO_4$	MAGS1	M2	K7	K8	MgO 35.9 %, Al_2O_3 22.8 %, Ga_2O_3 41.3 %, Eu_2O_3 0.5 %	7	-	-
$MgAlGaO_4$	MAGS2	M2	K7	K8		30	43.4	97.1
$MgAl_2O_4$	MAS1	M2	F800/10	-	MgO 28.4 %, Al_2O_3 70.6 %, Eu_2O_3 0.5 %	7	-	-
$MgAl_2O_4$	MAS2	M2	F800/10	-		30	27.9	56.6
$MgAl_2O_4$	MAS3	K11	K7	-		7	-	-
$MgAl_2O_4$	MAS4	K11	K7	-		30	26.1	98.1

SEM images of MgAl2O¬4: Eu3+ ceramic samples with different initial oxide powder compositions (MAS2 and MAS4) are shown in Figure 1. The surfaces of the samples have complex shapes characteristic of a solidified melt. The difference in the surface morphology of the synthesized samples can be explained by changes in the structural and phase composition from sample to sample.

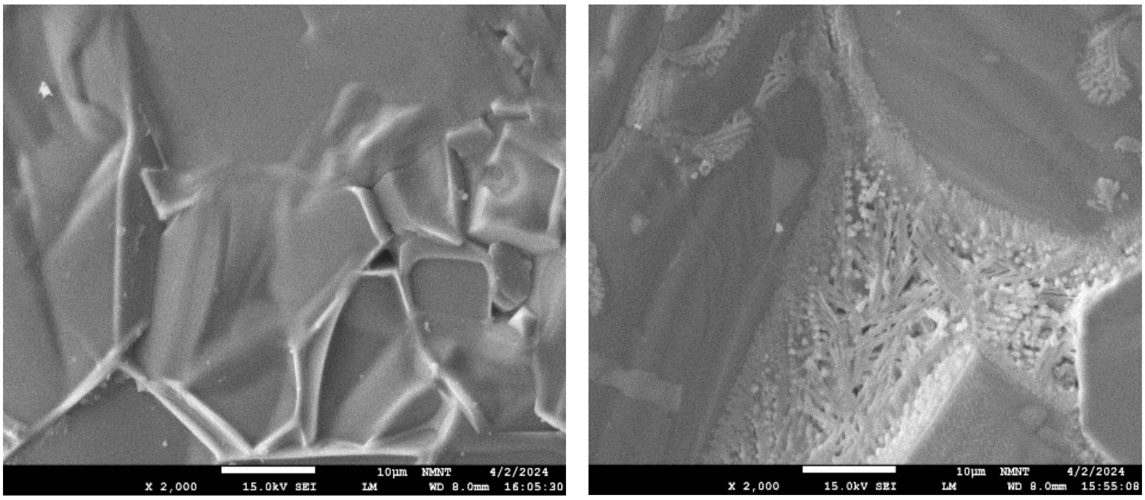

Figure 1. SEM images of the surface of MgAl2O-4: Eu3+ ceramic samples with different initial oxide powder compositions (MAS2 and MAS4)

Figure 2 shows the element distribution maps obtained with a scanning electron microscope. The microphotographs show that the surface layer contains Mg, Al, O. The introduced Eu impurities are distributed non-uniformly over the surface. During the synthesis, the Eu oxide dissociates and the Eu^{3+} and O^{2-} ions enter the spinel matrix independently of each other.

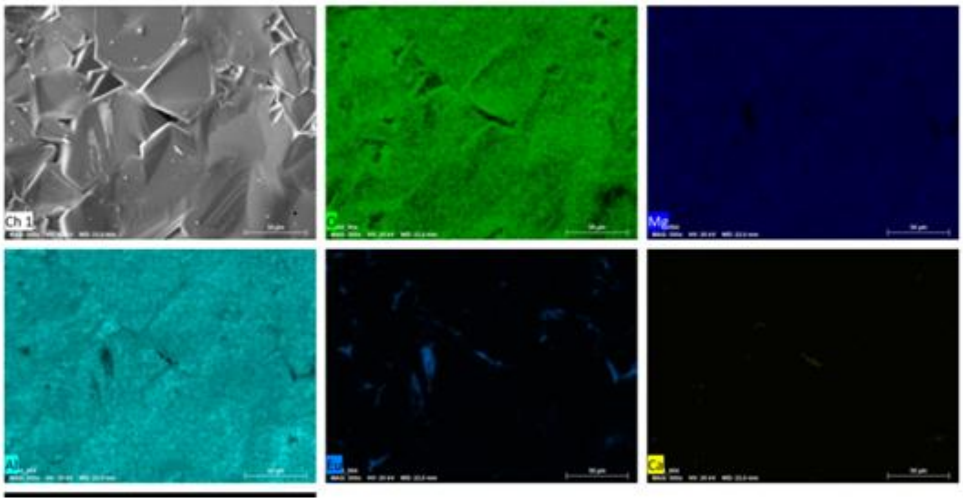

Figure 2. Result of mapping the distribution of elemental composition in the $MgAl_2O_4$: Eu^{3+} spinel sample (MAS2)

The elemental composition of the studied MgAl2O4: Eu3+ samples obtained by energy-dispersive analysis are shown in Figure 3. The energy-dispersive X-ray analysis spectra show elemental peaks, confirming the presence of Mg, Al, O, Eu and several impurity elements.

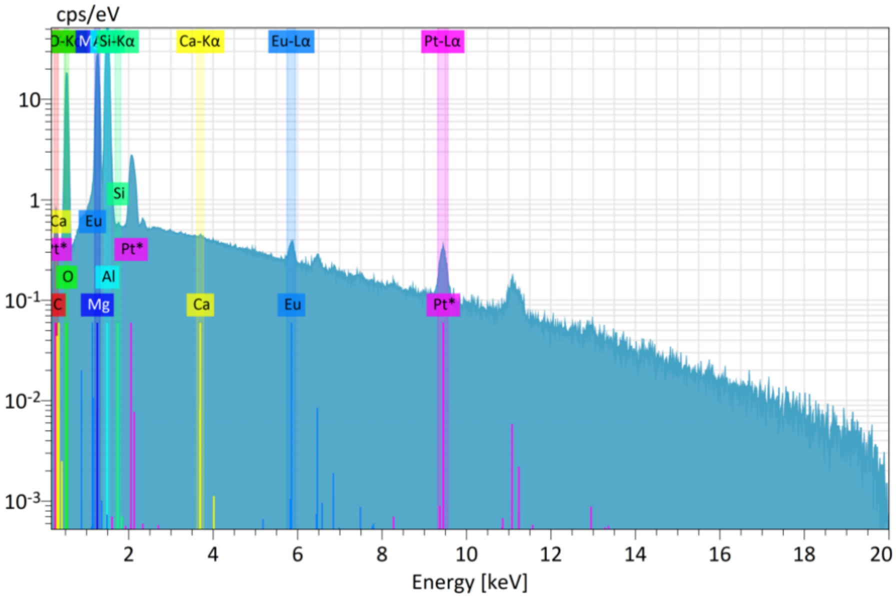

Figure 3. The elemental composition of the studied $MgAl_2O_4$: Eu^{3+} samples obtained by energy-dispersive analysis

Table 2

Mass composition of samples $MgAl_2O_4$: Eu^{3+}

Element	Mass (%)	Atom (%)
Oxygen (O)	37,27	50,39
Magnesium (Mg)	14,67	13,06
Aluminum (Al)	32,99	26,45
Silicon (Si)	0,03	0,02
Calcium (Ca)	0,02	0,01
Europium (Eu)	0,84	0,12
Platinum (Pt)	5,11	0,57

Quantitative elemental analysis of the samples allowed us to establish the composition of the ceramics, the data of which are shown in Table 2. The results show that the composition of the elements is uniformly distributed. The percentage of elements obtained in the samples is similar to the theoretical calculation.

The work investigated the efficiency of synthesis from the history of the initial oxide powder compositions with different particle sizes, as well as partial replacement of Al3+ with Ga3+. The symbols for the synthesized spinel samples are presented in Table 3. The efficiency of the synthesis process was determined as the ratio of the mass of the sample obtained after synthesis to the mass of the initial powder mixture of oxides according to the formula: Efficiency (Output) (%) = M_s/M_m 100 %, where M_s is the mass of the synthesized sample, M_m is the mass of the mixture.

Table 3

The average particle size and particle sizes for the distribution maximum

Powder	Grain sizes of starting substances, µm	Average particle diameter (µm)	Particle sizes at distribution maximum (µm)
MgO (M2)	0.05 — 60	4.697	22.795
MgO (K11)	0.01 — 30	2.327	3.564
Al2O3 (K7)	0.01 — 30	2.623	9.992
Al2O3 (F800/10)	0.5 — 20	8.103	9.992
Ga2O3 (K8)	0.1 — 50	5.037	6.232
Eu2O3 (K2)	0.01 — 20	0.523	2.008

In [9, 12], it was shown that the efficiency of YAG ceramic synthesis depends on the particle sizes of the powders. This hypothesis was tested on ceramics based on two types of spinels. The dispersion of the initial powders used for synthesis to obtain the ceramic samples was studied. The average particle size and the particle sizes at the maximum of the distribution are shown in Table 3.

Figure 4 shows photographs of the synthesized samples of MAGS2, MAS2, MAS4 in crucibles. The photographs demonstrate the appearance of the samples synthesized in the “scanning” mode under the action of electron beams with E = 1.4 MeV and a flux power density of 30 kW/cm2. The synthesized samples are porous ceramics, have the appearance of complex-shaped polycrystalline plates, the size is determined by the dimensions of the crucible. In order for the crucible material not to pass into the batch during synthesis, the thickness of the powder mixture layer was always greater than the electron path depth. Therefore, a layer of batch residues always remained between the bottom of the crucible and the lower surface of the sample. The MAS2 sample is characterized by the formation of ceramics in the volume of the mixture layer, the presence of powder residue on the ceramic surface (Fig. 4).

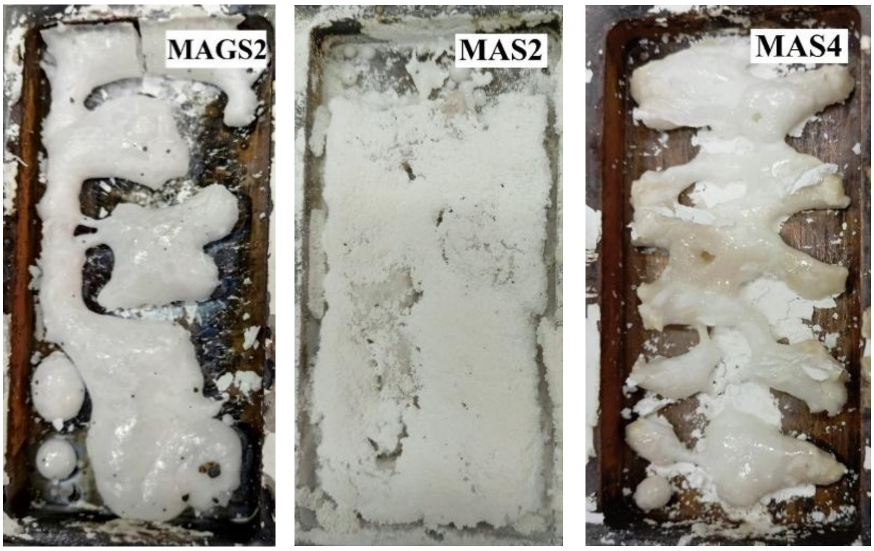

Figure 4. Photographs of synthesized spinel ceramics

A large difference in the efficiency of sample synthesis is observed depending on the granulometric composition. The synthesis results (Output) are given in Table 1. Aluminum oxide powder (K7) and magnesium oxide powder (K11) have the same average particle size and close particle size dispersion, which ensures high efficiency of radiation synthesis, sample MAS4 (98 %). Sample MAGS2 is synthesized from magnesium oxide powder (M2), aluminum oxide powder (K7) and gallium oxide powder (K8) with close average particle sizes and also has a high synthesis efficiency of up to 97 %. Aluminum oxide powder (F800/10) and magnesium oxide powder (M2) have significantly different average particle sizes (Table 3), the particle size differs by about two times, in addition, the M2 powder contains large particles (23 μm). This ratio of the particle sizes of the original powders leads to the fact that therefore the MAS2 spinel synthesized from this mixture of oxides has a rather low yield of 56 %. The reason for the dependence of the efficiency of synthesis of ceramics of complex compositions on the particle size is the difference in the dispersion of the powders of the initial compositions. When the sizes of the batch components of different chemical compositions differ significantly, local non-stoichiometry may occur, since large particles are surrounded by many small ones [12], respectively, the irradiation conditions for particles of different sizes are not identical. In addition, when filling and preparing the batch into the crucible, uneven distribution of large and small particles by volume may be observed. The dispersion composition of the activator, europium oxide, does not have a large effect on the efficiency of radiation synthesis, since it is introduced into the batch in a small amount. However, the radiation synthesis modes can affect the processes that determine the incorporation of the europium ion into the spinel lattice.

Cathodoluminescence

The cathodoluminescence characteristics of the ceramic samples were investigated. The results are presented in Figure 5. The analysis was performed for the luminescence spectra of the samples synthesized in two modes: “scanning” and “no scanning”. It was found that the luminescent properties of the sample pairs obtained in the “scanning” and “no scanning” modes are mainly qualitatively similar. The CL analysis showed that the luminescence spectra of MgAlGaO4 and MgAl2O4 spinels are similar (Fig. 5a, c) (samples MAGS1, MGAS2 and MAS3, MAS4). The spectra contain glow bands with maxima at 520, 615 and 710 nm, the ratio of band intensities can vary for the samples obtained under different conditions. In particular, samples MGAS2 and MAS4 demonstrated high synthesis efficiency (Table 1). The qualitative composition of the CL spectra in samples MAS1 and MAS2 is different (Fig. 5b); the spectrum is dominated by emission with a maximum at 690 nm and a set of peaks in the 690–800 nm region, which is associated with the luminescence of the chromium ion [13].

In samples MAGS1, MGAS2 and MAS3, MAS4, the dominant luminescence spectrum is a narrow band at 615 nm, caused by the luminescence of europium ions. In samples MAS1 and MAS2, a weak band is observed at 615 nm and an intense band in the 690–800 nm region with a maximum in the 690 nm region.

It is known that the presence of the dopant Eu3+ in the spinel lattice causes intense luminescence due to the $^5D_{0.1}\rightarrow{}^7F_J$ transitions (615 nm band) in europium ions [5, 6, 8]. Samples MAS1 and MAS2 differ from other types of synthesized ceramics. For their synthesis, F800/10 aluminum oxide was used. Al2O3 (F800/10) powders have a larger average particle size compared to magnesium oxide and a distinct difference in particle size distribution with MgO (M2). In this case, Al2O3 (K7) and MgO (K11) powders with a close average particle size and similar size distribution were used to synthesize samples MAS3 and MAS4. Apparently, a significant difference in the average particle size of the powders can affect both the formation of the spinel crystal lattice during radiation synthesis and the activation of spinel by Eu^{3+} ions. Intense luminescence in the 615 nm band associated with impurity Eu3+ ions (transition $^5D_0\rightarrow{}^7F_2$) is recorded in the MAGS1, MAGS2, MAS3 and MAS4 samples. This band is observed in samples MAS1 and MAS2, but its intensity is weak compared to the luminescence in the 690 nm band. Thus, it can be concluded that the method of spinel synthesis using a high-energy electron beam does not affect the appearance of the spectral bands, but changes the intensity ratio of the luminescence bands of impurity and intrinsic centers. The ratio of luminescence intensities between the spectral bands with maxima at 615 nm and 710 nm differs significantly for samples synthesized at different power densities: 4:1 for MAGS1 at 7 kW/cm2, 2:1 for MAGS2 at 30 kW/cm2. For samples MAS3 and MAS4, the effect of the method of action on the luminescence intensity is insignificant, i.e. the intensity ratio I_{615} / I_{710} is ~ 2:1 (Fig. 5). A band at 520 nm can also be recorded in the CL spectra; in [14], the authors associate this luminescence with oxygen vacancies in the spinel structure.

A band at 380 nm is recorded in the CL spectra of $MgAlGaO_4$ samples, while it is absent in $MgAl_2O_4$ samples. In [15] luminescence in the CL spectra of $MgGa_2O_4$ crystals is recorded in the range of 300–

450 nm with a maximum at ~362–393 nm, depending on the annealing conditions of the crystals. The authors associate the change in the peak position in this spectral region with the redistribution of cations in the inverted spinel structure and the corresponding differences in the localization energies of self-trapped excitons. $MgGa_2O_4$ phases can appear in the composition of $MgAlGaO_4$ ceramics during synthesis, which causes the appearance of a band with maximum 380 nm in the CL spectrum. In the CL spectrum of the MAS3 and MAS4 samples, a band is observed in the region of 440–460 nm. The luminescence in the region of 460 nm is due to the luminescence of clusters formed as a result of the interaction of F^+ centers with nearby negatively charged defects in the cationic sublattice of spinel [16]. In [16], the band in the spectrum of the $MgAl_2O_4$ phosphor with a maximum at 440 nm was attributed to luminescence centers in the form of Mg^{2+} vacancies.

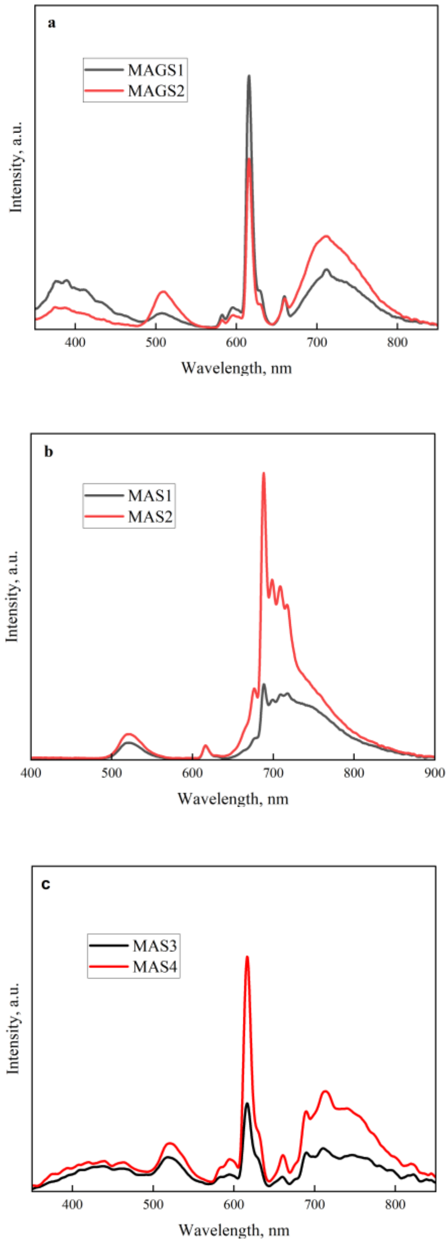

Figure 5. CL spectrum of samples: a) MAGS1 and MAGS2, b) MAS1 and MAS2 and c) MAS3 and MAS4

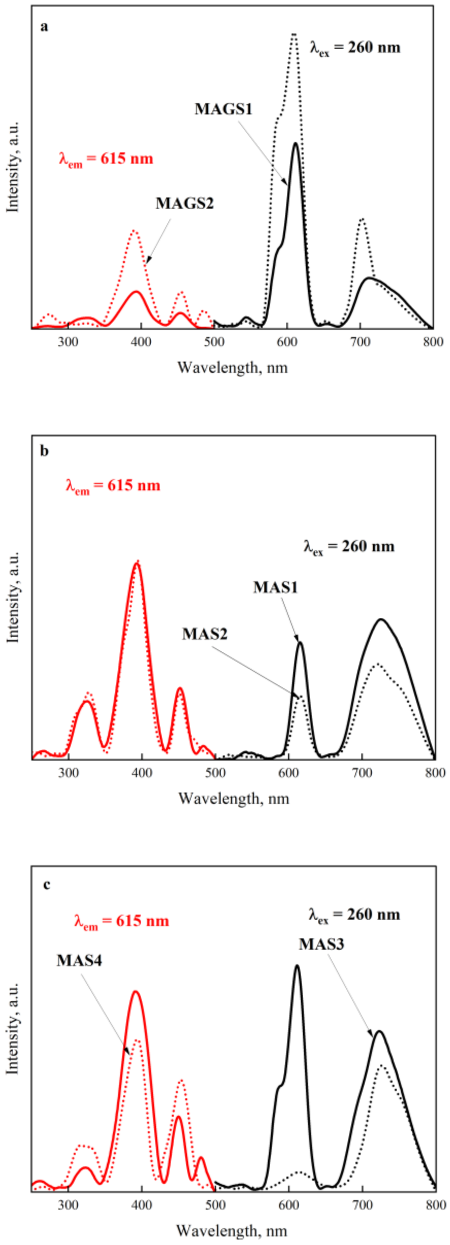

Figure 6. Excitation and PL spectrum at λ_{em} = 615 nm and λ_{ex} = 260 nm of samples: a) MAGS1 and MAGS2, b) MAS1 and MAS2 and c) MAS3 and MAS4

The kinetics of luminescence decay under pulsed electronic excitation in the region of 615, 690, and 710 nm has been studied. Luminescence can be described by the sum of two exponential components. Figure 7 presents the obtained results. In the region of 615, 690, and 710 nm, the characteristic decay times in the range up to 5 μs for each individual sample synthesized with different power densities are similar. It was found that the shape of the CL kinetic curves in the 615 and 710 nm band significantly differs for MAGS1, MAGS2, and MAS3 and MAS4 samples.

Table 4 summarizes the kinetic decay times for all the samples studied. In the spectral ranges of 615 and 710 nm, the $MgAlGaO_4$ spinel sample shows the largest decay time compared to other samples. The decay time of the $MgAlGaO_4$ spinel sample reaches its maximum in the spectral range with a maximum of 615 nm; the decay time of the fast component τ_1 and the slow component τ_2 in MAGS1 and MAGS2 samples in the 615 nm band is $\tau_1 \approx 0.1$ μs and $\tau_2 \approx 0.9$ μs.

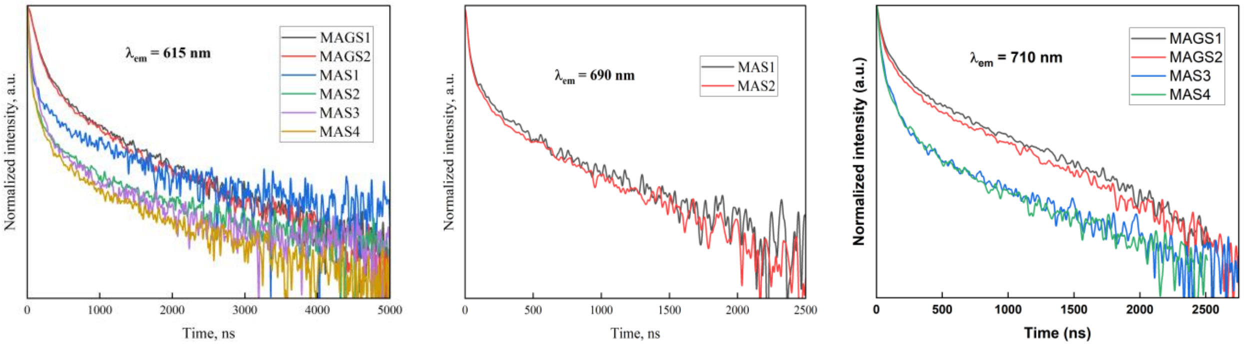

Figure 7. Kinetic characteristics of CL decay MAGS1, MAGS2, MAS1, MAS2, MAS3 and MAS4 in the region of 615, 690, 710 nm

Table 4

Luminescence decay time of MgAlGaO4 and MgAl2O4 ceramic samples in the characteristic bands

Sample	615 nm		690 nm		710 nm	
	τ1 (ns)	τ2 (ns)	τ1 (ns)	τ2 (ns)	τ1 (ns)	τ2 (ns)
MAGS1	120	902	-	-	41	453
MAGS2	118	896	-	-	38	436
MAS1	30	624	25	343	-	-
MAS2	23	421	24	352	-	-
MAS3	39	315	-	-	26	241
MAS4	24	320	-	-	25	275

Photoluminescence

Photoluminescence and excitation spectra (PL) of the synthesized spinel samples were studied. The photoluminescence excitation spectrum of Eu^{3+} ions in spinel was monitored at an emission wavelength of 615 nm (transition $^5D_0 \rightarrow {}^7F_2$). In the photoluminescence excitation spectrum, bands with a maximum at wavelengths of 393 nm ($^7F_0 \rightarrow {}^5L_6$), 463 nm ($^7F_0 \rightarrow {}^5D_2$) are recorded, corresponding to the f→f configuration transitions in the Eu^{3+} ion. Excitation bands at 330 nm and 260 nm are characteristic of the charge transition between Eu^{3+} and O^{2-} ions [17]. The PL spectrum of the samples at excitation at 260 nm was studied. Luminescence bands of Eu^{3+} ions appear in the emission spectrum of the spinel samples. In the structure of the band with a maximum at 615, a peak at 590 nm is observed, characterized by the transition $^5D_0 \rightarrow {}^7F_1$. In the PL spectra of all samples, a weak spectral band with a maximum at 535 nm appears, characteristic of the emission of europium ions with the transition $^5D_1 \rightarrow {}^7F_1$ [8, 14].

For spinels with gallium MAGS1 and MAGS2, the intensity of europium luminescence in the bands at 615, 690 nm is significantly higher in the samples obtained in the “scanning” mode. It is possible that europium ions are more effectively incorporated into the spinel lattice with gallium during synthesis in this mode.

Conclusions

The work shows that it is possible to synthesize luminescent porous ceramics based on spinels $MgAl_2O_4$, $MgAlGaO_4$ by means of the action of powerful flows of high-energy electrons with an energy of

1.4 MeV and a power of 7–30 kW / cm^2 directly on a batch of powders of metal oxides MgO, Al_2O_3, Ga_2O_3 in a stoichiometric ratio with activators europium oxide. The efficiency of radiation synthesis of spinel samples depends on the history of the initial oxide powder compositions. A mixture of oxide powders with close average particle sizes and similar particle distributions in the synthesis of ceramics by the radiation method gives a useful yield of up to 97 %. The particle size of about 5–10 µm, close average particle size and similar particle size distribution for various components of the batch is optimal for ensuring high efficiency of radiation synthesis

The structural and luminescent properties of spinel ceramic samples have been studied. The study revealed that Eu^{3+} ions are incorporated into the crystal lattice of both types of spinels. In the luminescence spectra of the synthesized spinel samples, luminescence of Eu^{3+} ions can be observed ($^5D_0$, $^5D_1 \rightarrow {}^7F_j$ transitions). The characteristic luminescent properties of the Eu^{3+} ion arise in the strongest spectral band at 615 nm ($^5D_0 \rightarrow {}^7F_2$ transition), which is more distinct in $MgAlGaO_4$ and $MgAl_2O_4$ samples synthesized from a mixture of oxide powders with a similar average particle size and granulometric composition. Superposition of the luminescence bands of chromium and europium ions ($^5D_0 \rightarrow {}^7F_4$ transition) is due to effective luminescence of chromium in the spectra of MAS1 and MAS2 samples excited by electrons. The emission peaks of the PL and CL spectra in MGAS1, MGAS2, MAS3 and MAS4 samples are similar; however, the PL spectrum of MAS1 and MAS2 samples does not exhibit a maximum peak at 690 nm compared to the CL spectrum.

Acknowledgments

The research was carried out at the expense of the grant of the Russian Science Foundation No. 23-73-00108, https://rscf.ru/project/23-73-00108/

The research was carried out using the equipment of the CSU NMNT TPU.

References

1 Goldstein A. Correlation between $MgAl_2O_4$-spinel structure, processing factors and functional properties of transparent parts (progress review) / A. Goldstein // J. European Ceramic Society. — 2012. — Vol. 32, No. 11. — P. 2869–2886. DOI: 10.1016/j.jeurceramsoc.2012.02.051

2 Pilania G. Prediction of structure and cation ordering in an ordered normal-inverse double spinel / G. Pilania, V. Kocevski, J.A. Valdez, C.R. Kreller, B.P. Uberuaga // Communication Materials. — 2024. — No. 84. DOI: https://doi.org/10.1038/s43246-020-00082-2

3 Tomokazu Ito Site Preference of Cations and Structural Variation in MgAl2–xGaxO4 (0≤x≤2) Spinel Solid Solution / Tomokazu Ito, Akihiko Nakatsuka, Hideki Maekawa, Akira Yoshiasa, Takamitsu Yamanaka // Zeitschrift für anorganische und allgemeine Chemie. — 2000. — Vol. 626, No. 1. — P. 42–49. DOI: https://doi.org/10.1002/(SICI)1521-3749(200001)626:1<42::AID-ZAAC42>3.0.CO;2-O

4 Kushwaha A.K. Structural, electronic, elastic and optical properties of double spinel $MgAlGaO_4$: a DFT investigation / Kushwaha, A.K., Güler, E., Özdemir, A. Genç A. E., Uğur G. // Indian J Phys. — 2024. — Vol. 98. — P. 4011–4017. DOI: https://doi.org/10.1007/s12648-024-03171-x

5 Luchechko A. Luminescence spectroscopy of Eu3+ and Mn2+ ions in MgGa2O4 spinel / A. Luchechko, O. Kravets, L. Kostyk, O. Tsvetkova // Radiation Measurements. — 2016. — Vol. 90. — P. 47–50. DOI: 10.1016/j.radmeas.2015.12.003

6 Bin-Siang T. Preparation and luminescent characteristics of Eu3+-activated MgxZn1−xGa2O4 nanocrystals / T. Bin-Siang, C. Yen-Hwei, C. Yu-Chung // Journal of Alloys and Compounds. — 2006. — Vol. 407. — P. 289–293. DOI: 10.1016/j.jallcom.2005.06.021

7 Jiang Bin. A self-activated MgGa2O4 for persistent luminescence phosphor / Bin Jiang, Fengfeng Chi, Xiantao Wei, Yonghu Chen, Min Yin // J. Appl. Phys. — 2018. — Vol. 124. — P. 063101. DOI: https://doi.org/10.1063/1.5024771

8 Yoon S.J. Synthesis and photoluminescence properties of $MgAl_2O_4$: Eu^{3+} phosphors / S.J. Yoon, D.A. Hakeem, K. Park // Ceramics International. — 2016. — Vol. 42. — P. 1261–1266. DOI: http://dx.doi.org/10.1016/j.ceramint.2015.09.059

9 Lisitsyn V. Radiation Synthesis of High-Temperature Wide-Bandgap Ceramics / V. Lisitsyn, A. Tulegenova, M. Golkovski, E. Polisadova, L. Lisitsyna, D. Mussakhanov, and G. Alpyssova // Micromachines. — 2023. — Vol. 14, No. 12. — P. 2193. DOI: 10.3390/mi14122193.

10 Lisitsyn V. Efficiency Dependence of Radiation-Assisted Ceramic Synthesis Based on Metal Oxides and Fluorides on Initial Powder Particle Sizes / V. Lisitsyn, E.Polisadova, L. Lisitsyna, A. Tulegenova, I. Denisov, M. Golkovski // Photonics. — 2023. – Vol. 10, No. 10. P.1084. DOI: https://doi.org/10.3390/photonics10101084

11 Kuksanov N. High Power DC Electron Accelerators of ELV-Type for Research and Industrial Application / N. Kuksanov, Yu. Golubenko, A. Lavruchin, D. Kogut, I. Chakin, S. Fadeev, P. Nemytov, A. Semenov, E. Domarov, V. Cherepkov, R. Salimov, A. Korchagin, M. Golkovsky, D. Vorobiev // 7th International Congress on Energy Fluxes and Radiation Effects (EFRE), Tomsk, Russia. — 2020. — P. 449–454. DOI: 10.1109/EFRE47760.2020.9241934.

12 Lisitsyn V. The Optimization of Radiation Synthesis Modes for YAG: Ce Ceramics / V. Lisitsyn, D. Mussakhanov, A. Tulegenova, E. Kaneva, L. Lisitsyna, M. Golkovski, A. Zhunusbekov // Materials. — 2023. — Vol. 16. — P. 3158 doi: https://doi.org/10.3390/ma16083158

13 Polisadova E.F. Pulse Cathodoluminescence of the Impurity Centers in Ceramics Based on the $MgAl_2O_4$ Spinel / E.F. Polisadova, V.A. Vaganov, S.A. Stepanov, V.D. Paygin, O.L. Khasanov, E.S. Dvilis, D.T. Valiev. R.G. Kalinin // Journal of Applied Spectroscopy. — 2018. Vol. 85. — P. 416–421. DOI: 10.1007/s10812-018-0666-9.

14 Gupta S.K. Why host to dopant energy transfer is absent in the $MgAl_2O_4$: Eu^{3+} spinel? And exploring Eu^{3+} site distribution and local symmetry through its photoluminescence: interplay of experiment and theory / S.K. Gupta, P.S. Ghosh, N. Pathaka, R.M. Kadam // RSC Advances. — 2016. — Vol. 6. — P. 42923–42932. DOI: https://doi.org/10.1039/C6RA03369E

15 Galazka, Z. $MgGa_2O_4$ as a new wide bandgap transparent semiconducting oxide: growth and properties of bulk single crystals / Z. Galazka, D. Klimm, K. Irmscher, R. Uecker, M. Pietsch, R. Bertram, M. Naumann, M. Albrecht, A. Kwasniewski, R. Schewski, M. Bickermann // Physica status solidi (a). — 2015. — Vol. 212. — P. 1455–1460. DOI: 10.1002/pssa.201431835.

16 Sawai S. Visible photoluminescence from $MgAl_2O_4$ spinel with cation disorder and oxygen vacancy / S. Sawai, T. Uchino // Journal of Applied Physics. — 2012. — Vol. 112. — P. 103523. DOI: https://doi.org/10.1063/1.4767228

17 Li Y. Monochromatic blue-green and red emission of rare-earth ions in $MgGa_2O_4$ spinel / Y. Li, P. Niu, L. Hu, X. Xu, C. Tang // Journal of Luminescence. — 2009. — Vol. 129. — P. 1204–1206. DOI: https://doi.org/10.1016/j.jlumin.2009.06.005

Е.Ф. Полисадова, Н.Д. Чан

Еуропиймен легирленген $MgAl_2O_4$ және $MgAlGaO_4$ кеуекті керамиканың құрылымы мен люминесценттік қасиеттерін электронды сәулені қолдана отырып синтездеу

Еуропиймен легирленген $MgAl_2O_4$ (MAS) және $MgAlGaO_4$ (MAGS) кеуекті керамикасы радиациялық әдіспен синтезделді. Радиациялық синтез синтезді ынталандыру үшін қоспаларды немесе басқа материалдарды пайдаланбай, оксид ұнтақтарының қоспасынан электронды іске қосу мен шихтаның сәулелену энергиясын пайдалана отырып, 1 секундтан аз уақыт ішінде жоғары тиімділікпен жүзеге асырылады. Жоғары энергиялы электронды сәулені қолдана отырып, синтездеу әдісі жоғары өнімділігі бар отқа төзімді материалдарды алуға, процестің технологиялық жағдайларын басқаруға және сәйкесінше берілген қасиеттері бар материалдарды синтездеуге мүмкіндік береді. Синтезделген кеуекті керамиканың құрылымдық қасиеттері рентгендік дифракция әдісімен (XRD-7000s дифрактометрі, Shimadzu), сканерлеуші электронды микроскопия әдістерімен зерттелген. Нәтижелер синтезделген MAS текше құрылымды және $MgAl_2O_4$ шпинелінің кристалдық құрылымына сәйкес келетінін көрсетті, ал MAGS синтезделген қос шпинельді екі негізгі фазалық компоненттен тұрады: $MgAl_2O_4$ және $MgGa_2O_4$. Еуропий қосылған синтезделген шпинельдің MAS және MAGS люминесценция қасиеттерін зерттеу үшін фотолюминесценцияны өлшеу жүргізілді. Шпинельдегі Eu^{3+} иондарының қозуының фотолюминесценция спектрі λ_{em} = 615 нм ($^5D_0 \to {}^7F_2$) кезінде бақыланды. PLE Eu^{3+} иондарының конфигурациясындағы f→f ауысуын көрсетеді 393 нм ($^7F_0 \to {}^5L_6$), 463 нм ($^7F_0 \to {}^5D_2$)). 330 нм және 260 нм-дегі қозу диапазоны Eu^{3+} және O^{2-} иондары арасындағы зарядтың ауысуына тән. 260 нм қозған үлгілердің фотолюминесценция спектрі зерттелді. Шпинель үлгілерінің PL спектрінде Eu^{3+} иондарының эмиссиясы айқын көрінеді. Ең көбі 615 диапазонының құрылымында шыңы 590 нм-де көрінеді, $^5D_0 \to {}^7F_1$ ауысуымен сипатталады. Үлгілердің ФЛ спектрінде $^5D_1$–$^7F_1$ ауысуымен Eu^{3+} иондарының шығарылуына тән максимум 535 нм болатын әлсіз спектрлік диапазон пайда болады. Радиациялық синтездің тиімділігі бастапқы оксид ұнтақтарының гранулометриялық құрамына байланысты екендігі көрсетілген.

Кілт сөздер: керамикалық шпинель, қос шпинель, Eu легирлеу, радиациялық синтез, люминесценция, $MgAl_2O_4$, $MgAlGaO_4$.

Е.Ф. Полисадова, Н.Д. Чан

Синтез с использованием электронного пучка, структура и люминесцентные свойства пористой керамики $MgAl_2O_4$ и $MgAlGaO_4$, легированной европием

Пористая керамика $MgAl_2O_4$ (MAS) и $MgAlGaO_4$ (MAGS), легированная европием, синтезирована радиационным методом. Радиационный синтез осуществлен с высокой эффективностью в течение менее 1 сек с применением энергии излучения электронного пуска и шихты из смеси порошков оксидов без использования добавок или других материалов для стимуляции синтеза. Метод синтеза с применением высокоэнергетического электронного пучка позволяет получать тугоплавкие материалы с высокой производительностью, управлять технологическими условиями процесса и, соответственно, синтезировать материалы с заданными свойствами. Структурные свойства синтезированной пористой керамики исследованы методом рентгеновской дифракции (дифрактометр XRD–7000S, Shimadzu), методами сканирующей электронной микроскопии. Результаты показали, что синтезированные MAS имеют кубическую структуру и соответствуют в кристаллической структуре шпинели $MgAl_2O_4$, в то время как синтезированная двойная шинель MAGS содержит два основных фазовых компонента: $MgAl_2O_4$ и $MgGa_2O_4$. Для изучения люминесцентных свойств синтезированных MAS и MAGS шпинели, легированной европием, были проведены измерения фотолюминесценции (ФЛ). Спектр фотолюминесценции возбуждения ионов Eu^{3+} в шпинели контролировался при λ_{em} = 615 нм ($^5D_0\rightarrow{}^7F_2$). ФЛ показывает переход f→f в конфигурации ионов Eu^{3+} (при 393 нм ($^7F_0\rightarrow{}^5L_6$), 463 нм ($^7F_0\rightarrow{}^5D_2$)). Полосы возбуждения при 330 нм и 260 нм характерны для зарядового перехода между ионами Eu^{3+} и O^{2-}. Изучен спектр фотолюминесценции образцов при возбуждении при 260 нм. В спектре ФЛ образцов шпинели отчетливо видно излучение ионов Eu^{3+}. В структуре полосы с максимумом 615 виден пик при 590 нм, характеризующийся переходом $^5D_0\rightarrow{}^7F_1$. В спектре ФЛ образцов появляется слабая спектральная полоса с максимумом при 535 нм, характерная для излучения ионов Eu^{3+} с переходом $^5D_1$–$^7F_1$. Показано, что эффективность радиационного синтеза зависит от гранулометрического состава исходных порошков оксидов.

Ключевые слова: шпинель керамическая, двойная шпинель, легирование Eu, радиационный синтез, люминесценция, $MgAl_2O_4$, $MgAlGaO_4$.

References

1 Goldstein, A. (2012). Correlation between MgAl2O4-spinel structure, processing factors and functional properties of transparent parts (progress review). *J. European Ceramic Society, 32*(11), 2869–2886.

2 Pilania, G., Kocevski, V., Valdez, J.A., Kreller, C.R., & Uberuaga, B.P. (2024). Prediction of structure and cation ordering in an ordered normal-inverse double spinel. *Communication Materials, 84.*

3 Tomokazu, Ito, Akihiko, Nakatsuka, Hideki, Maekawa, Akira, Yoshiasa, & Takamitsu, Yamanaka (2000). Site Preference of Cations and Structural Variation in MgAl2–xGaxO4 (0≤x≤2) Spinel Solid Solution. *Zeitschrift für anorganische und allgemeine Chemie, 626* (1), 42–49.

4 Kushwaha, A.K., Güler, E., Özdemir, A. Genç, A. E., & Uğur, G. (2024). Structural, electronic, elastic and optical properties of double spinel $MgAlGaO_4$: a DFT investigation. *Indian J Phys., 98*, 4011–4017.

5 Luchechko, A., Kravets, O., Kostyk, L., & Tsvetkova, O. (2016). Luminescence spectroscopy of Eu3+ and Mn2+ ions in MgGa2O4 spinel. *Radiation Measurements, 90,* 47–50.

6 Bin-Siang, T., Yen-Hwei, C., & Yu-Chung, C. (2006). Preparation and luminescent characteristics of Eu3+-activated MgxZn1−xGa2O4 nanocrystals. *Journal of Alloys and Compounds, 407,* 289–293.

7 Bin, Jiang, Fengfeng, Chi, Xiantao, Wei, Yonghu, Chen, & Min, Yin (2018). A self-activated MgGa2O4 for persistent luminescence phosphor. *J. Appl. Phys., 124,* 063101.

8 Yoon, S.J., Hakeem, D.A., & Park, K. (2016). Synthesis and photoluminescence properties of $MgAl_2O_4$: Eu^{3+} phosphors. *Ceramics International, 42,* 1261–1266.

9 Lisitsyn, V., Tulegenova, A., Golkovski, M., Polisadova, E., Lisitsyna, L., Mussakhanov, D., & Alpyssova, G. (2023). Radiation Synthesis of High-Temperature Wide-Bandgap Ceramics. *Micromachines, 14* (12), 2193.

10 Lisitsyn, V., Polisadova, E., Lisitsyna, L., Tulegenova, A., & Denisov, I., Golkovski, M. (2023). Efficiency Dependence of Radiation-Assisted Ceramic Synthesis Based on Metal Oxides and Fluorides on Initial Powder Particle Sizes. *Photonics, 10* (10), 1084.

11 Kuksanov, N., Golubenko, Yu., Lavruchin, A. et al. (2020). High Power DC Electron Accelerators of ELV-Type for Research and Industrial Application. *7th International Congress on Energy Fluxes and Radiation Effects (EFRE),* 449–454. Tomsk, Russia.

12 Lisitsyn, V., Mussakhanov, D., Tulegenova, A., Kaneva, E., Lisitsyna, L., Golkovski, M., & Zhunusbekov, A. (2023). The Optimization of Radiation Synthesis Modes for YAG: Ce Ceramics. *Materials, 16,* 3158.

13 Polisadova, E.F., Vaganov, V.A., Stepanov, S.A. et al. (2018). Pulse Cathodoluminescence of the Impurity Centers in Ceramics Based on the $MgAl_2O_4$ Spinel. *Journal of Applied Spectroscopy, 85,* 416–421.

14 Gupta, S.K., Ghosh, P.S., Pathaka, N., & Kadam, R.M. (2016). Why host to dopant energy transfer is absent in the $MgAl_2O_4$: Eu^{3+} spinel? And exploring Eu^{3+} site distribution and local symmetry through its photoluminescence: interplay of experiment and theory. *RSC Advances, 6,* 42923–42932.

15 Galazka, Z., Klimm, D., & Irmscher, K. et al. (2015). $MgGa_2O_4$ as a new wide bandgap transparent semiconducting oxide: growth and properties of bulk single crystals. *Physica status solidi (a), 212,* 1455–1460.

16 Sawai, S., & Uchino, T. (2012). Visible photoluminescence from $MgAl_2O_4$ spinel with cation disorder and oxygen vacancy. *Journal of Applied Physics, 112,* 103523.

17 Li, Y., Niu, P., Hu, L., Xu, X., & Tang, C. (2009). Monochromatic blue-green and red emission of rare-earth ions in $MgGa_2O_4$ spinel. *Journal of Luminescence, 129,* 1204–1206.

Information about the authors

Elena Polisadova (corresponding author) — Doctor of physical and mathematical sciences, Professor, National Research Tomsk Polytechnic University, Lenin av., 30, 634050, Tomsk, Russia; e-mail: *elp@tpu.ru*; https://orcid.org/0000-0002-4644-5967

Tran Nhan Dat — PhD student, National Research Tomsk Polytechnic University, Lenin av., 30, 634050, Tomsk, Russia; e-mail: *nhandattran94@gmail.com;* https://orcid.org/0000-0002-0710-5863

Article
https://doi.org/10.31489/2024PH4/168-174
UDC537.533.9, 519.245

Received: 10.06.2024
Accepted: 19.08.2024

D.A. Mussakhanov[1*], A.S. Kobey[1], M.G. Golkovsky[2], A.T. Tulegenova[3]

[1]Institute of Physical and Technical Sciences, L.N. Gumilyov Eurasian National University, Astana 010000, Kazakhstan
[2]Budker Institute of Nuclear Physics, SB RAS, 11, Lavrentiev Ave., Novosibirsk 630090, Russia
[3]Department of Dosimetry and Physico-Technical Support of Radiation Therapy, Kazakh Institute of Oncology and Radiology, 91 Abay Ave., Almaty 050022, Kazakhstan
([*]Corresponding author's e-mail: dosymma@gmail.com)

Dependence of the distribution of absorbed electron flux energy in matter on the beam cross section

Beams of electrons confined in space are widely used in technological operations on welding, cutting, surface treatment. During the passage of electrons in matter, redistribution of beam energy losses occurs. The results of energy loss modeling using the Monte Carlo method presented in this paper demonstrate the redistribution of energy losses in the volume of the substance. There is an increase and then a decrease in energy loss as the electron beam moves deeper into the material. In the direction perpendicular to the beam axis there is an expansion of the energy loss region and then a decrease in the diameter of this region. The presented calculations well explain the results of synthesis of refractory dielectric ceramics. The redistribution of energy losses in the substance determines the morphology of the synthesized samples.

Keywords: synthesis, YAG: Ce ceramics, high-power electron flux, energy loss, Monte Carlo method, Gaussian flux distribution, CASINO V2.5, specific energy losses.

Introduction

High-energy electron fluxes are widely used in a wide variety of applications. Electron fluxes are used for the treatment of oncological diseases [1–4], in tomography [5–10]. Broad electron beams with energies up to tens of megaelectronvolts and narrow focused streams are used for these purposes. Radiation sterilization of medical preparations and medical devices is becoming the main method [11–13]. Widespread especially in recent years electron fluxes have been used for the treatment of products, surface cleaning, welding, cutting. As there are many variants of directions of use, technological electron accelerators of various power and energy of electrons have been created [14–16]. One of the main qualities of electron beam technologies is high efficiency (up to 70–80 %) of conversion of the supplied electrical energy into electron beam energy.

In recent years, attempts have been made to use electron beams for the synthesis of dielectric refractory materials needed for photonics, semiconductor electronics, light sources, and optics. In [17-18] it is shown that by direct impact of a powerful flow of high-energy electrons on the charge of refractory metal oxides it is possible to obtain ceramics in a time less than 1 second, without the use of any other substances to stimulate the process.

Obviously, due to the variety of electron beam applications, which differ in energy, power, and beam geometry, methods of rapid assessment of quantitative characteristics of the energy loss of electron beams as they pass through matter are required. Such methods have been developed and allow predicting quite correctly the distribution of absorbed energy during the passage of electron flow through matter [19-20]. In [21] it is shown that the distribution of energy losses of electron beams of Gaussian shape or limited in cross-section is inhomogeneous. There is a redistribution of energy in the target volume. This effect is very important to take into account when using narrowly directed beams.

The purpose of the present work is to investigate the energy losses of a space-limited flow of high-energy electrons in the volume of irradiated matter.

Modelling methodology

Monte Carlo calculations were performed for beams with a Gaussian flux distribution over the cross section and the number of incident electrons equal to 10 000 and 100 000 at an energy of 1.4 MeV. Water with a density of 1 g/cm^2 and the charge for the synthesis of yttrium-aluminum garnet (YAG) with a density of 1.1 g/cm^2 The CASINO V2.5 software developed at Sherbrooke University [22] was used as an object for energy loss calculations.

The programme does not take into account the effect of inelastic scattering on electron deflection and groups all electron energy loss events into a continuous energy loss function [23]. Under this assumption, the energy between collisions can be calculated using the following equations:

$$E_{i+1} = E_i + \frac{dE}{dS} L \tag{1}$$

$$\frac{dE}{dS} = \frac{-7.85 \times 10^{-3} \rho}{E_i} \times \sum_{j=1}^{n} \frac{C_j Z_j}{F_j} \ln\left(1.116\left(\frac{E_i}{J_j} + k_j\right)\right) \left[\text{keV} / \text{nm}\right] , \tag{2}$$

where Z_j and J_j are the atomic number and average ionisation potential of element j, respectively. K_j is a variable depending only on Z_j.

The elastic collision angle is determined using pre-calculated values of the partial elastic cross section [24]. For regions containing multiple chemical elements, the atom responsible for electron deflection is determined using the full cross section ratio [25].

Many features were added to the first version of CASINO 2.5 to improve the overall use of modelling. A graphical interface allows the user to view results while the simulation is running to avoid wasting time on simulations with incorrectly specified simulation conditions. A step-by-step wizard guides the user through various dialogue boxes to define the sample, set parameters and select the distributions to be created. All simulation data is stored in a single file to simplify the processing of results.

Modeling results

Water and charge for the synthesis of cerium-activated yttrium-aluminium garnet ceramics (YAG: Ce) were chosen as objects for synthesis. Water is the closest medium in terms of absorption capacity to the tissues of living organisms. The charge is used for the radiation synthesis of YAG: Ce ceramics studied with the authors. The electron beam entering the material is scattered by atoms, ions of the substance, transfers its energy to ionisation, generation of secondary electrons. As a result of these processes, as electrons pass through the substance, there is a change in the spatial structure of the beam energy transfer. Part of the energy is transferred to the substance outside the beam cross-section. There is a concentration of energy losses along the beam axis.

Figure 1 shows the results of modelling the distribution of electron energy losses in water as a function of the beam width in water. The lines indicate the boundaries of equal losses indicated in the table. At beam widths from 1 mm to 5 mm, the distribution function has a mushroom shape. As the beam width increases, the general pattern of energy loss distribution approaches a rectangular form. The maximum of the absorbed energy shifts from the surface along the beam. We emphasise that the above results correspond to the distribution of losses in matter of fluxes with equal integral doses.

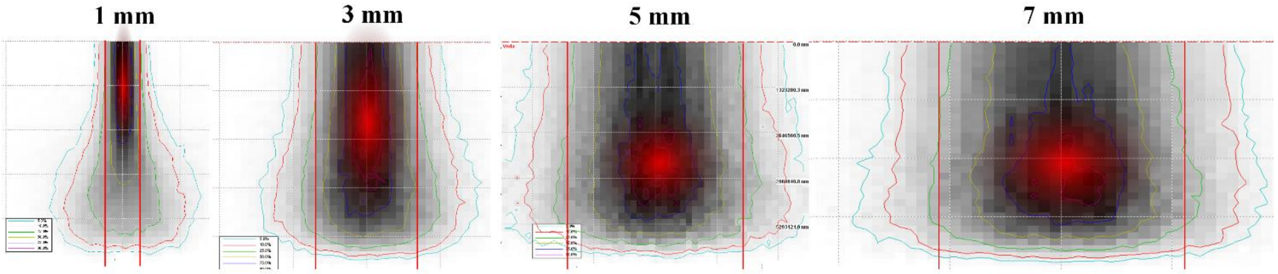

a b c d

Figure 1. Distribution of electron flux energy losses in matter as a function of beam width (a) 1 mm, (b) 3 mm, (c) 5 mm, (d) 7 mm

At the electron flow width of 1 mm, the regions of equal losses have an oval shape. As the electron beam width increases, the areas of maximum energy loss shift along the beam axis, and the oval shape of the energy loss maximum approaches a circular shape.

Figure 2 shows the results of the modelling of energy losses by depth when passing through water. It follows from the presented results that the distribution of energy losses along the beam depth has a complex character. As the beam passes through, the energy absorption by matter increases, reaches maximum values, and then decreases. The electron travelling depth mainly depends on the electron energy. The influence of the beam width on the energy loss distribution is insignificant. Electrons with energy of 1.4 MeV of beams of different diameters penetrate into water to a depth in the range of 6.4mm-6.6mm.

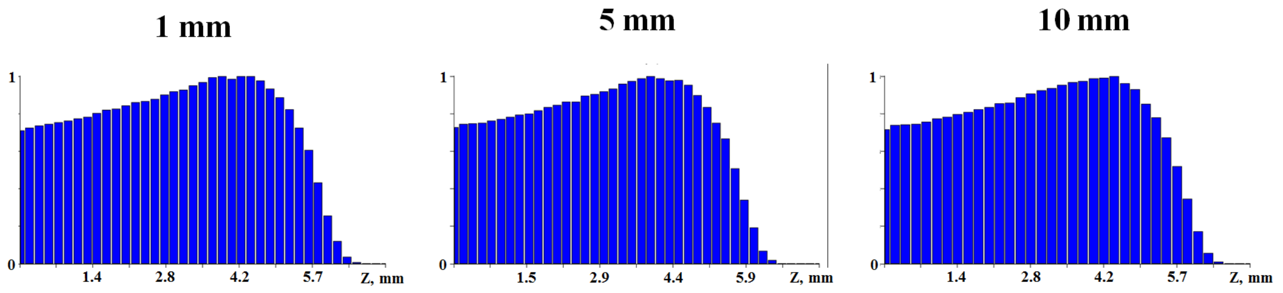

a b c

Figure 2. Electron spacings in matter as a function of beam width(a) 1 mm, (b) 3 mm, (c) 5 mm

Figure 3 shows the energy loss distribution of 1.4 MeV electrons when passing through the charge for YAG synthesis. The charge is a mixture of Al_2O_3 (43 %) and Y_2O_3 (56 %) powders with Ce_2O_3 (1.0 %) as activator. The density of the charge was 1.1 g/cm^2. Calculations were performed by Monte Carlo method using 100 000 iterations. Figure 3 on the left shows the distribution of electron beam energy losses in a cross-section of the irradiated volume along the beam axis. Figure 3 on the right shows the calculated values of electron energy losses in cross sections perpendicular to the beam axis. The coloured lines indicate the boundaries of the energy loss region of equal value indicated in the table.

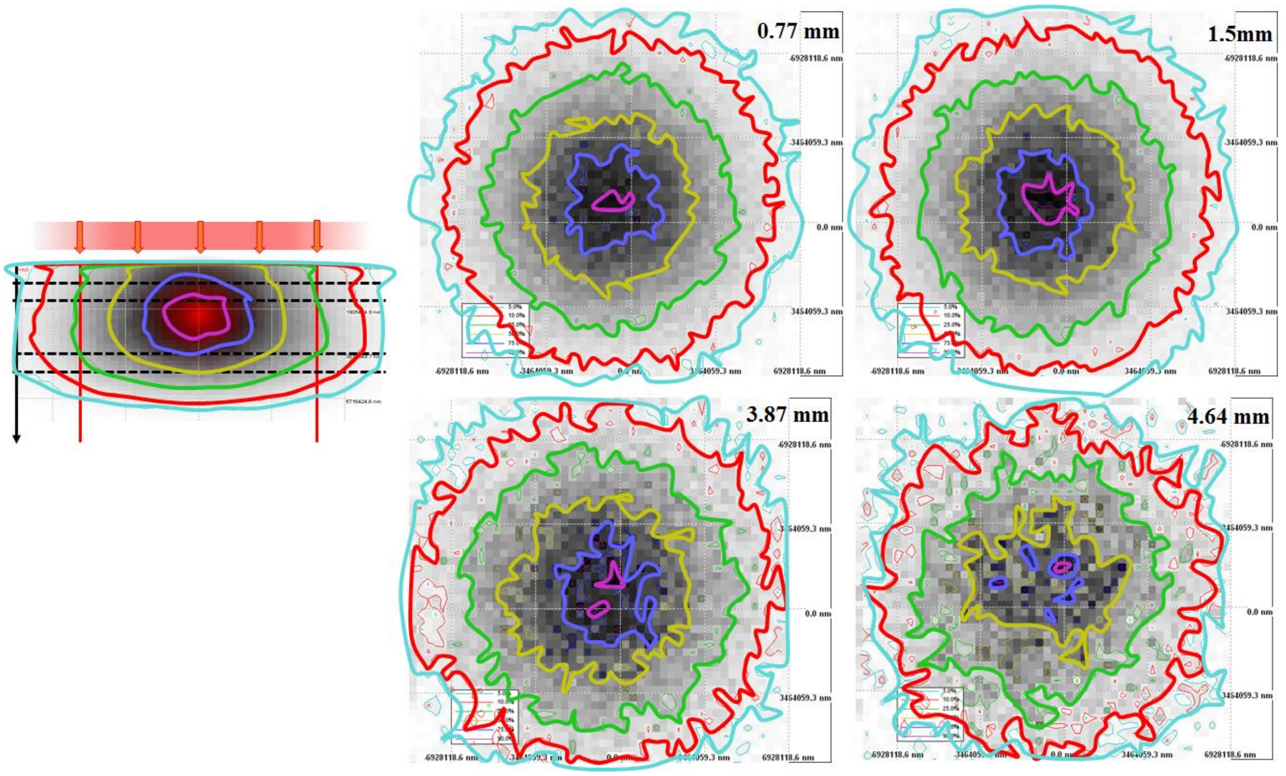

Figure 3. Distribution of electron energy losses along the beam axis and cross sections perpendicular to the beam axis

The maximum electron beam energy losses are near the beam axis. The distribution of specific energy losses in sections perpendicular to the beam axis at depths of 0.77, 1.5, 3.87, and 4.64 mm is similar along the entire beam path, but differs in absolute value. In general, the energy losses along the beam axis change according to the regularity shown in Figure 2. The losses are maximum in the region of the beam axis. The losses decrease with distance from the axis. In the section perpendicular to the axis, the specific losses are described by a circle with the centre on the axis. However, they differ due to the variation of the cross-sectional diameter of the energy loss region as the beam passes through. The diameter of the circle increases as it moves away from the surface, reaches a maximum value, and then decreases.

Discussion

In order to optimize the modes of radiation synthesis of ceramics, studies of the dependence of the synthesis result on the electron flux power density on the charge surface, which is set in the experiment and well controlled, are carried out. As shown above, the distribution of the absorbed radiation dose is not homogeneous over the irradiated volume both in the depth of the beam passage and in the cross section. The redistribution of absorbed energy in the volume should affect the morphology of the synthesized sample. This effect should certainly be taken into account during synthesis. Therefore, it is necessary to establish a relationship between the electron flux power density on the charge surface and the beam energy losses in the irradiated region of the charge. To establish the relationship, we introduce the following definitions: integral electron beam power density and specific beam energy losses in the charge volume. Under integral we will understand the power density averaged over the entire beam area on the charge surface P_I. Under specific energy losses we will understand the energy losses of the electron flux in the unit of elementary volume W_L in the irradiated area of the material with given coordinates.

For the synthesis of ceramics in the field of high-energy electron flow in [17-18], a Gaussian electron beam with a diameter of 1.2 cm was usually used on the surface of the charge with an area of about 1 cm^2. The energy loss is maximum along the axis of the beam passing through the medium along the entire electron flow path. Along the beam axis, the energy loss increases, then decreases to 0 (Fig. 2). Energy losses along the beam axis are maximum at some depth from the surface, depending on the electron energy and absorption capacity of the substance. In the cross-section transverse to the axis, the energy losses of the electron flow decrease from the maximum on the beam axis to 0. The diameter of the specific energy loss distribution area grows along the beam axis to the maximum, then decreases. The distribution of specific energy losses in the cross-section of the beam has a bell-shaped form similar to the one shown in Figure 4.

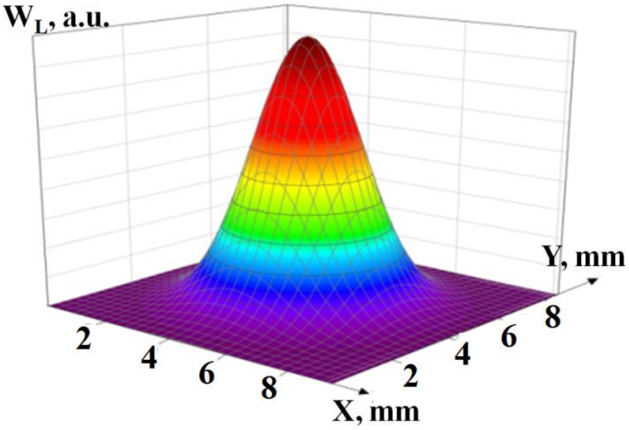

Figure 4. Distribution of specific energy losses of electron flow in the cross-section perpendicular to the beam axis

This distribution of specific losses is qualitatively similar for all modes of radiation exposure at the same experiment geometry and electron energy. With increasing integral power density, only absolute values of specific losses grow proportionally, but the picture does not change qualitatively. Specific energy losses in the whole volume of irradiated matter also grow proportionally.

In order to form ceramics in the radiation field it is necessary to overcome the threshold for the realisation of this process. Synthesis is realised in those areas of the charge in which specific energy losses of the radiation flux exceed this threshold. Therefore, the morphology of the sample obtained by the radiation method reflects the distribution of energy losses.

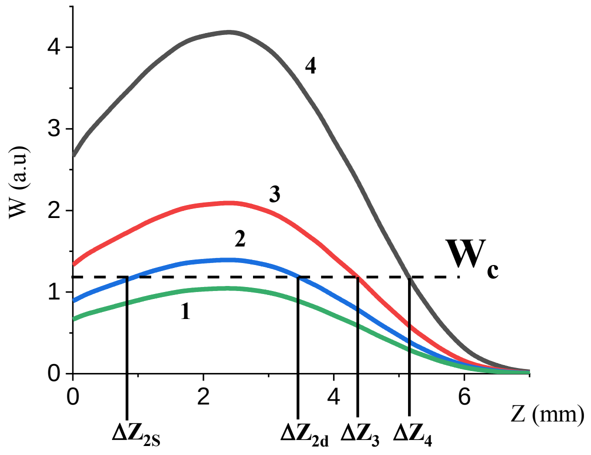

Figure 5. Distribution of specific energy losses of electron flux along the beam axis

Figure 5 shows the results of calculations of the values of specific energy losses of the electron flux with energy of 1.4 MeV along the beam axis in the charge. The results are presented in relative units of integral values of the electron flux power density $W_{L,\ a.u.}$ at the same exposure time, differing in the ratio 4:3:2:1. The dotted line indicates the value of the threshold of specific electron flux energy losses W_c, sufficient to realise the synthesis. Synthesis is realised in those regions where specific electron flux energy losses are sufficient or exceed the threshold. Synthesis is not realised at $W_{L,\ a.u.}$ (1), it is realised on the electron flow path with $W_{L,\ a.u.}$ (3), $W_{L,\ a.u.}$ (4) in the range from 0 to ΔZ_3 and ΔZ_4, respectively, as well as in the range from ΔZ_{2s} to ΔZ_{2d} at $W_{L,\ a.u.}$ (2). This explains the experimentally observed facts. At small values of the integral power density of the electron flux, fusion is realised in the subsurface layer. The thickness of the synthesised ceramics increases with increasing integral electron flux power density.

Acknowledgements

This research has been/was/is funded by the Science Committee of the Ministry of Science and Higher Education of the Republic of Kazakhstan (Grant No. AP23490986)

This research was funded by the Ministry of Trade and Integration of the Republic of Kazakhstan (Grant No. BR12967832)

References

1 Voogt, E. L. K., van Rees, J. M., Hagemans, J. A. W., Rothbarth, J., Nieuwenhuijzen, G. A. P., Cnossen, J. S., Peulen, H. M. U., Dries, W. J. F., Nuyttens, J., Kolkman-Deurloo, I.-K., Verhoef, C., Rutten, H. J. T., & Burger, J. W. A. (2021). Intraoperative electron beam radiation therapy (IOERT) versus high-dose-rate intraoperative brachytherapy (HDR-IORT) in patients with an R1 resection for locally advanced or locally recurrent rectal cancer. *International Journal of Radiation Oncology*Biology*Physics*, *110*(4), 1032–1043. https://doi.org/10.1016/j.ijrobp.2021.02.006

2 Kurokawa, C. (2023). 3 physics for electron beam therapy. *Japanese Journal of Radiological Technology*, *79*(10), 1194–1199. https://doi.org/10.6009/jjrt.2023-2264

3 Sehrish Abrar, Bilal Mazhar Qureshi, Asim Hafiz, Nasir Ali, Agha Mohammad Hammad Khan, & Ahmed Nadeem Abbasi (2022). Total skin electron beam therapy (TSEBT) in management of mycosis fungoides: A case series. *Journal of the Pakistan Medical Association*. https://doi.org/10.47391/jpma.3784

4 Tavallaie, M., Hariri Tabrizi, S., & Heidarloo, N. (2022). Implementation of pencil beam redefinition algorithm (PBRA) for intraoperative electron radiation therapy (IOERT) treatment planning. *Physica Medica*, *104*, 32–42. https://doi.org/10.1016/j.ejmp.2022.10.015

5 Gan, L., & Jensen, G. J. (2011). Electron tomography of cells. *Quarterly Reviews of Biophysics*, *45*(1), 27–56. https://doi.org/10.1017/s0033583511000102

6 Koike, T., & Yamada, H. (2018). Methods for array tomography with correlative light and electron microscopy. *Medical Molecular Morphology*, *52*(1), 8–14. https://doi.org/10.1007/s00795-018-0194-y

7 Wan, W., & Briggs, J. A. G. (2016). Cryo-electron tomography and subtomogram averaging. *Methods in Enzymology*, 329–367. https://doi.org/10.1016/bs.mie.2016.04.014

8 Bárcena, M., & Koster, A. J. (2009). Electron Tomography in life science. *Seminars in Cell & Developmental Biology*, *20*(8), 920–930. https://doi.org/10.1016/j.semcdb.2009.07.008

9 Zheng, T., & Cai, S. (2024). Recent technical advances in cellular cryo-electron tomography. *The International Journal of Biochemistry & Cell Biology*, *175*, 106648. https://doi.org/10.1016/j.biocel.2024.106648

10 Wu, Y. C., Zhu, B., Li, G., Zhang, X. H., Yu, M. H., Dong, K. G., Zhang, T. K., Yang, Y., Bi, B., Yang, J., Yan, Y. H., Tan, F., Fan, W., Lu, F., Wang, S. Y., Zhao, Z. Q., Zhou, W. M., Cao, L. F., & Gu, Y. Q. (2018). Towards high-energy, high-resolution computed tomography via a laser driven micro-spot gamma-ray source. *Scientific Reports*, *8*(1). https://doi.org/10.1038/s41598-018-33844-7

11 Sharifi, S., Sharifi, H., Guild, C., Islam, M. M., Tran, K. D., Patzer, C., Dohlman, C. H., Paschalis, E. I., Gonzalez-Andrades, M., & Chodosh, J. (2021). Toward electron-beam sterilization of a pre-assembled Boston keratoprosthesis. *The Ocular Surface*, *20*, 176–184. https://doi.org/10.1016/j.jtos.2021.02.009

12 Sharifi, S., Islam, M. M., Sharifi, H., Islam, R., Huq, T. N., Nilsson, P. H., Mollnes, T. E., Tran, K. D., Patzer, C., Dohlman, C. H., Patra, H. K., Paschalis, E. I., Gonzalez- Andrades, M., & Chodosh, J. (2021). Electron beam sterilization of poly(methyl methacrylate)—physicochemical and biological aspects. *Macromolecular Bioscience*, *21*(4). https://doi.org/10.1002/mabi.202000379

13 Wilińska, J., Turek, A., Borecka, A., Rech, J., & Kasperczyk, J. (2019). Electron beam sterilization of implantable rods with risperidone and with 17-β-estradiol: a structural, thermal and morphology study. *Acta of Bioengineering and Biomechanics*, *21*(3), 39–47.

14 Ulakhanov, N. S., Mishigdorzhiyn, U. L., Shin, V. I., Moskvin, P. V., Mokeev, M. A., Vorobyov, M. S., & Tikhonov, A. G. (2024). Electron beam treatment of diffusion B–al layers on 3Kh2V8F steel surfaces. *Bulletin of the Russian Academy of Sciences: Physics*, *88*(4), 664–670. https://doi.org/10.1134/s1062873823706347

15 Egorov, I.S., Kaikanov, M.I., Lukonin, E.I., Remnev, G.E., & Stepanov, A.V. (2013). The astra repetitive-pulse electron accelerator. *Instruments and Experimental Techniques*, *5*, 81–84. DOI: https://doi.org/10.7868/s0032816213050030

16 Vorobyov, M. S., Ivanov, Y. F., Akhmadeev, Y. H., Moskvin, P. V., Petrikova, E. A., & Lopatin, I. V. (2018). Surface structure and properties of high-chromium steel irradiated with a submillisecond pulsed electron beam. *Journal of Physics: Conference Series*, *1115*, 032064. https://doi.org/10.1088/1742-6596/1115/3/032064

17 Lisitsyn, V., Tulegenova, A., Golkovski, M., Polisadova, E., Lisitsyna, L., Mussakhanov, D., & Alpyssova, G. (2023). Radiation synthesis of high-temperature wide-bandgap ceramics. *Micromachines*, *14*(12), 2193. https://doi.org/10.3390/mi14122193

18 Lisitsyn, V., Tulegenova, A., Kaneva, E., Mussakhanov, D., & Gritsenko, B. (2023). Express synthesis of YAG:CE ceramics in the high-energy electrons flow field. *Materials*, *16*(3), 1057. https://doi.org/10.3390/ma16031057

19 Tabata, T., Andreo, P., & Shinoda, K. (1998). An algorithm for depth–dose curves of electrons fitted to Monte Carlo data. *Radiation Physics and Chemistry*, *53*(3), 205–215. https://doi.org/10.1016/s0969-806x(98)00102-9

20 Tatsuo, T., Pedro, A., Kunihiko, S., & Rinsuke, I. (1994). Energy deposition through radiative processes in absorbers irradiated by electron beams. *Nuclear Instruments and Methods in Physics Research Section B: Beam Interactions with Materials and Atoms*, *93*(4), 447–456. https://doi.org/10.1016/0168-583x(94)95633-2

21 Lisitsyn, V., Mussakhanov, D., Tulegenova, A., Kaneva, E., Lisitsyna, L., Golkovski, M., & Zhunusbekov, A. (2023). The optimization of Radiation Synthesis Modes for YAG:CE Ceramics. *Materials*, *16*(8), 3158. https://doi.org/10.3390/ma16083158

22 Joly, D., Poirier-Demers, N., & Demers, H. (2011). *Casino 3.2 user manual*. Casino 3.2 User Manual. https://casino.espaceweb.usherbrooke.ca/fichiers/User_Manual_Casino_3.2.pdf

23 Joy, D. C., & Luo, S. (1989). An empirical stopping power relationship for low- energy electrons. *Scanning*, *11*(4), 176–180. https://doi.org/10.1002/sca.4950110404

24 Drouin, D., Hovington, P., & Gauvin, R. (1997). Casino: A New Monte Carlo Code in C language for electron beam interactions—part II: Tabulated values of the Mott Cross section. *Scanning*, *19*(1), 20–28. https://doi.org/10.1002/sca.4950190103

25 Hovington, P., Drouin, D., & Gauvin, R. (1997). Casino: A New Monte Carlo Code in C language for electron beam interaction — part I: Description of the program. *Scanning*, *19*(1), 1–14. https://doi.org/10.1002/sca.4950190101

Д.А. Мусаханов, А.С. Көбей, М.Г. Голковский, А.Т. Тулегенова

Электрон ағыны энергиясының заттағы сіңірілуінің таралуының сәуле көлденең қимасына тәуелділігі

Кеңістікте шектелген электрон сәулелері дәнекерлеу, кесу, бетті өңдеу сияқты технологиялық операцияларда кеңінен қолданылады. Электрондардың зат арқылы өтуі кезінде сәуле энергиясының шығындары қайта бөлінеді. Осы жұмыста Монте-Карло әдісін қолдана отырып ұсынылған энергия шығынын модельдеу нәтижелері зат көлеміндегі энергия шығынын қайта бөлуді көрсетеді. Электрон сәулесі материалға тереңірек енген сайын энергия шығынының артуы және кейіннен кемуі байқалады. Сәуле осіне перпендикуляр бағытта энергия шығыны аймағының кеңеюі және кейіннен осы аймақтың диаметрінің азаюы байқалады. Ұсынылған есептеулер отқа төзімді диэлектрлік керамиканы синтездеу нәтижелерін жақсы түсіндіреді. Заттағы энергия шығындарының қайта бөлінуі синтезделген үлгілердің морфологиясын анықтайды.

Кілт сөздер: синтез, YAG:Ce керамикасы, жоғары қуатты электрон ағыны, энергия шығыны, Монте-Карло әдісі, Гаусс ағынының таралуы, CASINO V2.5, меншікті энергия шығындары.

Д.А. Мусаханов, А.С. Кобей, М.Г. Голковский, А.Т. Тулегенова

Зависимость распределения поглощенной энергии потока электронов в веществе от поперечного сечения пучка

Пучки электронов, ограниченные в пространстве, широко используются в технологических операциях сварки, резки и обработки поверхности. При прохождении электронов в веществе происходит перераспределение потерь энергии пучка. Результаты моделирования потерь энергии с использованием метода Монте-Карло, представленные в данной работе, демонстрируют перераспределение потерь энергии в объеме вещества. Наблюдается увеличение, а затем уменьшение потерь энергии по мере углубления электронного пучка в материал. В направлении, перпендикулярном оси пучка, происходит расширение области потерь энергии, а затем уменьшение диаметра этой области. Представленные расчеты хорошо объясняют результаты синтеза тугоплавкой диэлектрической керамики. Перераспределение потерь энергии в веществе определяет морфологию синтезированных образцов.

Ключевые слова: синтез, керамика YAG:Ce, высокомощный поток электронов, потери энергии, метод Монте-Карло, гауссово распределение потока, CASINO V2.5, удельные потери энергии.

Information about the authors

Mussakhanov D.A. (corresponding author) — Candidate of technical sciences, Senior teacher, Institute of Physical and Technical Sciences, L.N. Gumilyov Eurasian National University, Astana 010000, Kazakhstan; e-mail: *dosymma@gmail.com*, ORCID ID: 0000-0002-1823-2526

Kobey Abylay — PhD student, Institute of Physical and Technical Sciences, L.N. Gumilyov Eurasian National University, Astana 010000, Kazakhstan; e-mail: kobeyablay@gmail.com, ORCID ID: https://orcid.org/0009-0005-8707-4671

Golkovski M.G. — Candidate of physical and mathematical sciences, Senior researcher, Budker Institute of Nuclear Physics, Academician Lavrentiev avenue, 11, Novosibirsk, Russia, e-mail: *golkovski@mail.ru*. ORCID ID: https://orcid.org/0000-0003-4399-444X

Aida Tulegenova — Candidate of physical and mathematical sciences, Acting assistant professor, Institute of Applied Science & Information Technology, al-Farabi Kazakh National University, Almaty, Kazakhstan; e-mail: *tulegenova.aida@gmail.com*; https://orcid.org/0000-0002-5701-6674

Article
https://doi.org/10.31489/2024PH4/175-182
UDC661.961.6

Received: 01.07.2024
Accepted: 28.08.2024

M.K. Skakov[1], A.Zh. Miniyazov[2,3], I.A. Sokolov[2,3], A.A. Agatanova[2,3*]
T.R. Tulenbergenov[2,3], A.V. Gradoboev[4]

[1]*RSE "National Nuclear Center of the Republic of Kazakhstan", Kurchatov, Kazakhstan;*
[2]*"Institute of Atomic Energy" Branch RSE NNC RK, Kurchatov, Kazakhstan;*
[3]*JSC "Shakarim University of Semey", Semey, Kazakhstan;*
[4]*National Research Tomsk Polytechnic University, Tomsk, Russia*
([*]Corresponding author's e-mail: agatanova@nnc.kz)

Hydrogen from Methane: Application of Microwave Discharge and Catalyst

This paper presents the results of experiments to produce hydrogen using methane pyrolysis with microwave (MW) discharge and steel catalyst in an applied research installation PM-6. The experiments were conducted to determine the fullest extent of methane decomposition in microwave discharge in the PM-6 installation using steel catalyst with varied nickel content. The results showed that the use of nickel catalysts provides the highest hydrogen yield under optimal conditions. Hydrogen production technology was implemented using catalyst in MW discharge with the maximum rate of methane conversion up to 32±2 % and hydrogen selectivity up to 85±1 % at MW discharge of 0.6 kW, methane flow rate of 0.25±0.05 l/min and argon 8.0±0.2 l/min. Overall, the results of the study highlight the importance of choosing catalysts to achieve optimal conditions for methane pyrolysis and create efficient technologies for hydrogen production. The data obtained from the experiments could be useful for the development of industrial pyrolysis plants, which will contribute to a more sustainable energy future and a reduced carbon footprint.

Keywords: hydrogen, methane pyrolysis, hydrogen energy, microwave discharge, methane conversion, carbon, hydrogen selectivity, catalyst.

Introduction

Hydrogen energy has been gaining increasing popularity in recent years. Hydrogen can be used for energy storage, accumulation, and delivery. In this context, hydrogen energy stands out as one of the most promising directions. Consequently, developed countries are developed their own hydrogen energy strategies to meet the annually increasing demand for clean energy [1, 2].

Hydrogen can be produced from various raw material sources using a wide range of technologies. Currently, natural gas is the primary feedstock for hydrogen production, accounting for 68 % of the total hydrogen production worldwide in 2023 [3]. Therefore, to ensure the sustainable use of hydrogen, it is necessary to develop efficient and environmentally friendly production methods. Methane pyrolysis is one such method, which, unlike traditional methods, significantly reduces CO_2 emissions [4–6]. Furthermore, research results have shown that methane pyrolysis is more economically advantageous compared to traditional hydrogen production methods due to lower feedstock costs, high product purity, and the possibility of utilizing by-products [7–10].

In this article, methane pyrolysis is implemented using a microwave discharge. The pyrolysis process in a microwave discharge allows for the achievement of the necessary temperatures and conditions for pyrolysis, significantly reducing reaction time and increasing the yield of target products [11]. It is necessary to optimize the process, particularly through the use of catalysts to enhance the efficiency of pyrolysis and achieve high selectivity for hydrogen.

Catalysts can be used to increase the efficiency of moment pyrolysis and research is currently underway into various materials for use in this process. One of the key factors in enhancing the conversion rate of methane is increasing the temperature of the catalyst since it heats the passing gas. As a result, excited atoms and molecules of methane passing through the catalyst, heated by the energy of the microwave discharge, undergo the decomposition of methane molecules under the influence of chemically active plasma particles (ions, electrons, free radicals).

In addition, the catalyst must have both good catalytic activity and a long service life, as well as low cost. In this regard, many studies of catalysts such as Ni and Fe have been conducted to improve the catalytic activity of methane pyrolysis [8, 12–19]. The main factors affecting the effectiveness of the catalyst application should be taken into account, such as temperature and time of gas contact with the catalyst, textural properties, material composition and method of catalyst synthesis when choosing the material used in the catalyst.

The integration of methane pyrolysis with high-frequency discharge technologies and metallic catalysts can lead to the creation of closed cycles that promote cleaner and more sustainable hydrogen production. Thus, this article presents the current results of experimental studies on methane pyrolysis in a microwave discharge using a catalyst.

Experimental

Experiments were conducted using the setup for studying the plasma-chemical decomposition of methane in the microwave discharge PM-6 [20]. Data on the pyrolysis of methane have previously been obtained at the IAE RSENNC RK, and the results are presented in works [21, 22]. The schematic layout of the catalyst in the PM-6 installation is shown in Figure 1.

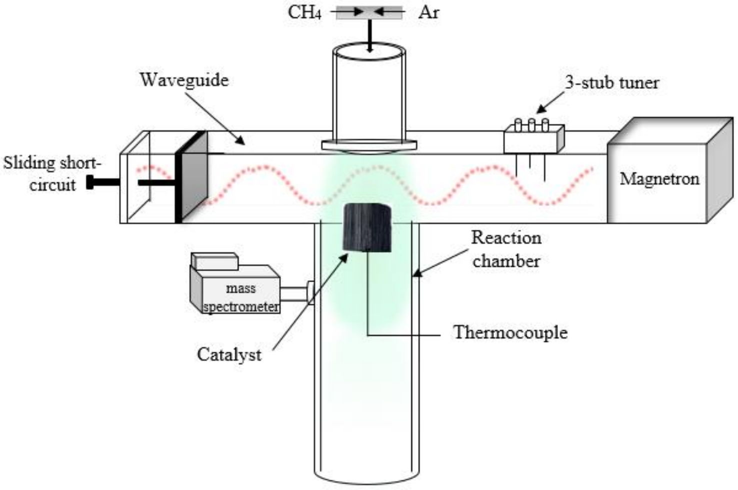

Figure 1. The schematic layout of the catalyst placement in the PM-6 installation

Astainless-steel metal sample was chosen as a catalyst according to literature data [5, 23, 24]. The research [7] has been shown that the use of a catalyst made of nickel and carbon-containing materials in the pyrolysis of natural gas can increase the formation of hydrogen in the mixture of gaseous products. In this regard, it was decided to apply a Ni coating to the steel catalyst.

During this research, 3 series of experiments were fulfilled using the following materials:

- Stainless Steel catalyst (Initial);
- Stainless Steel catalyst, plated nickel catalyst;
- Stainless Steel catalyst electrochemically plated by nickel.

For nickel coating, the steel catalyst was placed in a nitric acid (HNO_3) solution to remove contaminants. Nickel nitrate ($Ni(NO_3)_2$) was used as the solution for electroless nickel coating. The composition of the liquid electrolyte in which the product was immersed for electroless coating also included nickel nitrate ($Ni(NO_3)_2$). Figure 2 shows a 20 mm long and 25.5 mm diameter steel catalyst.

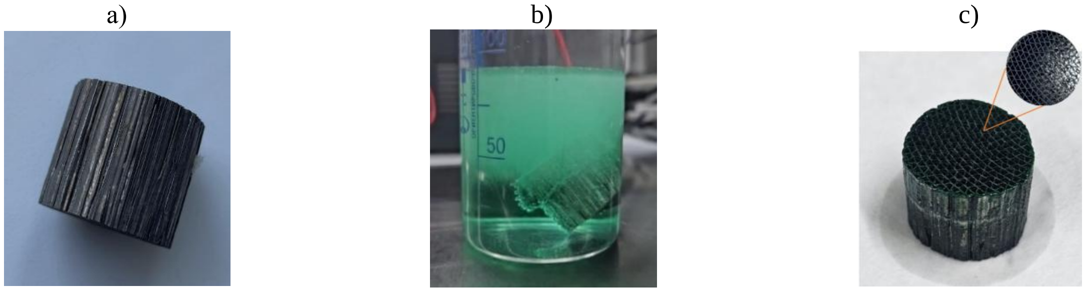

a) Initial; b) During electrochemical deposition; c) Nickel plated;

Figure 2. Process of coating the initial catalyst

Upon coating, elemental analysis of the catalysts was performed using a Hitachi TM4000Plus scanning electron microscope (SEM) with an EDS attachment. Figure 3 shows the results.

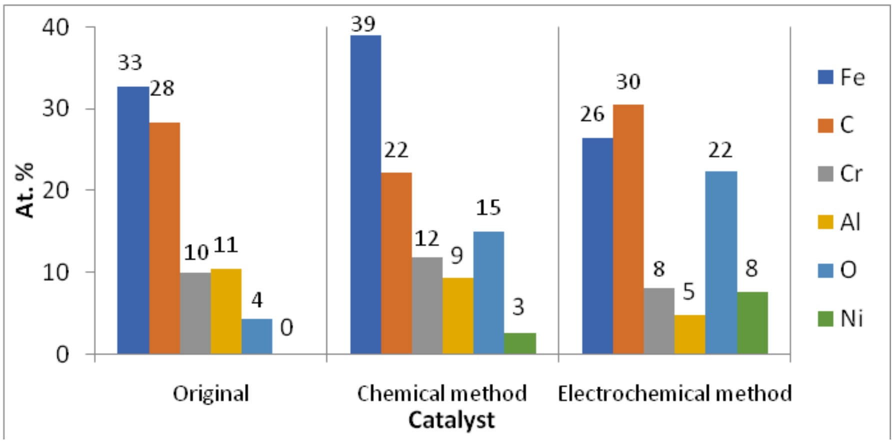

Figure 3. Elemental analysis of the catalyst surface after nickel coating

According to the results of elemental analysis, it is obvious that the electrochemical method of coating is more effective, since the composition of Ni in the catalyst increased by 5 at.%.

Experiments on methane decomposition in the PM-6 installation were conducted in a microwave discharge. A mixture of working gases of methane and argon was fed into a reaction chamber made of quartz glass with a length of 460 mm and an internal diameter of 26 mm. The reflected power was monitored on the magnetron control unit in all experiments and was reduced to “0”. Argon was used as a plasma-forming gas for igniting the plasma, into which methane was smoothly fed. The carbon powder deposited on the catalyst (Fig. 4) on the wall of the quartz tube was mechanically removed and collected for analysis after each experiment.

a) catalyst

b) reaction chamber

Figure 4. View after the experiment

Results and Discussion

The reaction products were analyzed using a mass spectrometer “CIS100Gas Analyzers” based on partial gas pressures.

Based on the mass spectrometric analysis data, a qualitative and quantitative evaluation of the methane decomposition rate and hydrogen selectivity was performed.

The methane conversion rate K_{CH_4} is a qualitative value that determines the proportion of methane that has entered into a chemical reaction from the overall original methane. The methane conversion rate was calculated using the following formula:

$$K_{CH_4} = \frac{P_{CH_4}(\text{in}) - P_{CH_4}(\text{out})}{P_{CH_4}(\text{in})} \cdot 100\ \% \quad (1)$$

Product selectivity S_{H_2} is a qualitative evaluation determining the proportion of methane from a chemical reaction was used to form the target product that is hydrogen. In this work, hydrogen selectivity was calculated using the formula [25]:

$$S_{H_2} = \frac{1}{2} \cdot \frac{P_{H_2}(\text{out}) - P_{H_2}(\text{in})}{P_{CH_4}(\text{in}) - P_{CH_4}(\text{out})} \cdot 100\,\% \qquad (2)$$

Figure 5 shows the partial pressure diagram of gases. In formulas (1) and (2) $P_{H_2}(\text{in})$ and $P_{CH_4}(\text{in})$ are the partial pressures of hydrogen and methane at the beginning of the experiment, $P_{H_2}(\text{out})$ and $P_{CH_4}(\text{out})$ are the partial pressures of hydrogen and methane at the end of the experiment.

a) Ni = 0 at.%; b) Ni = 3 at.%;

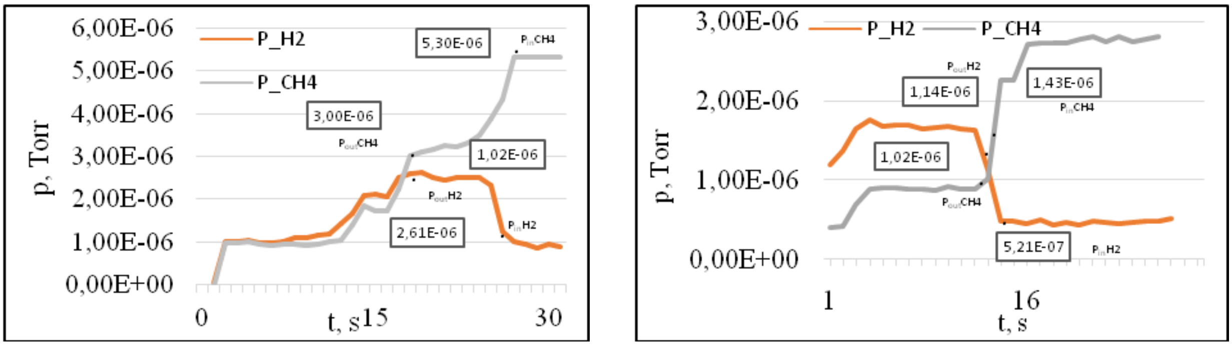

c) Ni = 8 at.%.

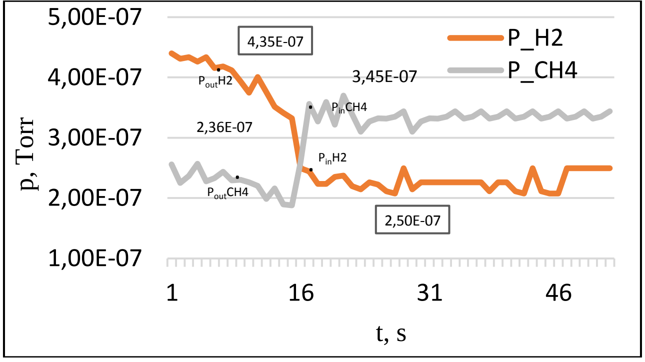

Figure 5. Diagram of partial pressures of gases in the result of the decomposition of methane with different nickel content in the catalyst

Table 1 shows the calculation data for the rate of methane conversion and hydrogen selectivity.

Table 1

Results of calculations of qualitative characteristics of conversion

#	W_{MW}, kW	Q_{Ar}, l/min	Q_{CH4}, l/min	T, °C	, %	, %
1	0.6	8.0±0.2	0.25±0.05	650±70	36±1	34±2
2					28±1	74±1
3					32±2	85±1
Note – W_{MW} — magnetron power, Q_{Ar} — argon consumption, Q_{CH4} — methane consumption, T — catalyst temperature, K_{CH_4} — methane conversion rate, S_{H_2} — hydrogen selectivity.						

Figure 6 shows a diagram of the dependence of the rate of methane conversion and hydrogen selectivity on the amount of nickel in the elemental composition of the catalyst.

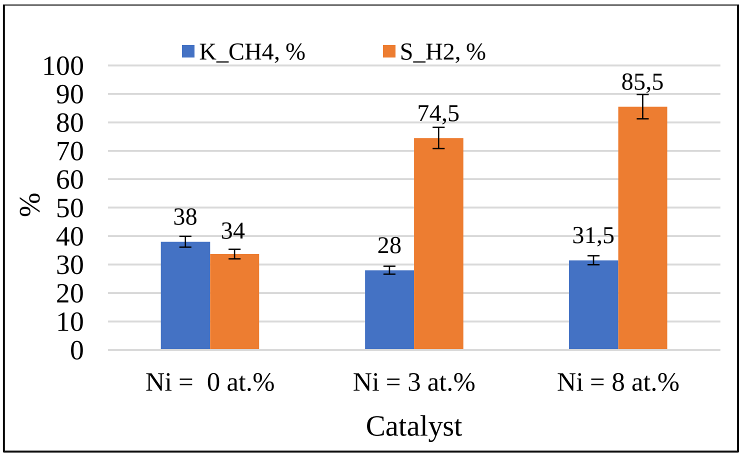

Figure 6. Diagram of the dependence of the rate of methane decomposition and hydrogen selectivity on at.% Ni in the catalyst

Figure 6 evidences that increasing the nickel content in the catalyst contributes to an increase in hydrogen selectivity.

Conclusions

Experiments were conducted to determine the maximum of methane decomposition rate in the microwave discharge using the PM-6 installation with a steel catalyst with varied nickel content. Three series of experiments were conducted with the same microwave discharge power, catalyst temperature, argon and methane flow rates. Based on the results of the experiments, it was found that increasing the Ni content in the steel catalyst to increase the rate of methane conversion and hydrogen selectivity is effective. The catalyst with 8 at.% nickel content, deposited electrochemically, showed the maximum hydrogen selectivity value.

Analysis of the reaction kinetics showed that the use of catalysts not only increases the rate of pyrolysis, but also helps improve the energy efficiency of the process.

Acknowledgements

The work was carried out within the framework of program-targeted financing by the Ministry of Science and Higher Education of the Republic of Kazakhstan (No. BR21882200).

References

1 Midilli A. On hydrogen and hydrogen energy strategies. I. Current status and needs / A. Midilli, M. Ay, I. Dincer, M.A. Rosen // Renewable Sustainable Energy Rev. — 2005. — 9, No. 3. — P. 255—271.

2 Чистые технологии для устойчивого будущего Евразии / под ред. Е. Винокурова. — М.: Евразийский банк развития; Ассоциация «Глобальная энергия», 2021.

3 Global Hydrogen Review 2023, Source: IEA. International Energy Agency. — [Electronic resource] — Access mode: www.iea.org.

4 Gaudernack B., Lynum S. Hydrogen from natural gas without release of CO2 to the atmosphere // International Journal of Hydrogen Energy. — 1998. — Vol. 23. — No. 12. — P. 1087–1093. — DOI: https://doi.org/10.1016/S0360-3199(98)00004-4.

5 Czernichowski A. Pyrolysis of natural gas in the gliding electric discharges / A. Czernichowski, P. Czernichowski // 10th Canadian Hydrogen Conference. — 2000. — P. 28–31.

6 Макарян И. Современные подходы к получению водорода из углеводородного сырья / И. Макарян, И. Седов, А. Никитин, В. Арутюнов // Науч. журн. Российского газового общества. — 2020. — Вып. 1 (24). — С. 50–68.

7 Lestinsky P., Zikmund Z., Grycova B., Ryczkowski R., Grams J., Inayat A. Production of hydrogen over Ni/carbonaceous catalyst // Fuel. — 2020. — Vol. 278. — P. 118398. — DOI: 10.1016/j.fuel.2020.11839.

8 Guil-López R., La Parola V., Peña M. A., Fierro J. L.G. Hydrogen production via CH4 pyrolysis: Regeneration of ex hydrotalcite oxide catalysts // Catalysis Today. — 2006. — Vol. 116(3). — P. 289–297. — DOI: 10.1016/j.cattod.2006.05.07.

9 Keipi T., Tolvanen H., Konttinen J. Economic analysis of hydrogen production by methane thermal decomposition: Comparison to competing technologies // Energy Conversion and Management. — 2018. — Vol. 159. — P. 264–273. — DOI: 10.1016/j.enconman.2017.12.063.

10 Serrano D. P., Botas J. A., Fierro J. L. G., Guil-López R., Pizarro P., Gómez G. Hydrogen production by methane decomposition: Origin of the catalytic activity of carbon materials // Fuel. — 2010. — Vol. 89(6). — P. 1241–1248. — DOI: 10.1016/j.fuel.2009.11.030.

11 Kassel L.S. The thermal decomposition of methane // Journal of the American Chemical Society. — 1932. — Vol. 54(10). — P. 3949–3961. — DOI: 10.1021/ja01349a019.

12 Abdullah A., Shakeel A., Fahad Al-Muh. Thermochemical Hydrogen Production — Plasma-Based Production of Hydrogen from Hydrocarbons // In: Hydrogen Science and Engineering: Materials, Processes, Systems and Technology. — 2016. — P. 131–150. — DOI: 10.1002/9783527674268.ch07.

13 Suelves I., Lázaro M. J., Moliner R., Corbella B. M., Palacios J. M. // International Journal of Hydrogen Energy. — 2005. — Vol. 30. — P. 1555–1567.

14 Jang H. O., Cha W. S. // Korean Journal of Chemical Engineering. — 2007. — Vol. 24. — P. 374–377.

15 Qian W., Liu T., Wei F., Wang Z., Li Y. // Applied Catalysis A: General. — 2004. — Vol. 258. — P. 121–124.

16 Li Y., Chen J., Qin Y., Chang L. // Energy Fuels. — 2000. — Vol. 14. — P. 1188–1194.

17 Villacampa J. I., Royo C., Romeo E., Montoya J. A., del Angel P., Monzón A. Catalytic decomposition of methane over Ni–Al2O3 coprecipitated catalysts: reaction and regeneration studies // Applied Catalysis A: General. — 2003. — Vol. 252. — P. 363–383.

18 Wei J., Iglesia E. Mechanism and site requirements for activation and chemical conversion of methane on supported Pt clusters and turnover rate comparisons among noble metals // Journal of Physical Chemistry B. — 2004. — Vol. 108. — P. 4094–4103.

19 Zhao N. Q., He C. N., Ding J., Zou T. C., Qiao Z. J., Shi C. S., et al. Bamboo-shaped carbon nanotubes produced by catalytic decomposition of methane over nickel nanoparticles supported on aluminum // Journal of Alloys and Compounds. — 2007. — Vol. 428. — P. 79–83.

20 Патент на изобретение № 36605 Республики Казахстан. Устройство для получения водорода и твердого углерода на основе плазменного пиролиза метана в СВЧ-разряде / М.К. Скаков, А.Ж. Миниязов, В.В. Бакланов, Е.Т. Коянбаев, Т.Р. Туленбергенов, И.А. Соколов, Ғ.Қ. Жанболатова, Е.С. Бейсенов; заявитель на патентообладатель: РГП НЯЦ РК. — № 2022/0518.1; заявл. 25.08.2022; опубл. 16.02.2024.

21 Skakov M. Hydrogen production by methane pyrolysis in the microwave discharge plasma / M. Skakov, A. Miniyazov, Tulenbergenov T., Sokolov I., Zhanbolatova G., Kaiyrbekova A., Agatanova A. Hydrogen // AIMS Energy. — 2024. — Vol. 12(3). — P. 548–560. — DOI: 10.3934/energy.2024026.

22 Скаков М.К. Экспериментальное исследование конверсии метана в сверхвысокочастотном разряде/ М.К. Скаков, Т.Р. Туленбергенов, И.А. Соколов, А.Ж. Миниязов, А.А. Агатанова // Вестн. НЯЦ РК. — 2024. — Вып. 3. — С. 123–128. — DOI: 10.52676/1729-7885-2024-3-123-128.

23 Potapkin B. Microwave Discharge for the Environment Protection / B. Potapkin, V. Rusanov, V.K. Jivotov // Electrical Discharges for Environmental Purposes. Fundamentals and Applications / Ed. E.M. Van Veldhuizen. — Nova Science Publishers Inc., Huntington, 2000.

24 Fridman A. Plasma Chemistry. — Drexel University. — 2008. — ISBN-13 978-0-511-39857-5.

25 Wnukowski M., Gerber J., Mróz K. Shifts in product distribution in microwave plasma methane pyrolysis due to hydrogen and nitrogen addition // Methane. — 2022. — Vol. 1. — P. 286–299. — DOI: 10.3390/methane1040022.

М.К. Скаков, А.Ж. Миниязов, И.А. Соколов, А.А. Агатанова,
Т.Р. Туленбергенов, А.В. Градобоев

Метаннан сутегі өндірісі: аса жоғары жиілікті разряд пен катализаторды қолдану

Мақалада ПМ-6 қолданбалы зерттеу қондырғысында аса жоғары жиілікті (АЖЖ) разрядты және металл катализаторын қолдана отырып, метан пиролизі әдісімен сутегін алу бойынша тәжірибенің нәтижесі келтірілген. ПМ-6 қондырғысында аса жоғары жиілікті разрядта метан конверсиясының жоғары дәрежесін анықтау үшін, құрамында никель бар катализатор арқылы эксперименттер жүргізілді. Нәтижелер катализаторда никель құрамы жоғарылауы сутегі селективтілігінің жоғарылауына ықпал ететінін көрсетті. Метанның ең жоғары конверсия дәрежесі 32±2 % -ға дейін және сутегінің селективтілігі 85±1 % -ға дейін көрсеткіші, аса жоғары жиілікті разрядтың қуаты 0,6 кВт, метан шығыны 0,25±0,05 л/мин және аргон 8±0,2 л/мин қондырғы параметрлерінде қол жеткізілді. Жалпы алғанда, зерттеу нәтижелері метан пиролизінің оңтайлы шарттарына қол жеткізу және сутегі өндірісінің тиімді технологияларын құру үшін катализаторларды таңдаудың маңыздылығын көрсетеді. Тәжірибелерден алынған деректер өнеркәсіптік деңгейде метан пиролизін дамыту үшін пайдалы болуы мүмкін, бұл өз кезегінде энергияның тұрақты болашағына және көміртегі ізінің азаюына ықпал етеді.

Кілт сөздер: сутегі, метан пиролизі, сутегі энергетикасы, аса жоғары жиілікті разряд, метан конверсиясы, көміртек, сутегінің селективтілігі, катализатор.

М.К. Скаков, А.Ж. Миниязов, И.А. Соколов, А.А. Агатанова,
Т.Р. Туленбергенов, А.В. Градобоев

Водород из метана: применение СВЧ разряда и катализатора

В статье представлены результаты экспериментов по получению водорода методом пиролиза метана с применением сверхвысокочастотного (СВЧ) разряда и металлического катализатора с различным содержанием никеля на установке для прикладных исследований ПМ–6. Эксперименты проводились с целью определения наиболее полной степени разложения метана в микроволновом разряде на установке ПМ–6 с использованием стального катализатора с различным содержанием никеля. Результаты показали, что применение никелевых катализаторов обеспечивает наиболее высокий выход водорода при оптимальных условиях. Реализована технология получения водорода с использованием катализатора в СВЧ разряде с максимальной степенью конверсии метана до 32±2 % и селективностью водорода до 85±1 % при мощности СВЧ разряда 0,6 кВт, расходе метана 0,25±0,05 л/мин и аргона 8±0,2 л/мин. В целом, результаты исследования подчеркивают важность выбора катализаторов для достижения оптимальных условий пиролиза метана и создания эффективных технологий для производства водорода. Данные, полученные в ходе экспериментов, могут быть полезны для разработки промышленных установок пиролиза, что, в свою очередь, будет способствовать более устойчивому энергетическому будущему и снижению углеродного следа.

Ключевые слова: водород, пиролиз метана, водородная энергетика, сверхвысокочастотный разряд, конверсия метана, углерод, селективность водорода, катализатор.

References

1 Midilli, A., Ay, M., Dincer, I., & Rosen, M. A. (2005). On hydrogen and hydrogen energy strategies. I. Current status and needs. *Renewable Sustainable Energy Reviews, 9*(3), 255–271. https://doi.org/10.1016/j.rser.2004.05.002.

2 Vinokurov, E. (Ed.). (2021). *Chistye tekhnologii dlia ustoichivogo budushchego Evrazii [Clean technologies for the sustainable future of Eurasia].* Moscow: Evraziiskii bank razvitiia; Assotsiatsiia «Globalnaia energiia» [in Russian].

3 International Energy Agency (2023). Global hydrogen review. Retrieved from www.iea.org

4 Gaudernack, B., & Lynum, S. (1998). Hydrogen from natural gas without release of CO2 to the atmosphere. *International Journal of Hydrogen Energy*, *23*(12), 1087–1093. https://doi.org/10.1016/S0360-3199(98)00004-4.

5 Czernichowski, A., & Czernichowski, P. (2000). Pyrolysis of natural gas in the gliding electric discharges. In *Proceedings of the 10th Canadian Hydrogen Conference*, 28–31.

6 Makaryan, I., Sedov, I., Nikitin, A., & Arutyunov, V. (2020). Sovremennye podkhody k polucheniu vodoroda iz uglevodorodnogo syria [Modern approaches to hydrogen production from hydrocarbon feedstock]. *Nauchnyi zhurnal Rossiiskogo gazovogo obshchestva — Scientific Journal of the Russian Gas Society, 1* (24), 50–68 [in Russian].

7 Lestinsky, P., Zikmund, Z., Grycova, B., Ryczkowski, R., Grams, J., & Inayat, A. (2020). Production of hydrogen over Ni/carbonaceous catalyst. *Fuel, 278*, 118398. https://doi.org/10.1016/j.fuel.2020.118398.

8 Guil-López, R., La Parola, V., Peña, M. A., & Fierro, J. L. G. (2006). Hydrogen production via CH4 pyrolysis: Regeneration of ex hydrotalcite oxide catalysts. *Catalysis Today, 116*(3), 289–297. https://doi.org/10.1016/j.cattod.2006.05.007.

9 Keipi, T., Tolvanen, H., & Konttinen, J. (2018). Economic analysis of hydrogen production by methane thermal decomposition: Comparison to competing technologies. *Energy Conversion and Management*, *159*, 264–273. https://doi.org/10.1016/j.enconman.2017.12.063.

10 Serrano, D. P., Botas, J. A., Fierro, J. L. G., Guil-López, R., Pizarro, P., & Gómez, G. (2010). Hydrogen production by methane decomposition: Origin of the catalytic activity of carbon materials. *Fuel*, *89*(6), 1241–1248. https://doi.org/10.1016/j.fuel.2009.11.030.

11 Kassel, L. S. (1932). The thermal decomposition of methane. *Journal of the American Chemical Society*, *54*(10), 3949–3961. https://doi.org/10.1021/ja01349a019.

12 Abdullah, A., Shakeel, A., & Fahad Al-Muh. (2016). Thermochemical hydrogen production — Plasma-based production of hydrogen from hydrocarbons. In *Hydrogen Science and Engineering: Materials, Processes, Systems and Technology*, 131–150. https://doi.org/10.1002/9783527674268.ch07.

13 Suelves, I., Lázaro, M. J., Moliner, R., Corbella, B. M., & Palacios, J. M. (2005). *International Journal of Hydrogen Energy, 30*, 1555–1567.

14 Jang, H. O., & Cha, W. S. (2007). *Korean Journal of Chemical Engineering*, *24*, 374–377.

15 Qian, W., Liu, T., Wei, F., Wang, Z., & Li, Y. (2004). *Applied Catalysis A: General*, *258*, 121–124.

16 Li, Y., Chen, J., Qin, Y., & Chang, L. (2000). *Energy Fuels, 14*, 1188–1194.

17 Villacampa, J. I., Royo, C., Romeo, E., Montoya, J. A., del Angel, P., & Monzón, A. (2003). Catalytic decomposition of methane over Ni–Al2O3 coprecipitated catalysts: Reaction and regeneration studies. *Applied Catalysis A: General*, *252*, 363–383.

18 Wei, J., & Iglesia, E. (2004). Mechanism and site requirements for activation and chemical conversion of methane on supported Pt clusters and turnover rate comparisons among noble metals. *Journal of Physical Chemistry*, *108*, 4094–4103.

19 Zhao, N. Q., He, C. N., Ding, J., Zou, T. C., Qiao, Z. J., Shi, C. S., et al. (2007). Bamboo-shaped carbon nanotubes produced by catalytic decomposition of methane over nickel nanoparticles supported on aluminum. *Journal of Alloys and Compounds*, *428*, 79–83.

20 Skakov, M. K., Miniyazov, A. Zh., Baklanov, V. V., Koyanbaev, E. T., Tulenbergenov, T. R., Sokolov, I. A., Zhanbolatova, G. Q., & Beysenov, E. S. (2024). Patent No. 36605, Republic of Kazakhstan. Device for hydrogen and solid carbon production based on microwave discharge plasma pyrolysis of methane (Patent No. 2022/0518.1; filed August 25, 2022; published February 16, 2024) [in Russian].

21 Skakov, M. K., Miniyazov, A. Zh., Tulenbergenov, T. R., Sokolov, I. A., Zhanbolatova, G., Kaiyrbekova, A., & Agatanova, A. (2024). Hydrogen production by methane pyrolysis in the microwave discharge plasma. *AIMS Energy*, *12*(3), 548–560. https://doi.org/10.3934/energy.2024026.

22 Skakov, M.K., Tulenbergenov, T.R., Sokolov, I.A., Miniyazov, A.Zh., & Agatanova, A.A. (2024). Eksperimentalnoe issledovanie konversii metana v sverkhvysokochastotnom razriade [Experimental study of methane conversion in a high-frequency discharge]. *Vestnik Natsionalnogo yadernogo tsentra Respubliki Kazakhstan — Bulletin of the National Nuclear Center of the Republic of Kazakhstan, 3,* 123–128. https://doi.org/10.52676/1729-7885-2024-3-123-128 [in Russian].

23 Potapkin, B., Rusanov, V., & Jivotov, V. K. (2000). Microwave discharge for the environment protection. In E.M. Van Veldhuizen (Ed.). *Electrical discharges for environmental purposes: Fundamentals and applications*, 145–160. Nova Science Publishers Inc.

24 Fridman, A. (2008). Plasma Chemistry. Drexel University. ISBN 978-0-511-39857-5.

25 Wnukowski, M., Gerber, J., & Mróz, K. (2022). Shifts in product distribution in microwave plasma methane pyrolysis due to hydrogen and nitrogen addition. *Methane, 1*, 286–299. https://doi.org/10.3390/methane1040022.

Information about the authors

Alina Agatanova (corresponding author) — Engineer of the Laboratory of Hydrogen and Plasma Technologies, "Institute of Atomic Energy" Branch RSE NNC RK, Kurchatov, Kazakhstan; e-mail: *Agatanova@nnc.kz*; https://orcid.org/0009-0008-1404-1782

Mazhyn Skakov — Doctor of physical and mathematical sciences, Professor, Academician of KazNANS, Chief researcher of the Department of Budget Programs and Personnel Training, RSE National Nuclear Center of the Republic of Kazakhstan; e-mail: *skakov@nnc.kz*; https://orcid.org/0000-0003-3716-8846

Igor Sokolov — Head of the Laboratory of Hydrogen and Plasma Technologies, "Institute of Atomic Energy" Branch RSE NNC RK, Kurchatov, Kazakhstan; e-mail: *sokolov@nnc.kz*; https://orcid.org/0000-0002-7665-4022

Timur Tulenbergenov — Senior researcher of Hydrogen and Plasma Technologies, "Institute of Atomic Energy" Branch RSE NNC RK, Kurchatov, Kazakhstan; e-mail: *tulenbergenov@nnc.kz*; https://orcid.org/0000-0002-1541-6231

Arman Miniyazov — PhD, Director of the Center for Technological Competence in the Field of Hydrogen Energy of the branch of the Institute of Atomic Energy, RSE National Nuclear Center of the Republic of Kazakhstan; e-mail: *Miniyazov@nnc.kz*; https://orcid.org/0000-0002-2188-8075

Alexandr Gradoboev — Doctor of technical sciences, Professor of the Department of Experimental Physics of the School of Nuclear Engineering, National Research Tomsk Polytechnic University, Tomsk, Russia; e-mail: *Gava@tpu.ru*; https://orcid.org/0000-0002-2803-5972.

2024 жылғы
«Қарағанды университетінің хабаршысы. “Физика” сериясы»
журналында жарияланған мақалалардың көрсеткіші

Указатель статей, опубликованных в журнале
«Вестник Карагандинского университета. Серия “Физика”»
в 2024 году

Index of articles published in
«Bulletin of the Karaganda University. “Physics” Series»
in 2024

КОНДЕНСАЦИЯЛАНҒАН КҮЙДІҢ ФИЗИКАСЫ
ФИЗИКА КОНДЕНСИРОВАННОГО СОСТОЯНИЯ
PHYSICS OF THE CONDENSED MATTER

ТЕХНИКАЛЫҚ ФИЗИКА
ТЕХНИЧЕСКАЯ ФИЗИКА
TECHNICAL PHYSICS

ЖЫЛУФИЗИКАСЫ ЖӘНЕ ТЕОРИЯЛЫҚ ЖЫЛУТЕХНИКАСЫ
ТЕПЛОФИЗИКА И ТЕОРЕТИЧЕСКАЯ ТЕПЛОТЕХНИКА
THERMOPHYSICS AND THEORETICAL THERMOENGINEERING

КОНДЕНСАЦИЯЛАНҒАН ОРТАЛАРДАҒЫ РАДИАЦИЯЛЫҚ ПРОЦЕСТЕР
РАДИАЦИОННЫЕ ПРОЦЕССЫ В КОНДЕНСИРОВАННЫХ СРЕДАХ
RADIATION PROCESSES IN CONDENSED MATTER